UNIVERSITY OF SOUTHAMPTON

Microstructured polymer optical fibres fabricated from 3D printers for sensing applications

by

Wanvisa Talataisong

ORCiD ID: 0000-0003-1375-7830

A thesis submitted for

the degree of Doctor of Philosophy

in the

Faculty of Engineering and Physical Sciences

Optoelectronics Research Centre

August 2020

University of Southampton

ABSTRACT

FACULTY OF ENGINEERING AND PHYSICAL SCIENCES

OPTOELECTRONICS RESRACH CENTRE

Doctor of Philosophy

by Wanvisa Talataisong

ORCiD ID: 0000-0003-1375-7830

This research project had focused on the development of a novel optical fibre drawing technique based on a 3D printer to fabricate microstructured polymer optical fibres (MPOFs) in a single step for the sensing applications. The aim of this work is to overcome the drawbacks of the conventional drawing-tower based fabrication techniques, including the time-consuming, incapable of producing more complex non-geometrical structures, and high-cost.

The research starts with studying the sensing capabilities of micro/nanofibre devices. A nanofibre coupler (NFC) operating near the cut-off region of the higher order supermodes for thermal and refractive index sensing was proposed and experimentally demonstrated. The microfibre coupler (MFC) was also considered for biological sensing applications due to its large evanescent field. DNA covalent attachment on the coupler surface has been demonstrated through the functionalisation, immobilization and hybridization processes. Covalent attachment and hybridization of the DNA on the MFC surface was confirmed via the fluorescent image that shows successful bonding to the complementary DNA strand that contains a fluorescent label.

Then, the research was moved to establish new methods for manufacturing MPOFs sensors with built-in fluidic channels. The research started focusing on fibre preforms, with the design and 3D printing of a structured hollow-core polymer fibre preform. A commercial 3D printer was used to manufacture the preform, which was drawn into a hollow-core MPOF using a conventional fibre drawing tower. Guiding in the mid-IR was observed, with a propagation loss of 0.3 dB/mm at the wavelength of 4.5 μm. Although 3D printed structured polymer fibre preforms can be drawn into MPOF, large deformations in the fibre geometry were observed during the drawing process. Therefore, extrusion of MPOFs directly from a modified structured nozzle of a 3D printer was investigated.

3D printer nozzles, with structures complimentary to those of the MPOFs, were developed and fabricated by two techniques: micromachining and metal 3D printing. Simulations of heat transfer and material flow in the heated nozzle were also studied. Two structures of MPOFs were fabricated using this technique: the suspended-core fibre and the hexagonal hollow-core fibre. The suspended-core fibre was fabricated for guiding in the optical communication and Terahertz (THz) bands, while the hollow-core fibre for mid-IR and THz. The microstructure inside the MPOFs was maintained, and guiding in near-IR, mid-IR, and THz region was observed.

This research was the first successful attempt of direct extrusion of microstructured polymer optical fibres from a 3D printer which reduce the MPOF fabrication time and a step of optical fibre fabrication into a single step.

CONTENTS

List of Figures

Declaration of Authorship

I, Wanvisa Talataisong, declare that the thesis entitled *Microstructured polymer optical fibres fabricated from 3D printers for sensing applications* and the work presented in the thesis are my own, and have been generated by me as the result of my own original research.

I confirm that:

- This work was done wholly or mainly while in candidature for a research degree at the University;
- Where any part of this thesis has previously been submitted for a degree or any other qualification at this University or any other institution, this has been clearly stated;
- Where I have consulted the published work of others, this is always clearly attributed;
- Where I have quoted from the work of others, the source is always given. With the exception of such quotations, this thesis is entirely my own work;
- I have acknowledged all main source of help;
- Where the thesis is based on work done by myself jointly with others, I have made clear exactly what was done by others and what I have contributed myself;
- Parts of this work have been published in conference proceedings and journal articles as listed in List of Publications.

Signed: ……..

Date: ……24/09/2020…….

Acknowledgments

Firstly, I would like to express my sincerest gratitude to my supervisor Prof. Gilberto Brambilla, for the trust he put in me to do my research based on my preference. He is always providing me the advice, guidance and also invaluable technical and moral supports. I would also like to thanks my co-supervisor, Dr. Martynas Beresna for his help and suggestions on theoretical, experimental, technical, and every parts of my research. The intelligent ideas and very useful suggestions he gave me have driven this research work to be done. I am also grateful to Dr. Rand Ismaeel, who also co-supervised me. She helps me going through the early year of my PhD with her helpful suggestion, support and help on the fabrication of microfibre, and many things to start my PhD research. I am very appreciating her moral support she gave me since I started my PhD research until now. I would like to thank Dr. Tracy Melvin for her help and suggestions in DNA functionalisation process. Many of the ideas that are presented in this thesis were conceived during our numerous discussions and I shall remember these occasions fondly.

I would also like to express my gratitude all of the members of Optical Microfibre Devices and Sensors group for their help and support. I am very grateful to Dr. Timothy Lee for his kind help and suggestions in experiment and also his valuable time to read my thesis writing. I am thankful to Dr. Ali Masoudi for his suggestions in some theoretical parts of my research and electronics parts of my setup, and also Dr. Lieke van Putten, who help me and teach me in the modal simulation of hollow-core fibre. I would like to thanks all alumni and present members of this research group for their friendship, their help and many things that I will not forget.

I would like to thank Prof. Cristiano Cordeiro and Mr. Thiago Henrique Rosales Marques for their help working with polymer fibre drawing, Dr. Vasilis Apostolopoulos and Dr. Jon Gorecki for their help in THz experiment and their suggestions about THz, Prof. Daniel Schwendemann who manufactured the cyclic olefin copolymer (TOPAS) filament, Dr. James Williamson and Dr. Katie Addinall who provided the cross-section images of nozzle using the X-ray computed tomography.

This work could not be done without the help of these three persons, Mr. Glenn Topley who first fabricated the structured nozzle and always help me with all mechanic's parts in my setup, Dr. Sam Catchpole-Smith and Mr. Richard Dooler who spent their effort in manufacture the metal 3D printed structured nozzle.

Over many years of my studies at Optoelectronics Research Centre (ORC), University of Southampton, I am extremely grateful to be the part of ORC and have met a number of kind, bright, and intelligent people who were always provided me with the helpful assist throughout my studies. Thank you everyone in ORC and my friends, for your moral support, nice friendship, and all good memories. I feel lucky to have been a part of ORC.

I would like to thank the Development and Promotion of Science and Technology Talents Project of Royal Thai Government (DPST) for the financial support through my PhD study.

My other half, Teerapat, your love and support gave me all the courage I need. Thank you for your trust and endless confidence you gave me to do everything in my life. I know that you are always by my side and I know that everything will be better when we are together.

Finally, I am indebted to my dear father and mother, my sister, my family and all of my teachers, for all of love, encourage, and support that they gave me. I owe you any success I have achieved in my life. I couldn't have done this without you.

Nomenclature

Abbreviations

ABS	Acrylonitrile butadiene styrene
ARF	Antiresonant fibre
CLIP	Continuous liquid-interface production
CNC	Computer numerical control
COC	Cyclic olefin copolymer
FDM	Fused-deposition modelling
FEM	Finite element simulations
FFT	Fast Fourier Transform
HC-ARF	Hollow-core antiresonant fibre
HC-BF	Hollow-core Bragg fibre
HC-MOF	Hollow-core microstructured optical fibres
HC-MPOF	Hollow-core microstructured polymer optical fibres
HDPE	High-density polyethylene
MFC	Microfibre coupler
MOF	Microstructured optical fibre
MPOF	Microstructured polymer optical fibre
NFC	Nanofibre coupler
OFS	Optical fibre sensor
PBG	Photonic bandgap
PBGF	Photonic bandgap fibre
PCF	Photonic crystal fibre
PETG	Polyethylene terephthalate glycol
PML	Perfectly matched layer
PMMA	Polymethylmethacrylate
POF	Polymer optical fibre

PTFE	Polytetrafluoroethylene
SC-MOF	Suspended-core microstructured optical fibres
SC-MPOF	Suspended-core microstructured polymer optical fibres
SLM	Selective laser melting
SLS	Selective laser sintering
TDS	Time-domain spectroscopy
THz	Terahertz

Mathematical symbols

A	Area of heat transfer surface
A_0	Cross-section area of material flow through the nozzle
C	Coupling coefficient between supermodes
CL	Confinement loss of the hollow-core fibre
$D_{cladding,}D_{core}$	The diameter of the cladding and core apertures (at the bottom of nozzle)
E	Electric field
F	Extrusion force
I, I_0	The intensity of light propagated through the material; The intensity incident light on the sample
J_{l-1}	Bessel function
L	Thickness of etalon
P	Power of light in the microfibre coupler
Q	Amount of heat flow through a cross-section of material
$R(\lambda)$	Reflection of etalon
T	Absolute temperature
T_g	Glass transition temperature
T_m	Melting temperature
T_n	Nozzle temperature

ΔT	Temperature different
V	Normalised frequency V-number
a	Radius (e.g. fibre core radius)
$d_{cladding,} d_{core}$	The diameter of the cladding and core of drawn fibre
h_c	Convective heat transfer coefficient
k	Wavenumber
n_{core}	Refractive index of fibre core
n_{clad}	Refractive index of fibre cladding
n_{eff}	Effective (mode) index
n_{lm}	Effective indies of air modes in hollow-core fibre
Δp	The change of pressure on material flow through the nozzle
q	Heat transfer
s	Filament feeding speed
v_{draw}	Fibre draw speed
$v_{extrude}$	Polymer extrusion speed
z_{opt}	Optimum jacket distance from the fibre core
α	Optical loss
β_e, β_o	Propagation constant for even and odd supermodes
ϕ_{eo}	Phase different between the even and odd supermodes
γ	Shear rate
λ	Wavelength
ν_m	Resonance frequency of Fabry-Perot interference
η	Shear viscosity
δ	Phase acquired by light in a round trip propagation within the etalon
τ	Shear stress

Chapter 1. INTRODUCTION

In this research project, a novel technique to manufacture microstructured polymer optical fibres was developed, with the aim of providing a quick and inexpensive fabrication process. A prototype compact fibre drawing tower based on a modified desktop 3D printer was designed and built. Solid-core and hollow-core microstructured polymer optical fibres were fabricated and the possibility to use these fibres for mid-IR and THz guidance was examined.

1.1 History and background

The use of material waveguides instead of free space for light propagation dates back to the early nineteenth century, when the physicists Daniel Collodon and Jacques Babinet demonstrated that light could be guided along jets of a water fountain[1]. In 1854, light propagation through a stream of curved water was presented by John Tyndall. A tank of water with a pipe that ran out from one side was used in his demonstration. By shining light through the tank into the stream of water that flowed from the pipe, it was shown that light experienced internal reflection and followed the flow of water. This proved the ability to steer light through the guiding medium. At that time, glass was too opaque to be used as a light transmission medium. In 1888 a medical team in Vienna used bent glass rods as a light guiding medium to illuminate body cavities. In the late 1920s, the first successful demonstrations of light guidance and imaging in an air clad glass fibre to transmit an image for television was patented. The idea of applying a dielectric cladding layer with a smaller refractive index around the fibre was introduced 30 years later. A cladded fibre system greatly reduced signal interference and crosstalk between fibres. This significantly improved the achievable optical properties, renewing the interest in research on optical fibres and starting the quest for more transparent glasses for optical fibre fabrication. In 1966, Charles Kao, a scientist from Standard Telecommunication Laboratories, England, invented a dielectric optical fibre with a refractive index 1% higher than its surrounding material (cladding) for communications. Although the proposed optical fibres experienced excessive optical loss which limited the transmission distance, Kao suggested that the fundamental limit on the loss of optical fibres could be below 20 dB/km by improving the purity of glass, which would be practical for optical fibre communications [2]. Only a few years after Kao's demonstration, a single mode optical fibre was fabricated by Maurer, Keck, and Schultz from Corning. They developed a modified chemical vapour deposition process that heats chemical vapours and oxygen to form ultra-transparent glass that can be mass-produced into low-loss optical fibre, with 16 dB/km attenuation at 633 nm [3]. This breakthrough is recognised as the beginning of optical fibre communication and this fabrication process still remains the standard for manufacturing optical fibres. At the end of the 1970s, by further improving the optical fibre fabrication technology to reduce the amount of glass impurities, an optical fibre with the remarkably

low optical loss of nearly 0.2 dB/km at 1550 nm [4] was demonstrated. Since then, the development of conventional optical fibres together with the invention of solid state diode lasers, optical amplifier, and high-speed optical detectors, have revolutionised the telecommunications system to become the physical layer on which internet technology is based. Additionally, optical fibres have become crucial components in many other technologies, from medical imaging and sensing to high power applications, including machining, welding, and active device such as amplifier and optical fibre lasers.

Unlike conventional optical fibres, which are a solid combination of glasses with different refractive indices, a novel type of optical fibre, known as a microstructured optical fibre (MOF) is made of one material with the introduction of microscopic air holes that run along the entire length of the optical fibre. MOFs were first reported and fabricated by Kaiser *et al.* at Bell labs in 1974 [5]. The fibre was made from pure fused silica and consisted of a suspended small-rod with the diameter of 25 μm supported by a thin polished strand (thickness ~ 2.2 μm). The small rod was connected with a large diameter protective tube and the small core was left hanging at the centre of the tube as shown in Figure 1.1(a). This first reported MOFs showed a promising low loss of 3 dB/km at the wavelength of 1.1 μm. In the meantime, doped-core all-solid conventional fibres were also developed. Due to an easier fabrication process, better mechanical robustness and potentially lower loss than the MOFs, doped-core fibre fabrication took the spotlight in research and MOFs were temporarily set aside.

In 1987, the idea of controlling spontaneous emission by modifying the radiation field was first proposed by Yablonovitch [6] and John [7]. They suggested that fully destructive interference of light can occur in a periodic structure of dielectric material that has a period comparable to the wavelength of light, resulting in the propagation of light at certain wavelengths, in analogy to the bandgaps observed in Bragg resonators. This pioneering concept inspired many researchers in optics to study this area. In 1995, Birks and co-workers proposed a 2D photonic bandgap structure for out-of-plane propagation in order to confine the light in a defect region and guide it [8]. From this study, they suggested that a microstructured optical fibre with an appropriate periodic arrangement of holes around the fibre core running along the length of fibre could be used to trap the light in the fibre air core.

The idea of MOFs was brought back to the attention of the research community nearly 20 years after the first MOF demonstration by Phillip Russell and colleagues. This new MOF design combined the single material microstructured design with the photonic bandgap structure into the so-called "*Photonic Crystal Fibre*" and was fabricated by Knight *et al.* at the University of Southampton in 1996 [9]. As shown in Figure 1.1(b), the air holes were placed in a 2D periodic array surrounding a solid fibre core where light can be trapped. In this structure, the refractive index of the surrounding was modified by the air hole array and resulted in a reduced average refractive index of the cladding.

Light in this fibre structure is by no means guided through a photonic bandgap effect, but by a modified total internal reflection. Following the demonstration of the MOF structure in the late 1990s, many applications have been proposed by combining the effort of theoretical and experimental works. In 1998, the observation of the first single mode guidance in a low index region by photonic bandgap effect was reported by the same research group [10]. A 5 cm long MOF with a honeycomb cladding (Figure 1.1 (b)) was fabricated according to the theoretical design suggested by Bjarklev's group [11]. This was a milestone in the MOF's history which proved the concept of "*Photonic bandgap fibres*" (PBGFs). Although part of the guided mode in this fibre overlaps with the low index region, its fundamental mode was localised in the solid core region and presented as a donut shape resulting in a poor overlap with most of the laser sources that generated a Gaussian mode profile.

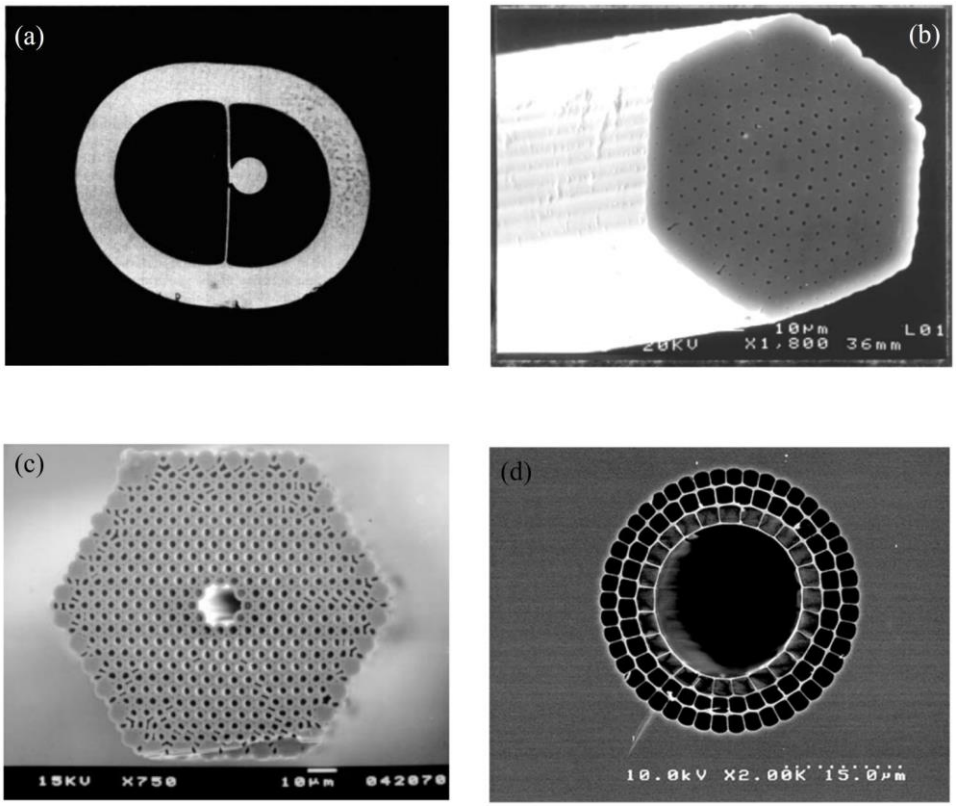

Figure 1.1 (a) The first demonstrated all-silica microstructured optical fibre reported by Kaiser et al. in 1974 [5]. (b) First ever reported single mode microstructured silica optical fibre [9]. (c) Single mode air-guiding optical fibre reported in 1999 [12]. (d) A single material hollow-core Bragg fibre developed in 2004 [13].

The development in manufacturing technology led to the next improvement of the PBGFs, designed by increasing the air-filling fraction using a triangular hole arrangement. In 1999, the first single mode photonic bandgap guidance in an air-core fibre was reported by Cregan *et al.* [12]. This newly designed air-core fibre was fabricated by forming a hexagonal bundle of capillaries and then

removing the 7 central capillaries as shown in Figure 1.1(c). This multilayer stack with a periodic pattern produced a Bragg layer, in which light at wavelengths within the bandgap is reflected by the multilayer cladding and is transmitted along the hollow-core. This approach has also been used to manufacture rolled Omniguide optical fibres, in which a multilayer of two materials was rolled up to generate a hollow-core fibre [14]. In order to obtain a very high refractive index contrast, this rolled "*Bragg fibre*" required the use of two different materials, raising issues of material compatibility which can be significant during the drawing process. Therefore, a single material Bragg fibre was developed, consisting of rings of holes used to produce the bandgap (Figure 1.1 (d)).

A few years after the first demonstration of hollow-core photonic bandgap fibres, another hollow-core fibre geometry design was proposed with a Kagome lattice, as shown in Figure 1.2(a) [15]. This new design has a similar geometry to that of the hollow-core photonic bandgap fibre, but with a typically larger core diameter. These fibres exhibit several transmission bands, a broadband guidance, although often associated with high loss and multimode propagation. The guiding mechanism of the "*Kagome fibre*" is different from that of the photonic bandgap fibre as the cladding of this fibre does not support bandgaps, and light in the fibre core can propagate through the cladding lattice. Coupling to the cladding is prevented only in specific wavelength ranges owing to a low density of cladding modes and small overlap with the solid material of the fibre. The latter reduces the overlap between the core and the cladding modes and any perturbation that would facilitate their coupling leading to the strong confinement of the core mode. To achieve the low confinement loss in the hollow-core Kagome optical fibres, the research group at the University of Bath showed that the core wall shape is an important parameter. The core wall is mainly responsible for low-loss guidance in hollow-core Kagome fibres. The overlap between the core and cladding modes can be further reduced with phase mismatch. The spectral regions of high mode density and high loss were found to correspond to resonances of the struts around the fibre core. A new guiding mechanism for hollow-core optical fibres with a geometry close to that of the Kagome lattice fibre was reported in 2008 by Argyros *et al.*[16]. A discussion of the fibre's guidance mechanism in terms of antiresonance and inhibited coupling showed that the transmission properties of the guided mode depend on the thickness of the struts in the cladding. These were likely the basis upon which a new hollow-core fibre design was fabricated in 2011 by Pryamikov *et al.* (Figure 1.2(c)) [17]. The guiding mechanism of this new kind of hollow-core fibre is due to the antiresonance of certain wavelengths of guided core modes with the layers of core surrounding it; therefore these optical fibres are called "*Antiresonant (AR) fibres*". The development of AR fibres had a fast evolution and in a few years several designs were proposed, including hexagram [18], nested [19], touching tubes [20], and non-touching tubes structures [21]. Numerical studies showed that a nested version of the AR fibres could offer an ultra-low loss and more complex structures were proposed to improve the modal properties or to alter some optical parameters such as birefringence. The hollow-core AR fibres and hollow-

core Kagome fibres have similar optical properties but the main differences are the low loss that can be achieved with hollow-core AR fibres for the same core size and the typically higher bend loss of hollow-core AR fibres.

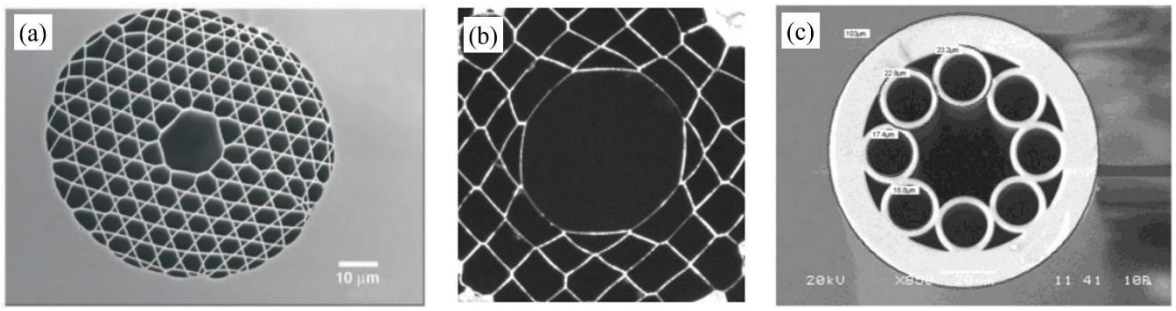

Figure 1.2 (a) First reported hollow-core Kagome fibre with a star of David shape cladding [15]. (b) Hollow-core square lattice optical fibre which presented guidance using antiresonant effect [16]. (c) First antiresonant hollow-core fibre fabricated in 2011 [17].

As the guided mode in hollow-core optical fibres is predominantly in the hollow core and has minimal overlap with the solid material, these fibres support modes even at wavelengths at which the material has high absorption. The new hollow-core fibre also allows guidance in low index materials such as liquids or gases, as it does not rely on total internal reflection. This opens up a multitude of new potential applications, from ultrahigh-power transmission to laser guiding of small particles and also gas and biological sensing.

In summary, several types of microstructured optical fibres have been reported to date, including photonic bandgap (PBG) fibres, Bragg fibres, Kagome fibres, antiresonant (AR) fibres, and the modified total internal reflection or index guiding (IG) fibres. Although each of these optical fibres has its own applications and specific theoretical and numerical tools, they have similar fabrication processes and related issues.

1.2 Scope and objective of thesis

In the past decade, research on microstructured optical fibres has been fuelled by the wide variety of proposed geometries and their potential applications. Due to the intrinsic presence of air-holes, index modulation in MOFs can be easily achieved. Therefore, these fibres have been investigated for many applications, especially for sensing [22]. Among all optical sensing schemes, use of the mid-infrared (mid-IR) is gaining strong attention, especially for biological applications. This is attributed to the high inherent molecular selectivity and strong signal of optical sensing schemes. Fibre-optic materials transparent in the mid-IR spectral region up to a wavelength of λ=20 µm offer access to fundamental vibrational and rotational fingerprint absorptions of molecules. To date, mid-IR optical fibres are mainly based on materials transparent in the mid IR window, such as heavy metal fluorides, chalcogenides, tellurium halides, silver halides, and sapphire. To overcome the limitation of mid-IR fibre materials and the loss associated to material absorption, hollow-core

microstructured optical fibres (HC-MOF) emerged as a suitable alternative. Light in HC-MOFs is confined in the air core, which reduces the potential loss arising from the interaction between the mid-IR wave and the optical fibre material. Thus, microstructured optical fibres based on air-cores have excellent potential as mid-IR waveguides.

Another region of the electromagnetic spectrum that has caught the attention of researchers in the last decade are the terahertz (THz) frequencies. The novel appeal of THz technology and functionality have no doubt demonstrated the attractive nature of THz radiation to science and public communities alike. As the last part of the electromagnetic spectrum to be fully utilized, THz radiation has promising potential in innovation and also integration with other areas of scientific study. Dynamic growth in research concerning generation and detection of THz radiation has contributed to better understanding the physical light-matter interaction, non-invasive biological imaging, chemical substance fingerprinting, and also active homeland security scanners. Many non-polar and dielectric materials are transparent to THz waves, which have the capability to penetrate through clothing and plastic. Therefore, one of the interesting applications of THz frequencies is to detect drugs, explosives, and weapons even if they are concealed. Biological and chemical sensors are one of the main applications using the THz frequency because biological macromolecules and DNA molecular vibrations and rotations lie in the THz. Due to the various applications of THz radiation, the development of the THz waveguides is in the spotlight [23-30].

Since the first report on the fabrication of microstructured optical fibres, many fabrication techniques have been developed. The manufacture of MOFs typically starts from the fabrication of the structured optical fibre preform (a large version of the fibre with a similar structure), which include tube stacking, multilayer deposition, drilling, and extruding techniques. Generally, silica MOFs have been manufactured using the stack and draw technique, where capillaries are manually assembled into a hexagonal structure prior to draw. Despite this being the most popular method, it is labour intensive, mainly limited to the hexagonally packed periodic structure and difficult to implement for complex designs. The use of polymers as a material of choice has been proposed to reduce manufacturing cost and increase the fibre mechanical ductility for applications in environments exposed to vibrations. Many techniques have been suggested and implemented to fabricate microstructured polymer optical fibres (MPOFs) and their related preforms, including stacking, drilling, milling, and polymerization of liquid monomers [31, 32]. Yet, these conventional techniques have limitations on the number of transverse features or the hole shapes, and often involve multiple steps and require expensive facilities like clean-room environments for fabrication.

Because of the continuous improvement in additive manufacturing technologies (3D printing) and the related cost reduction, the fabrication of prototypes using 3D printing has gained interest in many fields including medicine, art, engineering and science. Currently, 3D printing is widely used for developing experiment equipment for photonics, such as lens holders, optical fibre holders,

optical positioning stages and also to fabricate optical fibre preforms. A solid core optical fibre preform fabricated using a 3D printer was successfully demonstrated in 2015 [33, 34]. Microstructured polymer optical fibres based on 3D printed preforms have attracted significant interest because of the short time needed for preparing the fibre preform, as well as the low cost and the extreme flexibility for changing the design.

A key objective for my research is to design and develop an efficient technique to fabricate polymer-based MOFs. In this work, I will demonstrate that a 3D printer is capable to fabricate the microstructured polymer optical fibre preform with a hollow-core geometry. So far, only the 3D printed solid core polymer optical fibre preforms have been reported. In this work, the manufacturing of hollow-core Bragg fibre preforms will be investigated using a prototype 3D printing technique.

The challenge in the fabrication of microstructured polymer optical fibres is not only the design of the structure and the fibre preform fabrication, but also the drawing process during which the geometric structure inside the optical fibre must be maintained. Therefore, another approach investigated in this research is the direct drawing of MPOFs from a 3D printer by using a nozzle with a structured profile in a desktop 3D printer. This novel development promises low-cost MPOF fabrication by combining the advantages of (i) optical fibre preform extrusion, (ii) a compact material feeding system, (iii) a small heater (3D printer head), and (iv) the possibility to microstructure 3D printer nozzle dies. One of the main challenges in this work is the design and fabrication of the structured nozzle. 3D modelling of the nozzle dies, heat transfer and material flow simulations will be used to optimise the nozzle design and make it compatible with the selected polymer and 3D printer. Several techniques to manufacture the structured nozzle including micromachining and metal 3D printing will be investigated. The MPOF drawing parameters including material feeding speed, nozzle temperature, and drawing speed will be optimised to achieve and maintain the microstructure inside the extruded polymer optical fibre. In this work, both solid-core and hollow-core MPOFs will be manufactured and characterised for various wavelength ranges including the near-infrared, mid-infrared, and THz.

To summarise, the main goals of the work presented in this thesis are to:

- Optimise the 3D printing parameters to achieve a hollow-core fibre preform with the required geometry and uniformity in the material structure.
- Investigate and optimise the design of 3D printer structured nozzle dies for fabricating both solid-core and hollow-core fibres.
- Investigate and develop low-cost prototyping of a fibre drawing tower system based on a desktop 3D printer for fabricating microstructured polymer optical fibres.

- Investigate the fabrication procedure of a novel optical fibre drawing tower based on a 3D printer for fabricating solid- and hollow-core microstructured polymer optical fibres.
- Fabricate solid-core and hollow-core microstructured polymer optical fibres from materials compatible with the desktop 3D printer.
- Characterise the guiding properties of the fabricated solid-core and hollow-core microstructured polymer optical fibres in the near-IR, mid-IR and THz regimes.

In the next section, the thesis layout will be presented with a summary of each chapter.

1.3 Thesis outline

The aim of this introduction chapter was to provide an overview of the history of the optical fibre fabrication and highlight the potential of microstructured optical fibres to produce optical properties unreachable with conventional fibres, to exploit novel physical effects and to open entirely new applications. The remainder of this thesis is organised as follows:

Chapter 2 will focus on the background of microstructured optical fibres. Different structures and their guiding mechanisms will be presented, followed by the background and history of the micro-structured polymer optical fibres. Techniques used to fabricate MPOF preforms will be reviewed, and the 3D printing techniques and the fabrication of MPOF based 3D printed preform will be discussed.

Chapter 3 will present the manufacturing of a 3D printed hollow-core polymer fibre preform operating in the mid-IR, its 3D model design and the optimisation of printing parameters to achieve a highly transparent preform. The drawing procedure of the polymer fibre and the characterisation of a MPOF drawn from the 3D printed preform will conclude this chapter.

Chapter 4 will introduce the breakthrough design and manufacture of the 3D printer nozzle used for fabricating suspended-core microstructured polymer optical fibres and hollow-core microstructured polymer optical fibres. The two main techniques used to fabricate these nozzles will be explained, with emphasis on the details important to achieve and maintain the structure inside the MPOFs.

Chapter 5 will present the design and manufacturing of a novel fibre drawing tower based on a modified desktop 3D printer and will include mechanic and electronic controlling systems. The characterisation of parameters used in the fabrication of MPOF including fibre drawing speed, material feeding speed, and nozzle temperature will be discussed.

Chapter 6 will present the fabrication of a suspended-core microstructured polymer optical fibre using our developed optical fibre drawing system with the micromachined structured nozzle. The material selection used to fabricate the suspended-core polymer fibre for guiding in near-IR and THz

will be explained. The SC-MPOF characterisation and related numerical simulations and experimental results for guidance in near-IR and THz will be presented.

Chapter 7 will detail the fabrication of a hollow-core antiresonant polymer fibres using a metal 3D printed structured nozzle. The material selection used to fabricate the hollow-core microstructured polymer optical fibre for different guided wavelengths will be explained. The HC-MPOF will be characterised for both mid-IR and THz regimes, and numerical simulations and experimental results for THz and mid-IR guidance will be reported.

Chapter 8 will provide an overall summary of this thesis and present the conclusions. The outlook for the future of the MPOF fabrication using the novel optical fibre drawing system will be also outlined.

Appendix A will detail the fabrication of nano-fibre couplers (NFC) from the single mode silica optical fibre (SMF-28). The NFC characterisation and related numerical simulations and experimental results for guidance in near-IR will be presented. Follow by the use of NFC as a temperature and a refractive index sensor when it was operating near the cut-off,wavelength.

Appendix B will present the fabrication of micro-fibre couplers with the diameter of ~ 2 μm. The process of biological and chemical functionalisation on the coupler surface for DNA sensor application will be revealed. The possibility to attach the DNA on the micro-fibre coupler surface will be reported.

Chapter 2.

PROPERTIES OF MICROSTRUCTURED OPTICAL FIBRES, THEIR FABRICATION TECHNIQUES AND SENSING APPLICATIONS

The attraction of microstructured optical fibres (MOFs) lies in the ability to achieve control over propagation properties using solely the geometry of the fibre cross-section. This is a paradigm shift from conventional design approaches, in which the materials play key roles in defining propagation losses, dispersion, and modal confinement. In this chapter, an overview of MOFs will be presented, followed by the guiding principle of solid- and hollow-core MOFs. Since this research focuses on novel techniques to fabricate microstructured polymer optical fibres (MPOFs), section 2.2 will provide an overview of MPOFs and their fabrication technique. Finally, sections 2.3 and 2.4 will deal with the 3D printing techniques and the fabrication of MPOFs based on 3D printed preforms and an overview of optical fibre sensors will be given.

2.1 Microstructured optical fibre (MOF)

A conventional optical fibre is a cylindrical waveguide made from a higher refractive index material (core) surrounded by a lower refractive index material (cladding). Light propagates in the core of the conventional optical fibre because of total internal reflection due to the refractive index difference between the core and the cladding.

Microstructured optical fibres are optical fibres in which air holes are introduced in the core or cladding region and extend unperturbed in the longitudinal direction of the fibre. These fibres come in a variety of different shapes, sizes, and distributions of air-holes. Research on MOFs was focused on the guiding properties of the fundamental mode localized in the core region of the fibre, such as bending loss, mode field diameter, cut-off wavelength, and dispersion. The presence of holes in the microstructure is intrinsically dispersive, and the size and placement of holes can dramatically affect the overall optical performance. Indeed, the microstructure can be used as a modal selection tool that confines the fundamental mode more effectively than higher order modes. This effect allows MOFs to operate in the single-mode regime over a very broad frequency range [35].

The possibility to modify the structure within MOFs enables targeting an increasing number of specialty applications. For example, by giving the arrangement of holes or the holes themselves different profiles in the x and y directions, it is possible to achieve highly birefringent or polarization maintaining fibres [36]. The dispersion properties of MOFs have also drawn attention because of their ability to compensate for the material dispersion [37]. By changing the core size of the fibre, it

is also possible to control its optical nonlinearity [38], allowing development of fibre systems for supercontinuum generation [39]. By flowing chemical gas or biological liquid through micro-holes in the MOFs, it is possible to use the MOFs as chemical and biological sensors, as these substances modify the effective refractive index of light propagating in the MOFs [40].

When considering the structure of their core, MOFs can be classified in two major groups: solid-core and hollow-core MOFs. As the core of an optical fibre generally refers to the region in the fibre cross-section containing the majority of guided power, this classification is frequently interchanged with a classification based on the presumed guiding mechanism. Unlike the guiding mechanism of conventional optical fibres based on the general total internal reflection, the guiding mechanism of MOFs is a combination of many optical principles based on their structure.

2.1.1 Solid-core microstructured optical fibres

A solid-core MOF can be identified by the fact that guided modes in the optical fibre are mostly localised into a material region. The holes in the solid-core MOFs may serve to provide light confinement, in what is referred to as average index guiding MOFs. Solid-core MOFs with a large variety of hole shapes and arrangements have been investigated in order to achieve a host of different functionalities. The most typical cross-section structure of the solid-core MOFs is the solid-core photonic crystal fibre (solid-core PCF), which is presented in Figure 2.1(a-c). The solid-core PCFs, surrounded by a small number of large air-holes or by an array of air-holes, are generally fabricated by using the widely employed procedure of stack and draw, thus exhibiting a hexagonal structure with equal size holes.

The two parameters used to define the structure of this type of solid-core PCFs are the hole diameter (d) and the hole-to-hole spacing (Λ). Missing air holes at the centre within the otherwise regular array are usually used to define the solid core. The defect at the centre can be generated by removing two [41], three [42], or even more holes. The array of air holes will act as the cladding due to the lower average refractive index of this region: light can be guided in the solid-core via a modified form of total internal reflection, since refractive index of core (n_{core}) > effective cladding index (n_{clad}, defined as the effective modal index of the lowest order of cladding mode).

Chromatic dispersion in optical fibre occurs due to different wavelengths of light travel with different speeds which can be divided into two types (material dispersion) and (wave guide dispersion). In solid-core PCF, the presence of air holes in the region surrounding the solid core imposes a wavelength dependency on the fundamental optical mode, guided in the core, similar to that of the cladding modes. Due to the high refractive index difference between silica and air holes in PCF, and to the flexibility of changing air-hole sizes and patterns, a chromatic dispersion in PCF is much broader than in conventional optical fibre. By proper designing of photonic crystal fibre, it is possible to design such a fibre which gives zero dispersion wavelengths at operating wavelength.

PCF with missing air hole in solid core or missing ring can be exploited to obtain zero dispersion at different wavelengths. Hence by using different layers we can obtain zero dispersion at different wavelengths. Suitable solid-core PCF design allows us to remove the guidance of all higher order modes, irrespective of their propagating wavelength, providing endlessly single mode guidance as shown in Figure 2.1(c) [35]. The phenomenon of endlessly single mode operation can be explained in direct similarity with a conventional step index fibre: in the step index fibre, the number of supported modes is a function of the V number, which can be expressed as:

$$V = \frac{2\pi}{\lambda} a \sqrt{n_{core}^2 - n_{clad}^2} = \frac{2\pi}{\lambda} NA = \frac{2\pi}{\lambda} a \sin\theta = k_{\perp} a \qquad 2\text{-}1$$

where a is the core radius, NA is the numerical aperture of the fibre, θ is the divergence angle, and $k_{\perp} = k \sin\theta$ which is the free-space transverse wavenumber. For the step index fibre, the single mode condition occurs when $V < 2.405$. As the V number increases for decreasing wavelength, the fibre will become multimoded when the wavelength is shorter than a certain cut-off wavelength.

Differently from conventional step index fibres, propagation in solid-core MOFs is dependent on the cladding. Numerical studies show that $V_{MOF} \simeq \pi$ is needed to observe significant losses in higher order modes and thus ensure the fibre is single-moded over practical lengths; $d/\Lambda < 0.406$ provides endlessly single mode operation for all possible values of λ.

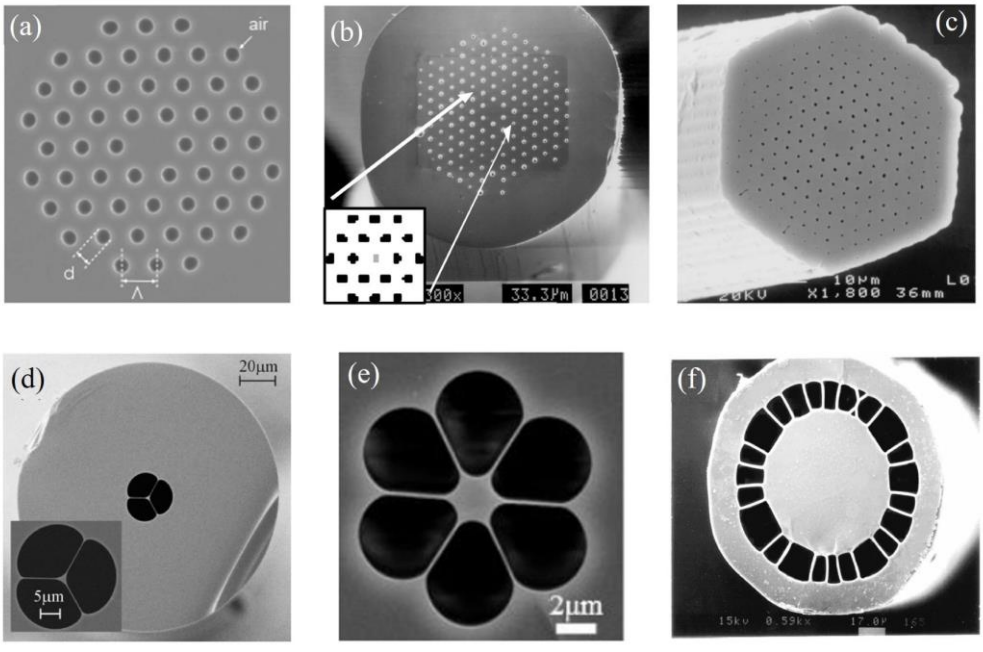

Figure 2.1 (a, b) Cross-section images of solid-core photonic crystal fibre [43], (c) Endlessly single mode fibre, (d) Suspended-core MOF [44], (e) Grapefruit MOF [45], (f) Air-cladding MOF [43].

Suspended-core fibres (SCFs) or suspended-core microstructured optical fibres (SC-MOFs) were firstly reported in 2001 by Monro *et al* [46]: a very small core is supported by thin struts and

surrounded by large air holes. In 2002, Kiang *et al* demonstrated a lead-silicate SC-MOF [47], swiftly followed in 2003 by Ravi Kanth Kumar *et al* and Petropoulos *et al* with tellurite and lead silica glasses respectively [48, 49], showing an interesting alternative for implementing fibres with high *NA*. The SC-MOF has a cladding consisting essentially of air and not only is much simpler, therefore potentially easier to make, but also offers potential for higher *NA* due to high contrast between material core and air cladding, thus enabling designs with even smaller mode field diameters (MFD) and shorter zero dispersion wavelengths. Such extremely high *NA* can be difficult to achieve with solid-core PCFs due to the practical limit of air filling factor achievable using a hexagonal stack of capillaries. By suspending a very small silica core in the centre of the fibre via a very thin bridge between the large air-holes, it is possible to make fibres which are essentially air-clad: light in this MOF is guided via total internal reflection at a very large numerical aperture (Figure 2.1(c-f)). In this research, only the SC-MOF guiding by total internal reflection has been considered.

2.1.2 Hollow-core microstructured optical fibres

Apart from the solid-core MOFs, particularly interesting sub-classes of MOFs are the photonic band gap (PGB) and antiresonant fibres (ARF), which have received considerable attention due to their ability to guide light in air or in other low index substances, and are thus called hollow-core microstructured optical fibres (HC-MOF). They are widely used for many applications such as gas sensing [46], enhanced Raman scattering [15], CO_2 laser guidance [50], and particle transportation [51]. Moreover, they could potentially provide a reduction of fibre losses where the material has high absorption at the guided wavelength [31].

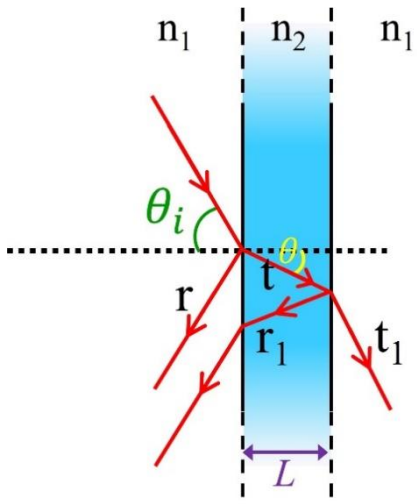

Figure 2.2 Schematic of the Fabry-Perot etalon of thickness *L*.

The guidance mechanism of HC-MOFs relies on a simple structure based on a single dielectric and air, which could be described by a basic 1D system. The idea of hollow-core guidance was first proposed by Litchinitser *et al* [52]: the arrangement of cladding interfaces provides a Fabry-Perot

resonator (Figure 2.2) ensuring that the reflection of light could be confined in an air-core. The analytical solution was provided for a dielectric HC fibre with a circular hollow-core and an infinite dielectric cladding, and the effective indices of the air modes in this HC were found to be:

$$n_{lm}(\lambda) = \sqrt{1 - \left(\frac{u_{lm}\lambda}{\pi d}\right)^2} \qquad 2\text{-}2$$

where n_{lm} is the effective index of the l^{th} azimuthal and m^{th} radial order mode, u_{lm} is the mth zero (root) of the Bessel function J_{l-1}, λ is the operating wavelength, and d is the fibre air core diameter. For the Fabry-Perot etalon presented in Figure 2.2, the incident angle (θ_i) can be expressed as:

$$\theta_i = \arcsin\left(n_{lm}(\lambda)\right) \qquad 2\text{-}3$$

The amplitude of the reflection (r and r_1) and transmission (t and t_1) coefficients for p- and s-polarisation for the two interfaces can be calculated as a function of θ_i through the Fresnel equations, to account for the effective index of the fundamental core mode. The phase (δ) acquired by light in a round trip within the etalon can be written as eq. (2-4) while the etalon reflection can be calculated as eq. (2-5).

$$\delta = \frac{4\pi n_2 L\cos(\theta)}{\lambda} \qquad 2\text{-}4$$

$$R(\lambda) = \left(1 - \frac{(tt_1)^2}{(1-rr_1)^2 + 4\sqrt{rr_1}\sin^2(\delta/2)}\right)^{1/2} \qquad 2\text{-}5$$

The typical etalon reflectance shows several high reflectance bands separated by narrow resonances with high transmittance. The frequency at the narrow resonance peaks can be calculated from eq. (2-6) when *c* is the speed of light in vacuum and *m* is an integer:

$$\nu_m = m\frac{c}{2n_2 L\cos(\theta)} \qquad 2\text{-}6$$

As there are many types of hollow-core MOFs, classified by their guiding mechanism, in this research only the hollow-core Bragg fibres and hollow-core antiresonant fibre (HC-ARF) will be presented.

A hollow-core Bragg fibre is a MOF composed of two materials rolled into a multi-layer stack to produce a hollow core fibre (Figure 2.3)[50]. The wavelengths of the light confined in the hollow-core Bragg fibre depend on the period of the layers and their refractive index difference. Light in the hollow-core Bragg fibre is guided through a coherent Bragg scattering of a periodic array of air-holes and exhibit a so-called the photonic bandgap effect [53]. The photonic bandgap effect can be simply explained for one-dimensional structures such as periodic layers of materials with different refractive

indices, which can be designed to reflect particular wavelengths that correspond to the characteristic period. These reflected wavelengths are said to fall into the 'band gap' of the structure, thus they cannot be transmitted, and so are reflected. The wavelengths within the band gap are transmitted along the hollow core. MOF hollow-core Bragg fibres can be produced with a ring structure or more commonly with a two-dimensional array of holes (Figure 2.3) which is used to produce the bandgap [54].

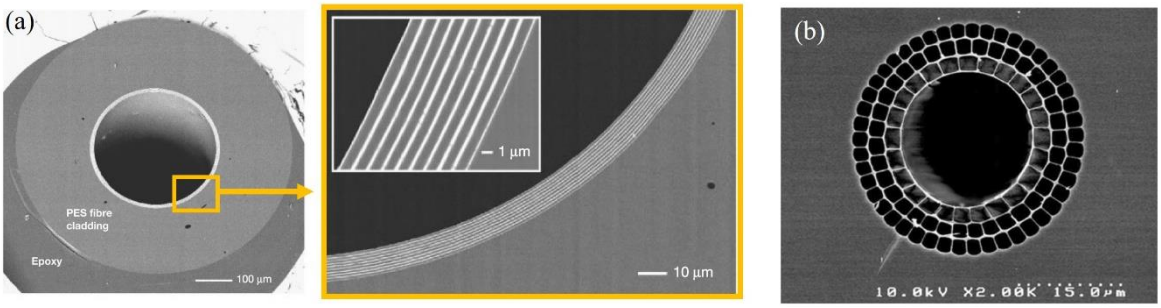

Figure 2.3 (a) Hollow-core Bragg fibre fabricated from periodic layer of PES and As_2Se_3[50], (b) Nanobridge hollow-core Bragg fibre [54].

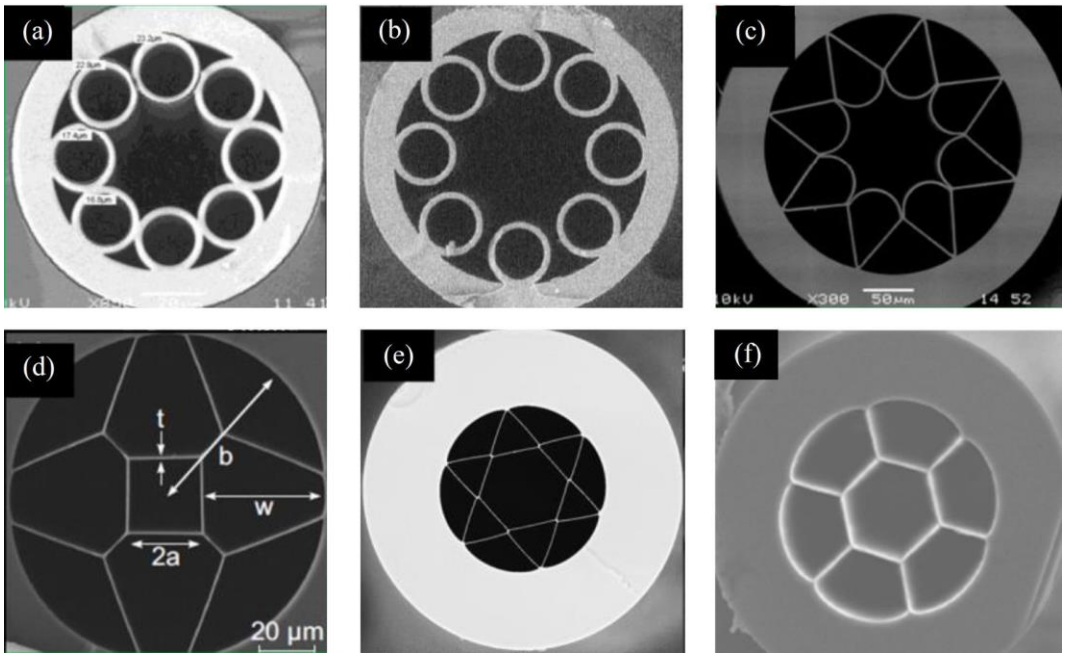

Figure 2.4 Scanning electron micrographs (SEMs) of different kinds of HC-ARFs [55]. (a) Touching and (b) Non-touching tubes antiresonant hollow-core fibres. (c) Simplified HC-ARF with 'negative curvature' core surround. (d) Simplified HC-ARF with a double antiresonant cladding and (e-f) hexagrams [56].

Another type of increasingly-popular hollow-core fibres is the hollow-core antiresonant fibre (HC-ARF), which has a variety of geometries, as presented in Figure 2.4. The structure that will be considered in this research is the antiresonant hexagram hollow-core fibres, shown in Figure 2.4(f). The guidance mechanism of theses fibres is similar to that of hollow-core photonic band gap fibres; yet, the resonator that provides antiresonant reflection is different.

In order to describe guiding in this kind of fibre, the analysis of dielectric tube modes is considered; e.g. a *capillary optical fibre* in which a simple circular tube has a thick glass cladding [57], and the thickness of (t) of the layer is much larger than the wavelength (λ) and a *tubular fibre*, ($t >> \lambda$) [58, 59]. When considering optical fibres that have core radius $r >> \lambda$, the loss dependence (α) on the core radius (r) and bend radius (R) for the capillary fibre is given by:

$$\alpha(r, R, \lambda) \propto k_1 \left(\frac{\lambda^2}{r^3}\right) + k_2 \left(\frac{r^3}{\lambda^2}\frac{1}{R^2}\right) \qquad 2\text{-}7$$

The first term on the right-hand side is the loss of the unbent fibre, while the second term introduce additional loss due to bending (k_1 and k_2 are constants). For the tubular fibre, the local minimum loss between high loss peaks is given by eq.(2-8) when w_1 and w_2 are constants that depend on the modal number.

$$\alpha_{min}(r, R, \lambda) \propto w_1 \left(\frac{\lambda^3}{r^4}\right) + w_2 \left(\frac{r^2}{\lambda}\frac{1}{R^2}\right) \qquad 2\text{-}8$$

The peaks of high loss come directly from the solutions for the various air guided modes of the hollow slab waveguide but they can also be explained by resonances of the air-guided core-mode with the tube modes. The wavelength of these high-loss resonances is given by eq.(2-9) where n is the refractive index of the material and m is the order of resonance (1, 2, 3, …).

$$\lambda_m = \frac{2t}{m}\sqrt{n^2 - 1} \qquad 2\text{-}9$$

As presented in eq.(2-7) and (2-8), the loss in straight fibres can be reduced by making the core radius arbitrarily large but this adversely affects bending loss. Thus, the ideal jacket tubular fibre is introduced to achieve low-loss in HC-ARF. The jacket tubular fibre is a hollow-core fibre where a core tube is suspended coaxially without support in a hollow jacket. The optimum jacket distance (z_{opt}) can be estimated in eq.(2-10) by combining a semi-analytical expression for the effective index (n_{eff}) of the fundamental core mode with the quarter wave condition for the air layer.

$$z_{opt} = \frac{\lambda}{4\sqrt{1 - n_{eff}^2}} \approx \frac{\pi}{2J_{01}} r \cong 0.65r \qquad 2\text{-}10$$

where J_{01} is the first zero of the Bessel function and r is the core radius. The guidance properties of the hollow-core antiresonant fibre largely depend on the thickness of the material webs forming the cladding structure. In addition, it has been shown that the properties of HC-ARF depend mainly on the first thin layer surrounding the hollow-core. Due to its guiding property, a modified structure of HC-ARF comprising of a single ring of air holes in the cladding space has been proposed and thoroughly investigated [60]. Some modified forms of the basic design for HC-ARFs have been

proposed in order to demonstrate low bending loss in the mid-infrared and the possibility of reduced attenuation in the near-infrared spectral range.

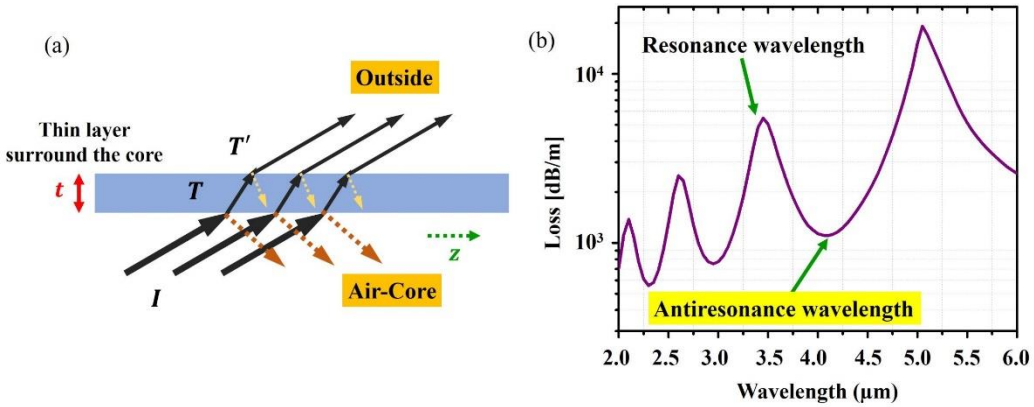

Figure 2.5 (a) Schematic drawing of a slab layer (thickness t) surrounding the air-core showing how light propagating in the air-core can be confined when the light is propagating in the z direction. (b) Simulation of loss profile for the HC-ARF showing peaks of resonant (high loss) and antiresonant wavelengths (low loss).

One of the most important features of a hollow-core MOF (besides overcoming material absorption) is that it allows guidance in materials with low refractive index, such as liquids or gases, not possible in fibres operating by the total internal reflection.

2.2 Microstructured polymer optical fibre (MPOF)

In the history of the development of optical fibres, polymer optical fibres (POFs) made their first appearance at the very beginning. The need and goal to achieve lower transmission loss pushed silica fibres forward, compared to polymer fibres, due to an intrinsically higher polymer loss at communication wavelengths. However, the silica fibres have limiting factors: Rayleigh scattering at short wavelengths (UV and visible), impurities and absorption due to water vibrational levels at long wavelengths (visible and near infrared). For the POFs, the absorption band given by the C-H bond overtone has an increasingly high absorption for the wavelengths > 600 nm. Although the C-H band has no significant absorption at short wavelengths, Rayleigh scattering dominates the loss at short wavelengths, leading to a region of minimum loss for POFs at around 550 nm (Figure 2.6). Since the C-H bonds are the basic components of all polymers, the loss due to the absorption of C-H bonds cannot be removed. One approach to solve this problem is by substituting the hydrogen atoms with heavier elements or isotopes. A heavier component will shift the excitation of vibrations towards longer wavelengths, reducing the loss and expanding the transmission window into the infrared. Deuterium [61] and fluorine [62] are the most common choices used for substitution of hydrogen. This is particularly attractive because it allows the use of low-cost components such as sources and detectors which were developed for use with silica fibres. However, the production of these materials

is expensive and in the case of fluorine, the product of hydrofluoric acid is harmful, and the fabrication process is complicated. Thus, POFs made of polymethylmethacrylate (PMMA) are more widely used due to the simplicity in producing the PMMA, non-toxic property of the material, and acceptable loss compared with fluorinated polymers (e.g. CYTOP). A loss comparison between silica, PMMA, and CYTOP fibres is shown in Figure 2.7. While the POFs revealed high loss, the commercial development of POFs has continued due to major advantages over silica fibres, such as ductility and cost-effectiveness.

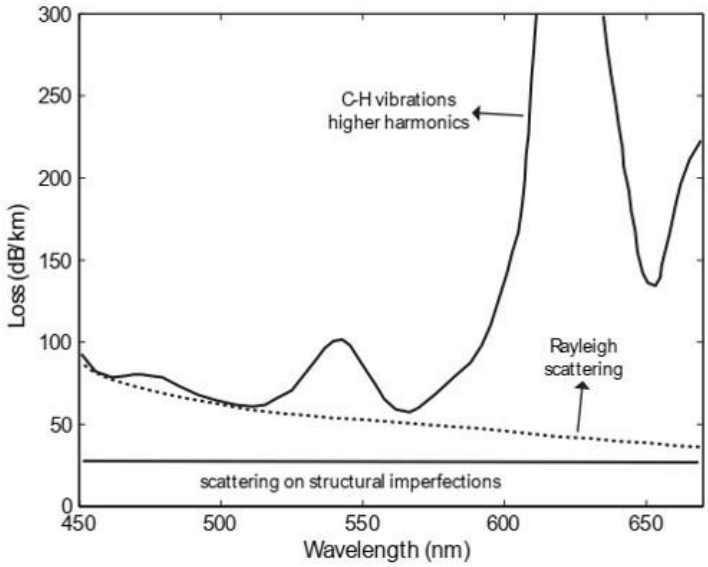

Figure 2.6 Loss spectrum of PMMA over its transparency window [63].

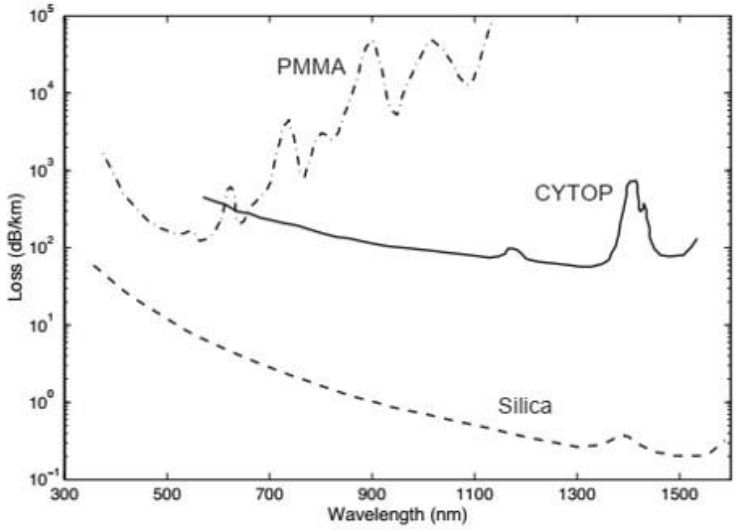

Figure 2.7 Loss spectra of silica fibres, PMMA fibres, and fluorinated polymer (CYTOP) [64].

Another approach of reducing the loss due to intrinsic material absorption of POFs is to introduce microstructures inside the optical fibres to reduce interaction between the guiding wave

and material, especially in the hollow-core fibres. In 2001, Eijkelenborg *et al* [31] reported the first microstructured polymer optical fibres (MPOFs) by using commercial PMMA fibre preforms.

The fabrication of MOFs from a single material shows significant advantages over conventional core-clad optical fibres because issues related to thermal and chemical compatibility between different materials are intrinsically decreased.

Besides silica and soft glasses, polymers are one of the most interesting materials for manufacturing optical fibres. Although POFs exhibit relatively low transmission compared to silica-based fibres, POFs remain flexible even with a large core diameter. The utility of polymers for fabricating optical fibres has been demonstrated due to their low cost for manufacturing and their resistance to ductile fracture for applications in environments exposed to vibrations. Polymer is also an attractive material for sensing, especially biological and chemical, as it is permeable to gases and can be easily functionalized.

POFs can be fabricated via multiple different techniques, and it is relatively easy to incorporate various dopants into the host material. Indeed, POFs are widely used for local area network transmission and sensing applications. The most commonly used polymer for POFs is PMMA which has a theoretical loss limit of ~106±6 dB/km at λ=650 nm based on the Rayleigh scattering and C-H absorption [65]. Many techniques have been used to fabricate preforms for MPOFs, including stacking of tubes or machining of a bulk cylinder of plastic in which the hole pattern is extruded, cast or drilled. This particular feature of MPOF fabrication gives the possibility of obtaining almost any kind of hole pattern, enabling the design of specific fibres for different applications. Many different microstructure designs have been developed but the most used is a uniform hexagonal structure with equally spaced holes (Figure 2.1(a)). Some others structures of MPOFs which have been designed and fabricated are the graded index MPOF (GI-MPOF) [66], hollow-core MPOF (HC-MPOF) [67], high birefringence MPOF [68], rectangular core MPOF [69], twin core MPOF [69], and suspended-core MPOF (SC-MPOF) [70]. Different materials have been used for MPOFs such as polycarbonate (PC) [71], cyclic olefin copolymer (TOPAS) [70], biodegradable materials [72], and the commonly used PMMA.

The fabrication of MPOFs involves at least two stages as presented in the schematic of Figure 2.8. It generally starts with the manufacturing of a structured fibre preform, which is then drawn into a MPOF, a 2nd preform with a smaller diameter or a fibre cane, using a drawing tower. The basic drawing process involves heating the preform to temperatures higher than the glass transition temperature, T_g (around 200 °C for PMMA), to reduce the viscosity of the polymer, and exerting tension to one of the preform extremities, to decrease the diameter. The drawing process often involves intermediate stages, such as the process of drawing a fibre cane [73], which has an intermediate size between the fibre preform and the final fibre (diameter ~ 2 - 6 mm). The cane can

be sleeved/jacketed to increase its diameter for specific fibre structures or combined with other canes to form a new preform with even more complex structures. As presented in Figure 2.8, all three main fabrication procedures involved a primary preform fabrication except the fourth one in which the preform fabrication process can be skipped: this new MPOF fabrication procedure with a single production step will be developed as part of the work in this thesis.

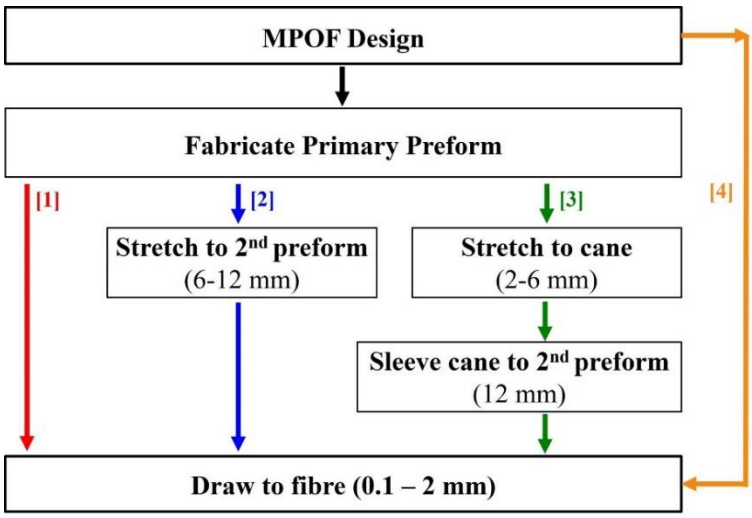

Figure 2.8 Schematic of microstructured polymer fibre fabrication, showing (1 to 3) the conventional three main fabrication procedures [74] and the new fabrication procedure (4) implemented in this work.

Due to the lower processing temperature and ease of machining, polymer is an attractive material for optical fibre devices and sensors because it is deemed suitable for a wider range of fibre fabrication techniques than silica. Drilling was firstly used to fabricate MPOF preforms in 2001 by making holes with the desired structure into an extruded PMMA cylinder and then drawing it into a MPOF using a polymer fibre drawing tower [31]. MPOF preforms can also be manufactured using stacking [75], milling [76], polymerization of liquid monomers [77], and casting/moulding [31, 32]. Moreover, there are techniques used to fabricate MPOF preforms for specific structures or applications, such as billet extrusion, used to fabricate preforms with non-circular holes, and rolling of planar stacks for fabricating hollow-core Bragg fibres.

2.2.1 Stack and draw

The "stack and draw" technique is commonly used to fabricate silica MOFs because it is a versatile and flexible method. By stacking small capillaries, not only can various structures be generated, but also different material besides silica glass can be utilized. Preforms can be created by assembling rods or capillaries into the desired arrangement and inserting the bundle inside a tube to hold the structure securely in place. For MPOFs, the polymer rods are inserted into a polymer tube to create a MPOF preform as shown in Figure 2.9. Before the drawing process, the stacked preform is annealed to remove air and moisture as these can affect the final MPOF structure [78]. The

advantage of this method is that very large air fractions can be achieved by using very thin-walled tubes. Conventional hexagonal air-hole structures and some complicated superlattice structures can be fabricated using circular capillaries that are arranged in patterns to approximate triangular holes, square holes, and elliptic holes [16, 79-83]. Despite this being the most popular method, it is labour-intensive and it is limited to the hexagonal packed periodic structure, thus it is difficult to implement for more complicated designs.

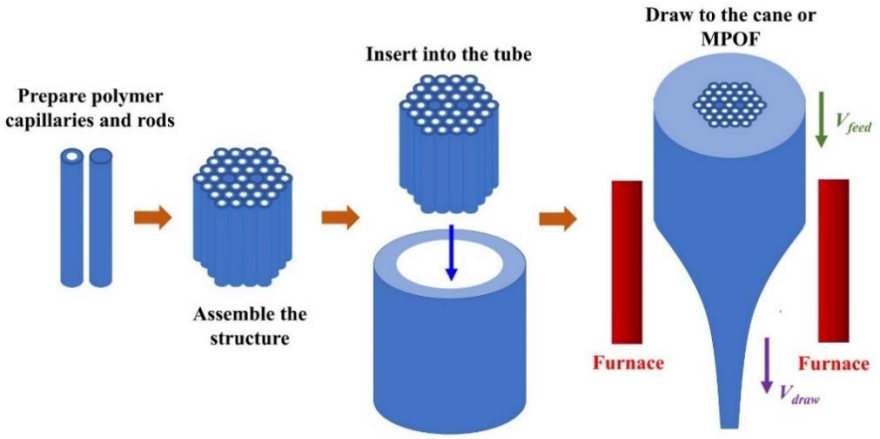

Figure 2.9 Schematic of the stack-and-draw method used to fabricate MPOFs and their preform.

2.2.2 Drilling

Drilling is a straightforward approach for the fabrication of MPOF preforms. The structure preform is created by drilling the pattern of holes into a solid polymer rod using a drill or a laser (Figure 2.10) which is connected to an XY translation stage to create the required pattern [84-87]. Using computer numerical control (CNC) machining it is possible to execute a sequence of automatized instructions over a monolithic polymer cylinder to fabricate complex structured preforms with high resolution. CNC machining offers an easy way to obtain preforms with vast varieties of geometries by changing the diameters of the holes, their spacing and distribution in the polymer. Drilling monolithic preforms allows rapid prototyping of new MPOF designs. This approach can readily produce structures that are difficult to produce by capillary stacking. However, preform drilling does have many serious limitations, the most common of which is that the process is slow. Moreover, preforms are usually short and large in diameter, typically exceeding 70 mm.

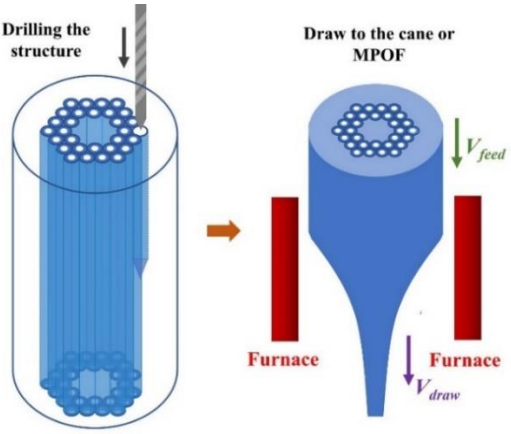

Figure 2.10 Schematic of the drilling method used to fabricate MPOFs and their preforms.

2.2.3 Rolling

As far as the MPOF preform rolling technique is concerned, it usually involves two different polymers or a polymer and a compound glass. The final preform consists of a hollow-core surrounded by a dielectric stack made of two different polymers or two materials with different refractive indices. The initial dielectric stack is fabricated in planar form using some form of deposition and it is then rolled into a cylinder to generate the fibre preform. This technique was also commercially exploited to make an Omniguide fibre (Bragg structured fibre [88]) by using a solvent deposition to deposit two polymers (PMMA/Polystyrene) inside of a rotating polymer tube by using a solvent-evaporation process. The contrast between the refractive index of different layers generates a Bragg reflector that confines light in the hollow-core [50, 89-92].

2.2.4 Casting

Casting is another technology used to produce both glass and polymer preforms [32, 77, 93]. The necessary chemical precursors (i.e. monomers, initiators and chain-transfer agents) are introduced into a mould to produce the required geometry. The polymerizing mixture generally requires degassing to avoid bubble formation. After the polymerization is complete, the solid structure is removed from the mould leaving only the desired polymer preform structure.

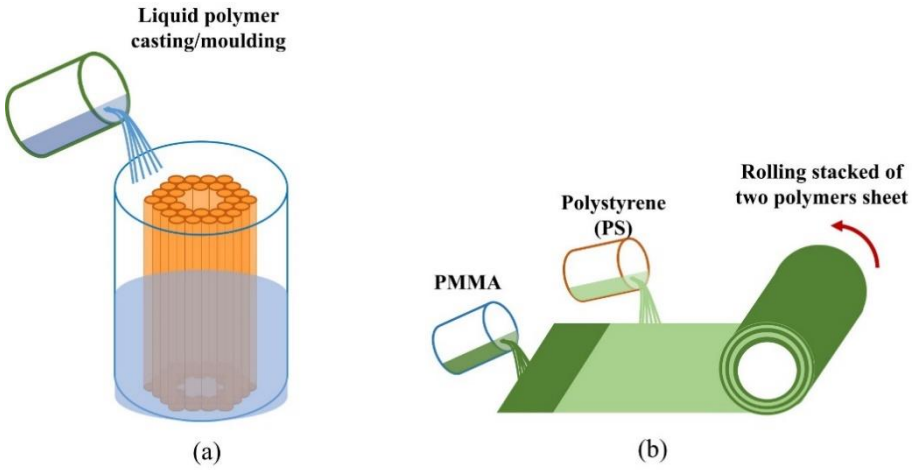

Figure 2.11 Schematic MPOFs preform fabrication using (a) Casting/moulding. (b) Rolling of planar stack made by solvent deposition.

2.2.5 Extrusion

The fabrication of a MPOF preform using billet extrusion was first proposed in 2007 [94]. It has been mainly used for compound glasses to produce preforms with complex geometries such as suspended-core and antiresonant fibres[95-101]. To fabricate the preform, a polymer billet, a monomer, or a resin is forced through a die to form a fibre preform with a complex transverse profile, as shown in Figure 2.12. One advantage of this method is that it involves a single automated step by which non-circular holes, large air fractions and long preforms can be obtained.

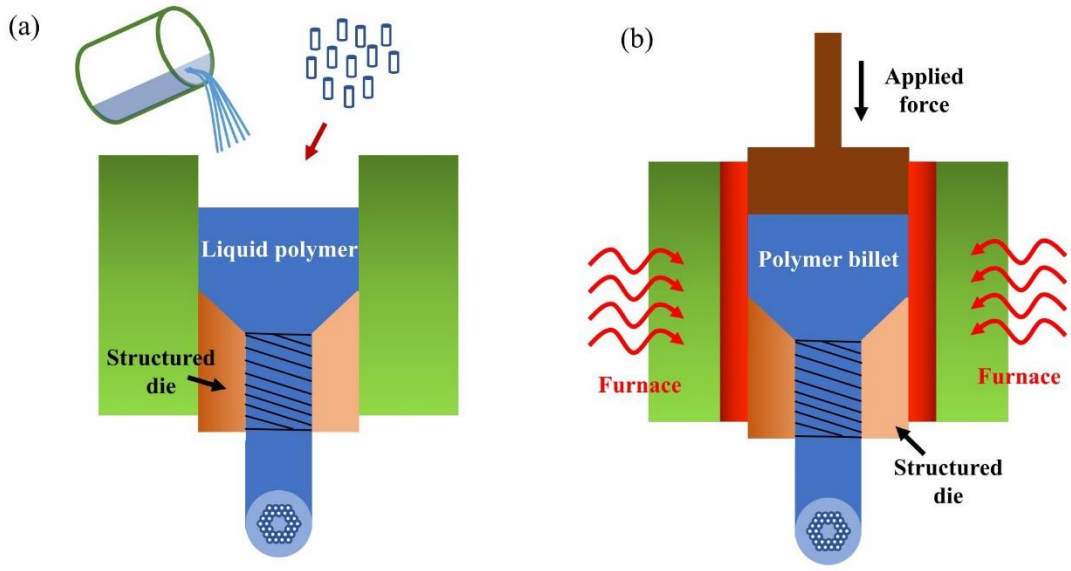

Figure 2.12 Schematic of MPOF preform fabrication using (a) a liquid polymer extrusion and (b) billet extrusion technique.

2.2.6 3D printing for MPOF fabrication

Rapid development of additive manufacturing technologies and the related reduction in cost moved the fabrication of 3D models into the next generation of high precision manufacturing. 3D printing has drawn great interest in many fields such as medicine, art, engineering, and science. Many manufacturing techniques allow to print 3D models, including photo-polymerization, selective laser sintering (SLS), continuous liquid-interface production (CLIP), and fused-deposition modelling (FDM).

In photo-polymerization, a laser or light-emitting diode (LED) is used to scan across a plane and the material polymerisation occurs when light interacts with the monomer. To achieve the 3D profile, the laser or LED is controlled using a three-axial stage and the process is repeated layer by layer. Selective Laser Sintering (SLS) is one of the most popular 3D printing techniques because it can be used to print not only polymer materials but also glass, metal, and ceramic powders. In SLS, a high-power laser is scanned on the horizontal plane layer-by-layer whilst lowering the printing bed. Under the laser irradiation, the printing material is fused together forming the desired 3D model. Polyjet 3D printing relies on the use of liquid polymer jetted onto the 3D printer bed. For the Polyjet 3D printing technique, the liquid polymer is fed into the 3D printer bed and then cured through exposure to ultraviolet (UV) light before depositing the subsequent layer.

Fused Deposition Modelling (FDM) is the most commonly used (and cheapest) technique and relies on a polymer filament fed through a heated nozzle oozing molten polymer. Gluing the molten polymer layer-by-layer generates the 3D profile.

In photonics, 3D printing is widely used for manufacturing optical devices due to its low cost and ease of fabrication [102]. Recent works reported the fabrication of waveguides, beam splitters, plasmonic devices, lenses, and antennas [103, 104]. Optical waveguides operating in the telecom, mid-infrared and terahertz spectral regions were the first optical devices fabricated by using 3D printing.

Hollow-core fibres were also investigated and revealed its potential to confine light in the air-core. Since the devices operating in the terahertz region do not require small dimensions, the hollow-core fibre could be directly 3D printed without any subsequent drawing [105-107]. The first reported 3D printed hollow-core fibre was based on a hollow-core PCF (Figure 2.13(a-b)) that was fabricated using the Polyjet technique applying a UV-resin with a dielectric constant of 2.75 [108]. In this work, a propagation loss of 0.03 dB/mm (0.3 dB/cm) at 105 GHz was achieved. The embedding of metal wires within the 3D printed hollow-core THz fibre was demonstrated in 2014 [109]. This fibre revealed broadband THz propagation in the range of 0.2 – 1.0 THz. 3D printed special structures of THz waveguides, with a helical structure, were reported in 2015 [110]. Hollow-core helical THz waveguides were 3D printed using UV curable polymer via the Polyjet technique, and revealed a low

loss, broadband and close-to-zero dispersion guidance of THz radiation in the frequency range from 0.5-1.0 THz. In 2016, a terahertz hollow-core fibre based on photonic bandgap propagation was 3D printed via the Polyjet technique [111]. One of the challenges using 3D prototyping is to build longer length structures since the currently available printers have height limitations (around 30 cm). In order to overcome this issue, the mechanical connection of two 3D printed THz-guiding optical fibres has been reported, with an average power propagation loss of 0.02 cm^{-1} (0.08 dB/cm) over 0.2–1.0 THz.

Another interesting structure for the hollow-core fibre is the antiresonant fibre. In 2015, the 3D printing of hollow-core fibres based on the antiresonant effect with negative curvature (Figure 2.13 (c)) was first reported [105]. This negative curvature helps to inhibit coupling between the fundamental core mode and the cladding modes, which considerably decreases propagation losses. ABS polymer was used to print the fibre, which revealed a low-loss in the transmission windows between 0.10–0.21, 0.30–0.40, and 0.5–1.1 THz. Polycarbonate (PC) was also used to 3D print a hollow-core antiresonant fibre via the FDM technique. This fibre can guide terahertz radiation with losses around 10 dB/cm over a 1.5–6.0 THz range [30]. In 2015, FDM technology together with ABS polymer was used to fabricate hollow-core Bragg fibres which demonstrated low-loss propagation in a 93 mm long fibre [112]. In 2017, a 3D printed terahertz Bragg fibre (Figure 2.13(d)) was used as a powder and thin film sensor with sensitivity close to 0.1 GHz/μm [106]. The fibre was built using a stereolithography (SLA) system, which has a transverse resolution of 50 μm and a longitudinal resolution of 1 μm. This fibre revealed a propagation loss of 0.15 cm^{-1} (0.65 dB/cm) over frequencies higher than 0.35 THz. Digital Light Processing Rapid Prototyping was also used to 3D print a hollow-core Bragg fibre in 2017 [113]: single mode propagation and an average propagation loss of around 3 dB/m at 0.27 THz were achieved.

The first attempt to draw a HC-MOF from a FDM 3D printed preform was reported in 2016 [114]. In this work, the authors presented the potential of drawing a fibre cane from a 3D printed hollow-core fibre preform by using a PMMA filament. In 2017, the first drawn hollow-core cane based on a 3D printed preform was demonstrated[115], but no guiding was observed. Both circular and rectangular hollow-core fibre preforms were 3D printed using the ABS filament, but neither resulted in an operational HC-MOF. The first 3D printed hollow-core fibre for the mid-IR guiding was reported in 2018 [116]. In this work, guidance of the fibre in the $\lambda = 3.5 – 5$ μm spectral region was observed.

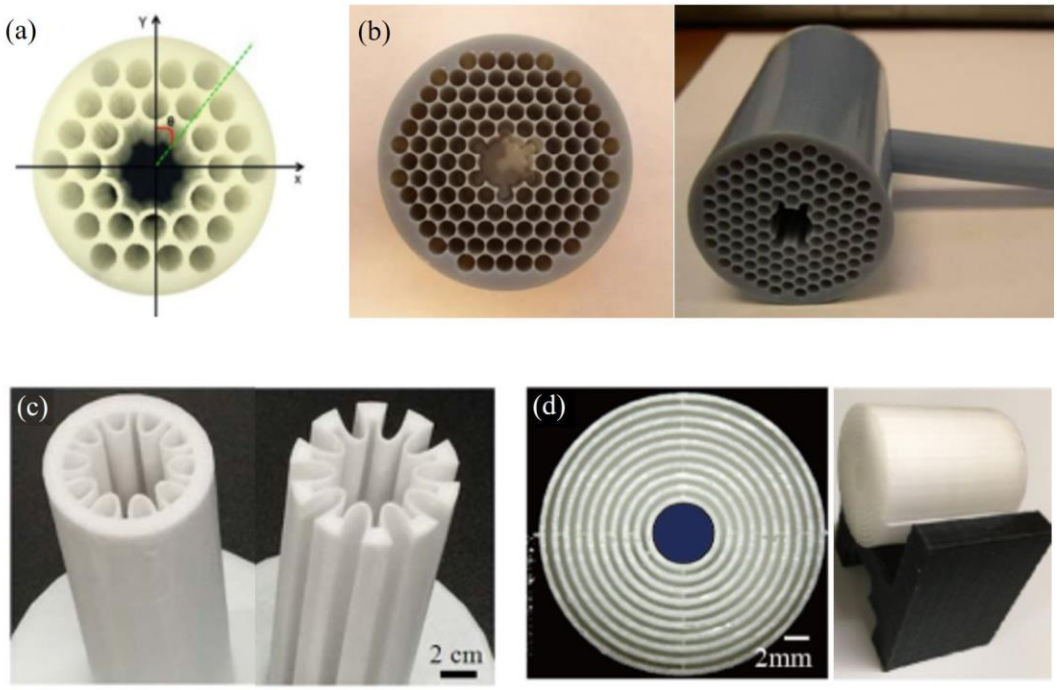

Figure 2.13 (a) A 3D printed hollow-core photonic crystal fibre [111]. (b) Cross-sectional and full views of a 3D printed THz waveguide, with lattice constant of 3 mm, centre core radius of 4.2 mm, and cladding air cylinder radius of 1.3 mm [108]. (c) 3D printed hollow-core antiresonant THz fibres manufactured using the FDM technique [117]. (d) Cross section and side-view of a 3D printed Bragg waveguide with a uniformly periodic reflector [106].

In the same year, solid core optical fibres were drawn from 3D printed preforms [34]. The air-structured optical fibre preform was printed using the FDM technique and then drawn into an optical fibre by using a drawing tower with a low-temperature furnace. A step-index polymer fibre preform 3D printed from two materials was drawn in 2016 [33]. With further advances in 3D printing technology, a two-nozzle 3D printer was used for manufacturing step-index fibre preforms using ABS and polyethylene terephthalate glycol (PETG) filaments. This fibre revealed the possibility of guiding light at telecom wavelengths. Solid core fibres with various core shapes were 3D printed and proposed in the same year [118]. Fibre cladding and core with circular, triangular, square, and rectangular shapes were 3D printed using ABS polymer. In this work, printing parameters such as the printing temperature, printing speed, and layer height have been optimised to achieve acceptable optical transparency. This shows the flexibility of using the 3D printing technique to fabricate optical fibre preforms.

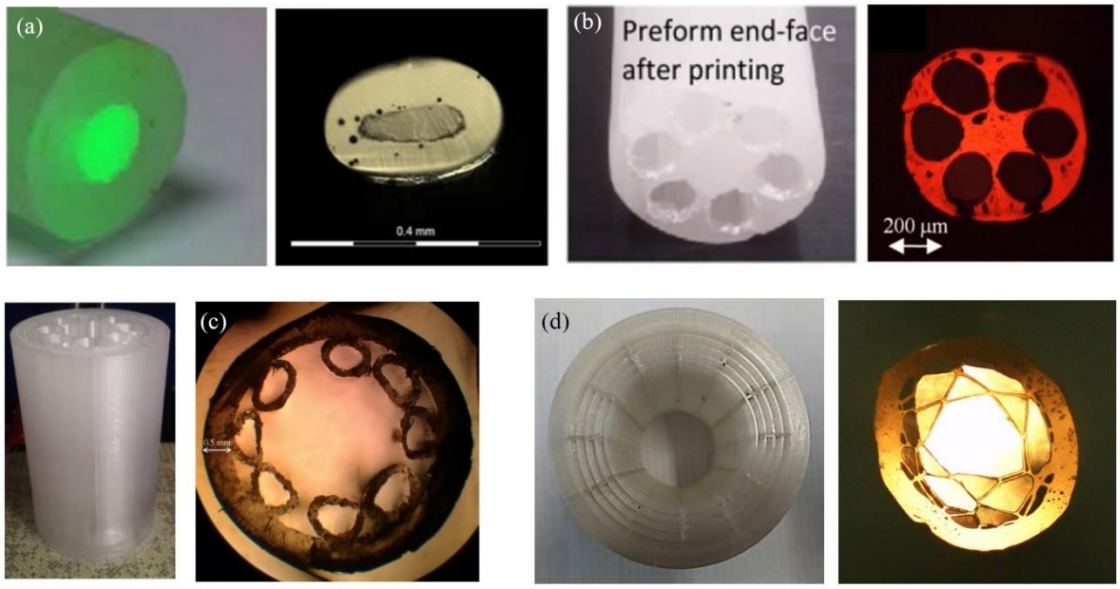

Figure 2.14 (a) 3D printed step-index polymer fibre preform and cross-section of the drawn step index fibre [33]. (b) Suspended core optical fibre preform fabricated from the FDM 3D printer and drawn fibre [34]. (c) First 3D printed hollow-core antiresonant preform and drawn fibres [114]. (d) 3D printed mid-IR hollow-core fibre preform and its fibre cross-section [116].

As presented in the previous section, drilling and casting are widely used to make MPOFs, but exhibit limitations to the number of transverse features and hole shapes, involve complex steps and require expensive facilities such as a clean-room environment for fabrication [119]. Extrusion seems to be a favourable technique to fabricate MPOF preforms with non-circular holes, long length, and complex structures. Optical fibres based on 3D printed preforms have attracted increased interest due to the rapid and flexible procedure for preparing low-cost fibre preforms. Moreover, it can be used to print complicated fibre structures that cannot otherwise be realized using drilling/machining or the stack-and-draw technique. Therefore, the use of extrusion and 3D printing seems to be a good method to fabricate complex MPOF preforms with flexible design. Nevertheless, these techniques still require two steps. To skip preform preparation, MPOFs can be fabricated in a single step by combining extrusion with the 3D printing, to provide the so called "direct extrusion and drawn". The extrusion of coreless solid optical fibres in one low-cost process has been reported in 2016 [120]. The details of MOPF design and fabrication using direct extrusion and drawn technique will be presented in chapters 4 and 5.

2.3 Optical fibre sensors overview

MPOFs are compatible with a range of materials that are likely to become increasingly important. Organic materials cannot be incorporated into glass fibres during processing because the high temperatures used in fibre drawing causes them to denature. The most useful application of the MPOFs are in sensing, due to their flexibility, low processing costs, and variety of materials. Biomedical sensing is one of the dominant sensing applications based on MPOFs as biological

materials are much more compatible with organic polymers than with glasses. The surfaces of polymers are readily functionalised with materials of biological interest. Thus, the aim of this research is to develop not only a novel technique to fabricate MPOFs in a single step but also their sensing applications. This sub-section will present an overview of optical fibre sensors (OFSs) and their important sensing parameters.

The development of optical fibre sensors represents a major market driver for the optoelectronic and fibre optic communication industry. Advances in research and development of OFS devices have extended their applications to various fields of technology, such as medical, defence, geological, and telecommunications. In the past decades, various optical fibre sensor devices have been proposed, to monitor a variety of measurands such as temperature [121-126], refractive index [127-129], pressure [130-133], magnetic field and current sensor [134-137], biological sensors [138-140], rotation, liquid level, and displacement. OFSs offer a number of advantages, such as increased sensitivity compared to the other existing techniques and geometric versatility. Additionally, OFSs are lightweight, extremely compact, passive, exhibit low attenuation, and above all exhibit immunity to electromagnetic interference, high sensitivity, and an extremely wide bandwidth. OFSs can be used in areas with strong electric fields, high temperatures, as well as in corrosive environments due to their dielectric nature. In addition, these sensors are compatible with optical communications systems and have the capacity to operate in a remote sensing configuration.

Generally, an OFS system is composed of three key components: an optical source, a sensing device based on an optical fibre, and a detector (Figure 2.15). The optical source of this system can be a light bulb, a laser diode or a supercontinuum source depending on the parameter to be detected. The optical fibre is often used to directly detect the change of a measurand. For example, a fibre can be used as a magnetic field sensor by injecting linearly polarised light at one fibre extremity and monitoring the change of polarization azimuth at the output. The optical signal detected by the detector is then used to analyse the performance of the sensor.

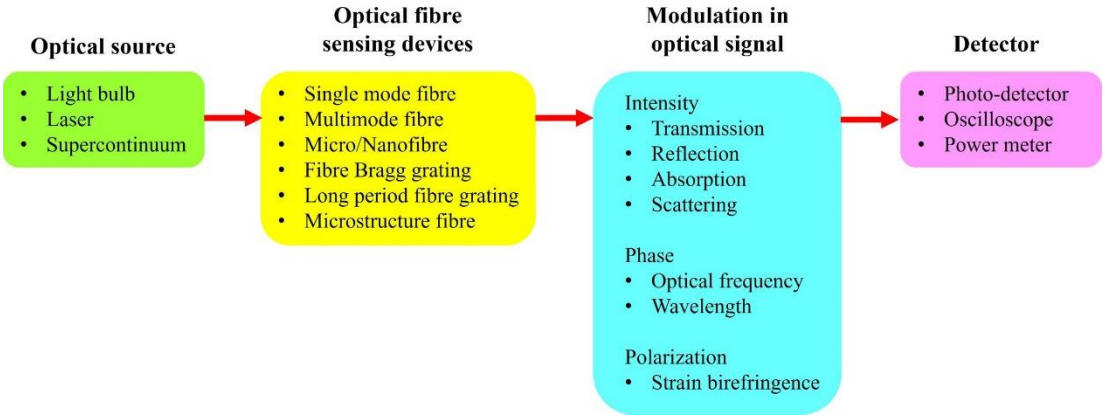

Figure 2.15 Schematic of a generic optical fibre sensor system.

The important parameters used to identify the performance of the sensors are [141]:

- *Sensitivity (S):* also called responsivity, represents the change in parameter used for detection induced by a change in the measurand. For example, in temperature sensing, this will either be in units of (a) nm/°C when monitoring the shift in wavelength, or (b) dB/°C when monitoring the change in the power.
- *Resolution of detection system (R)*: is the smallest detectable change in the measurand.
- *Detection limit (DL)*: the smallest value of the measurand that can be detected by the sensor.
- *Response time (τ)*: the time required taken for the detection parameter to rise from 10% to 90% of its final value when subjected to a change in the measurand.
- *Dynamic range (DR)*: the range of measurand values which can be unambiguously measured by the sensor.
- *Repeatability*: the variation in the detection parameter for measurements taken on the same sample under the same experimental conditions. It is an indicator of the agreement between two different measurements carried out on the same sample.
- *Reproducibility*: the performance of the different samples taken under the same experimental condition.

2.4 Summary

This chapter has outlined the guiding mechanisms of both solid-core and hollow-core MOFs. A special emphasis was given to the review of the techniques used to fabricate MPOFs and their drawbacks, leading to the development of the novel technique, direct extrusion and drawing, which is the main content of this research. More details about the development of this fabrication technique and the characterisation of the MPOFs fabricated by using this technique will be presented in the later chapters.

Chapter 3.

POLYMER FIBRE BASED ON A 3D PRINTED PREFORM

Sensors based on polymer optical fibres (POFs) are in general low-cost and easy to use. In comparison with conventional glass fibres, POFs are especially advantageous due to their excellent flexibility, ease of manipulation and ductile fracture resistance. [142]. The use of POF satisfies also the requirements of biosensors and provides many advantages in comparison to other types of sensors, such as material bio-compatibility, flexibility, and robustness. [143].

Microstructured polymer optical fibres (MPOF) attracted increasing attention for biological sensing due to the presence of micro/nano holes inside the MPOF, which only require dozens of nanolitres to microlitres of derivatizing solutions for surface modification. The infiltration of solution for inner surface functionalisation is a flow process, which ensures constant renewal of the solution coming in contact with the surface, thus enhancing the rate and homogeneity of surface derivatization.

Conventional methods used to fabricate MPOF fibre preforms [74] are time-consuming and incapable of producing more complex non-geometrical structures. 3D printing of preforms is an excellent alternative to fabricate more complex structures, due to the rapid and flexible prototyping procedure for preparing the preform.

In this chapter, a breakthrough in the manufacturing of 3D printed optical fibres is presented. In this work, a MOF operating in the mid-IR region is manufactured: transmission losses 39 times lower than the material loss are achieved by using the anti-resonance effect in hollow-core Bragg fibres.

The 3D model design of the hollow-core Bragg fibre preform is shown in Section 3.1. The following Section 3.2 describes the fabrication process of manufacturing the structured polymer fibre preform and the optimisation of printing parameters to achieve a high transparent preform. Section 3.3 describes the drawing procedure of the polymer fibre. Finally, the characterisation of a MPOF drawn from the 3D printed preform is illustrated in Section 3.4.

3.1 3D model design of optical fibre preforms

A hollow-core Bragg fibre (HC-BF) is a circular air core surrounded by periodic cladding layers. The layers of the cladding are a periodic sequence of high refractive index (n_h) and low refractive index (n_l) materials. Light in the hollow-core Bragg fibre can be confined to the central air-core owing to the Bragg reflection from the periodic cladding structure. HC-BFs are particularly useful in bio-sensing because they enable analytes access to regions with strong overlap with an

optical field without taking off the fibre cladding or coating. HC-BF does not require a small hollow-core to guide the light (core diameter of 2 - 10 µm). Moreover, the HC-BF with a larger core exhibits smaller confinement loss and is easier for solution infiltration [144].

Our polymer HC-BF consists of a circular air-core and 4 periodic layers of cladding. Due to the small number of cladding layers, the structure requires large refractive index contrast between low- and high- index layers for a good modal confinement. The basic cladding structure of the 3D Bragg fibre preform used in this experiment is based on a sequence of polymer and air. Figure 3.1 shows the cross-section of the designed HC-BF preform. Different cladding polymer layers are connected by bridges. The material used to create the bridge is the same polymer as used for the rest of the fibre.

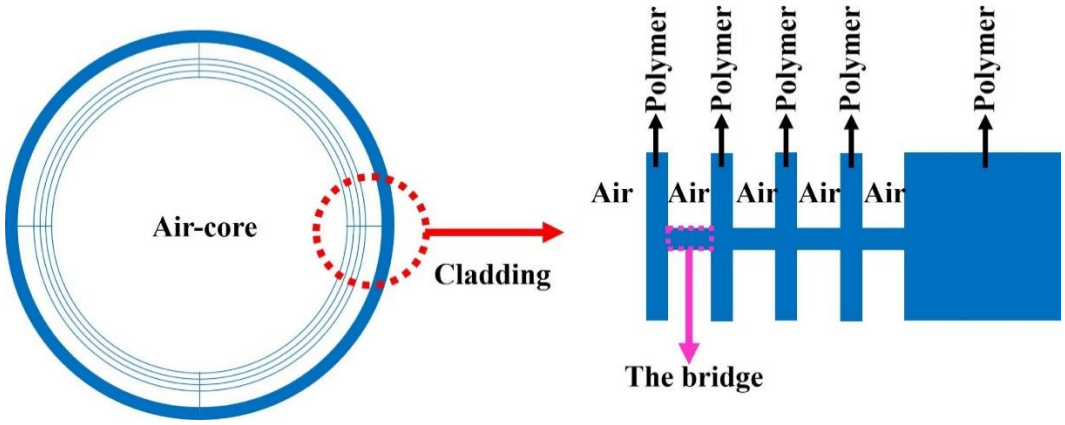

Figure 3.1 Schematic of HC-BF cross-section. A close-up of the preform is shown on the right.

The structured fibre preform was fabricated by using a FDM 3D printer. The fabrication procedure of the 3D printed preform was:

- Design the 3D model of a fibre preform.
- Prepare a 3D model file for a printer (slicing process) by using a dedicated software (Cura by *Ultimaker*).
- Print the preform by using a 3D printer

Here, the HC-BF preform 3D model was designed by using the Fusion 360 software. The parameters used in this design are the outer and inner diameter of the preform, the thickness of the polymer layer, the gap size between each layer, and the number of bridges. The preform was designed with two different bridge structures: the straight bridge and the spiral bridge. These two designs were compared to maintain the circular core during the drawing process. From the theory of the Bragg fibres, the resonant centre wavelength of the fibre fundamental bandgap can be written in eq. (3-1) where d_h and d_l are thickness of high and low index layers, n_h and n_l are the corresponding refractive

index, and n_c is the refractive index of fibre core. In both cases, the thickness of the cladding polymer layer and of the bridge was set to d_h = 0.54 mm, while the size of the air-gap between each layer to d_l= 1.8 mm. These two parameters were achieved from the simulation when the final diameter of optical fibre is expected to be~200 μm where the outer diameter of the designed preform was 70 mm and the length 90 mm. Figure 3.2 and Figure 3.3 illustrate the cross-section and the 3D model of the designed Bragg fibre preform with the straight and the spiral bridges, respectively.

$$\frac{\lambda}{2} = d_l\sqrt{n_l^2 - n_c^2} + d_h\sqrt{n_h^2 - n_c^2} \qquad 3\text{-}1$$

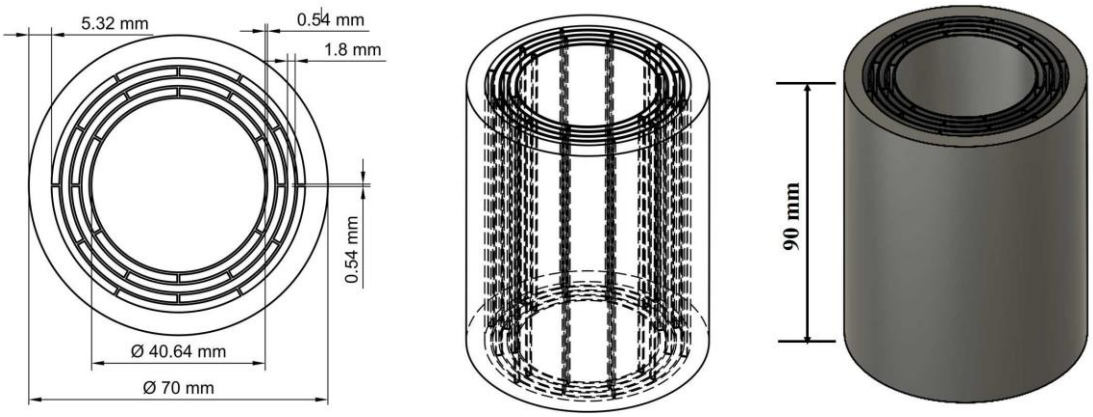

Figure 3.2 Cross-section and 3D model design of the Bragg fibre preform with straight bridges.

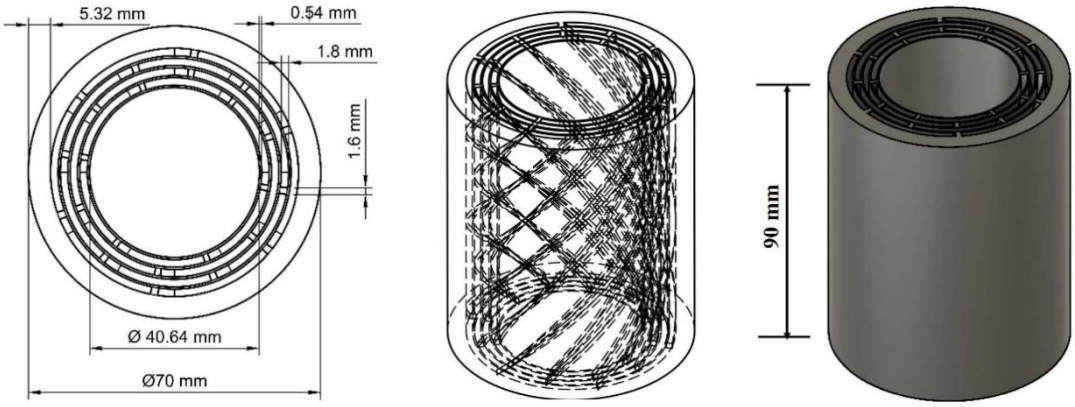

Figure 3.3 Cross-section and 3D model design of the Bragg fibre preform with spiral bridges.

3.2 3D printed optical fibre preforms

Optical fibre preforms were manufactured by using a FDM 3D printer (*Ultimaker2 Extended+*). In this experiment, the material used to print the preform was clear polyethylene terephthalate glycol (PETG), which has the advantages of remarkable strength and durability. More

importantly, it produces no fumes during the printing procedure. The PETG filament is suitable for fabricating the polymer fibre in this work because it is a non-biodegradable material, which has a potential for bio and chemical sensing.

A 3D printed preform was fabricated by layer by layer. Although the filament is transparent, the preform can easily become white or milky because of bubbles occurring during the printing process. These bubbles are the main problem for maintaining the fibre geometry while drawing. Bubbles expand when the preform is heated resulting in deformation of the drawn fibre. Bubbles can also reduce the strength between each layer, causing the preform to easily break during drawing. The less bubbles are in the 3D printed fibre preform, the stronger and more transparent the printed preform will be.

To get rid of the bubbles inside the preform, the parameters were optimised for both the 3D model design and the printing. The parameters that affect the transparency of the printed 3D model were (i) infill density and (ii) infill pattern, while those depending on the printer were (i) flow rate and (ii) extruder temperature.

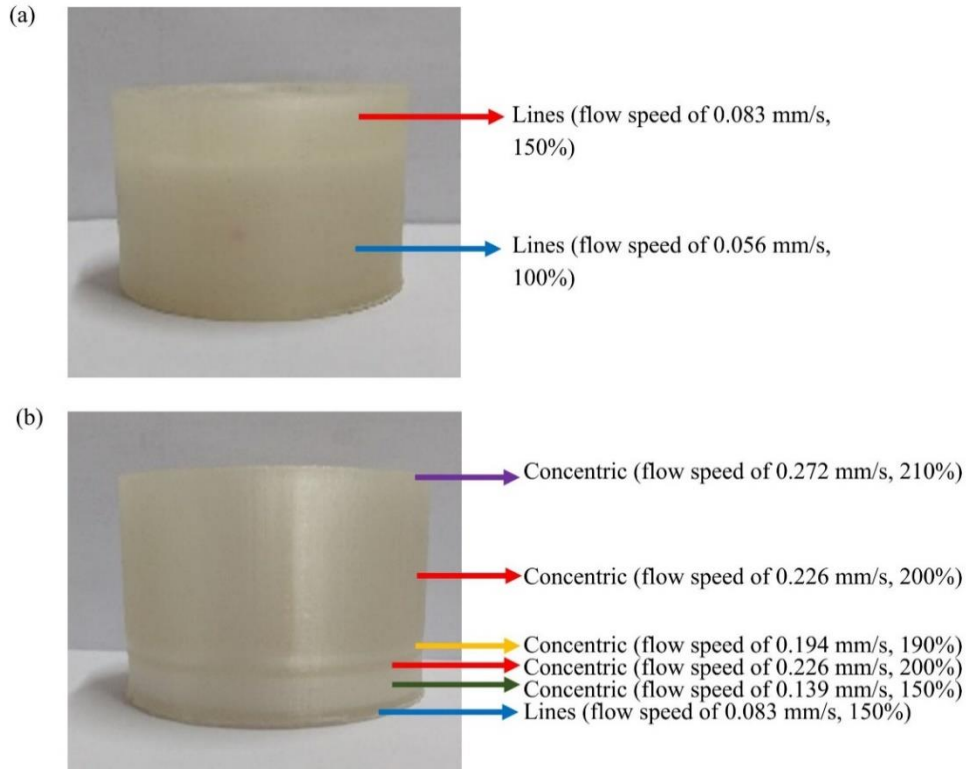

Figure 3.4 Printed preforms with different material flow rates in (a) lines infill pattern, and (b) lines and concentric infill pattern.

According to the manufacturer guidelines, the required extruder temperature for printing the PETG filament is in the range 230 – 255 °C. To get more a transparent prototype, higher temperatures are needed, so the temperature used in this experiment was set to 250 °C. The effect of flow rate and infill pattern on the transparency of the printed preform is shown Figure 3.4. Material flow rate for

printing is set by using the slicing software (Cura©). The 3D model file after slicing is in the format that the 3D printer can be read. Although the flow rate of material at each layer has been set by the software, the *Ultimaker* printer has a function to vary the flow rate of material during the printing process by adjusting the percentage of initial set flow rate. Therefore, 100% flow rate is when the material is fed through the nozzle with the same speed as the setting flow rate while more than 100% flow rate is when the material is fed at a higher speed. Results indicate that the printed preform with a flow rate of 150% is more transparent than that at 100% when the preform is printed with a linear pattern. The preforms were also printed with a concentric infill pattern. The printing time using the concentric pattern is 6 hours faster than that using the lines pattern for the same preform dimensions using the design shown in Figure 3.3. The effect of the flow rate on the transparency of the preform (based on the concentric pattern) is illustrated in Figure 3.4(b). The result shows that the printed preform at a flow rate of 190% is more opaque than 200% and 210% but the surface of the printed preform with 210% flow rate is not smooth due to filament overload. So, the most suitable flow rate for the concentric pattern was deemed to be 200%. The printed Bragg fibre preform with the optimised parameters of the straight and spiral bridge are shown in Figure 3.5(a) and Figure 3.5(b), respectively.

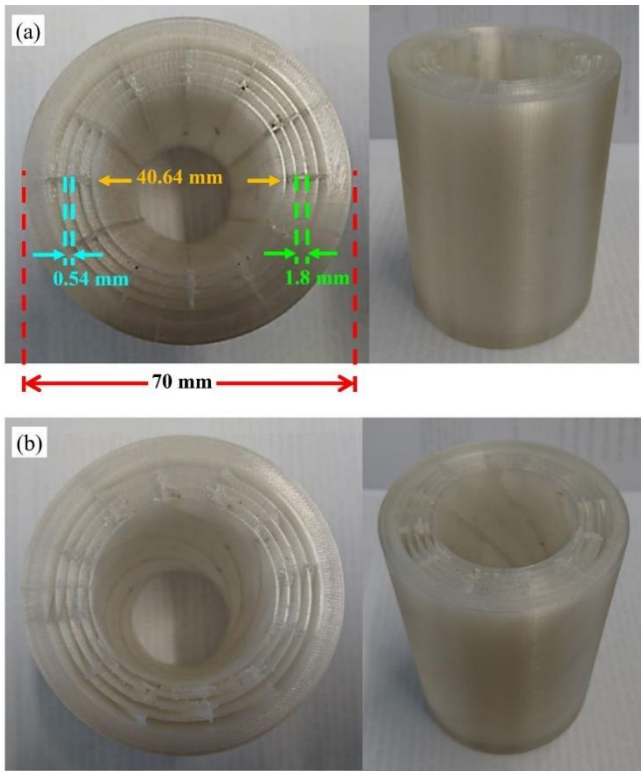

Figure 3.5 3D printed Bragg fibre preform using (a) straight bridges, (b) spiral bridges.

3.3 Hollow-core polymer fibre drawing from 3D printed preform

Fibre drawing was performed at the Physics Department of the Universidad de Campinas, Sao Paulo, Brazil. Three important steps were identified for the fibre drawing process: 1) tapering, where

the size of the preform is reduced to a pre-cane preform (diameter ~ 30 - 50 mm); 2) homogenization, where a cane with the diameter ~ 12 mm is achieved; 3) pulling, when the fibre is drawn from the cane. Figure 3.6 shows the fibre drawing tower and the furnace. Two furnaces are used in this experiment: the bigger one (primary furnace) is used for tapering and homogenization, while the smaller one (secondary furnace) is used to draw the optical fibre.

Figure 3.6 (a) The drawing tower, (b) and (c) furnaces used to heat the fibre preform and fibre cane during the drawing process.

3.3.1 Tapering

The top and the bottom parts of fibre preform were secured with holders to minimize changes of the fibre structure during the drawing in a manner similar to that used in the fabrication of solid PMMA fibres [145, 146]. The top holder was connected to an aluminium rod fixed to the 3D linear translation stage used to feed the preform into the furnace. The bottom holder was also connected to the aluminium rod. The preform was annealed before pulling by using the primary furnace (Figure 3.7). The pre-cane preform was created by pulling the rod at the bottom holder of the heated preform with a pulling speed of ~0.01 m/min.

Table 3-1 : Annealing and pulling temperature and time for the tapering stage.

Stage	Temperature (ºC)	Time (minute)
Annealing	110	60
Annealing	130	15
Annealing	145	5
Annealing	150	5
Pulling	150	-

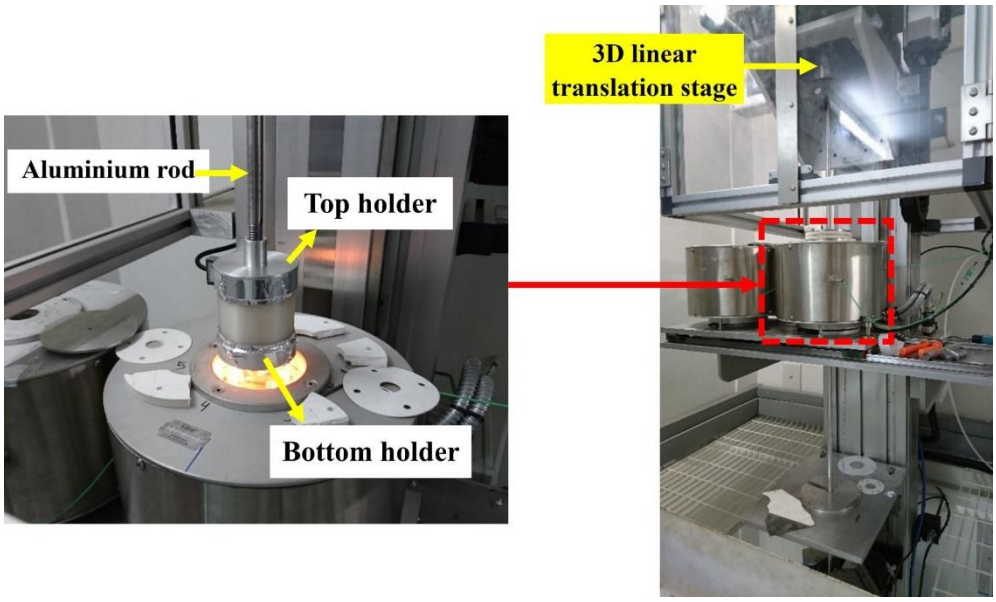

Figure 3.7 Annealing and pulling process of the fibre preform for the tapering stage.

3.3.2 Homogenization

In this stage the pre-cane preforms were pulled into canes. The annealing and pulling process are repeated at the same temperature as the previous stage, but for shorter times because the pre-cane preform is smaller than the preform. The cane is drawn by using the primary furnace. The approximate final diameter at the middle of the cane was 15 mm.

Table 3-2 : Temperature and time for annealing and pulling in the homogenization stage.

Stage	Temperature (°C)	Time (minute)
Annealing	110	15
Annealing	130	15
Annealing	145	5
Annealing	150	5
Pulling	150	-

Figure 3.8 The pulling process of the cane.

3.3.3 Pulling

Only the middle section of the cane was used to draw the optical fibre. The upper and lower parts were removed by using a saw. The cane was fixed to plastic holders at both the upper and lower extremities. At this stage, the cane was heated by using the secondary furnace due to the smaller size of the cane as compared with the size of the fibre preform. The cane was annealed and pulled at the temperature and time presented in Table 3. Figure 3.9 illustrates the fibre preform, the pre-cane preform, the cane, and the optical fibre. The microscope image of the cross-section of the drawn polymer fibre is shown in Figure 3.10. It illustrates that the periodic layers of the cladding structure were not maintained. The deformation in the structure occurred after the homogenization stage. The viscosity of PETG at this processing temperature was estimated to be above 10^5 Poise, providing an operational regime where viscosity dominates over surface tension, avoiding interstice closure [147].

Table 3-3 : Annealing and pulling temperature and time for the pulling stage.

Stage	Temperature (°C)	Time (minute)
Annealing	110	20
Annealing	130	15
Pulling	135	-

The HCF was cleaved by using a heated razor blade in order to image the fibre cross-section. Optical microscope images of its cross-section are presented in Figure 3.10. Although the fibre preforms' 3D printing parameters such as infill density and printing speed as well as additional preform pre-annealing were optimised to minimize air trapping, some air bubbles still occurred and can clearly be seen in the fibre cladding. The final optical fibre exhibited a slightly elliptical cross-section, which was ascribed to the asymmetry introduced by the small degree of swelling associated

to air and moisture trapped in the polymeric matrix due to the longitudinally layer-by-layer preform printing. A longitudinally layer-by-layer printed preform can also cause non-uniform stress in the radial direction of the preform, resulting in the non-uniform thermal expansion. The fibre diameter was measured to be d_{fibre1}~ 466 µm and d_{fibre2} ~ 417 µm along the major and minor axes, respectively. The core (hole) diameters for the major and minor axes were measured to be d_{core1} ~ 225 µm and d_{core2} ~ 177 µm, respectively.

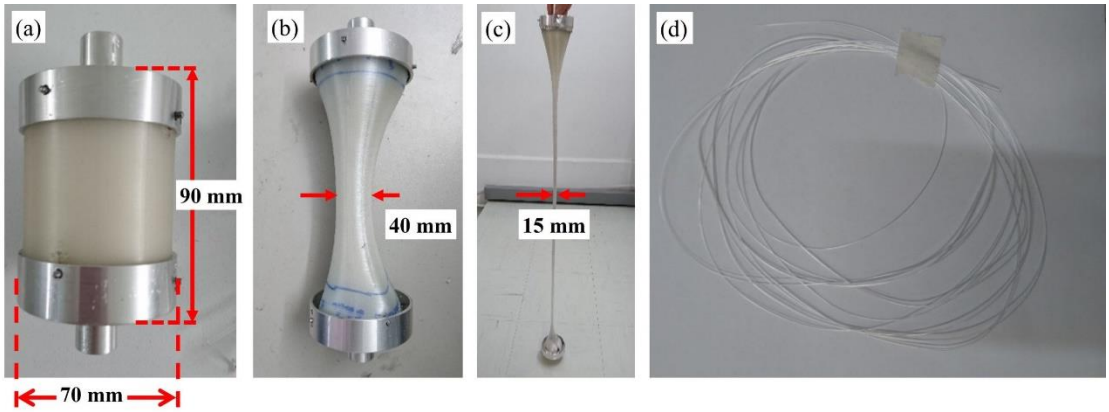

Figure 3.9 The optical fibre preform (a) before pulling, (b) after tapering, (c) after homogenization, and (d) optical fibre.

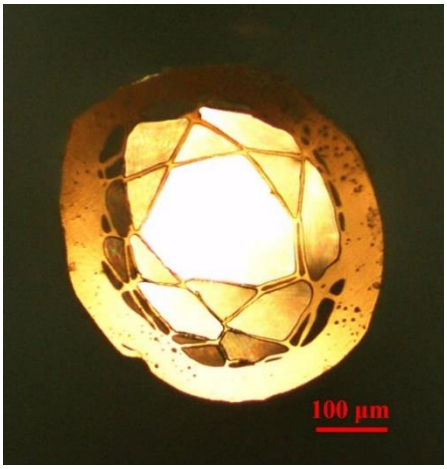

Figure 3.10 Cross-section of the drawn polymer fibre from the Bragg fibre preform with alternate straight bridge.

3.4 Fibre characterisation

Although the structure of HC-BF drawn from the 3D printed preform departed from the initial design, light confinement in this fibre was observed. The final structure of the hollow-core fibre is similar to the structure of anti-resonant fibres. Transmission in the mid-IR (λ~ 2 – 6 µm) of the HCF shows that guiding is due to the anti-resonant effect as shown below.

3.4.1 Filament material absorption

Attenuation is the loss of optical power as light travels along a material. Signal attenuation is defined as the ratio of optical input power to the optical output power. Loss in optical fibres is generally caused by material (electronic and vibrational) absorption, scattering, and bending. Material absorption and scattering are generally the major causes of propagation losses in an optical fibre. Absorption is defined as the portion of attenuation resulting from the conversion of optical power into another energy form such as thermal energy.

The dependence of attenuation on material thickness is usually expressed by the Beer-Lambert law:

$$I = I_0 e^{-\propto x} \qquad 3\text{-}2$$

where I denotes the intensity of light propagated through the material of thickness x, I_0 is the intensity incident on the sample and $\propto$ is an absorption coefficient. This means the intensity of light decreases exponentially with the propagation distance through the material.

In this work, material absorption of the filament used to print the fibre preform (PETG) was measured in the wavelength range λ~ 2 – 6 µm. A schematic of the measurement set-up is shown in Figure 3.11. To analyse material absorption, the transmission spectra of light propagating through PETG filaments with different thicknesses were measured (similar to cut-back measurements).

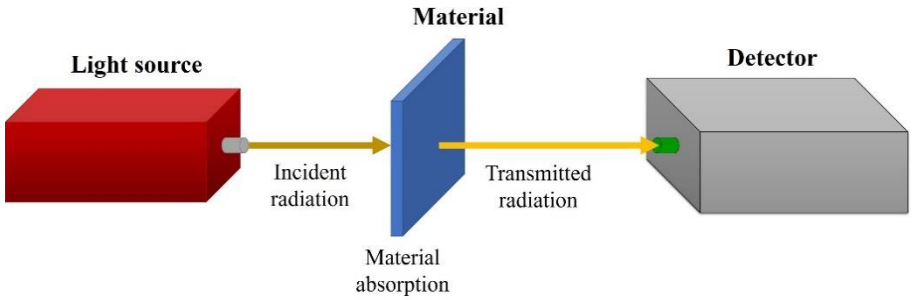

Figure 3.11 Schematic of measuring setup for material absorption.

Figure 3.12 Different thickness flat PETG samples for material absorption measurements.

To minimise the measurement error due to aberrations, reflection and scattering on the standard cylindrical shape filament, planar PETG samples were created. A short piece of a filament (length ~6 cm) was placed on top of a glass slide (microscope slide) and heated to temperature of T~180^{o}C using a hot air gun to ensure uniformity in the temperature profile. The filament viscosity decreased and when another glass slide was placed on the top of the heated filament and force was applied to the top glass slide, the polymeric filament changed shape into a flat sample. The thickness of the sample was controlled by optimising the force applied on the heated filament. Images of planar PETG filaments with different thicknesses are presented in Figure 3.12.

Light from a broadband source (visible to mid-IR) was shone through the PETG sample and was collected by a FTIR spectrometer (ARCspectro FT-MIR) to measure the transmission spectra. A chalcogenide fibre was used to collect the light from the light source (Thorlabs SLS202) and light propagated through the material as presented in Figure 3.13. The transmissivity and absorbance at λ~2 – 6 µm of PETG samples with thicknesses of 0.17, 0.58, 0.69, 0.73, and 0.82 mm are presented in Figure 3.14. The observed attenuation has been attributed to the vibration of C-O (λ = 2.7 and 4.3 µm) and C-H (λ = 3.25 µm) bonds. Results show that transmittance is less than 20 % when the material is thicker than 500 µm. The absorption of PETG was calculated to be 11.6 dB/mm at λ ~ 4.5 µm.

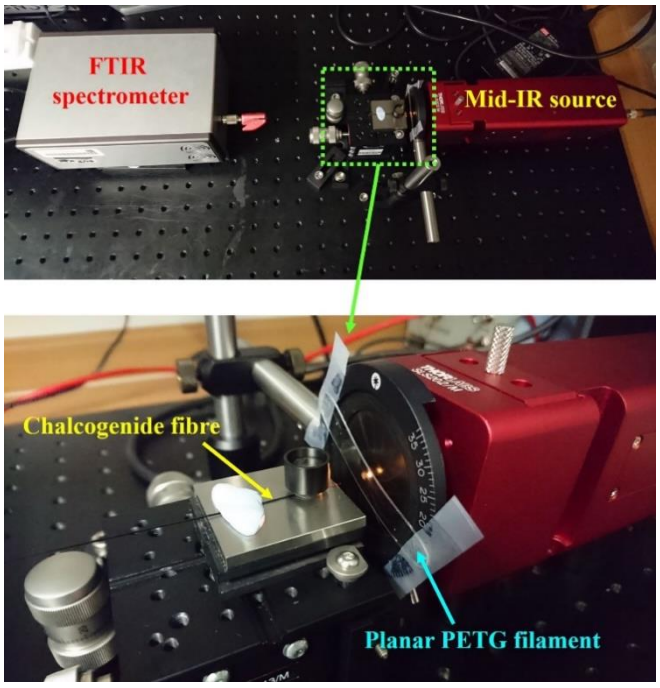

Figure 3.13 Experimental setup used to measure material absorption of a PETG filament at λ~ 2 - 6 µm.

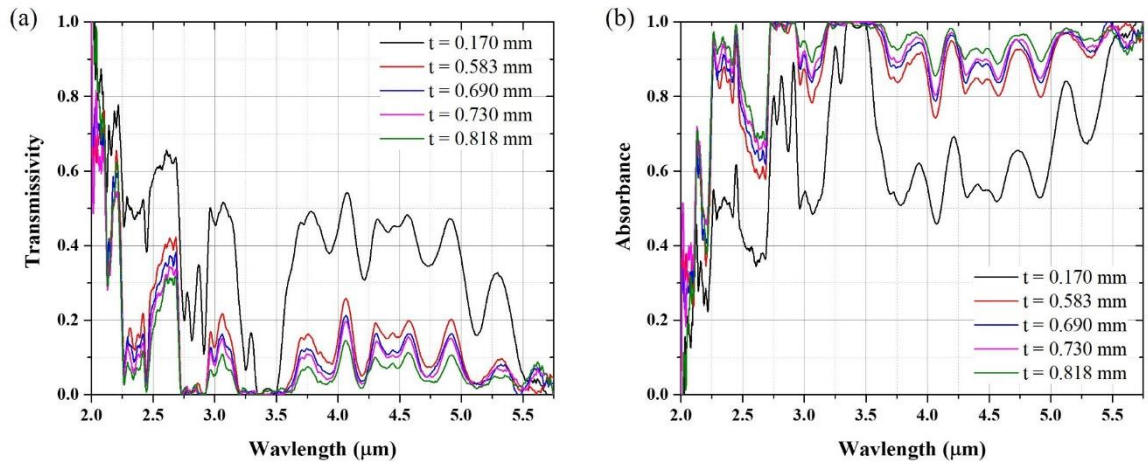

Figure 3.14 (a) Transmissivity and (b) absorbance of material used to print fibre preform with different thicknesses.

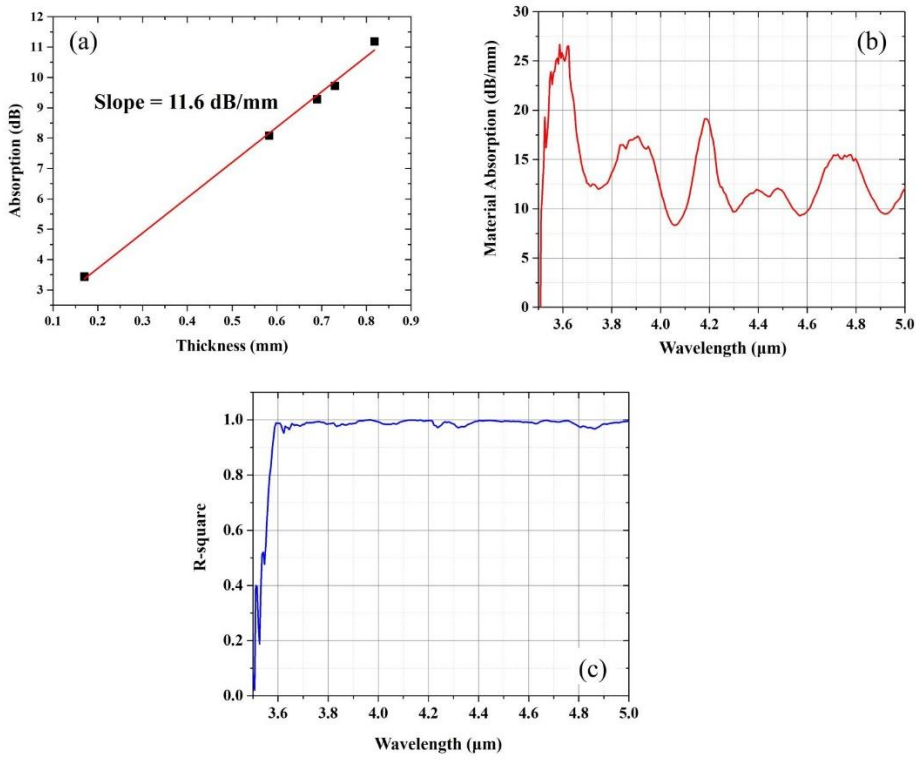

Figure 3.15 (a) Relationship between PETG absorption and sample thickness at λ~4.5 μm. (b) Plot of PETG material absorption (obtained from cut-back measurements as in (a)) versus wavelength. (c) Coefficient of determination (R-squared value) of material absorption at each wavelength of Figure 3.15(b).

3.4.2 Near-field measurements of PETG hollow-core fibre

In order to evaluate the optical guidance properties of the hollow-core fibre in the mid-IR, a broadband lamp with emission over λ~450 - 5500 nm (Thorlabs SLS202) was coupled into a 12 cm long section of the fibre using a bare-fibre adapter. The modal image was taken by collecting the fibre output at λ = 3.5 – 5 μm with a thermal infrared camera (Onca-MWIR-InSb) using a ZnSe

objective lens of 18 mm focal length. Figure 3.16 presents the thermal image and the intensity profile at the HCF output. Figure 3.16(b) confirms that mid-IR light is guided in the air-core.

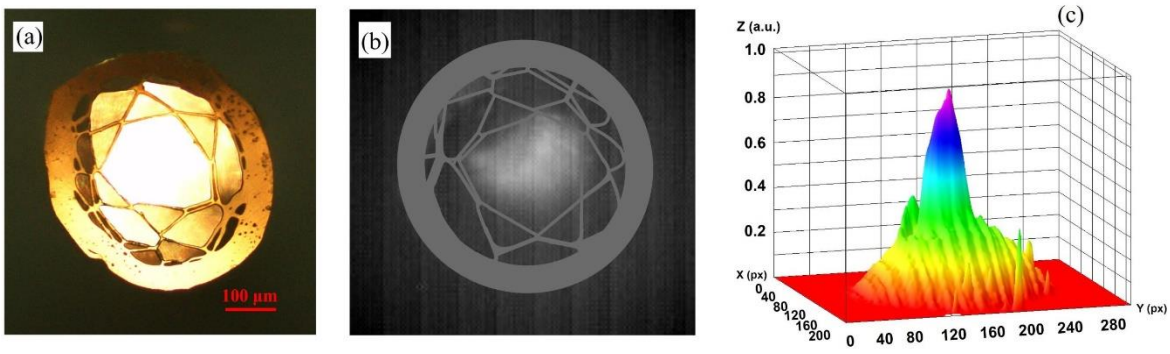

Figure 3.16 (a) Hollow-core fibre cross-section under an optical microscope operating in the visible. (b) Mid-IR mode profile and (c) its intensity profile.

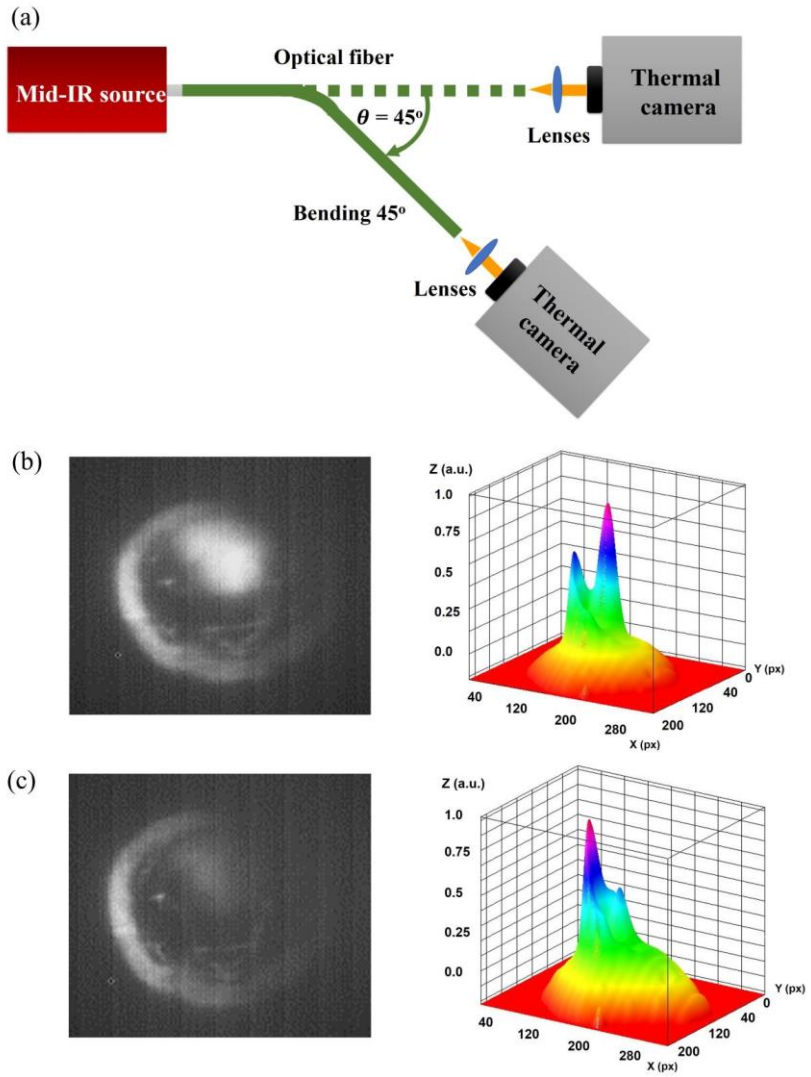

Figure 3.17 (a) Schematic diagram of the experimental setup used for the mid-IR modal imaging from the HCF during bending. (b) Modal image and intensity profile of light transmitted through the air-core fibre when straight, and (c) at 45° bending.

To confirm the HCF mid-IR guiding capability, the near-field image of the transmitted light at $\lambda \sim 3.5–5$ μm was recorded under different degrees of fibre bending using the set-up shown in Figure 3.17(a). The fibre angle varied from 0 to 45° reaching a radius of curvature of ~76 mm. Figure 3.17(b)-(c) show the HCF output and its intensity profile for both straight and bent fibres. While for the straight fibre most of the light is guided in the air-core (Figure 3.17(b)), when the fibre is bent, an increasingly large amount of light is coupled to the polymer cladding (Figure 3.17(c)). This behaviour of the HCF at different bending conditions is attributed to the multimode guidance, which is expected for the HCF's large air core. The HCF propagation loss at $\lambda \sim 4.5$ μm was measured to be ~0.3 dB/mm. The material absorption of the filament (PETG) used to print the fibre preform was measured in section 3.4.1 and at λ~4.5 μm showed a value of 11.6 dB/mm, 39 times higher than the HCF propagation loss. This has been ascribed to mid-IR light being guided in the air-core of the fabricated optical fibre over the length of 10 cm.

Simulations of the mode propagating through the HCF structure were performed by importing the fibre cross section, taken from a microscope image (Figure 3.18(a)), into a commercial finite element method software (COMSOL©). The modal profile of light in the fibre was simulated by using a maximum mesh size of 2/3 μm with a material refractive index of 1.57. Figure 3.18(b) shows the supported mode, confined in the air-core at $\lambda \sim 4.5$ μm. The high loss measured in the manufactured HCF has been attributed to the irregular fibre profile along the azimuthal direction, as supported by the different cross section profiles observed during fibre cleaving (see Figure 3.16(a) and Figure 3.18(a)).

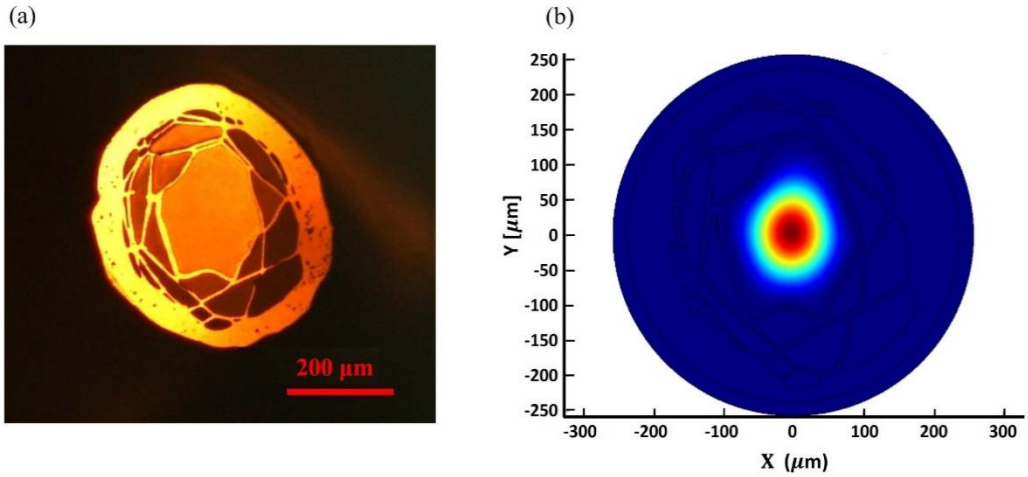

Figure 3.18 (a) Microscope image of the fibre cross-section used in the modal simulations; (b) Intensity profile of the mode supported in the air-core within the simulated fibre structure.

3.5 Summary

In conclusion, a polymer air-core optical fibre fabricated from a 3D printed preform was demonstrated. Although the final structure of the fibre experienced strong deformation during the

drawing process, transmission in the mid-IR wavelengths region ($\lambda \sim 3.5 – 5$ μm) over a 10 cm long fibre was achieved. The mid-IR near-field end facet image and the modal profile simulations show the fibre's ability to confine mid-IR light in the air-core. The measured propagation loss (of the order of 300 dB/m) is 39 times smaller than the polymer loss and can be improved by reducing the structural deformations associated with printing and drawing of the fibre.

Chapter 4.

DESIGN AND FABRICATION OF STRUCTURED 3D PRINTER NOZZLES

Several techniques have been used to fabricate microstructured polymer optical fibre (MPOF) preforms (Chapter 2), but they mostly have limitations, such as on the number of transverse features, or the shape of holes and their configuration. Drilling is limited to circular holes, short preform lengths and it is a time-consuming technique. Stacking is substantially limited to circular holes arranged in a hexagonal lattice, and it is time-consuming and difficult. Casting of polymer preforms with large numbers of holes has been demonstrated for circular holes using in-situ polymerization [32], but it requires the use of high processing temperatures, which leads to thermal degradation of the polymer. In recent years, 3D printing has emerged as a solution to print structured preforms with complex geometries. 3D printing allows long lengths of preforms (limited only by the printer height) with noncircular-holes structure to be prepared. The experimental results in Chapter 3 revealed the promising possibility of printing MPOF preforms using a 3D printer. Yet, deformations in the final structure of the MPOF occurred during the drawing, compromising its guiding properties.

A promising alternative to these approaches is billet extrusion, which has been shown to be a versatile, reproducible and single-step approach for the fabrication of soft glass and polymer structured preforms [48, 94, 148-150]. To produce these relatively simple structures, extrusion dies with relatively complex internal structures were used. Preforms are fabricated by forcing a bulk polymer billet through a die to form a preform with transverse complex profile. Non-circular holes, large air-filling fractions, and long preform can be achieved with this technique. 3D printers have been optimised for printing high quality objects from a variety of materials including polymers, glasses, and metals, resulting in improved control systems which include a built-in temperature controller and filament polymer feeding system, allowing for their potential use in fibre drawing. By combining the extrusion technique with the capabilities of 3D printers, a novel low-cost fabrication method for long stretches of MPOFs can be achieved.

In this chapter, the design and fabrication of a key device used to fabricate MPOFs from the 3D printer will be presented: the structured nozzle. The fabrication of MPOFs directly from the 3D printer, without the need for any intermediate stages requiring preform or cane fabrication, requires the manufacture of a structured nozzle with a geometry inverse to that of the MPOF. When the structured nozzle is inserted onto the 3D printer head, it can be heated up to 300 ^{o}C, accessing a wide temperature range useful for processing the printer filament polymer. In other words, the nozzle can act as a small furnace with a controllable temperature. To provide more details about the structured

nozzles used in this research, the simulation of heat transfer in the nozzles and the softened polymer flow through the nozzle are presented in Sections 4.1 and 4.2. Next, the design and fabrication of the structured nozzle for a 3D printer is discussed in Section 4.3. Section 4.4 summarises the work of this chapter.

4.1 Heat transfer

To design the structured nozzle, heat transfer is the first parameter to be considered, as it provides the working conditions for the MPOF extrusion. In this work, the MPOF is fabricated by pressing the filament polymer through the heated nozzle wherein the high temperature softens the polymer to allow it to be forced through the structured nozzle and be moulded into a new geometry.

Polymers are made up of the long chains of smaller molecular units (monomers) linked together and can be amorphous or crystalline. A crystalline polymer is where the molecular chains are largely locked in place against one another while amorphous polymers are the opposite. Rather than being rigid, the random molecular chains are moveable across each other when the polymer is pushed or pulled. In reality, most polymers are a combination of crystalline and amorphous structures. The proportion of each is influenced by the polymer synthesis process, the composition, and temperature. Most crystalline structure polymers have a clear point at which the solid state can be changed suddenly to the liquid state: the so called "melting point", reached at a specific melting temperature (T_m). On the other hand, amorphous polymers have an unclear melting point because during heating they will be gradually changed from the solid state to a rubbery state. The glass transition temperature (T_g) of the polymer is the temperature at which the amorphous polymer consistency changes from a hard rigid material (glassy state) to a soft malleable material (rubbery state). When heat is applied to a polymer, the mobility of the chains is increased but remains relatively low for temperatures $T< T_g$. For $T>T_g$, the mobility of polymer chains increases significantly resulting in the macro-manifestation of polymer plastic behaviour. Polymer properties can be dramatically different below and above T_g. In fact, T_g is not a discrete thermodynamic transition, but rather a range of temperatures over which the mobility of the polymer chains increases significantly. The value of T_g depends on the mobility of the polymer chains, and for most synthetic polymers, T_g lies between 80 °C– 230 °C [151]. Therefore, to extrude the polymer through the structured nozzle, it needs to be heated up to $T>T_g$.

In the direct extrusion technique, which uses 3D printers to fabricate MPOFs, the standard 3D printer nozzle is replaced with the structured nozzle by connecting the structured nozzle to the heater head of the 3D printer. Heat from the heater head is transferred to the structured nozzle via the nozzle thread, and then to the polymer through the nozzle inner surfaces. The softened polymer is then forced through the structured nozzle to form the structured fibre. In the structured nozzle, the polymer should experience a temperature higher than its T_g. Thus, the heat transfer simulations for the nozzle

are used to verify that for given dimensions of the structured nozzle, the temperature at the nozzle interface with the polymer exceeds T_g when the heat is applied to the nozzle thread.

There are three general ways in which heat is transferred in the medium: convection, conduction, and radiation.

- Convection: Heat transfer in fluids generally takes place via "convection" in which the motion of the fluid itself carries heat from one place to another. Convection occurs when particles with higher energy in a gas or liquid move and take place of particles with lower energy. Convection currents are set up in the fluid because the hotter part of the fluid is generally less dense than the cooler part. This is due to the expansion of liquid or gas when heated as the particles are moving faster than they do when colder. So, there is an upward buoyant force on the hotter fluid, making it rise while the cooler fluid (denser) sinks. The heat transfer per unit surface through convection can be expressed by the "Newton's Law of cooling":

$$q = h_c A \Delta T \qquad 4\text{-}1$$

  where q is heat transferred per unit time [W], h_c is convective heat transfer coefficient of the process [W/(m^{2}K)], A is heat transfer surface area [m^2], and ΔT is the temperature difference between the surface and the bulk of the fluid [K].

- Conduction: Another way to transfer heat is by conduction, which is the transfer of energy within a medium, not a motion of a medium as in convection. When heat is transferred via conduction, the medium itself does not flow or move but the heat energy is transferred due to the vibration of atoms or molecules of the medium. The delocalized electrons within a piece of metal can move as free electrons. The parts of the metal atoms left behind are now positively charged metal ions. The ions are packed closely together and they vibrate continually. The hotter the metal, the more kinetic energy these vibrations have. This kinetic energy is transferred from hot parts of the metal to cooler parts by the free electrons. As metals have many free electrons and electrons can also carry heat, the metals are generally very good heat conductors. The heat conduction of a medium can be defined by eq.(4-2) where k is the thermal conductivity of the medium [W/(mK)], ΔT is the temperature difference between the two ends [K], Δt is the time interval [s] during which the amount of heat Q [J] flows through a cross section of the material, A is the area of cross-section [m^2], and L is the length or thickness of medium [m].

$$Q = \frac{kA\Delta T\Delta t}{L} \qquad 4\text{-}2$$

- Radiation: Unlike convection and conduction, which require particles or molecules to transfer heat, radiation involves electromagnetic waves. By radiation, heat energy is

transferred in the form of electromagnetic waves and can be transferred through the vacuum of space because there are no particles involved.

The Autodesk Fusion 360 computer aided design (CAD) software previously used to create 3D models of the structured nozzle was also used to simulate heat transfer, as it has a built-in heat transfer simulation package. The modelling geometry (Figure 4.1) was created by using the design interface in the software and was then transferred to the thermal simulation interface. Heat applied to the top part of the nozzle (thread) is transferred to the bottom part via heat conduction in the metal.

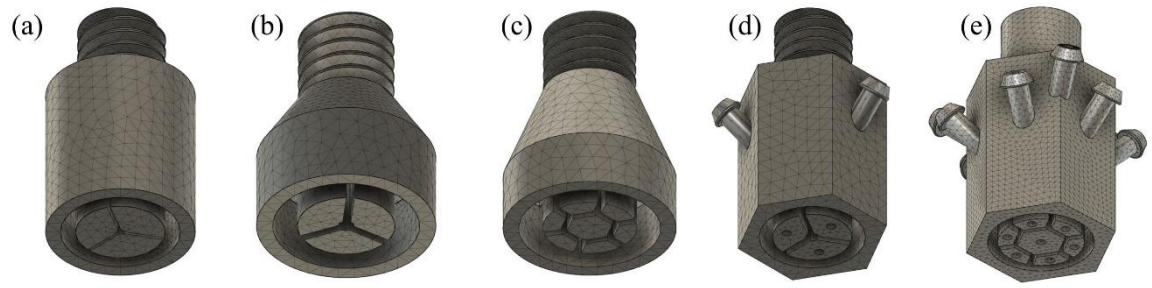

Figure 4.1 Modelling geometries of structured nozzles used for the heat transfer simulations (a) Structured nozzle for micromaching fabrication. (b-e) Structured nozzles for metal 3D printing fabrication.

In the simulations, the medium thermal conductivity is defined by the type of material used to fabricate the structured nozzle: Brass (~119 W/mK), Aluminium alloy (~121-180 W/mK), and Stainless steel (~20 W/mK)[152]. In the real fibre fabrication process, the nozzle is surrounded by air at room temperature (25 °C), thus the convective heat transfer coefficient of air at room temperature was used in the simulation. The convective heat transfer coefficient also depends on the air's velocity, which in the simulations is estimated to be ~ 0.1 m/s [153] leading to a convective heat transfer of ~12 W/m^2K [154]. The emissivity of the materials used in this experiment, Brass (~0.61), Aluminium alloy (~0.90), and Stainless steel (~0.44), was also included in the heat transfer simulations [155].

4.2 Material flow through the nozzle

Rheology can be defined as the science of flow and deformation of matter. Polymeric fluids show elastic properties, such as unequal normal stresses in shear and a prominent tensile viscosity in extension due to the complex shear viscosity. Thus, the rheology of polymeric fluids reveals a complex behaviour. All these rheological properties of polymeric fluids depend upon the rate of deformation, the polymer molecular weight and structure, the concentration of various additives and fillers, as well as the temperature.

The shear flow in the structured nozzle is similar to that of a rheometer [156]. The constitutive equation of shear flow can be expressed in eq.(4-3) where τ is the shear stress, η is the shear viscosity, and $\dot{\gamma}$ is the shear rate.

$$\tau = \eta \times \dot{\gamma} \quad 4\text{-}3$$

Polymer at temperatures above the glass transition temperature are generally non-Newtonian liquids and thus the viscosity itself depends on the shear rate [157]. Polymers exhibit shear thinning viscosity, a phenomenon characteristic of some non-Newtonian fluids in which the fluid viscosity decreases with increasing shear stress. This is generally considered to be the result of microscale structural rearrangements within the fluid, and the viscosity decrease with increasing shear rate is attributed to polymer chain disentanglement when heated. This flow behaviour is well described by the so-called power law:

$$\eta = m \times \dot{\gamma}^{n-1} \quad 4\text{-}4$$

where m is an empirical constant and the exponent n is a measure for the degree of shear thinning. The temperature dependence of the viscosity is included in m and is given by eq.(4-5). η_0 is a characteristic constant for the polymer, T is the absolute temperature, E is the activation energy for the flow process and R is the gas constant. By substituting eqs.(4-4) and (4-5) into eq.(4-3), the shear stress (τ) can be expressed by eq.(4-6).

$$\eta = \eta_0 \times \exp\left(\frac{E}{RT}\right) \quad 4\text{-}5$$

$$\tau = m \times \eta_0 \times \exp\left(\frac{E}{RT}\right) \times \dot{\gamma}^n = K \times \exp\left(\frac{E}{RT}\right) \times \dot{\gamma}^n \quad 4\text{-}6$$

where K is a new empirical constant which includes the constant η_0. For the polymer flow through the structured nozzle, shear flow through the nozzle (τ), shear stress, and apparent shear rate ($\dot{\gamma}$) are given by [158]:

$$\tau = \frac{\Delta p R_1}{2L_1} \quad 4\text{-}7$$

$$\dot{\gamma} = \frac{4Q}{\pi R_1^3} \quad 4\text{-}8$$

where Δp is the change of pressure over the nozzle, Q is the volume flow rate of the polymer, and R_1 and L_1 are the radius and length of the structured nozzle, respectively. Since the pressure at the nozzle end is atmospheric pressure, it can be neglected when compared with the pressure at the nozzle entrance. Thus, the change of pressure is given by the ratio of the force (F) applied on the polymeric filament to the cross section area (A_0). The volume flow rate is determined by the filament polymer cross section area and the filament feeding speed (s).

$$\Delta p = F/A_0 \quad (4\text{-}9)$$

$$Q = A_0/s \quad (4\text{-}10)$$

Combining eqs. (4-7) – (4-10) in eq. (4-6), the force applied to the feeding polymer can be obtained from eq. (4-11):

$$F = \frac{K2L_1A_0}{R_1}\left(\frac{4A_0}{\pi R_1^3}\right)^n \times \exp\left(\frac{E}{RT}\right) \times s^n \quad (4\text{-}11)$$

Grouping together all constants and parameters regarding the structured nozzle, the force required for extrusion (F) at a fixed feeding speed can be expressed as eq.(4-13).

$$K' = \frac{K2L_1A_0}{R_1}\left(\frac{4A_0}{\pi R_1^3}\right)^n \quad (4\text{-}12)$$

$$F = K' \times \exp\left(\frac{E}{RT}\right) \times s^n \quad (4\text{-}13)$$

The features inside the structured nozzle leading to different flow behaviours through the nozzle include flow velocity and flow direction. To optimise the design dimensions for the structured nozzle, the polymer flow inside the structured nozzle needs to be simulated. In this work, the commercial computational fluid dynamics simulation software (Autodesk CFD©) was used to estimate the flow of heated polymer through the designed structured nozzle. The 3D model of the nozzle was transferred directly from the CAD software (Autodesk Fusion 360) to the CFD software. The properties of the polymer used for the simulations are those of ABS, the polymer used to fabricate the optical fibres. The aim of this simulation is to roughly estimate the flow of polymer within the structured nozzle and ensure the temperature across the inner nozzle surfaces is suitable for drawing conditions. While the force required for extrusion decreases for increasing temperatures at fixed feeding speeds, the simulation was performed at the fixed temperature of 300 °C. At T=300 °C the viscosity, thermal conductivity, specific heat, bulk modulus, and emissivity of the ABS polymer are 2×10^{-8} poise, 0.25 W/mK, 1600 J/kgK, 2.9 GPa, and 0.917, respectively. Fluid velocity and pressure boundary conditions were applied to the nozzle entrance and exit. The velocity at the nozzle entrance was set to 250 mm/min, according to the manufacturer specifications in relation to the feeding speed applied to the filament polymer. Since the atmospheric pressure at the nozzle exit can be neglected compared to the pressure at the nozzle entrance, the pressure of the fluid at the nozzle exit was set to 0 Pa. These parameters for the fluid flow simulation were applied to all designs of the structured nozzles and the simulation results will be presented in the following section.

4.3 Structured nozzle design and fabrication

A 3D printer was used in this work to form a miniaturized version of a fibre drawing tower to directly draw the polymer fibre. The advantage of this particular approach is that fibres can be

manufactured on a tabletop without the need for expensive drawing towers or cleanrooms. Additionally, the fibre geometry can be easily changed by replacing the nozzle, which can be removed easily by unfastening the thread. To directly draw the fibre from a 3D printer, the structured nozzle cross section needs to be complementary to that of the final fibre.

Two nozzle geometries were considered: a solid-core and hollow-core MPOF. A suspended-core fibre structure was chosen for the solid-core MPOF because of its relatively simple geometry, which allows to fabricate index guiding fibres using a single material. The suspended-core microstructured polymer optical fibre (SC-MPOF) cannot be easily made by the conventional drilling technique due to its non-circular air holes. The final fibre is mechanically suspended from the outer solid by three fine struts. This fibre profile has been previously manufactured by extruding a fibre preform from a variety of soft glasses and polymers [47, 94, 148, 149] and then drawing the preform into a fibre on a conventional fibre drawing tower. A hexagonal structure was chosen for the hollow-core microstructured polymer optical fibre (HC-MPOF) owing to its relatively simple geometry, which uses an antiresonant effect for guiding light. The hollow-core hexagonal fibre consists of a hexagonal-air core surround by a thin layer which is connected to the cladding by 8 thin struts. Due to non-circular air holes inside the structure, this fibre structure is hard to fabricate using the conventional drilling or stacking techniques. Therefore, the direct extrusion technique seems an appropriate choice.

The structured nozzle can be manufactured using two different approaches: machining and metal 3D printing.

4.3.1 Micromachining

Mechanical machining is a traditional technique used to fabricate the dies used for extruding fibre preforms and is particularly suitable to deal with relatively large (few cm) sizes. The first structured nozzle design manufactured by micromachining was the nozzle for SC-MPOF. This structure is simpler than the HC-MPOF, which is not suitable for mechanical machining. Micromachining does not allow nozzles to be fabricated in a single piece due to the intrinsic access limitations of conventional machining tools. Therefore, the design of structured nozzles is separated into two pieces including: (a) the nozzle body and (b) the nozzle cover. The standard size of the filament polymer for the 3D printer used in this experiment is 2.85 mm in diameter, thus the nozzle body has a 3.0 mm aperture diameter at the input, where the polymer is fed into the nozzle. Figure 4.2(a) and (b) shows various views of the designed structured nozzles. The structured body of the nozzle shapes the extruded fibre, resulting in a solid suspended core connected by three struts to the outer cladding. The cover is a hollow cylinder with an inner diameter of 8.0 mm and outer diameter of 10.0 mm. The radial gap distance between the cover and the structured body determines the outer cladding thickness (2 mm) in the extruded SC-MPOF, as shown in Figure 4.2(c).

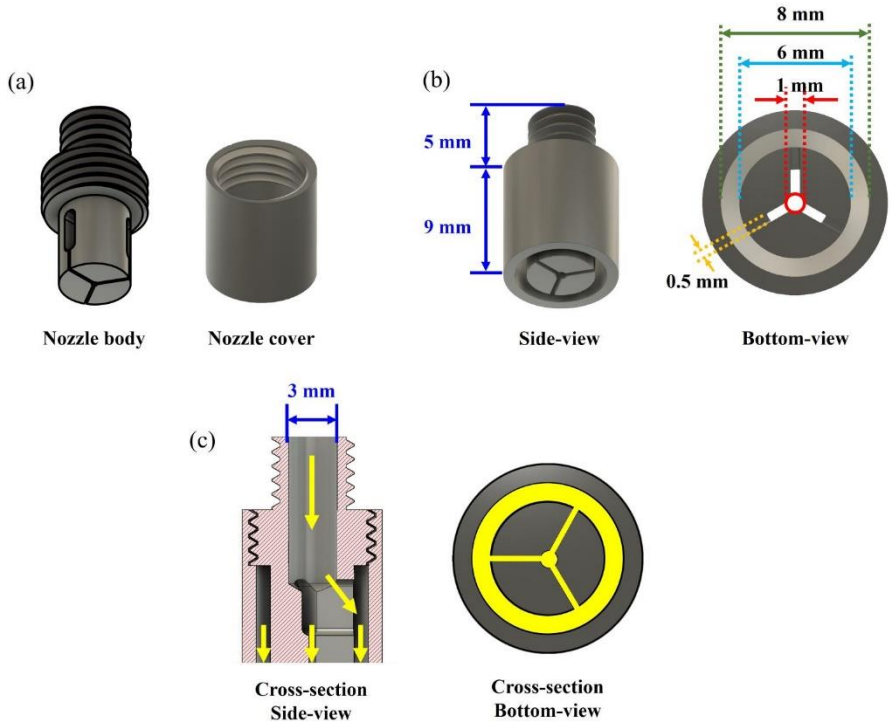

Figure 4.2 3D model design of a structured nozzle fabricated by micromaching. (a) Nozzle body and corresponding cover. (b) Side- and bottom-view of the assembled structured nozzle. (c) Side- and bottom-view cross-sections of the structured nozzle design.

The materials available for fabricating the structured nozzle by micromachining were aluminium and brass. Aluminium has a thermal conductivity in the range 121-180 W/mK which is higher than that of brass 119 W/mK. However, aluminium is not suitable for working at T> 300 °C and due to its low melting temperature of ~300 - 480 °C (depending on the composition) while brass can work with temperatures higher than 300 °C because it has a melting temperature of T_m ~ 900 - 940 °C [159]. Therefore, brass was the chosen material to fabricate the first structured nozzle, shown in Figure 4.3. In Figure 4.3(d) it is possible to notice the polymer left in the apertures at the end of the fibre drawing.

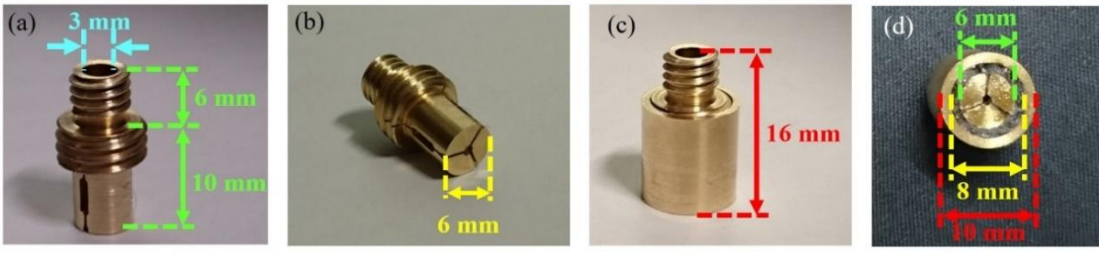

Figure 4.3 Brass structured nozzle fabricated by micromachining. (a-b) nozzle body, (c) body with cover, (d) after drawing suspended-core MPOF.

To test the machined structured nozzle, the direct extrusion and drawing of MPOF was first performed by using a commercial desktop 3D printer (Ultimaker 2 extended). The machined structured nozzle was mounted on the printing head to replace the standard nozzle (Figure 4.4) . Heat

from the heating element at the printing head was applied to the nozzle through the thread with an applied temperature of 250 °C. A commercially available 3D printer filament (ABS) was fed through the heated nozzle by using the built-in filament feeding system of the 3D printer. The extrusion quality was tested by extruding the fibre cane without any additional drawing. Different extrusion parameters (feeding speed (*s*) and nozzle temperature (T_n)) were tested to explore their impact on the quality of the extruded cane and achieve the optimal effective temperature experienced by the polymer during drawing. Diameter reduction (fibre drawing) took place by connecting the extruded polymer fibre to a constantly rotating spool. A stepper motor was used to rotate the spool and the pulling speed of fibre drawing was controlled by changing the rotation speed (Ω) of the stepper motor. More details about the fibre drawing process and its parameter optimisation will be explained in chapter 5.

Figure 4.4 Micromachined structured nozzle connected with the heating area of the 3D printer.

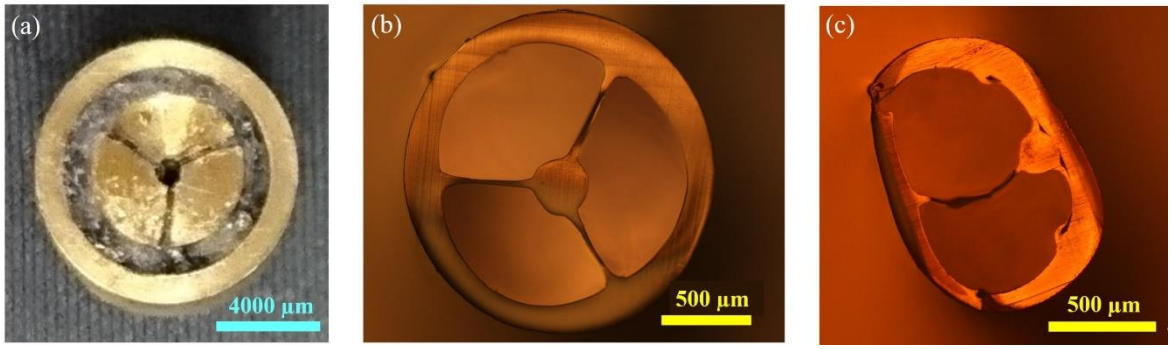

Figure 4.5 (a) Bottom-view of the machined structured nozzle used to fabricate the SC-MPOF. (b) Cross-section of the first drawn SC-MPOF with outer diameter d~1800 µm. (c) Deformation in the fibre structure after drawing lengths over 1 metre.

The first extruded and drawn SC-MPOF is shown in Figure 4.5. To observe the cross-section, the SC-MPOF was cleaved using a razor blade. Figure 4.5 (a) and (b) show the bottom-view of the structured nozzle used to fabricate the SC-MPOF and the cross-section of the drawn SC-MPOF, respectively. By comparing the microscope images, it is possible to see that the microstructure inside the fibre was maintained after drawing. The core is optically isolated from the outer cladding region by three fine supporting struts. This preliminary experiment successfully demonstrated MPOF fabrication from the brass structured 3D printer nozzle.

Although maintaining the SC-MPOF structure was achieved, issues occurred when longer lengths of the fibre were drawn: the fibre structure collapsed after 1 metre (Figure 4.5(c)).

4.3.2 Metal 3D printing

Current dies for extruding complex structures of MPOF canes exhibit mostly circular feed holes and blockages, which can be easily machined using traditional micromachining techniques, while other shapes are rarely made by machining because they are time-consuming or excessively costly. 3D printing allows almost any arbitrary shapes in three dimensions with high precision to be fabricated, including shapes that cannot be made using conventional subtractive machining techniques such as cooling channels.

Metal additive manufacturing, or metal 3D printing, is a new, versatile technique that has been used to fabricate complex three dimensional metal structures, including extrusion dies [160]. 3D printing has been developed for a range of metals, which opens up the possibility of producing 3D printed nozzle dies that withstand extrusion forces and elevated temperatures. The geometrical freedom offered by 3D printing has been exploited for the fabrication of an aluminium extrusion die including cooling channels which still preserve the initial structure strength [161]. Due to the high precision of metal 3D printing, fine resolution and complex structures can be achieved.

In section 4.3.1, the nozzle was separated into two parts due to the limitation in the fabrication using the micromachining technique. The inner part, which includes the central hole and notches, had to be created first, before being connected to the cover. Compared with micromachined nozzles, metal 3D printed structured nozzles can be made as a single piece. Due to the flexibility in the structure design, several iterations were made to design and develop suitable 3D printed metal dies.

4.3.2.1 First generation

The first metal 3D printed nozzle was designed in two sizes, which had a smaller volume in comparison with the one made by micromachining to keep the size of the structured nozzle similar to the size of conventional nozzles used for FDM 3D printers. This choice was made to ensure extrusion conditions similar to those used in conventional nozzles (Figure 4.6(a)). The total length of the nozzle, including the thread for connection with the 3D printer head, was 12 mm. The bottom-view of the nozzle is presented in Figure 4.6(b), showing that the nozzle diameter at the output is the same size as at the input, 3.5 mm, while the diameter of the hole at the centre (which will become the core of the extruded fibre) is 1 mm. The gap between the outer cover and the structured body, which determines the outer cladding thickness of the extruded SC-MPOF, is 0.7 mm for this design. The direction of material extrusion using this nozzle design is presented (red arrows) in the side-view cross-section of the fibre in Figure 4.6(b).

The small structure and the available manufacturing resolution limits the outer diameter of the final fibre, as fibre dimensions are related to the die sizes by eq.4-14. For this reason, a magnified version of the nozzle was designed to get larger diameters in the final fibre (Figure 4.6(c-d)). By assuming that the extruded cane maintains the same geometric proportions as the die and the final drawn fibre, the final size of the fibre drawn from the 3D printer can be estimated by:

$$\frac{D_{cladding}}{D_{core}} = \frac{d_{cladding}}{d_{core}} \qquad 4\text{-}14$$

when $D_{cladding}$ and D_{core} are the dimensions of the cladding and core apertures through which the fibre cane is extruded from the structured nozzle and $d_{cladding}$ and d_{core} are the cladding and core diameters of the optical fibre.

This enlarged nozzle has a total length of 14 mm, 2 mm longer than the smaller version as shown in Figure 4.6(c). The bottom-view shows that the nozzle inner diameter at the output is 9 mm, while the diameter of the structured body is 6 mm (inner region of nozzle). The gap between the outer cover and the structured body determines the outer cladding thickness in the extruded SC-MPOF from this nozzle, which will be 3 mm. For this design, the central hole diameter and width of the gaps which connect the centre hole with the outer cladding were 1 mm and 0.5 mm, respectively. The direction of material extrusion in this design nozzle is shown by green arrows in the side-view cross-section of the fibre (Figure 4.6(d)).

To fabricate the 3D model using a metal 3D printer, the starting process is the same as for any type of 3D printer. A CAD program (Autodesk Fusion 360) was used to create a detailed 3D structure and the design file then was converted into an .STL (Stereolithography) format to enable the metal 3D printer to interpret the construction. The term 3D printing covers a variety of additive processes in which material is joined or solidified under computer control to create a three-dimensional structure, with material such as liquid molecules or powder grains being sintered together layer by layer.

The metal 3D printing process is a multi-layered additive approach like other forms of 3D printing, which requires the 3D model design to be sliced very finely on the horizontal plane before the prototype can be built. In this work, a printing technique called “Direct metal laser sintering” (DMLS) was used to build the 3D structure. Within this technique, a laser is used to heat up the metal powder and then fuse the grains together. At the beginning of the printing process, the metal 3D printer receives the 3D model construction from the slicing software which instructs the laser the trajectory to trace out across the metal powder. Then, the laser will heat up the metal powder which subsequently creates a solid form of the object. Once this initial base has been laid out, more metal powder will be poured on the top of the first layer, then the laser will start fusing the metal powder by following the pattern of a second layer which will then be repeated to create the next layers. The

thickness of each metal 3D printed layer is typically no thicker than 0.1 mm. This very gradual additive process is how the metal 3D printer creates the final product, with heat from the laser to form a solid 3D volume.

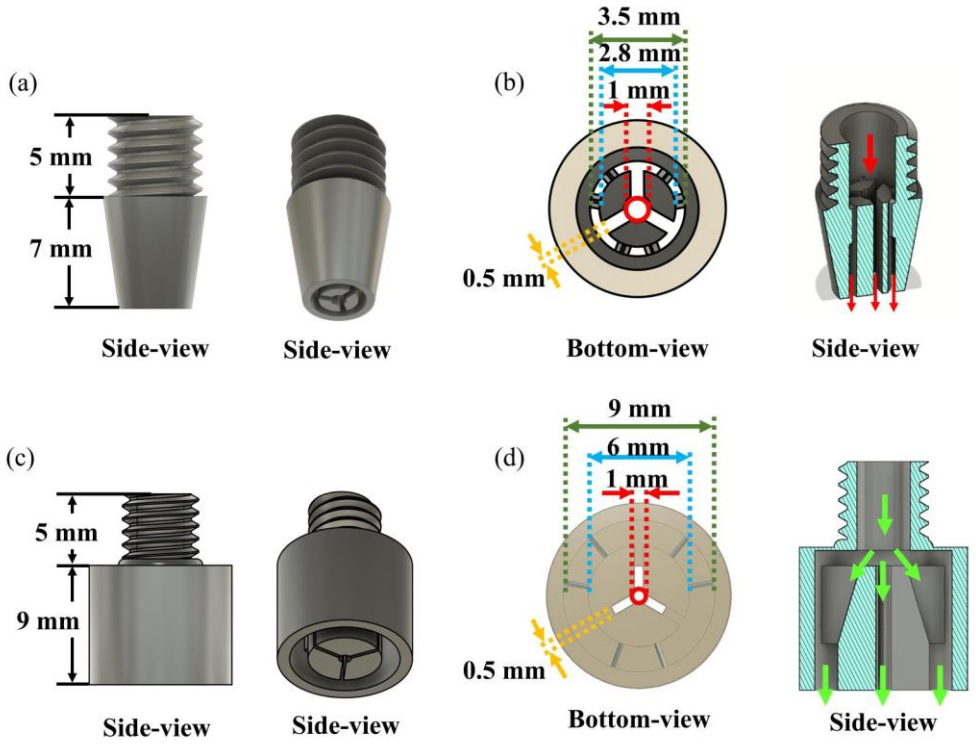

Figure 4.6 Examples of 3D model designs of structured nozzles. (a) Side-view and (b) bottom-view of the small structured nozzle. (c) Side-view and (d) bottom-view of large structured nozzle.

In this method, each layer of the structure has to be supported by the layer beneath. Therefore, if the model has an overhang layer which is not supported, it will collapse, resulting in poor fidelity to the CAD model (Figure 4.7(b)). Support structures are thus necessary for models with overhangs or bridges. However, post-processing work is needed to trim out the supports, which can damage the model surface. However, not all overhangs require the support structure. DMLS requires a fairly limited number of supports to overhangs when compared to other 3D printing technologies. Any design with an overhang greater than 0.5 mm in length usually requires additional support to prevent lack of fidelity from the CAD model, as shown in Figure 4.7(a). Another important parameter to be considered for the designed model for metal 3D printing is the angle tilt of any surface in the model. The general rule for all types of 3D printers is that if the tilted angle in the model is less than 45 degrees from the vertical plane, that part will be able to print without the support structures. This angle is called a self-supporting angle. The lower the angle, the more likely it is to support itself Figure 4.7(b).

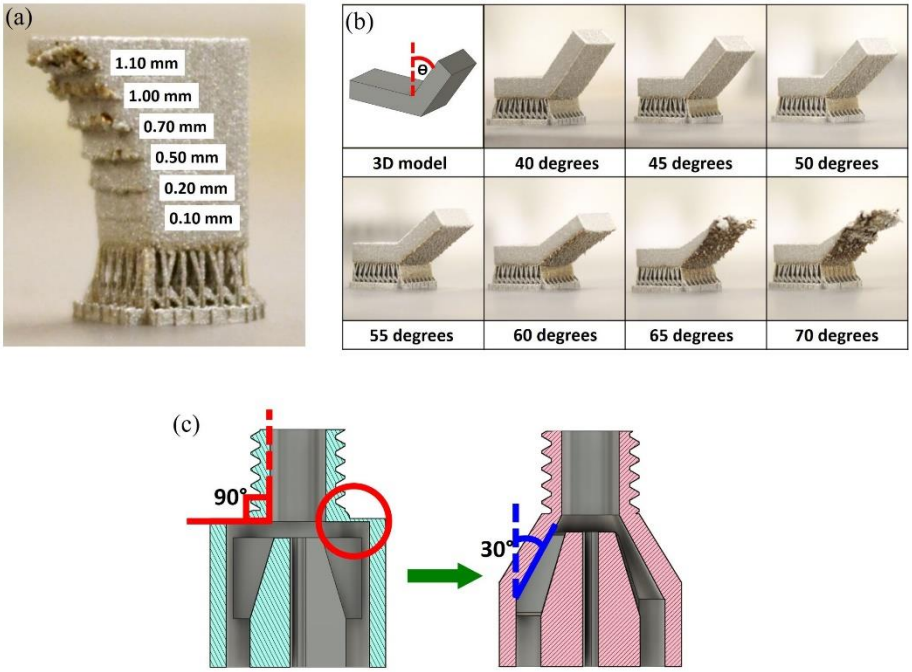

Figure 4.7 Printing quality comparison of metal 3D printed model with (a) different lengths of overhang layer and (b) different self-supporting angles [162]. (c) Cross-section of first design and improved design with tapered 30° slope-structure.

Due to these limitations in additive manufacturing, a detail (red circle in Figure 4.7(c)) of the first fabricated structured nozzle of the SC-MPOF cannot be reproduced, because the internal region near the thread is perpendicular to the vertical plane of the nozzle. Although a support can be added for printing hanging structures, it is not suitable for this detail because of its small dimension, meaning that the support cannot be easily removed at the end of the process as it is located inside the structure. To solve this problem, a new nozzle design with a funnel top was created as shown in Figure 4.7(c). The slope angle is set to be 30° from the vertical to ensure high fidelity in printing. The improved design of the structured nozzle for fabricating the SC-MPOF is shown in Figure 4.8(a-b).

The first design of the structured nozzle for fabricating the HC-MPOF is presented in Figure 4.8(c), and consists of a hexagonal air-core with the diameter of 2.6 mm surrounded by thin layers of 0.43mm thickness , resulting in an extruded fibre with a 9mm outer diameter (Figure 4.8 (d)). The diameter of the structured body is 6 mm while the inner diameter of the outer cover is 9 mm, leading to a 3mm gap between these two circles: this will become the thickness of the outer cladding in the extruded fibre.

Waves propagating in the designed fibre are confined by the antiresonant effect within the air core. Light in the HC-MPOF can be confined to the central air-core owing to the resonant reflection of the guided wave in the air-core, with the membrane surrounding the core behaving effectively as a Fabry-Perot cavity: for this particular design, the struts providing resonant reflections have a

thickness of 0.43 mm. Direction of material flow in this designed HC-MPOF nozzle is presented with red arrows in Figure 4.8(d).

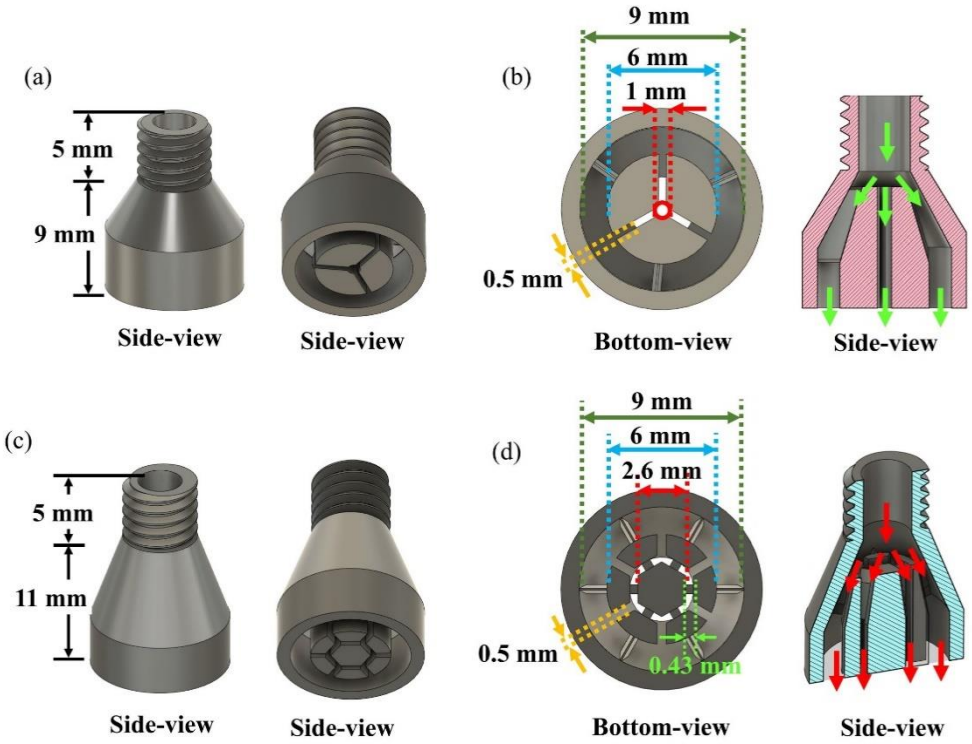

Figure 4.8 Improved design of the enlarged structured nozzle for fabricating SC-MPOF: (a) side-view and (b) bottom-view and cross-section. 3D model design of structured nozzle for creating the HC-MPOF: (c) side-view of the nozzle. (d) Dimension of the structure inside the nozzle and cross-section of nozzle. Green and red arrows represent polymer flow direction within the nozzle cavities.

Metal 3D printed nozzles in this work were first manufactured at the University of Nottingham (Centre for Additive Manufacturing). The best performance material (for thermal applications) available in metal 3D printing is an aluminium alloy (AlSi10Mg). This material has a thermal conductivity of 130 – 190W/mK and a melting temperature in the range of 570 – 590 °C, and thus seems suitable for extruding polymers as the nozzle needs to heat up to 300 °C. The first generation of metal 3D printed structured nozzles for fabricating MPOF is presented in Figure 4.9(a-c). A size comparison between the conventional nozzle for the polymer 3D printer and the metal 3D printed nozzles with different structures is shown in Figure 4.9(c). The smallest 3D printed nozzle for the SC-MPOF has the same length as conventional nozzle (12 mm) while the enlarged nozzle with the same structure is 14 mm long. The nozzle for HC-MPOF is the biggest of all because of its complex transverse structure and has a total length of 16 mm.

The first set of nozzles were used to fabricate MPOFs by connecting the nozzle onto the printing head, to replace the standard nozzle. ABS polymer was used to fabricate both the SC-MPOF and the HC-MPOF. The heating element temperature was set to 230 °C and heat was transferred to the nozzle through the thread. The temperature applied to the printing head was 20 °C lower than

that applied when using machined nozzles to achieve similar surface quality, due to the smaller size of the 3D printed nozzle and higher thermal conductivity of aluminium compared with brass. ABS polymer was fed through the heated nozzle by using the built-in filament feeding motor of the 3D printer. The drawing process took place with the same procedure as the machined nozzle by connecting the extruded polymer to the pulling system.

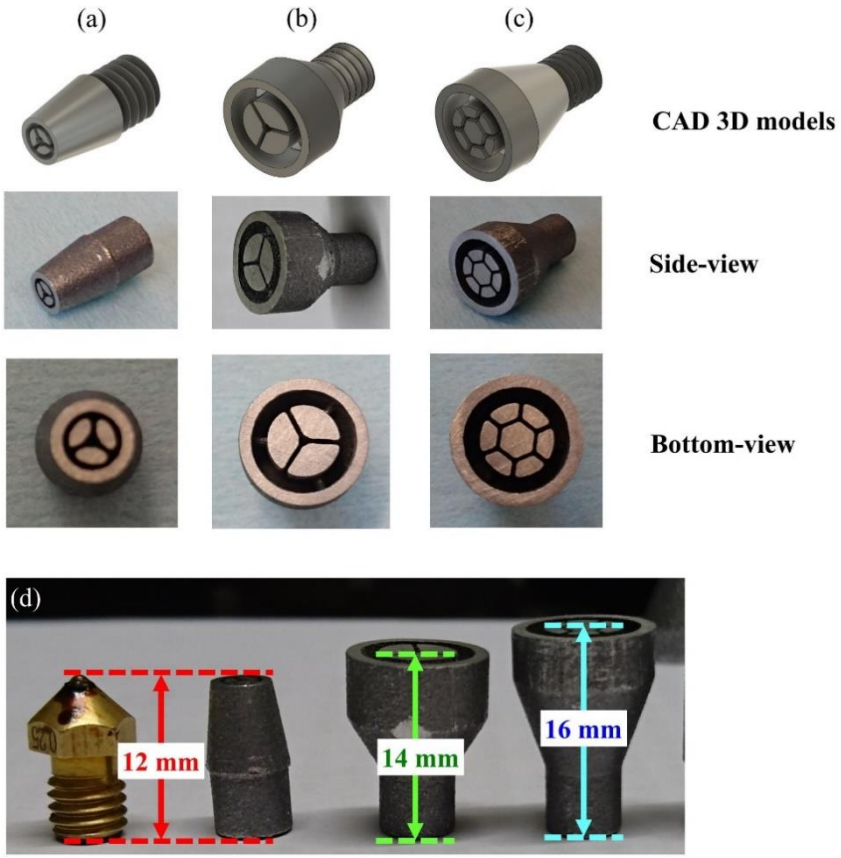

Figure 4.9 3D printed (a) small size and (b) enlarged size structured nozzle for SC-MPOF; (c) structured nozzle for HC-MPOF. (d) Size comparison between (from left to right) conventional 3D printer nozzle, small structured nozzle and enlarged structured nozzle for SC-MPOF, and structured nozzle for HC-MPOF.

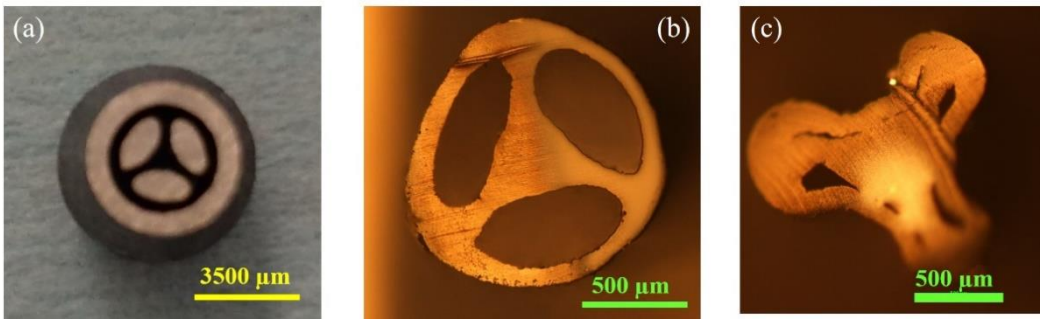

Figure 4.10 (a) Bottom-view of the metal 3D printed small structured nozzle used to fabricate the SC-MPOF. (b) Cross-section of the first drawn SC-MPOF from small metal 3D printed nozzle with outer diameter d~1000 µm. (c) The deformation in the fibre structure after drawing for lengths over 50 cm.

ABS polymer was extruded from all nozzles but only the structure inside the fibres extruded from the nozzle in Figure 4.9(a) could be observed. The fibre from the enlarged nozzle in Figure 4.9(b) was extruded from the nozzle with some degree of structure preservation, but this vanished when pulling was applied. The polymer extruded from the nozzle in Figure 4.9(c) came out as a tube because no material came out from the central part of the nozzle. Cross-sections of the SC-MPOF extruded and drawn from the small structure nozzle are presented in Figure 4.10(b). The deformation in the fibre structure after drawing for ~50 cm can be observed in Figure 4.10(c). The deformation in the fibre drawn from the small metal 3D printed nozzle is attributed to collapse of the cladding, similar to the fibre drawn from machined nozzles.

4.3.2.2 First generation: issues

The first generation of structured nozzles exhibited a major issue found when extruding and drawing the SC-MPOF and HC-MPOF using the machined and metal 3D printed nozzles: the loss of structure inside the extruded and drawn fibre.

Heat transfer simulations of the structured nozzle were performed to observe the gradient of temperature from the nozzle thread to the bottom and showed that the temperature at the nozzle bottom is reduced from the applied temperature of 250.0 °C to 233.2 °C in the machined structured nozzle, and 244.2 °C in the metal 3D printed nozzle This is attributed to the material used to fabricate the metal 3D printed nozzle (Aluminium alloy), which has higher thermal conductivity than the machined nozzle (Brass), and to the 2 mm difference in length of the metal 3D printed nozzle. Although the machined nozzle displayed a lower temperature than the metal 3D printed nozzle, the low temperature region is at the cover, as shown in Figure 4.11(a). For this design, the main nozzle structure is at the centre, with a similar diameter at the thread. Heat from the heater head is applied to the thread and then transferred to the body of the nozzle through heat conduction. For the nozzle cover, heat is transmitted to the nozzle cover through the large thread (green circle in Figure 4.11(a)) when it is connected to the nozzle body. Although the cover is in contact with the nozzle body via the thread, the small air gap in between causes poor heat transfer from the nozzle body to the cover. Owing to the poor heat transfer, the nozzle cover experiences a lower temperature at the bottom than the nozzle body. On the contrary, the 3D printed nozzle cover is one single piece with the nozzle thread, as shown in Figure 4.11(b), thus the applied heat at the thread will transfer directly to the nozzle cover through heat conduction. For this design, the structured body of the metal 3D printed nozzle is connected with the cover nozzle via thin struts (red circle in Figure 4.11(b)). Even though the metal 3D printed nozzles were printed as a single piece using the same material for the whole nozzle, the heat transfer from the nozzle cover to the nozzle body is quite poor due to the small size of the connecting struts. Thus, the temperature at the bottom of the nozzle body is lower than the cover for the metal 3D printed nozzle.

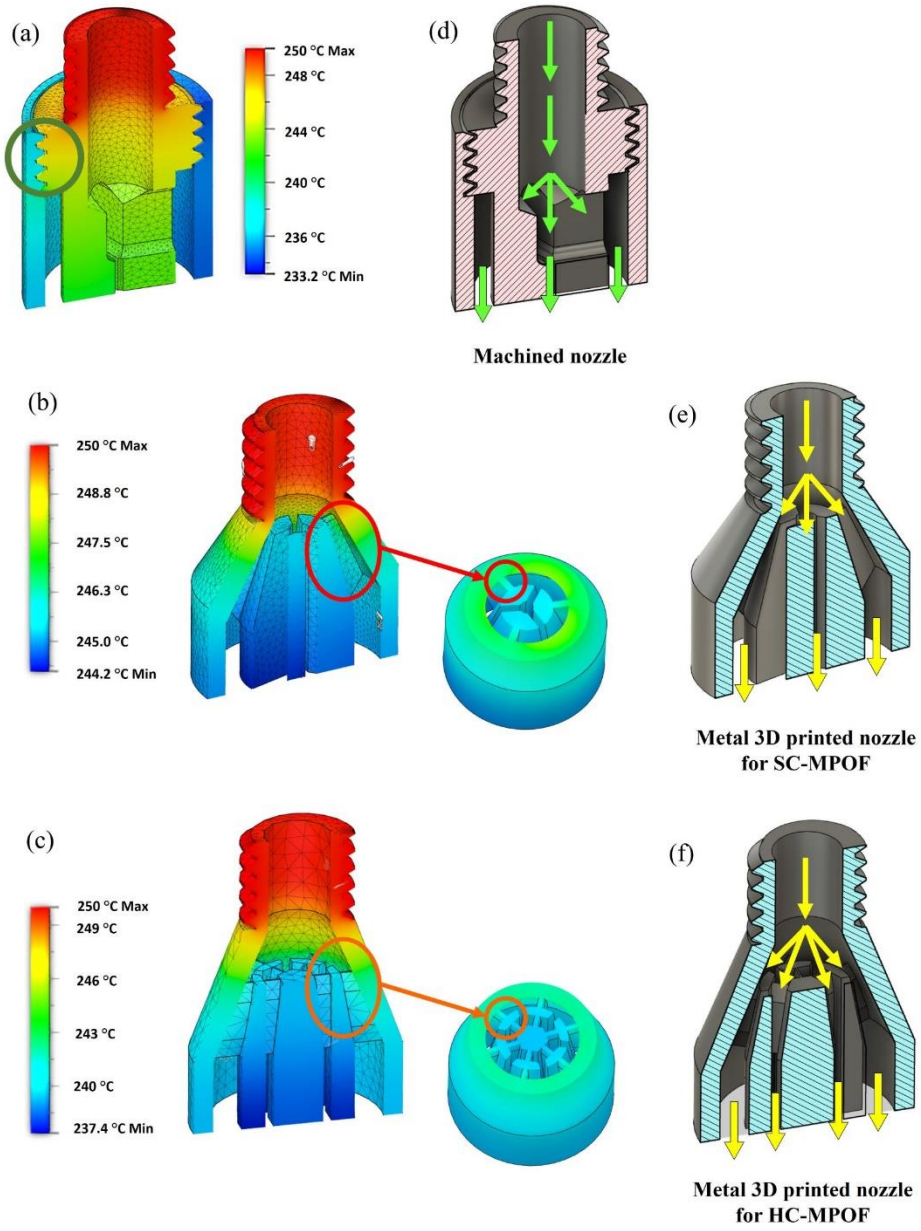

Figure 4.11 (Left) Heat transfer simulation of (a) the machined structured nozzle; (b) the metal 3D printed nozzle for SC-MPOF (c) and the metal 3D printed nozzle for HC-MPOF when a temperature of 250 °C is applied to the nozzle thread. (Right) Side-view cross-section with the direction of material flow in (d) the machined structured nozzle; (e) the metal 3D printed nozzle for SC-MPOF; and (f) the metal 3D printed nozzle for HC-MPOF.

The direction of polymer flow in the nozzle was also considered to improve the nozzle design. The polymer is fed through the top part of the nozzle, where heat is applied, and heats up moving towards the lower part of the nozzle. For the machined nozzle, the heated polymer will move directly through the nozzle body. Some of the heated polymer will flow to the outer region forming the fibre cladding (Figure 4.11(d)). When the heated polymer is fed through the small gap and hole in the nozzle body, the velocity of the polymer in this region is increased, resulting in a lower fictive temperature and related increase in the polymer viscosity at the bottom of the nozzle body. The fictive temperature of the polymer that flows out of the nozzle body is also reduced due to the lower

temperature of the nozzle cover, resulting in an even larger increase of the polymer viscosity outside the nozzle body. Although the temperature of the nozzle body is higher than that of the cover, the fictive temperature of polymer flowing through the nozzle body is closely approximated by the polymer flow outside the nozzle body due to the faster velocity of the polymer flowing through the nozzle body. Because of this, polymer inside the nozzle body and outside the nozzle body will have similar viscosity at the bottom of the nozzle leading to the same extrusion speed for all parts of the extruded polymer. Simulation of heated polymer flow in the machined nozzle (Figure 4.12(a)) shows that the extrusion speed for all parts of the polymer is ~3 mm/s.

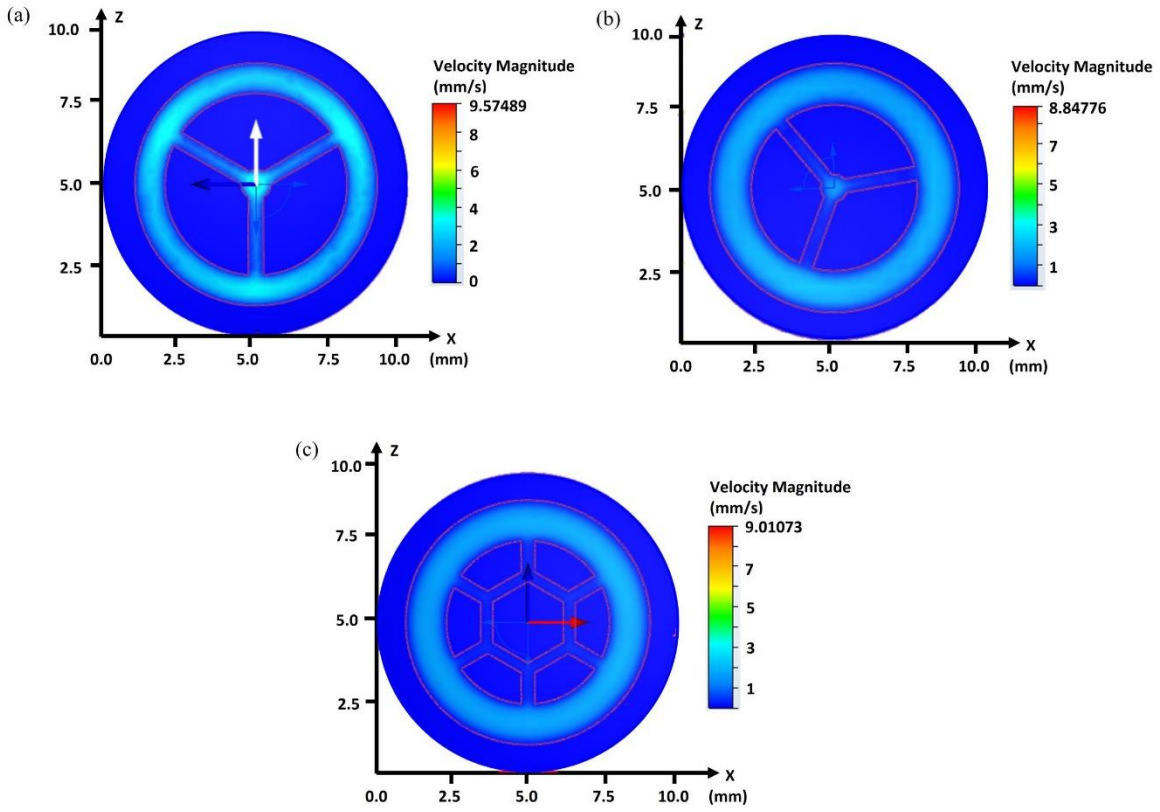

Figure 4.12 Simulation of polymer flow inside the structured nozzle. Velocity magnitude of polymer flow at the bottom of (a) the machined structured nozzle; (b) the metal 3D printed nozzle for SC-MPOF; and (c) the metal 3D printed nozzle for HC-MPOF.

When considering the direction of material flow in the metal 3D printed nozzle, note the heated polymer separates when passing through the nozzle thread region, as shown in Figure 4.11(e). A fraction flows through the structured nozzle body while a fraction flows out through the body/cover interface to form the fibre cladding. Similar to the machined nozzle, when the heated polymer is fed through the small apertures in the nozzle body, the velocity of the polymer in this region is increased leading to a decrease in its fictive temperature and an increase in viscosity. The fictive temperature of the polymer that flows around the nozzle body also decreases due to the gradient of temperature of the nozzle cover resulting in increased polymer viscosity outside the nozzle body. Because of the higher velocity of the material flowing in the nozzle body and the lower temperature of the nozzle

body, the fictive temperature of the polymer at the end of the nozzle body is considerably lower than that of the polymer outside the nozzle body. Since the associated viscosity of the polymer flowing inside the nozzle body is higher than that flowing outside, it results in different extruded velocities of the polymer from inside and outside the nozzle body and a lack of structure inside the fibre. Figure 4.12(b) shows that the velocity of the polymer outside the nozzle body is ~3 mm/s while the velocity of the polymer inside the nozzle body is less than 1 mm/s.

The same issue also occurred when the HC-MPOF was drawn from the metal 3D printed nozzle. In the HC-MPOF nozzle, the structured nozzle body hung from the nozzle cover by thin struts while the nozzle cover is connected with the nozzle thread as presented in Figure 4.11(c). Because of this design, the heat transfer simulation in Figure 4.11(c) shows that the temperature at the bottom of the nozzle body is lower than that of the nozzle cover when heat is applied to the thread. The direction of polymer flow inside the nozzle is shown in Figure 4.11(f). This is similar to the metal 3D printed nozzle for SC-MPOF. Heated polymer will be partitioned when passing through the nozzle thread region. A fraction flows inside the nozzle body while a fraction flows out into the gap between the body and cover. The velocity of the polymer flowing through small gaps inside the nozzle body increases resulting in a decrease of its fictive temperature and because of the relatively low temperature of the nozzle body, the velocities of the extruded polymer from inside and outside the nozzle body are different, resulting in the loss of structure inside the extruded HC-MPOF. Figure 4.12(c) shows that there is no extruded polymer from inside the nozzle body. The polymer velocity inside the nozzle body is close to 0.1 mm/s, while outside the nozzle body it is ~3 mm/s, resulting in an extruded polymer cylindrical tube instead of the HC-MPOF structure.

A second, related issue of the first generation nozzles is the collapse of fibre structure when the fibre is drawn for lengths over 50 cm. This collapse depends on the drawing parameters, including drawing speed, temperature, and air pressure inside the fibre cavities. Different from the traditional drawing process of microstructured optical fibres, the MPOF fabricated by direct extrusion is extruded and drawn directly from the structured nozzle of the 3D printer. In other words, preform fabrication is not needed. By drawing the MPOF from the fibre preform, the air-gap and air-holes inside the fibre preform are filled with atmospheric air before drawing to the fibre size. Therefore, there is air inside the holes along the length of the drawn MPOF. However, when the MPOF is fabricated from direct extrusion, the air-holes inside the MPOF experience a decreasing pressure because there is no inlet to allow air flow into the hole regions. Although air can get into the hole inside the fibre from the fibre end, this is severely limited by the small hole size when the fibre is drawn.

4.3.2.3 Second generation

To solve the issues mentioned in 4.3.2.2, a second generation of nozzles for the SC-MPOF and HC-MPOF was developed by connecting the nozzle body to the thread for providing better heat transfer. This improvement is to adjust the velocity of the extruded polymer, so that all the fractions coming out from different apertures at the bottom of the nozzle have the same velocity. This improvement aims to retain the structure inside the SC-MPOF and HC-MPOF after extrusion and drawing from the nozzle. To address the deformation of the MPOF structure due to the reduced air pressure inside the fibre structure, small tubes were added into the second generation of nozzles. These tubes were placed in the centre of the inverse structure of the air-holes inside the extruded fibre, and were meant to equalise the pressure in the air holes with external pressure.

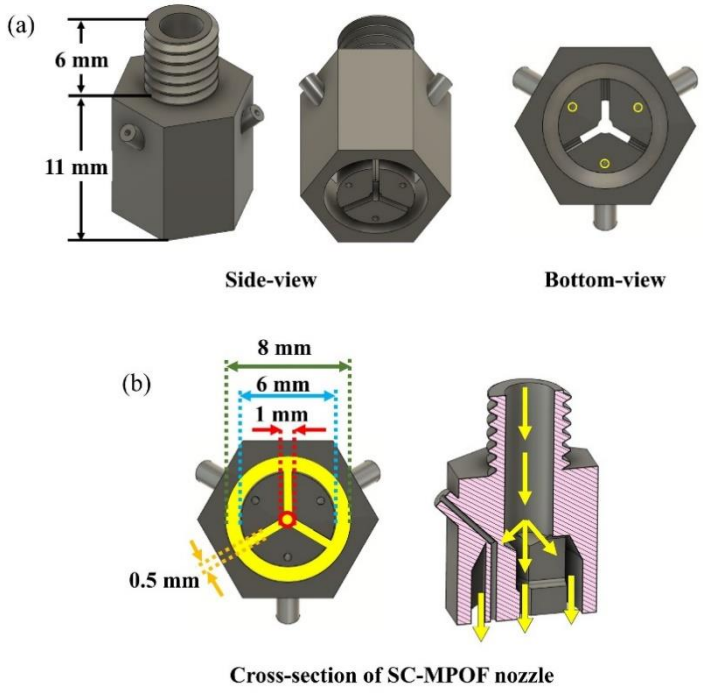

Figure 4.13 Second generation nozzle for SC-MPOF (a) side-view and bottom-view of the nozzle. Yellow circles in the bottom-view of the nozzle indicate the new feature of the nozzle. (b) Dimensions of the structure inside the nozzle and cross-section of the structured nozzle.

The second generation of the structured nozzle for fabricating SC-MPOF had a total length of 17 mm. The positions of the added pressurization tubes can be observed in the bottom-view of the structured nozzle as presented in Figure 4.13(a) (yellow circles). The bottom-view shows the inner diameter of the nozzle output is 8.0 mm, while the diameter of the structured body is 6 mm, providing an outer cladding thickness in the extruded SC-MPOF of 2 mm. For this design, the hole at the centre and the width of the gaps connecting the centre hole to the outer cladding are 1 mm and 0.5 mm, respectively. The direction of material extrusion is presented by yellow arrows in the side-view nozzle cross-section in Figure 4.13(b).

The second generation of the structured nozzle for HC-MPOF is presented in Figure 4.14(a), and has a total length of 18 mm. Pressure equalization tubes were added to this design, and can be observed in the bottom-view in Figure 4.14(a) (green circles). In this design, the hexagonal air-core has a diameter of 2.16 mm, the thin layer surrounding the fibre core has a thickness of 0.65 mm, and the outer diameter of the extruded fibre is 8 mm (Figure 4.14(b)). The diameter of the structured body is 6 mm leading to a gap between the structured body and the outer diameter of the extruded fibre of 2 mm. The direction of material flow in this nozzle is presented by green arrows within the side-view cross-section of the fibre in Figure 4.14(b).

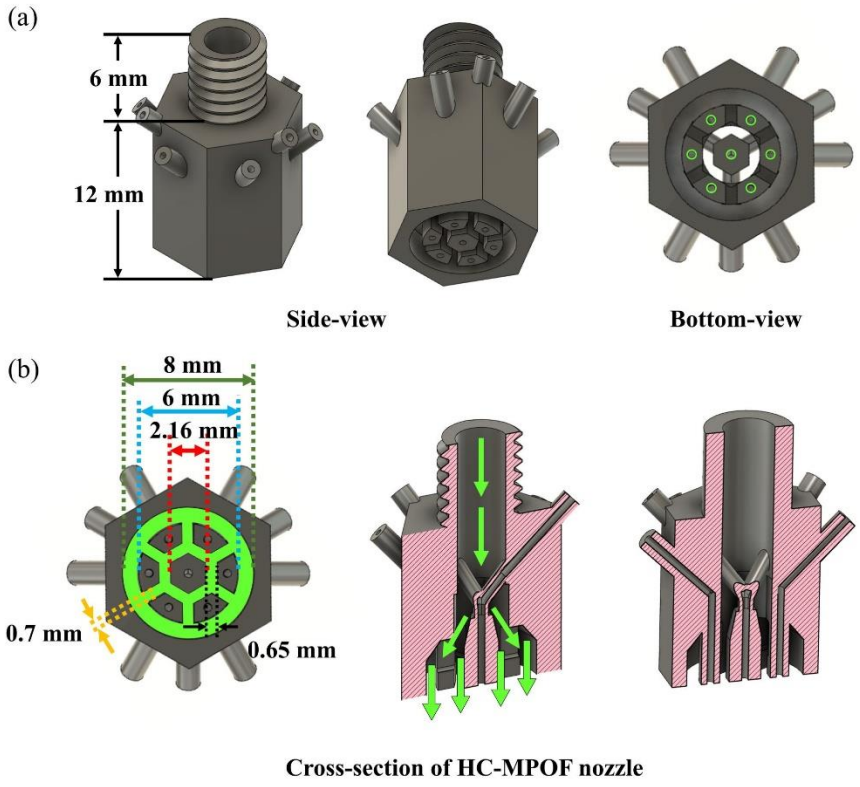

Figure 4.14 Second generation structured nozzle for HC-MPOF: (a) side-view and bottom-view of the nozzle. Green circles in the bottom-view indicate the newly added pressurization tubes. (b) Dimensions of the structure inside the nozzle and its cross-sections.

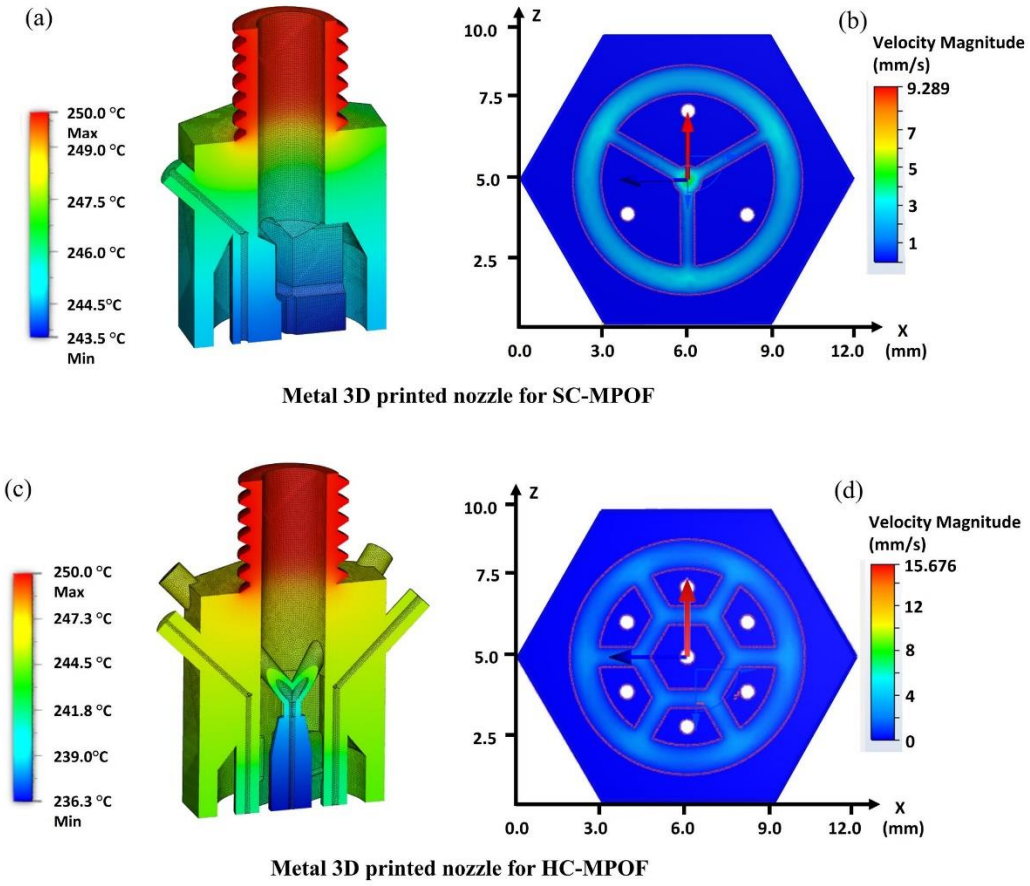

Figure 4.15 (left) Heat transfer simulation and (right) velocity of polymer flow at the bottom of the second generation nozzle for (top) SC-MPOF and (bottom) HC-MPOF.

Heat transfer simulations were carried out to determine the temperature gradient within the nozzle. The temperature at the bottom of the nozzle for SC-MPOF is reduced from the applied temperature of 250.0 °C at the thread to 243.5 °C (Figure 4.15(a)). Thus, a better heat transfer from the thread to the nozzle body can be observed in comparison with the first generation. Although the lowest temperature is at the nozzle body, the difference in temperature between the body and the cover is ~1 °C. To extrude the SC-MPOF, heated polymer moves directly through the nozzle body, with a part of it flowing out to the outer region of the nozzle body forming the fibre cladding. Material flow simulations were also performed to examine the velocity of polymer exiting the nozzle. The result (in Figure 4.15(b)) shows that the polymer inside and outside the nozzle body have a similar velocity (~4 mm/s) at the bottom, leading to the same extrusion speed for all parts of the extruded polymer.

In the nozzle for HC-MPOF, the temperature at the bottom is 236.3 °C (Figure 4.15(c)), with a better heat transfer across the nozzle body compared with the first generation. Temperatures at the bottom of the nozzle body and the nozzle cover are about 5 °C different. Material flow simulations, reported in Figure 4.15(d)), show the polymer exits all parts of the nozzle at a similar velocity (~5 mm/s).

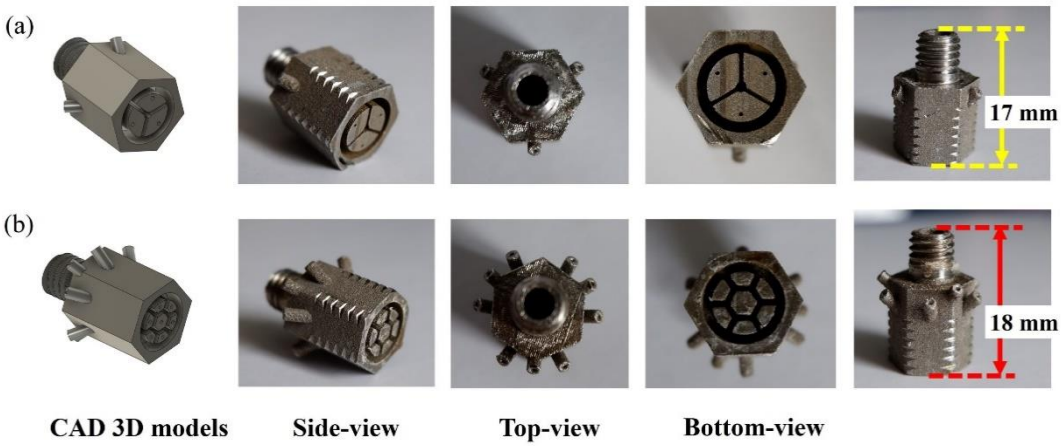

Figure 4.16 Second generation of metal 3D printed structured nozzles for (a) SC-MPOF, and (b) HC-MPOF.

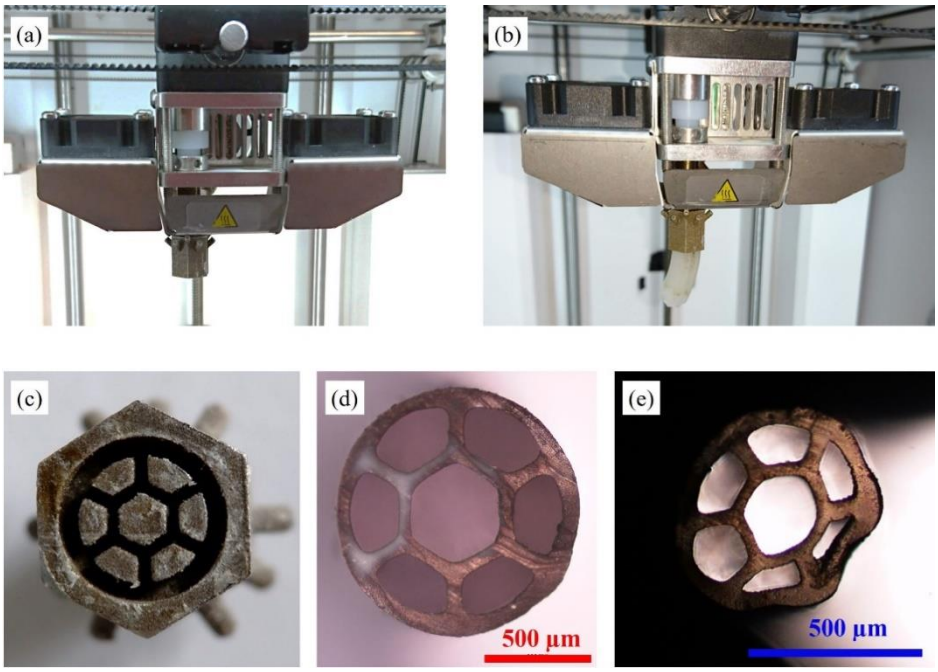

Figure 4.17 (a) Metal 3D printed structured nozzle connected with the heater of the 3D printer. (b) Extrusion of the HC-MPOF from the metal 3D printed nozzle. (c) Bottom-view of the nozzle for HC-MPOF. (d) Cross-section of the first drawn HC-MPOF with fibre diameter d~1600 µm. (e) The deformation in the fibre structure after drawing for lengths over 1 metre.

The second generation of metal 3D printed nozzles were submitted to the additive manufacturing team of Mechanical Engineering, at the University of Southampton, for fabrication. The material of choice for metal 3D printing at this workshop is CL20ES stainless steel powder. This material has a thermal conductivity of 15W/mK and melting temperature of 1510°C. To date, stainless steel has been the most widely used material of choice for extrusion dies. It exhibits high mechanical strength at elevated temperatures (up to ~650 °C), is cost-effective and does not show surface abrasion against material flowing at elevated temperatures with a material viscosity and

material feeding speed mentioned above. The nozzles were printed out with high fidelity (~99% due to the ± 0.1 mm tolerance) to the 3D model designs. Various views of the second generation metal 3D printed structured nozzles are presented in Figure 4.16(a-b).

These nozzles were used to fabricate the MPOFs using the direct extrusion technique as shown in Figure 4.17(a-b). Commercial ABS polymer was used with all these nozzles to fabricate the SC-MPOF and HC-MPOF. A temperature of 250 °C from the heating element at the printing head was applied to the nozzle through the thread. This is 20 °C higher than the temperature applied to the first generation nozzles due to the larger nozzle size and lower thermal conductivity of stainless steel compared with aluminium. The built-in filament feeding motor of the 3D printer was used to feed the ABS polymer into the heated nozzle at 250 mm/min. Size reduction took place with the same procedure by connecting the extruded polymer to the pulling system. Cross-sections of the first HC-MPOF extruded and drawn from these nozzles are shown in Figure 4.17(d).

4.3.2.4 Second generation: issues

After drawing for a length of ~5 m, the fibre structure exhibited a significant deformation, as shown in Figure 4.17(e). The deformation in the fibre is attributed to the collapsing of the cladding structure, similarly to what was observed in the fibre drawn from the first generation of nozzle. Although tubes for pressure equalization were added in the 3D model design, in the metal 3D printed nozzles they were blocked. This was attributed to the small size of the tubes in the 3D model design, or to the incompatibility of the metal 3D printing parameters.

Another problem in this design is the poor contact between the nozzle and the heater head, causing poor heat transfer between the two parts. This is due to the tubes' position, above the top part of the nozzle cover, leading to a gap, as shown in Figure 4.18(a-b).

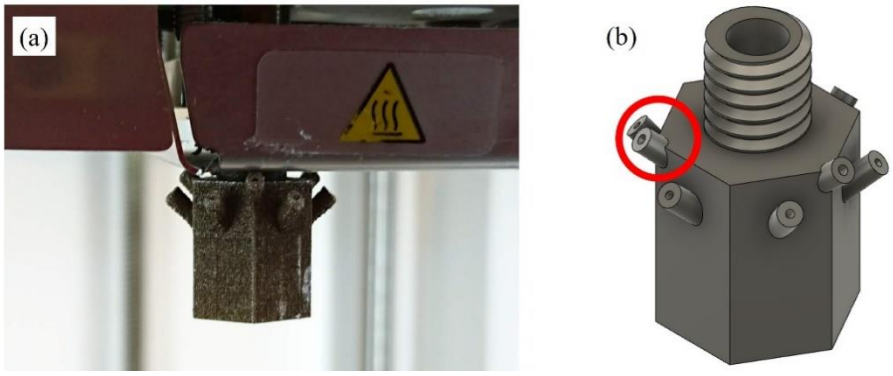

Figure 4.18 (a) Second generation metal 3D printed structured nozzle connected with the heater showing the gap between the structured nozzle and heater head due to the long length of (b) pressure-equalization tubes (red circle).

4.3.2.5 Third generation

The third generation of structured nozzles aimed to solve (1) the incompatibility between the structured nozzle and the heater head and (2) the clogged holes after metal 3D printing. To avoid the gap between the structured nozzle and the heater, the tubes could be tilted towards to horizontal plane or moved to a lower part of the nozzle. As described previously, the self-supporting angle of the 3D model for metal 3D printing should be larger than 45° with respect to the horizontal plane to avoid loss of fidelity. The angle of tubes in the second generation were set to 45° as presented in Figure 4.19 (a-b). Because of this, in third generation nozzles, the tubes are moved to a lower part of the nozzle, to avoid any gap between the structured nozzle and the heater head. The dimensions of the structure inside the nozzle body are the same as those in the second generation including width and height (green rectangle). This is to maintain the same behaviour of material flow inside the nozzle body. Thus, to move the tubes to the lower part, the total length of the nozzles was increased from 19 mm (Figure 4.20(a)) to 21 mm (Figure 4.20(c)).

The other significant problem of the second generation of nozzles was the blockage of the tubes, ascribed to the tolerance of metal 3D printing. For a general metal 3D printer, dimensional tolerance is ± 0.1-0.2 mm [163]. Thus, in the second generation nozzle, the diameter of the metal 3D printed tubes could be as small as 0.1 mm, although the targeted tube diameter was 0.5 mm. So, diameter of the tubes in the third generation was increased from 0.5 mm to 0.7 mm (Figure 4.19(c-d)).

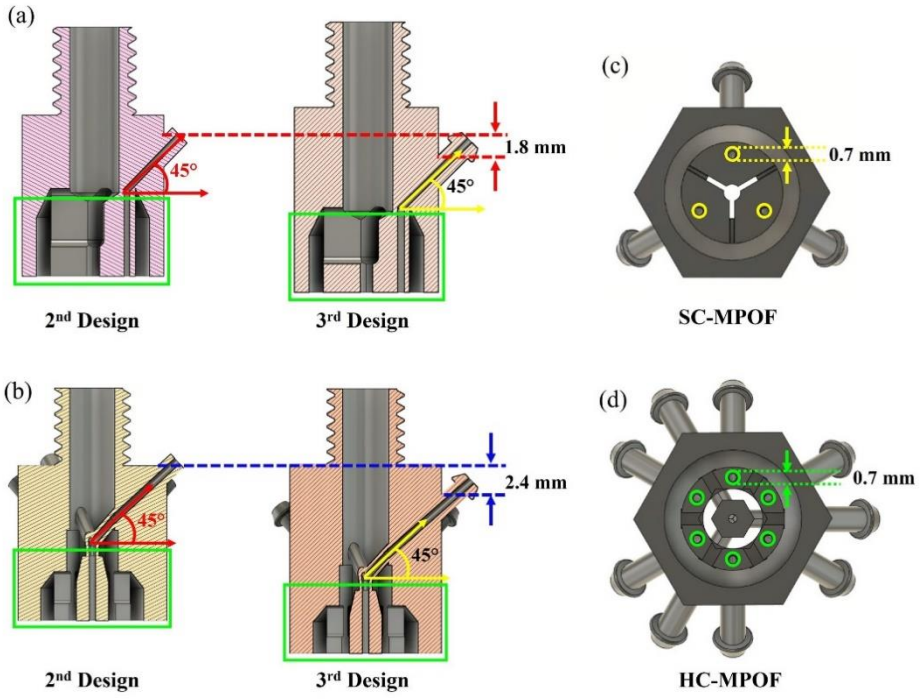

Figure 4.19 Comparison between cross-section of the 2nd and 3rd generation of the structured nozzles for (a) SC-MPOF and (b) HC-MPOF. Bottom-view of the improved design of the structured nozzle for (c) SC-MPOF and (d) HC-MPOF.

Apart from increasing nozzle length to move the tubes lower, all dimensions of the third generation of the nozzles are the same as the second generation as shown in Figure 4.20(b, d). The direction of material flow for this design is presented (yellow and green arrows) within the side-view cross-section of the fibre in Figure 4.20(b, d). The air-pressurised tubes are clearly observed in the cross-section of the structured nozzle.

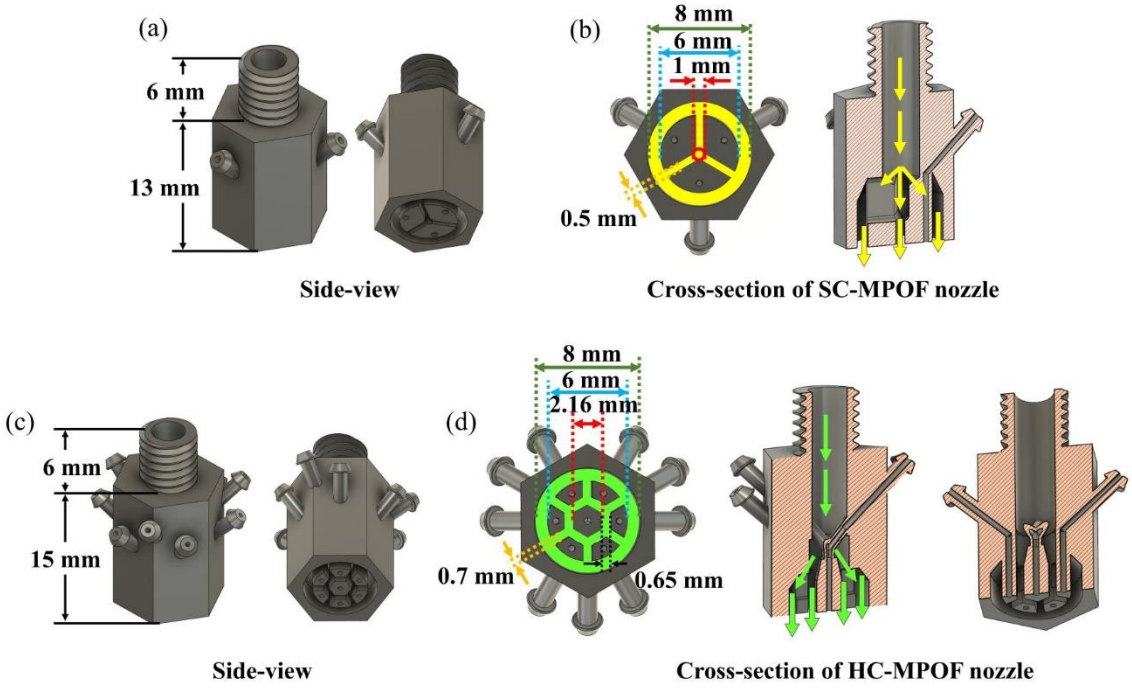

Figure 4.20 (a) Third generation nozzles for SC-MPOF. (b) Dimensions of the structure inside the nozzle and cross-section of the structured nozzle. (c) Third generation nozzle for HC-MPOF. (d) Dimensions of the structure inside the nozzle and cross-section of the structured nozzle for SC-MPOF.

The increased nozzle length can cause a decrease in the temperature at the bottom of the structured nozzle. To extrude the polymer through the structured nozzle, the nozzle temperature cannot be lower than the required printing temperature of the polymer used in this research (~ 210 – 240 °C). Therefore, heat transfer simulations were carried out also for this design of the structured nozzle. Figure 4.21(a) shows that the temperature at the bottom of the nozzle for SC-MPOF is reduced to 242.5 °C when a temperature of 250 °C is applied to the thread: the lowest temperature at the bottom of the nozzle for SC-MPOF is ~1 °C lower than the second generation nozzle. Material flow simulations were also carried out to examine the velocity of polymer at the bottom of the nozzle. Figure 4.21(b) shows that at the bottom of the structured nozzle, the velocity of polymer flow inside and outside the nozzle are the same, leading to the same extrusion speed (~3 mm/s) for all parts of the extruded polymer. For the heat transfer simulation of the HC-MPOF nozzle, the temperature at the bottom of nozzle is reduced to 234.6 °C (Figure 4.21(c)), ~2 °C lower than the second generation nozzle, yet still higher than the required printing temperature of the polymer. Material flow simulations in the nozzle for HC-MPOF (Figure 4.21(d)) show that all parts of the polymer at the

bottom of the nozzle have similar velocity (~4 mm/s) leading to the same extrusion speed for all parts of the extruded polymer.

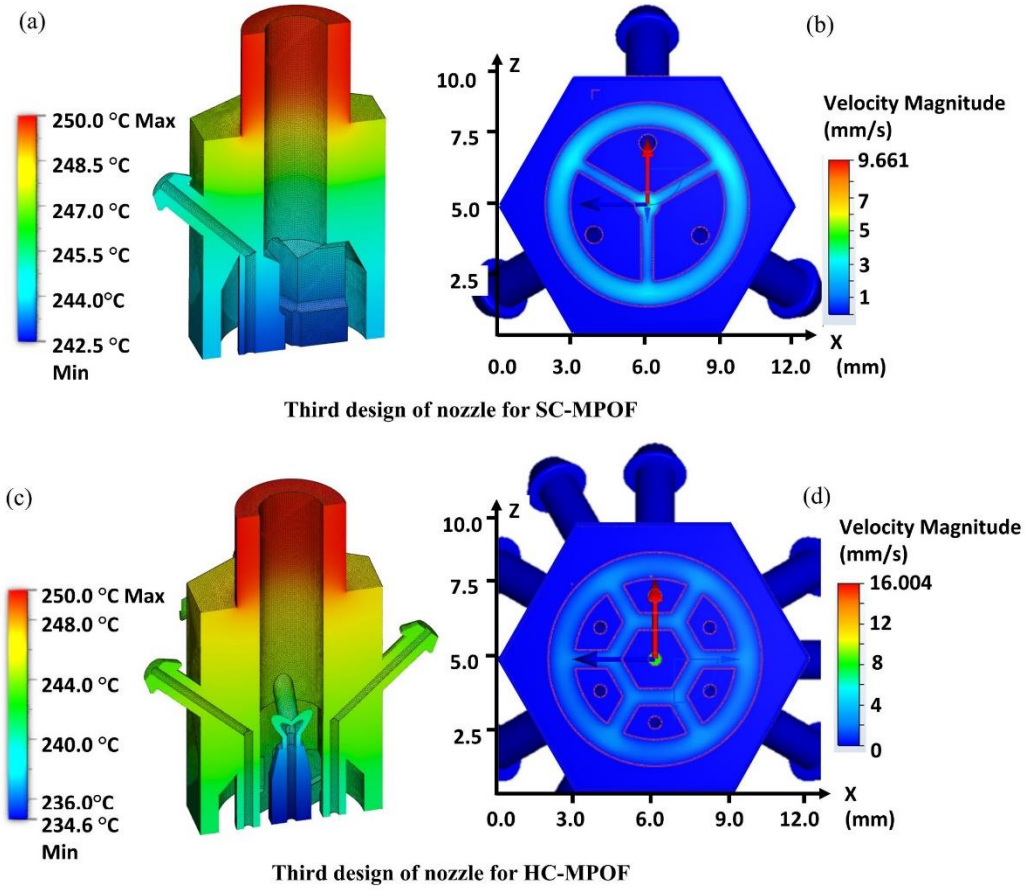

Figure 4.21 Heat transfer simulations in the third generation nozzles for (a) SC-MPOF and (c) HC-MPOF. (b) Velocity magnitude of polymer flow at the bottom of the nozzle for (b) SC-MPOF and (d) HC-MPOF.

The third generation of structured nozzles was printed at the University of Southampton using CL20ES stainless steel powder. Various views of third generation nozzles are presented in Figure 4.22(a-b). To fabricate the MPOFs, the standard 3D printer nozzle was replaced with the structured nozzle, as in Figure 4.22(c-d). As shown in Figure 4.22(c), no gap is present between the nozzle and the heater head, as the tubes were moved to the lower part of the nozzle. ABS polymer was used for manufacturing the SC-MPOF and HC-MPOF. A temperature of 290 °C from the heating element at the printing head was applied to the nozzle through the thread. This temperature is 40 °C higher than the temperature applied to the second generation of the metal 3D printed nozzles due to the longer length of this design compared with the previous one. The built-in filament feeding motor of the 3D printer was used to feed the ABS polymer into the heated nozzle with a feeding speed of 240 mm/min. The drawn HC-MPOF is shown in Figure 4.22(e).

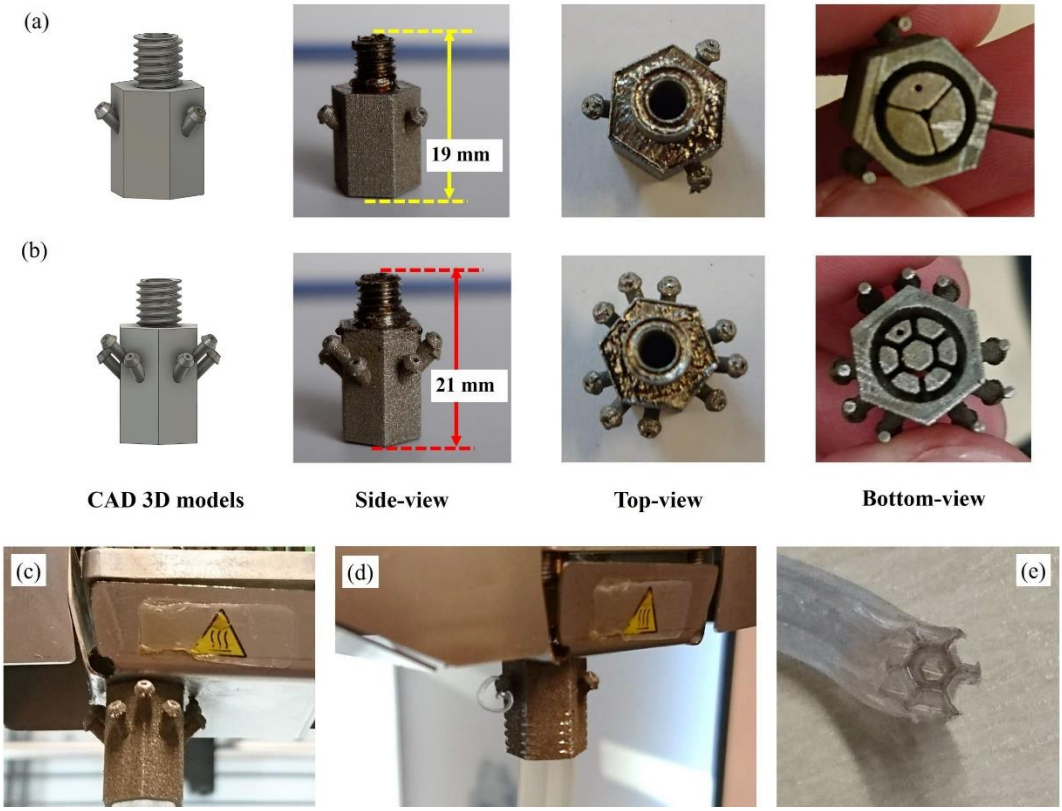

Figure 4.22 Third generation of metal 3D printed structured nozzles for (a) SC-MPOF and (b) HC-MPOF. (c) Nozzle connected to the heater. (d) Leakage of extruded polymer through the pressure equalizing tubes. (e) Extruded HC-MPOF.

4.3.2.6 Third generation issues

Although the diameter of the air-hole in the pressuring tubes was increased, some tubes were still blocked: the bottom-view in Figure 4.22(a-b) shows that only one hole in the metal 3D printed nozzle can be clearly observed, while the rest are obstructed. As the hole size of the third design nozzles is larger than the printing tolerance, the blockage in the pressuring tubes has been ascribed to unsuitable printing parameters.

Another issue found in this generation of nozzles is polymer leakage from the pressure equalizing tubes. Figure 4.22(d) shows that the polymer leaves the tube while extruding the polymer through the nozzle, pointing to the presence of apertures in the pressure equalizing tubes inside the nozzle. Another problem found in this design is the lack of pressure for structure preservation inside the extruded polymer fibres. As seen in Figure 4.22(e), the outer wall of the extruded polymer is broken because the polymer at the outer wall cannot merge properly before flowing out from the nozzle tip. To improve the structured nozzle design, internal cross-sections of its structure were examined to ascertain all critical regions for metal 3D printing.

X-ray computed tomography was used to observe the cross-section of the metal 3D printed structured nozzle. A µCT machine (Nikon XT H 225) at the Centre for Precision Technologies, University of Huddersfield, was used to obtain 3D scans of the internal features. The nozzle was

mounted inside the µCT machine upon a low density phenolic foam sponge while 2D X-ray images were obtained from all sides of the part before reconstruction into a 3D density point cloud using CT Pro software. VG studio max was then used to separate the 3D printed material from low density air/foam based on greyscale density values using ISO50 automated surface determination to acquire an outline of the part. Lastly, a manual 3-point planar registration tool was used to orient the scanned volume to the z-plane of the CAD model so that slices through the z-axis can be created to observe internal features of the metal 3D printed nozzle.

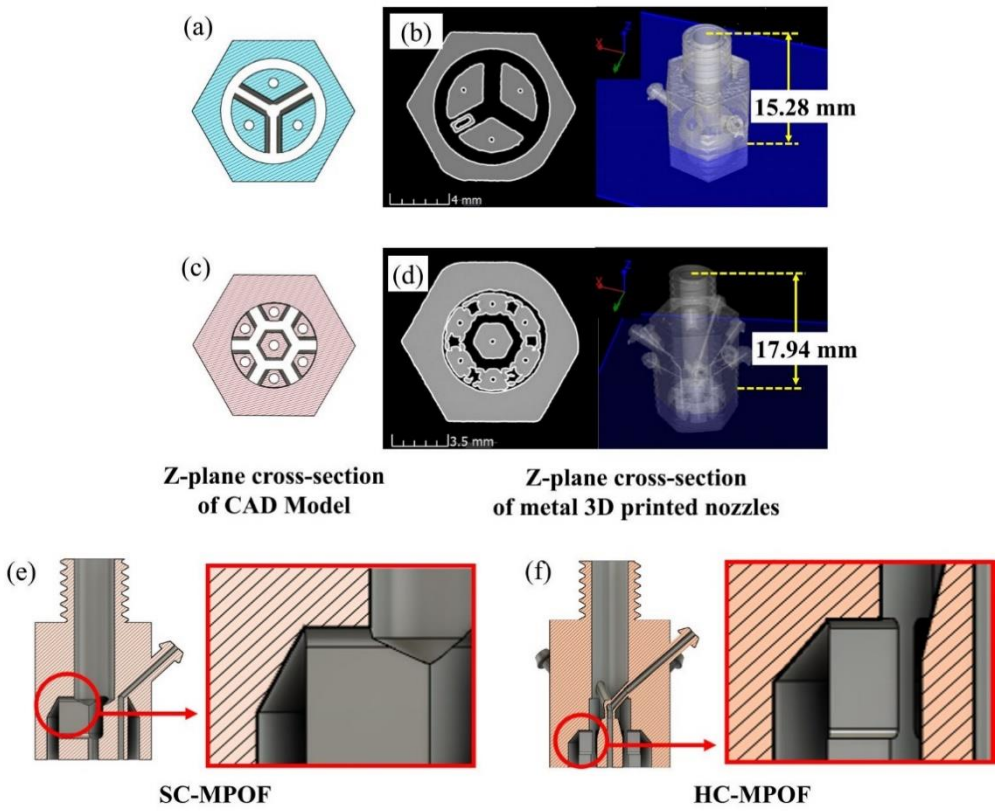

Figure 4.23 (a, c) Cross-sections of the 3D model design and (b, d) X-ray tomography images of the metal 3D printed nozzle for SC-MPOF and HC-MPOF. Vertical cross section and close up of flat surface regions in the third generation structured nozzles for (e) SC-MPOF and (b) HC-MPOF.

X-ray tomography images of the structured nozzle for SC-MPOF and HC-MPOF are reported in Figure 4.23(b, d), respectively, and visibly show that the features inside both metal 3D printed nozzles are not clearly printed. The expected cross-section of the nozzle at a depth of 15.28 mm and 17.94 mm from the top for the SC-MPOF and HC-MPOF are presented in Figure 4.23(a, c), respectively. In comparison, the cross-sections of the x-ray tomography images at the same depth clearly show fused metals in the gaps. This unexpected metal formation in the gaps obstructs the polymer when flowing in the structured nozzle resulting in the distortion of the extruded fibre.

To solve this problem, side-view cross-sections of the structured nozzles were closely studied to determine the critical region in the design. Side-view cross-sections of the structured nozzles in

Figure 4.23(e-f) show that there is a flat surface located above the gaps in the structured nozzles. These surfaces are paralleled to the horizontal plane. When the nozzles are metal 3D printed from bottom to top, these flat surfaces required support structures because the angle of these surfaces are higher than the self-supporting angle (45°). Because of the lack of support structures, metal powder meant to form the structure above the gap dropped down, resulting in the formation of the metal obstructions in the gaps.

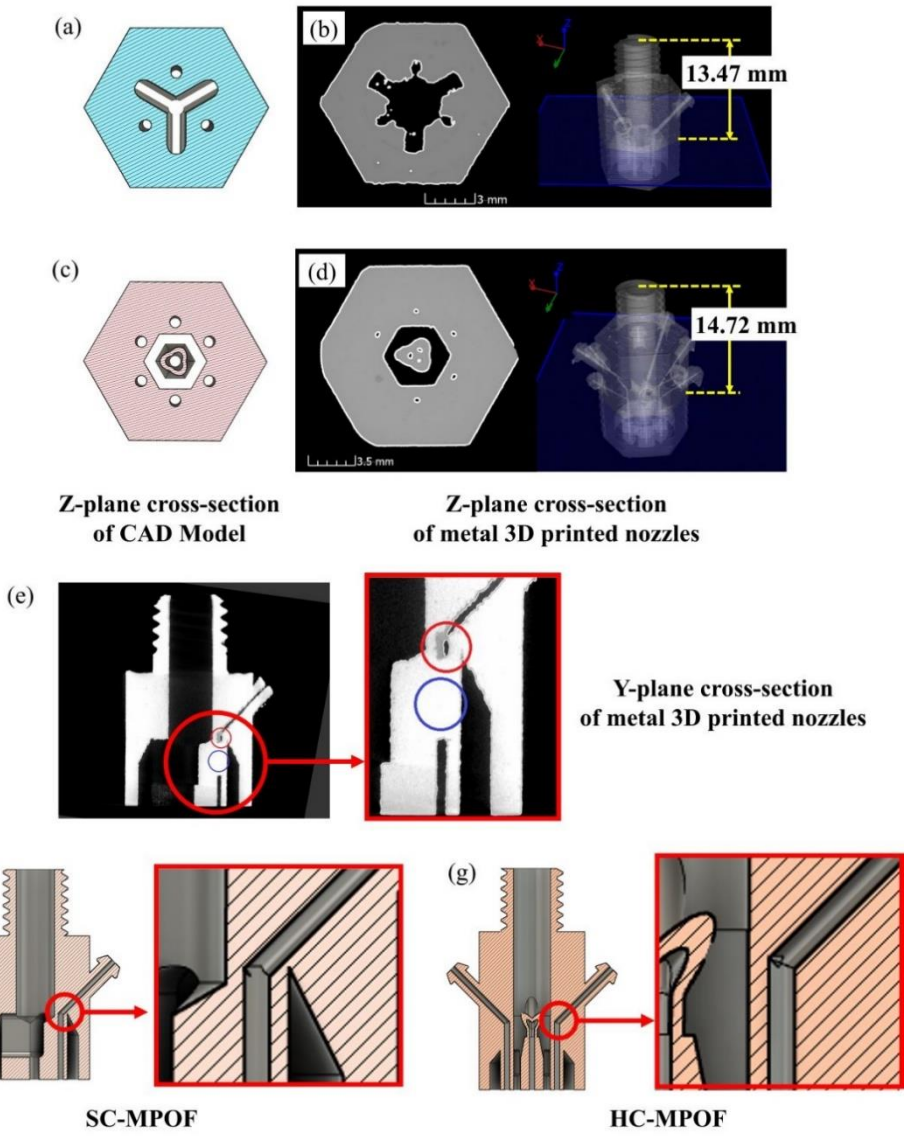

Figure 4.24 Cross-section of (a, c) the 3D model design and (b, d) X-ray tomography images of the metal 3D printed nozzle for SC-MPOF and HC-MPOF. Vertical cross sections and zoom in of sharp edge regions in the third generation structured nozzles for (e) SC-MPOF and (b) HC-MPOF.

Another problem found in the third generation of the structured nozzle is the presence of obstructions in the pressure equalizing tubes. Z-plane cross-sections of the metal 3D printed nozzle at the depth of 13.47 mm for SC-MPOF and 14.72 mm for HC-MPOF (Figure 4.24(b, d)) show that

some parts of the hole tubes are broken (Figure 4.24(b)), while some of the holes are filled (Figure 4.24(d)), when compared with the cross-section of the CAD model at the same depth. By looking at the Y-plane cross-section of the X-ray tomography image, it can be clearly seen that the tube is filled with material at the position below the bend (Figure 4.24(e)). Therefore, side-view cross-sections of the tubes inside the nozzle were observed to examine the cause of the clogging. The tubes had been designed to start vertically from the bottom of the nozzle, then tilt to the side of the nozzle. As exhibited in Figure 4.24(f-g), there is a sharp corner at the edge between the vertical tubes and the tilted tubes, which can cause distortion in the metal 3D printing. At the sharp angle region, metal powder can drop down because it is unsupported, resulting in hole blockages.

4.3.2.7 Fourth generation

Figure 4.25 shows the improved design of the structured nozzle when these two critical regions in the previous design were fixed. An angled (45°) slope replaces the flat surface above the gap to comply with the self-supporting angle for metal 3D printing (Figure 4.25(a-b)). During the metal 3D printing process (sintering), printing parts undergo thermal stresses in the furnace because a small degree of shrinkage is associated with sintering: most of the binder is removed, and the metal particles start to fuse and pull each other together, after which the furnace cools to room temperature. Drastic changes in part thickness can cause parts to warp or curl due to thermal stresses. Therefore, stress concentration can be reduced by filleting the edges, maintaining a consistent wall thickness, and designing gradual changes in thicknesses. The sharp angle at the edge between the vertical tube and the tilted tube are fixed by adding a fillet at the sharp corner, as shown in Figure 4.25(a, c).

This generation of the nozzles was metal 3D printed at University of Southampton using the same material, CL20ES stainless steel powder, as the previous generation. To improve the metal 3D printing parts, the printing parameters were also adjusted. The process of selective laser melting (SLM) for metal 3D printing involves a series of steps including powder deposition and laser scanning. It is conducted within an inert controlled-atmosphere chamber of choice to avoid oxidation during the printing process (melting and solidification). The SLM process can be divided into three stages. It starts from the scanning of the laser on metal powder to create individual scan tracks. Then, the overlap of individual scan tracks horizontally will form an individual layer. Finally, the individual layers overlap vertically to create a 3D bulk structure. A part is made up of a stack of layers overlapping vertically. The most influential parameters for SLM are presented in Figure 4.26. Scanning pattern is one of those important parameters: it defines the laser path within a layer. The scan strategy defines the different scan patterns between each layer: for example, rotating the orientation between layers by a set angle or scanning a layer multiple times. To minimise defects and control the microstructure, the scanning patterns and strategies need to be optimised.

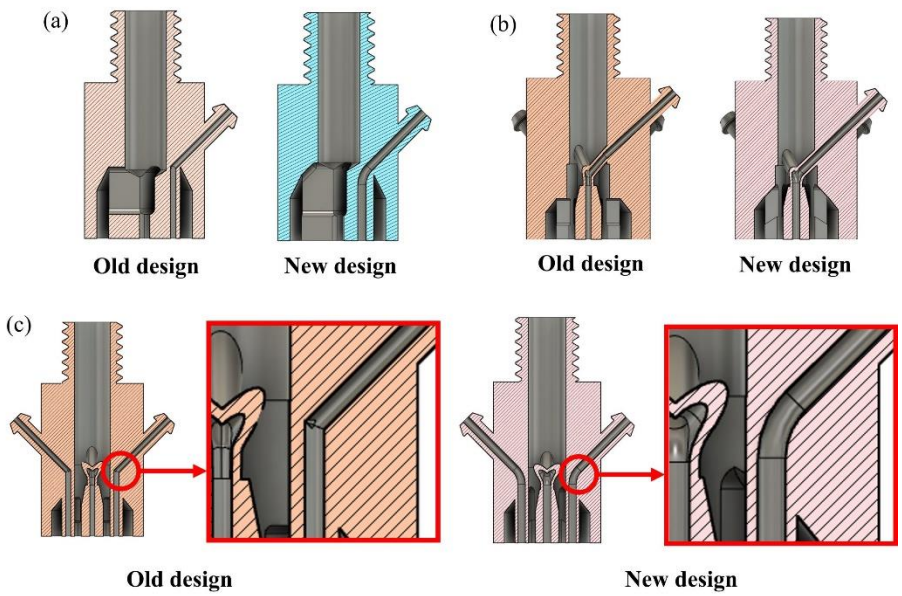

Figure 4.25 Side-view cross-sections of the third and fourth generation structured nozzles for (a) the SC-MPOF and (b) HC-MPOF. (c) Smoothing of the pressure equalization tubes.

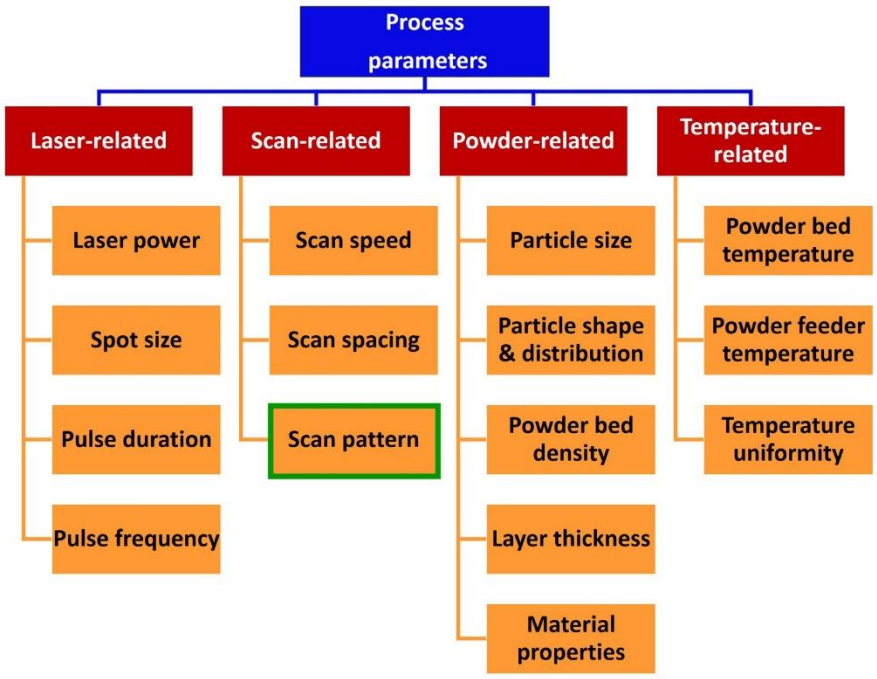

Figure 4.26 The most influential process parameters affecting the quality of a part processed by SLM [164].

For the past three designs of the structured nozzles, the randomised scanning strategy was used to print the nozzle. It provided a sample where only one tube remained clear, while the rest were closed. Although the size of tubes was increased to comply with the required minimum size for metal

3D printing (>0.4mm) and all critical regions in the design were edited, most of the tubes remained closed. To ensure that the distortion of the printed parts is not due to the design but rather to the unsuitable choice of printing parameters, the designed nozzles were enlarged by 2 times before printing. The same problem still occurred when printing with the randomised scanning strategy, although the nozzle size was increased. This suggested that the randomised scanning strategy was not suitable for printing the structured nozzle. Therefore, a different scanning strategy was used: the continuous strategy, which provided clear holes in the metal 3D printed nozzle.

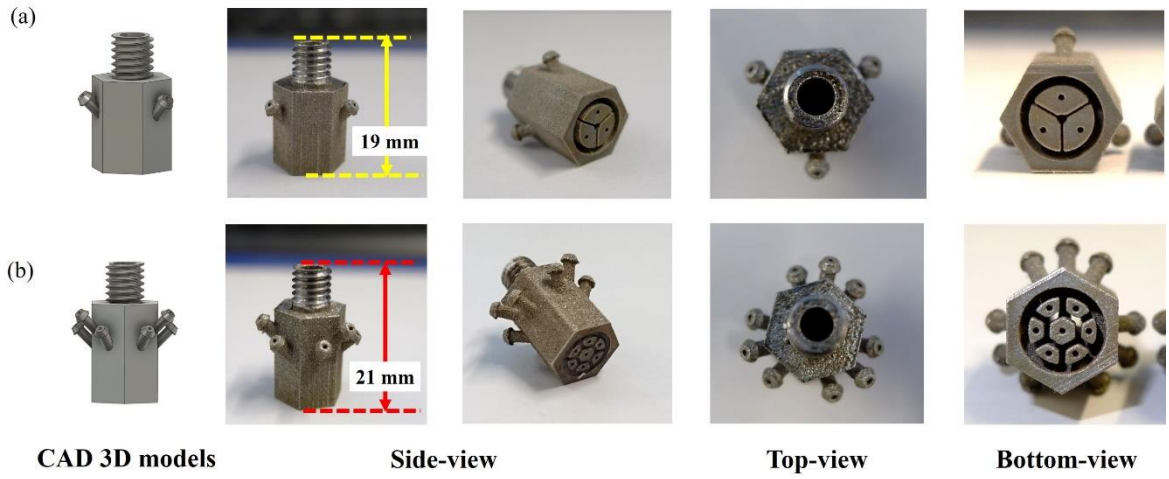

Figure 4.27 Fourth generation design of the metal 3D printed structured nozzles for (a) SC-MPOF, and (b) HC-MPOF.

Various views of the fourth generation nozzles are shown in Figure 4.27(a-b). It can be seen from the bottom-view that all the tubes are clear. To ensure that the narrow nozzle channels were fully formed throughout and that no residual fused metal powder remained from the additive manufacturing process, this nozzle was sent to the Centre for Precision Technologies, University of Huddersfield, for X-ray tomography using the same procedure as described in section 4.3.2.6. Slices through the X, Y and Z planes were created to verify all nozzle channels were clear and the features fully formed throughout.

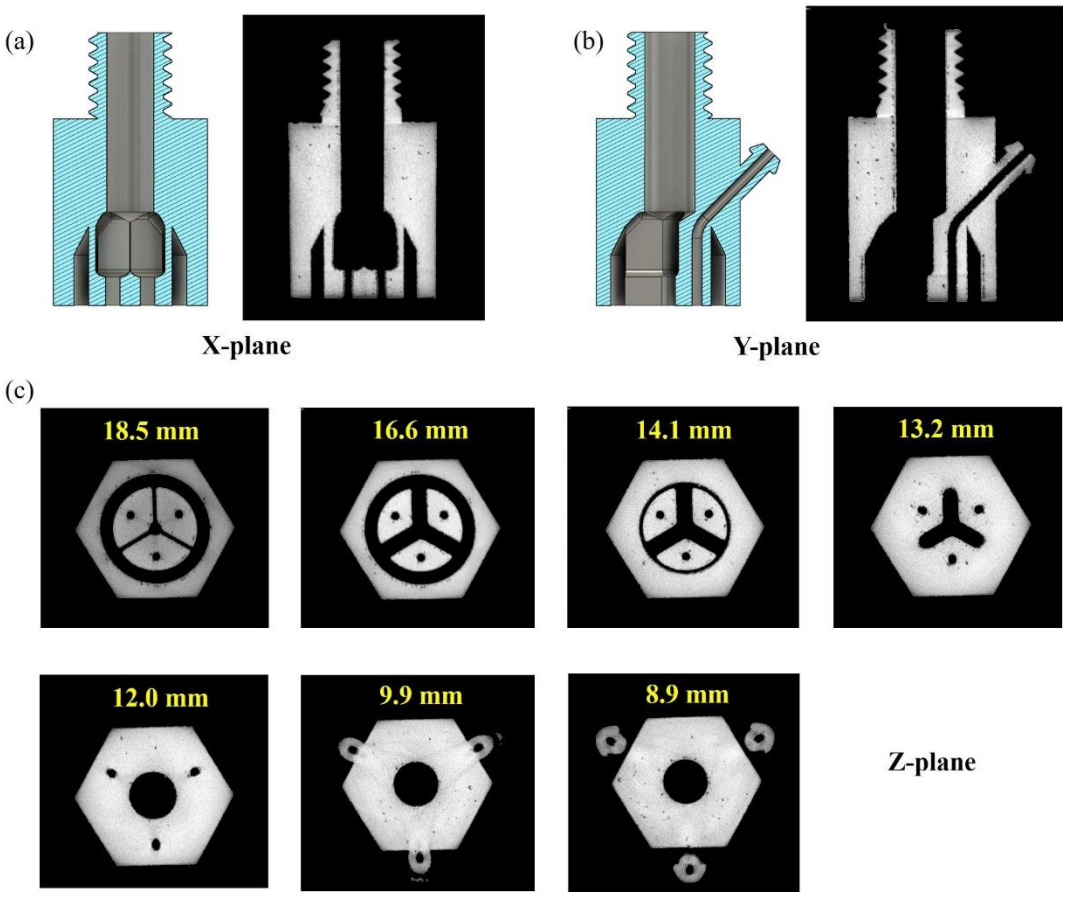

Figure 4.28 X-ray tomography cross sections of the fourth generation nozzle for SC-MPOF in (a) X-plane, (b) Y-plane, and (c) Z-plane at different depths from the top.

The X-ray tomography images of the structured nozzle for SC-MPOF are shown in Figure 4.28: it can be clearly seen in the cross-sections that the features inside the metal 3D printed nozzle are clearly printed. The cross-section of the nozzle in the X-plane (Figure 4.28(a)) and Y-plane (Figure 4.28(b)) show that the channel inside the nozzle is clear without any residual metal powder from the printing process. The structure inside the metal 3D printed nozzle shows high fidelity to the CAD model design. The Z-plane cross-sections of the nozzle at different depths from the top are presented in Figure 4.28(c). Compared with the cross-section of the X-ray tomography images of the previous design nozzle, it can be clearly seen that all the holes and gaps inside these nozzles are clearly printed at all depths. There is no leakage in the channels, as found in the previous design. X-ray tomography images of the structured nozzle for HC-MPOF were also taken. Figure 4.29(a) shows that the channel at the centre of the nozzle is clearly printed, with high fidelity to the CAD model design. Similarly, the cross-section in the Y-plane showed that all the tubes are clear throughout the nozzle. Z-plane cross-sections at different heights of the HC-MPOF nozzle are presented in Figure 4.29(c), showing that all the holes inside the nozzle are separated without any obstructed material inside the holes.

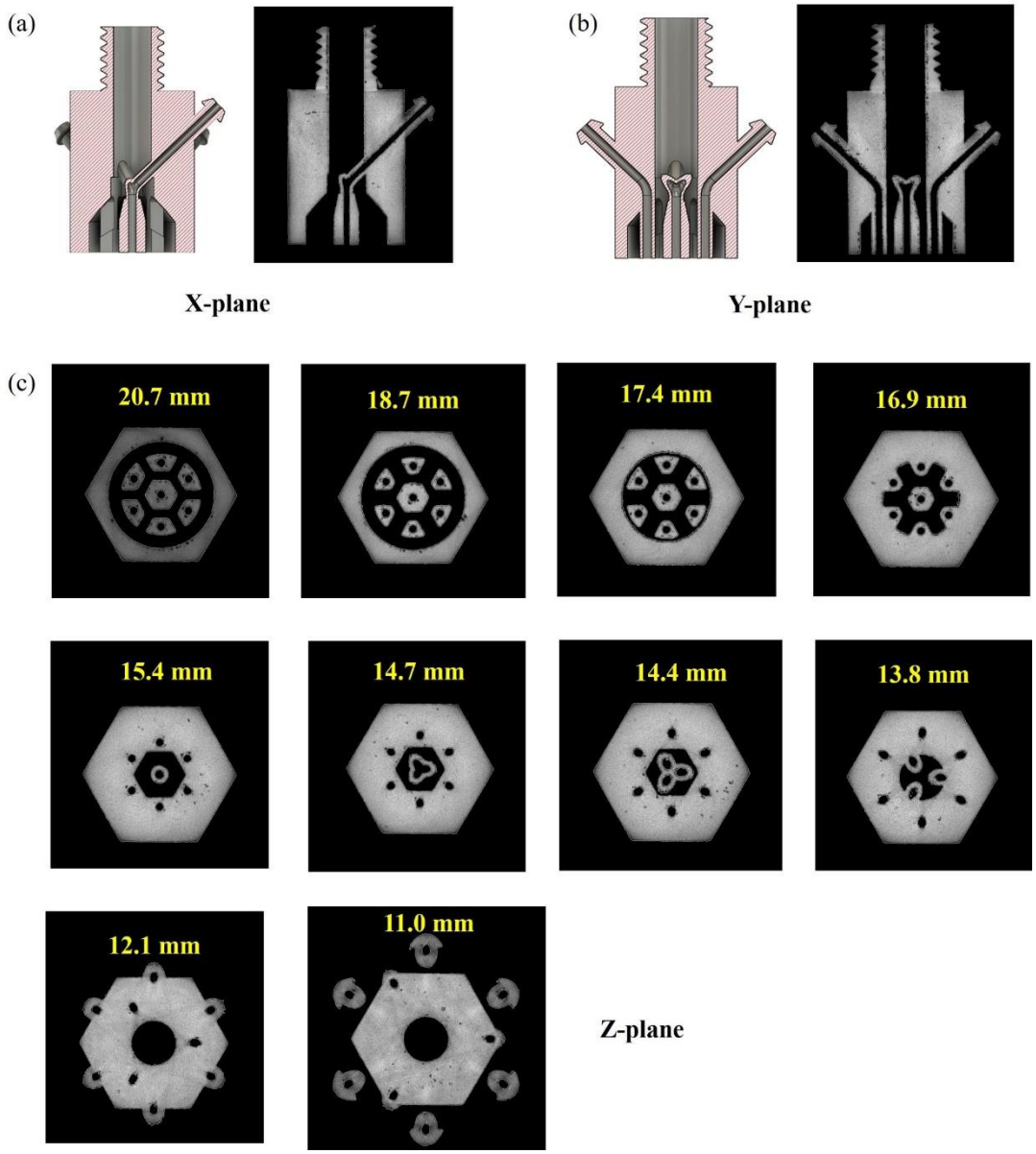

Figure 4.29 X-ray tomography images of fourth generation nozzle for HC-MPOF in (a) X-plane, (b) Y-plane, and (c) Z-plane at different depths from the top.

The improvements implemented in this generation by applying an angle of 45° to the flat surface above the gap show that the features inside the metal 3D printed nozzle are clearly printed. Moreover, this change also improved the flow of heated polymer inside the structured nozzle. Fluid flow simulations for both the old and new nozzle designs are presented in Figure 4.30(a-b). The results show that the sharp angle in the old design led to a critical change in the direction of the flow. This causes a drop in polymer flow velocity at the outer region of the nozzle, resulting in poor flow. The better flow in the new nozzle design leads to a uniform velocity profile for the extruded polymer.

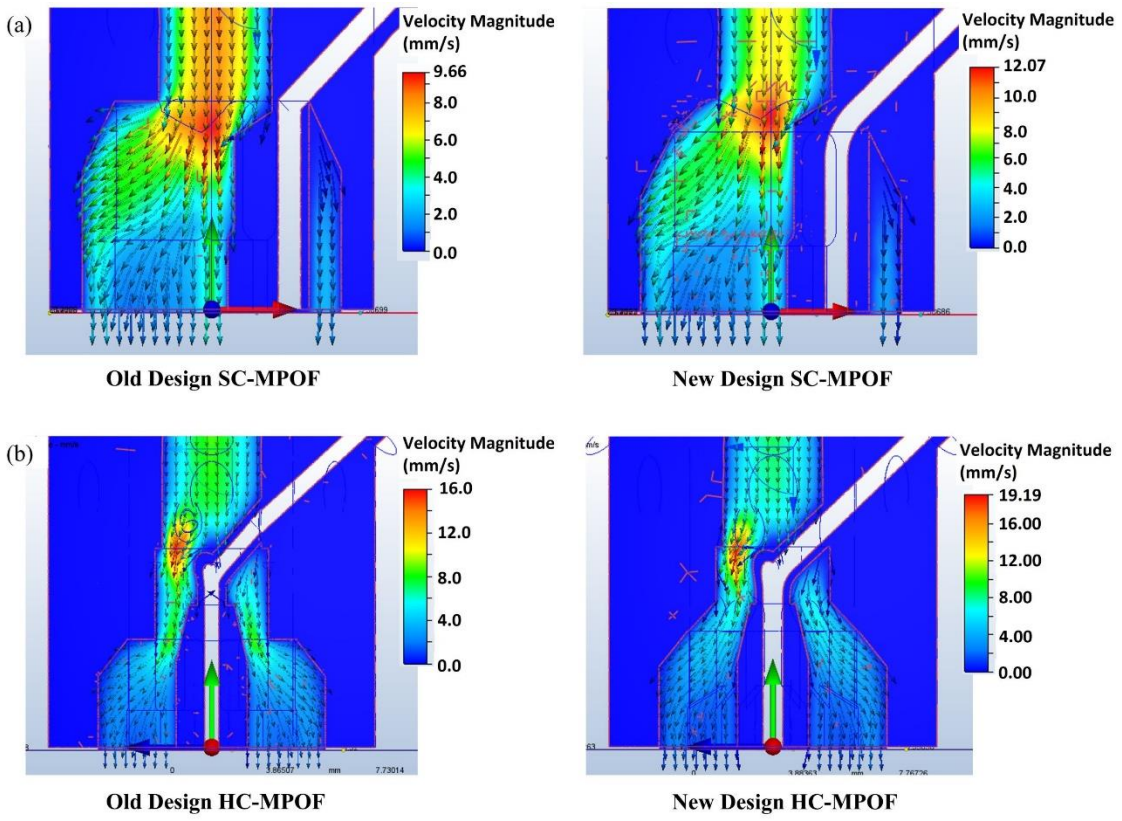

Figure 4.30 Side-view of simulated velocity magnitude of polymer flow inside the third (left) and fourth (right) generations of the metal 3D printed nozzles for (a) SC-MPOF (b) HC-MPOF.

To test these improved nozzles, the commercial ABS polymer was extruded from both metal 3D printed nozzles for manufacturing the SC-MPOF and HC-MPOF. A temperature of 290 °C from the heating element at the printing head was applied to the nozzle through the thread. The polymer was fed through the heated structured nozzle with a feeding speed of 240 mm/min. At this temperature and feeding speed, the ABS polymer can be extruded from these structured nozzles for SC-MPOF and HC-MPOF, as shown in Figure 4.31(a) and (d), respectively. It can be noticed that there is no more leakage of polymer through the pressure equalizing tubes that was found in the previous design. Next, the fibre drawing system was applied to the extrusion system to reduce the size of the fibre. At a temperature of 290 °C and feeding speed of 250 mm/min, the diameter of the extruded MPOF was reduced to ~ 300 µm when the fibre drawing speed was ~ 0.2 m/s. Figure 4.31(c) and (f) show that the microstructure inside the extruded and drawn SC-MPOF and HC-MPOF are preserved. The optical fibres reveal the same geometry as the nozzles (Figure 4.31(b) and (e)). Furthermore, the MPOF could be drawn to sub-micron size and in unlimited lengths while maintaining the microstructure. This demonstrates success in applying the pressuring tube into the structured nozzle to equilibrate the pressure inside the microstructure and outside the fibre.

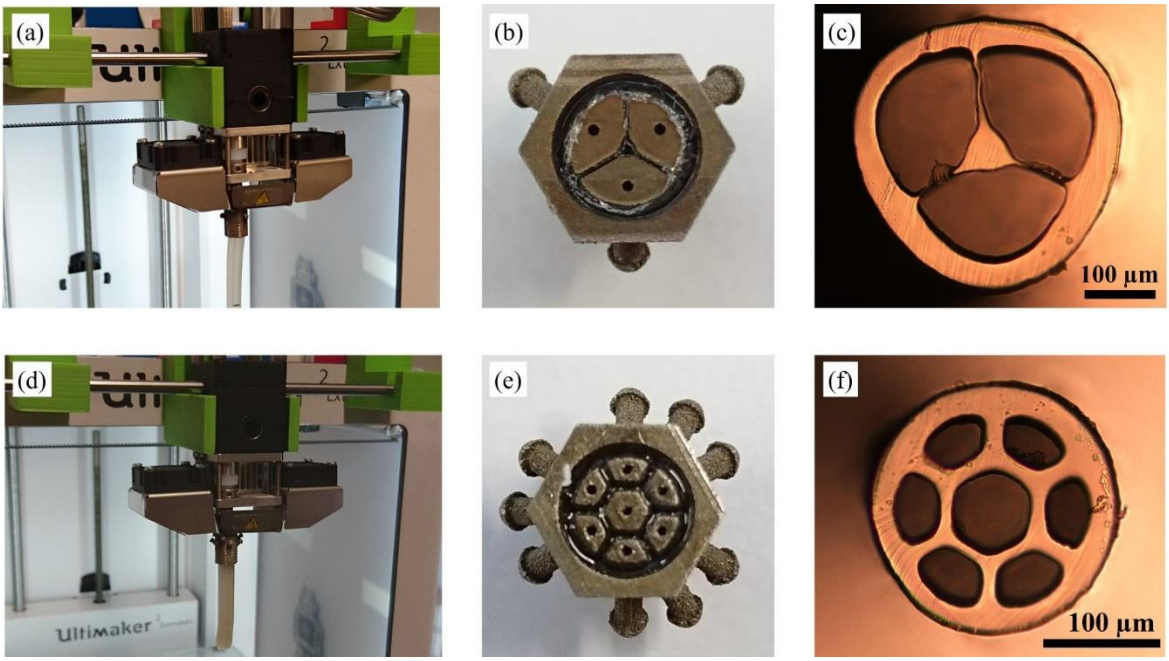

Figure 4.31 Extrusion of (a) the SC-MPOF and (d) HC-MPOF from the metal 3D printed nozzle. (b, e) Bottom-view of the metal 3D printed structured nozzle used to fabricate the SC-MPOF and HC-MPOF, respectively. (c, f) Cross-section of the SC-MPOF and HC-MPOF extruded and drawn from the metal 3D printed nozzle with fibre diameter d_{fibre}~400 µm and ~300 µm, respectively.

4.3.2.8 Fifth generation

In the fifth generation nozzles for SC-MPOF, the gaps where the struts will be formed when extruding the optical fibre are reduced from 0.5 mm to 0.25 mm while the overall dimensions remain unchanged (Figure 4.32(a)). For the SC-MPOF, light guidance in the fibre is due to total internal reflection at the solid-core of the fibre. The solid-core of the optical fibre in this design is suspended at the centre of the fibre, connected to the fibre cladding by three thin struts. The light guided in the fibre core can leak into the cladding via the struts resulting in high losses. Therefore, the thinner the struts, the higher the confinement of the mode in the fibre core.

The fifth generation nozzle for HC-MPOF was adjusted by increasing the fibre core diameter (d_{core} ~ 3.2 mm) and decreasing the thickness of the core surrounding layer (~ 0.35 mm) as shown in Figure 4.32(b). The light guided in the hollow-core antiresonant fibre depends directly on the thickness of the core surrounding layer; therefore any variation in the layer thickness results in a shift in the guided wavelength in the fibre core. Although the thickness of the core surrounding layer can be adjusted during the drawing process, the thinner the layer, the shorter the wavelength to be guided, when the total diameter of the fibre is the same.

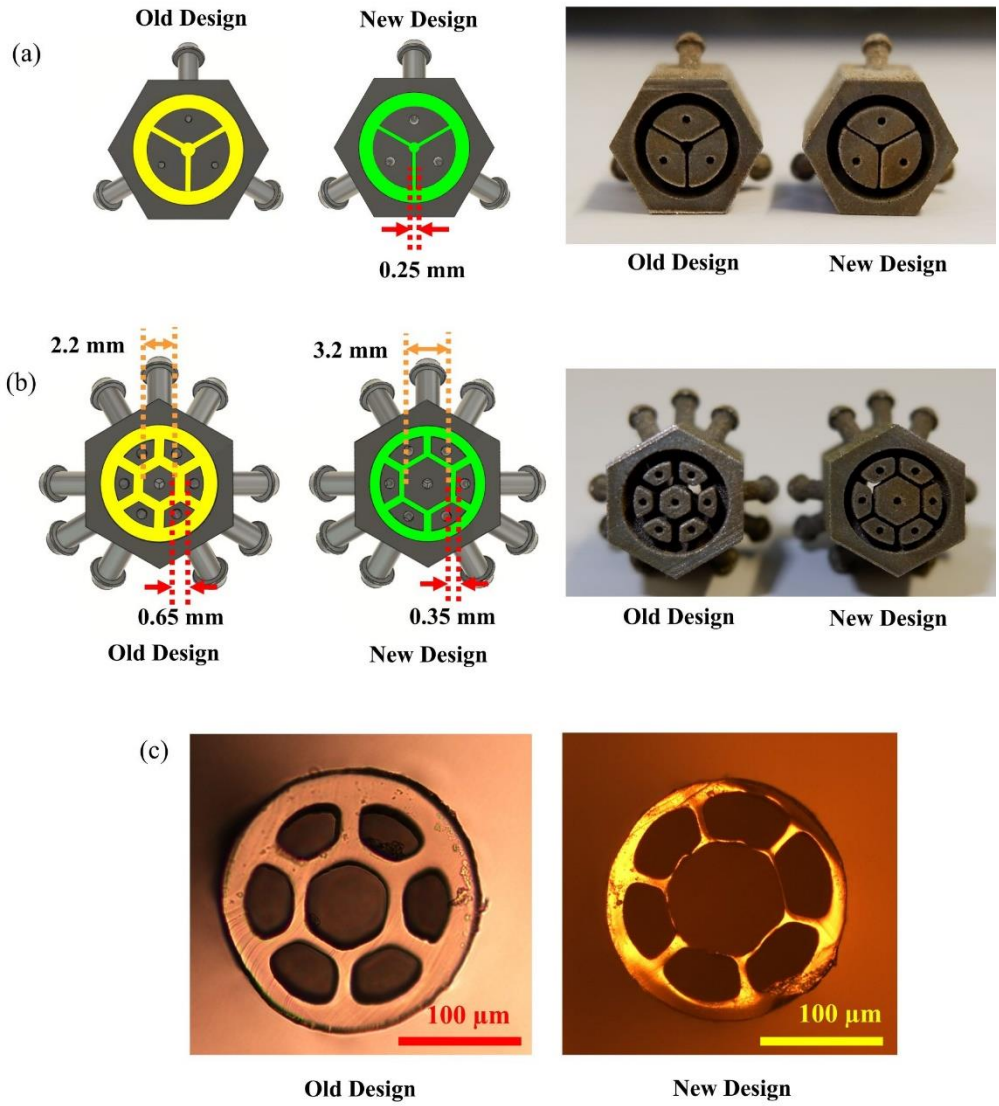

Figure 4.32 Fifth generation metal 3D printed structured nozzles for (a) SC-MPOF, and (b) HC-MPOF. (c) Cross-section of the HC-MPOF extruded and drawn from the fourth and fifth generation nozzles with fibre diameter of d_{fibre}~300 µm.

The fifth generation of the structured nozzle was metal 3D printed with the same printing parameters as the fourth generation by using the continuous scan pattern. Structures inside the nozzle exhibited high fidelity to the model for both the nozzle for SC-MPOF and HC-MPOF. The pressure equalizing tubes in the nozzle are clearly observed (Figure 4.32). ABS polymer was extruded and drawn from the new nozzle for the HC-MPOF. A temperature of 290 °C was applied to the heater while the polymer was fed through the nozzle with a filament feeding speed of 240 mm/min. The drawing system was connected to the extruded polymer to adjust the fibre diameter. It can be seen from Figure 4.32(c) that the structure inside the HC-MPOF extruded from the new nozzle can be maintained. Compared to the fibre drawn from the fourth generation nozzle, the fibre from the fifth generation nozzle has a larger core diameter and a thinner core surrounding layer when the fibre

diameter is the same. In this way, the ability to design the structured nozzle with different dimensions will open the way to fabricate optical fibres for a wide range of the guided wavelengths.

4.4 Summary

In conclusion, the structured nozzle, a key component for the direct extrusion of MPOFs using a low-cost desktop 3D printer, has been developed. Five generations of the structured nozzle have been developed to explore the optimal design parameters for extruding polymer through the structured nozzle with a uniform extrusion velocity profile. Simulations of the heat transfer and polymer flow through the nozzles were used to optimise the design. The structured nozzles were fabricated using the metal 3D printing technique. A clear structured nozzle was successfully printed from stainless steel powder with the continuous scan pattern. The metal 3D printed nozzle withstood a temperature of 300 °C and high pressure, demonstrating that 3D printed nozzles have sufficient mechanical strength to enable extrusion of optical fibres. Analysis of the fibre produced during this work proves the ability to maintain the microstructure inside the fibre after extrusion from a customised 3D printer head. This demonstration illustrates the potential to design and fabricate structured nozzles for manufacturing low-cost MPOFs with various geometries.

Chapter 5.

MICROSTRUCTURED POLYMER OPTICAL FIBRE EXTRUDED THROUGH A 3D PRINTER NOZZLE

3D printers have been optimised for printing high quality objects from a variety of materials including polymers, glasses, and metals, resulting in improved control systems which include built-in temperature controller and polymer filament feeding systems, allowing for their potential use in fibre drawing. By combining the extrusion technique with the capabilities of 3D printers, the fabrication of microstructured polymer optical fibres (MPOFs) in one low-cost process has been shown.

As presented in chapter 4, structured nozzles with a complementary structure to that of the desired fibre have been designed and fabricated via micromaching and metal 3D printing. By replacing a standard 3D printer nozzle with the structured nozzle, the nozzle will act as a small furnace with controllable temperature.

In this chapter, a 3D printer featuring a built-in filament feeding system and small nozzle furnace with structured die for extruding structured canes is used to directly extrude a complex fibre structure. Section 5.1 will introduce the table-top FDM 3D printer used to draw fibres and its hardware and controlling software. The MPOF fabrication process will be discussed in section 5.2. Finally, the design and important parameters for the novel table-top fibre drawing setup will be summarised in section 5.3.

5.1 Fibre drawing setup

5.1.1 Hardware design

A 3D printer was used in this work to form a miniaturised version of a fibre drawing tower to directly draw the polymer fibre. As presented in chapter 4, the structured nozzle cross section needs to be complementary to that of the final fibre and have a structure similar to that of a standard 3D printer nozzle. The 3D printer was chosen due to its flexibility in changing the nozzle.

The *Ultimaker 2 extended* is a tabletop FDM 3D printer 0.5m high and 0.3m wide. The printer includes a built-in polymer filament feeding system which is suitable for 2.85 mm diameter filaments. At the printer head, the heater block, which is connected to the nozzle, relies on a heater cartridge (24 V, 35 W) to control the nozzle operation temperature within the 180 – 260 °C range. A photograph and schematic of the *Ultimaker 2 extended* 3D printer is presented in Figure 5.1(a-b),

showing the dimension of the 3D printer, the location of the heater head (Figure 5.1(c)), and the filament feeding system.

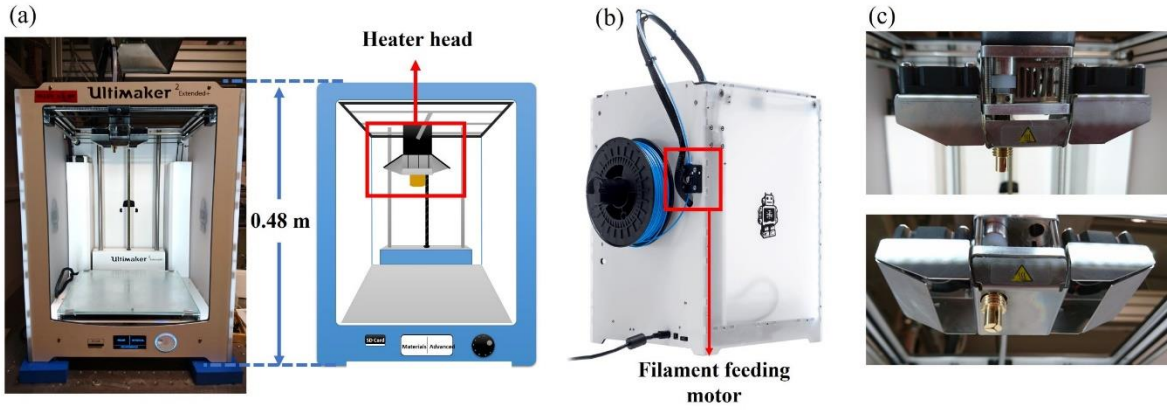

Figure 5.1 (a) Photograph and schematic of the *Ultimaker 2 extended* 3D printer used to create the fibre drawing setup. (b) Back of the *Ultimaker 2 extended* 3D printer showing filament holder and filament feeding system. (c) Heater head of the 3D printer where the nozzle is connected.

To test the correct operation of the printer, a cane was firstly extruded without any additional drawing. Different extrusion parameters (feeding speeds and nozzle temperatures) were used to explore their impact on the quality of the extruded cane. The machined structured nozzle for fabricating SC-MPOF was mounted on the 3D printer head while a commercially available 3D printer filament acrylonitrile butadiene styrene (ABS) was fed through the heated nozzle. The extrusion parameters were varied to explore their effect on the visual quality of the extruded fibre cane and achieve the optimal effective temperature experienced by the polymer optical fibre during drawing.

An initial nozzle temperature of T_n=250 °C was chosen to extruded ABS filament, close to the centre of its recommended printing temperature range of 220 – 270 °C. The filament is driven into the heated nozzle by a stepper motor (filament feeding system), and a feeding speed of s~50 mm/min was used for the first try. Air bubbles and a coarse surface were observed in the extruded cane, possibly caused by the high T_n. These bubbles were attributed to the expansion of air trapped in the filament due to high filament temperature inside the heated nozzle. These bubbles are extremely detrimental as they can result in deformation of the thin layer and structure inside the fibre, and cause the fibre to break during the drawing process. Filament feeding speed also affects the filament effective temperature. By pressing the filament through the heated nozzle at low feeding speed, the fictive temperature of the filament in the nozzle is higher than that when it is forced through the nozzle with higher speed, hence affecting the extruded polymer surface quality. To optimise the feeding speed, the nozzle temperature was fixed at T_n~250 °C, while the feeding speed was increased from s=50 mm/min to 250 mm/min: an extruded fibre cane with smooth surface was successfully

achieved at a feeding speed of 250 mm/min (Figure 5.2). Surface roughness and defect formation in the extruded polymer optical fibre cane are strongly dependent on the fictive temperature.

To observe the effect of temperature on the surface quality of the extruded fibre cane, T_n was varied from 230 – 260 °C. For T_n=250 °C, a smooth and shiny surface was observed, but defects in the inside structure also appeared, which were attributed to the presence of bubbles in the polymer. A matt surface appearance was observed at T_n=230 °C, and was attributed to instabilities in the polymer flow behaviour as result of wall slip. When T_n=240 °C, smooth and shiny surfaces were observed and both surface roughness and bubble formation were significantly reduced compare with others nozzle temperatures. Therefore, T_n= 240 °C and *s*=250 mm/min were selected as they provided the best quality of the extruded fibre cane. A visual comparison between the surface roughness of the extruded canes with feeding speeds of 100 mm/min and 250 mm/min (at the same nozzle temperature of 240 ˚C) is shown in Figure 5.3.

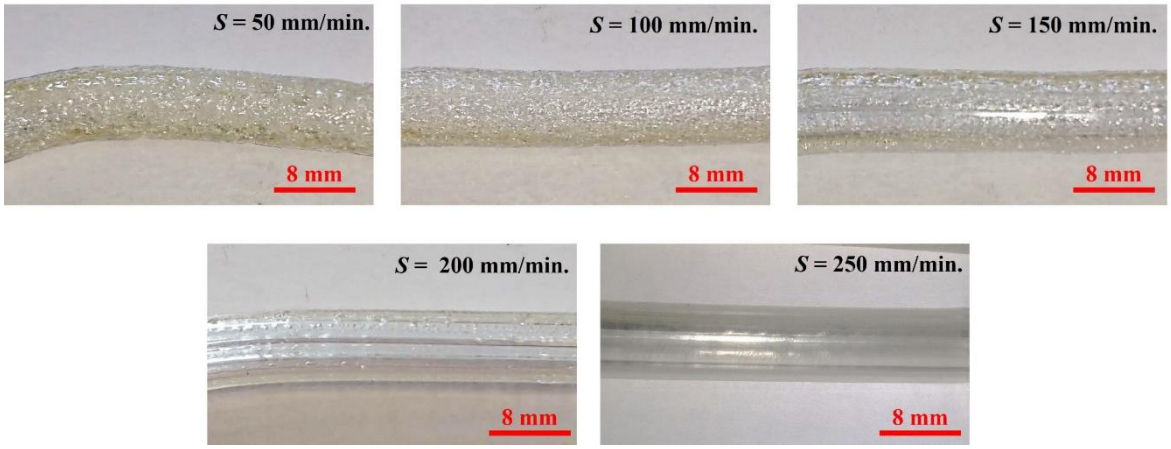

Figure 5.2 Extruded structured cane from the 3D printer with different filament feeding speeds *s* at T_n= 240°C.

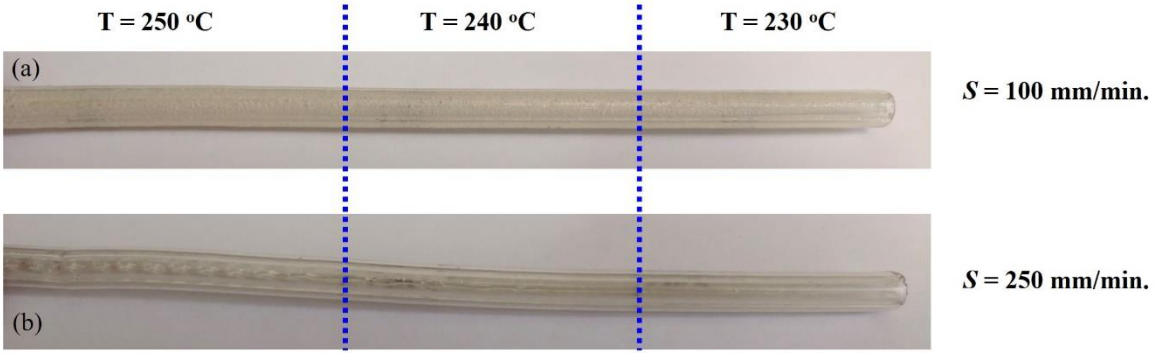

Figure 5.3 Structured cane extruded at (a) *s*= 100 mm/min; and (b) 250 mm/min using the same nozzle die and ABS filament.

It was then assumed that optimal conditions for the drawing process were T_n ~ 240 °C and *s*~ 250 mm/min for the ABS polymer with the brass machined structured nozzle. These two parameters

vary with the material and the features of the structured nozzle. Therefore, they require an optimisation when the structured nozzle or polymer are changed.

Fibre drawing requires reduction of the large-scale structured fibre cane to fibre dimensions. This process is virtually independent of the way structured fibre cane was fabricated. The cane and fibre fabrication stages can therefore be considered as essentially decoupled. In this research, the development of a novel technique to draw the MPOF directly from the 3D printer was invented, with no prior requirement to manufacture a fibre preform.

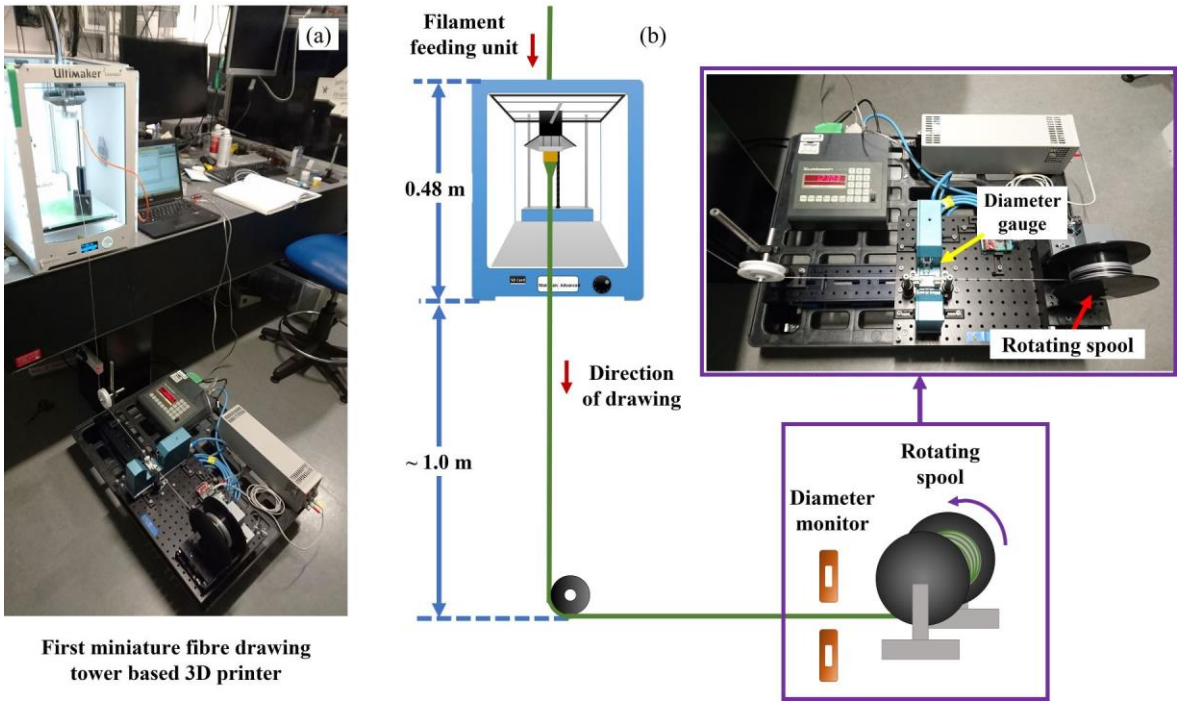

Figure 5.4 (a) Photograph and (b) Schematic of the first miniaturised optical fibre drawing setup used to extrude the microstructured polymer optical fibre from the 3D printer including a fibre pulling system and a diameter gauge.

The traditional MPOF drawing process is essentially the same as that used for conventional fibres. The preform is fed into a furnace at a rate that allows the polymer temperature to raise sufficiently above its glass transition temperature (T_g) and reduces its viscosity to a level such that the polymer can be readily pulled. In this work, the MPOF is pulled directly after the extrusion without any fibre preform fabrication where the structured nozzle acts as a small furnace. The ABS polymer material used in this work is a commercially available filament for the FDM 3D printer. This material was chosen for the initial trials because it can be easily dissolved in solvents and can be removed from the nozzles once the fibre drawing is completed. For the extrusion, the conventional printer nozzle was replaced by the structured nozzle, as shown in Figure 5.1(c). A polymer filament was extruded through the nozzle by using the built-in feeding motor (Figure 5.1(b)) of the printer.

To further reduce the MPOF diameter, the extruded structured polymer fibre was connected to a spool rotated at a constant speed by a stepper motor. The speed of fibre drawing was controlled

by varying the rotation speed of the stepper motor. The first spool used to pull the MPOF was 3D printed by using the same 3D printer and had a wheel diameter of 10 cm. The stepper motor used in this work is a high torque hybrid stepper motor (RS 535-0401) with a step angle of 0.9° (400 steps/round). The stepper motor's shaft was connected to the centre of the 3D printed spool, which rotated synchronously with the stepper motor. The fibre diameter was monitored in real time during drawing by an optical diameter gauge (Zumbach USYS 10). The first miniaturised fibre drawing setup is shown in Figure 5.4.

During the fibre drawing process, only the dimensions of the extruded polymer structure change, while the mass of polymer remains constant over time due to the conservation of mass. Under steady state operating conditions, the relationship between the cane feed rate, cane diameter (D_{cane}), fibre draw speed (v_{draw}), and fibre diameter (d_{fibre}) can be described by eq. (5-1). In this work, the MPOF will be drawn from the polymer cane extruded from the structured nozzle, thus the cane feed rate will be quoted as the polymer extrusion rate ($v_{extrude}$). The fibre diameter can be simply controlled by accurately setting the polymer extrusion rate and fibre drawing rate.

$$\frac{D_{cane}^2}{d_{fibre}^2} = \frac{v_{draw}}{v_{extrude}} \qquad 5\text{-}1$$

To test fibre drawing, the nozzle was heated at T_n ~ 240 °C for 5 mins to ensure the whole structured nozzle reached the set temperature. The polymer filament was driven into the heated nozzle at *s*~ 250 mm/min, resulting in the extrusion speed of $v_{extrude}$~41 mm/min at T_n ~240 °C for the brass machined structured nozzle. The MPOF cane extruded from the heated structured nozzle was initially pulled manually. As shown in Figure 5.4(b), the pulled MPOF was bent around a free-pulley to change the direction of the pulled MPOF from vertical to horizontal. On the horizontal plan, the MPOF passed through a diameter gauge, and was then connected to the rotating spool. The spool rotated at a speed of ~3.75 rpm, leading to a pulling speed of v_{draw} ~ 1178 mm/min: from eq. (5-1), the expected final fibre diameter is ~1.5 mm. The diameter of drawn MPOF was measured over time by using a laser-based system. The relationship between the fibre diameter and drawing time was monitored in real-time by connecting the diameter gauge to a computer with MATLAB© software to visualise the relation between fibre diameter and time.

Figure 5.5(a) presents the relationship between the diameter of the SC-MPOF drawn from the first miniaturised fibre drawing setup (Figure 5.4) and drawing time. Between 0 and 100 s (green area), large fluctuations (±0.7 mm) in the fibre diameter can be observed. In this time frame, the fibre was pulled manually by hand before being connected to the rotating spool, leading to an unstable pulling force and large fluctuations in the fibre diameter. Smaller fluctuations can be observed when the fibre was pulled by using the rotating spool. At drawing times > 100 s, the SC-MPOF was drawn by using a rotating spool with constant drawing speed: these fluctuations (± 200 µm) are still

significantly larger than those observed in conventional polymer optical fibres, generally within the range of ± 9 μm [165]. These fluctuations can be caused by many parameters, such as a variation of tension, and instability of the drawing and extrusion speeds. To minimise the variations in the fibre diameter, the sources of diameter fluctuations need to be investigated.

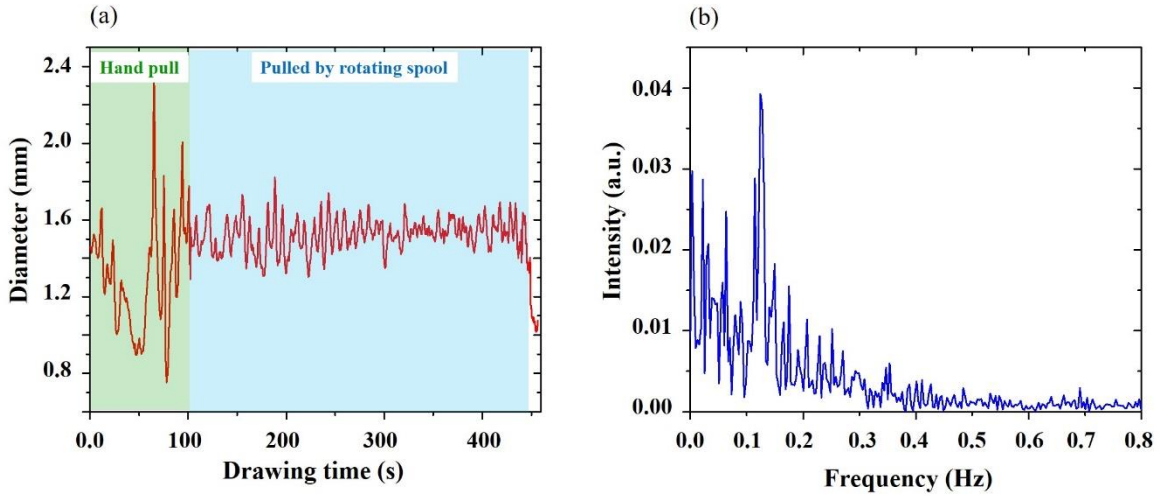

Figure 5.5 (a) Relationship between diameter of drawn MPOF and drawing time. (b) FFT plot of variation intensity against frequency for the fluctuations in the measured MPOF diameter.

The Fast Fourier Transform (FFT) was used to investigate the source of the fibre diameter fluctuations. The FFT was applied to the data in Figure 5.5(a) when the time difference between each data point is ~0.571 s and the total number of points is ~1397. The frequency plot of the FFT is presented in Figure 5.5(b), showing that there are no significant features at higher frequencies (> 0.5 Hz), while there is a clear peak located at ~0.124 Hz. High frequency features can be caused by vibrations of the whole setup and by the stepper motor while low frequency peaks can be related with the spool rotation. The ellipticity in the rotating spool can cause instabilities in the drawing speed, resulting in the variation of the fibre diameter. As the spool was rotated with a speed of ~3.75 rpm during the drawing process, the frequency of spool rotation was calculated to be ~0.063 Hz. It can be noticed that the peak at low frequency found from the FFT result is twice the frequency of rotation of the spool, pointing to a relation between the fluctuations in the diameter of the fibre drawn from the first drawing setup and the rotating spool geometry. To solve this problem, the rotating spool used in the setup was changed, from the home-made 3D printed spool to a commercially-available spool for packing optical fibres.

The uniformity of optical fibre diameter is essential, since any variation in the fibre diameter appreciably affects the mechanical and optical characteristics of the optical fibre. During the drawing process, the fibre diameter exhibits significant variations, owing to various disturbances, if there are no control techniques in place. Apart from the instability of the rotating spool, variation in the tension in the fibre during the drawing process can cause fluctuations of the fibre diameter. A tension

compensation system was added to the drawing setup for controlling the tension of the fibre during the drawing process. A three-wheel system, including two fixed position wheels and one movable wheel, was used to maintain the tension of the drawn fibre. There is a trade-off between draw temperature and draw tension, as changing the drawing temperature affects the drawing tension.

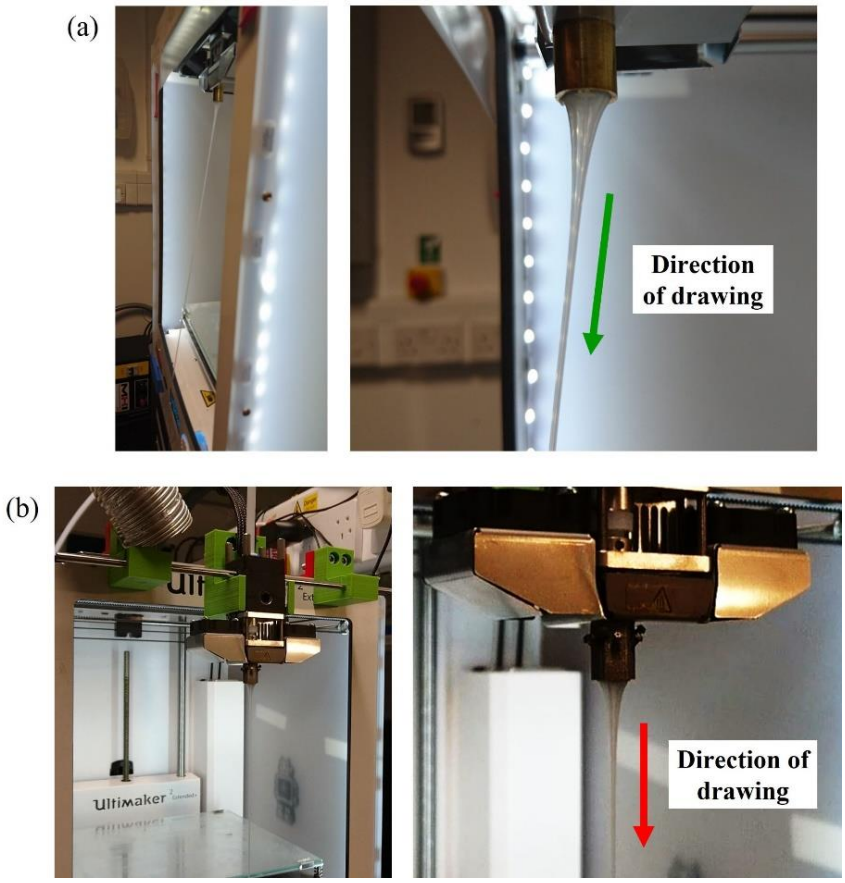

Figure 5.6 MPOF drawn from the structured nozzle when the heater head (a) is located inside the 3D printer, and (b) is moved out.

The mechanical design of the fibre drawing setup was also considered, to reduce the fluctuation of the fibre diameter. In the first design, the heater head is still located inside the 3D printer, leading to an angle between the drawn fibre and the structured nozzle, as presented in Figure 5.6(a). The speed of the drawn polymer from different radial positions within the structured nozzle is different, due to this angle, resulting in a difference in effective temperature experienced by the polymer. Thus, the tension of the drawn fibre at different radial positions will be non-uniform, leading to diameter fluctuation. As the heated polymer is pulled down, a characteristic neck-down region forms, where a rapid change in diameter occurs. The length of the neck-down region is set by a number of parameters, including the dimensions and heating rate of the structured nozzle, the speed at which the polymer is passing through the structured nozzle (feeding speed), and the thermal properties of the polymer. Of particular importance is the temperature dependence of polymer viscosity. The shape of the deformed cane within the neck down region is critically important when

drawing microstructured fibres because of its effect on hole deformation. A key consideration when seeking to minimise deformation of the microstructure during drawing process is the need for a radial temperature profile as uniform as possible. To solve this problem, the heater head was moved out of the 3D printer to avoid misalignments between the drawn fibre and the nozzle during the drawing process (Figure 5.6(b)).

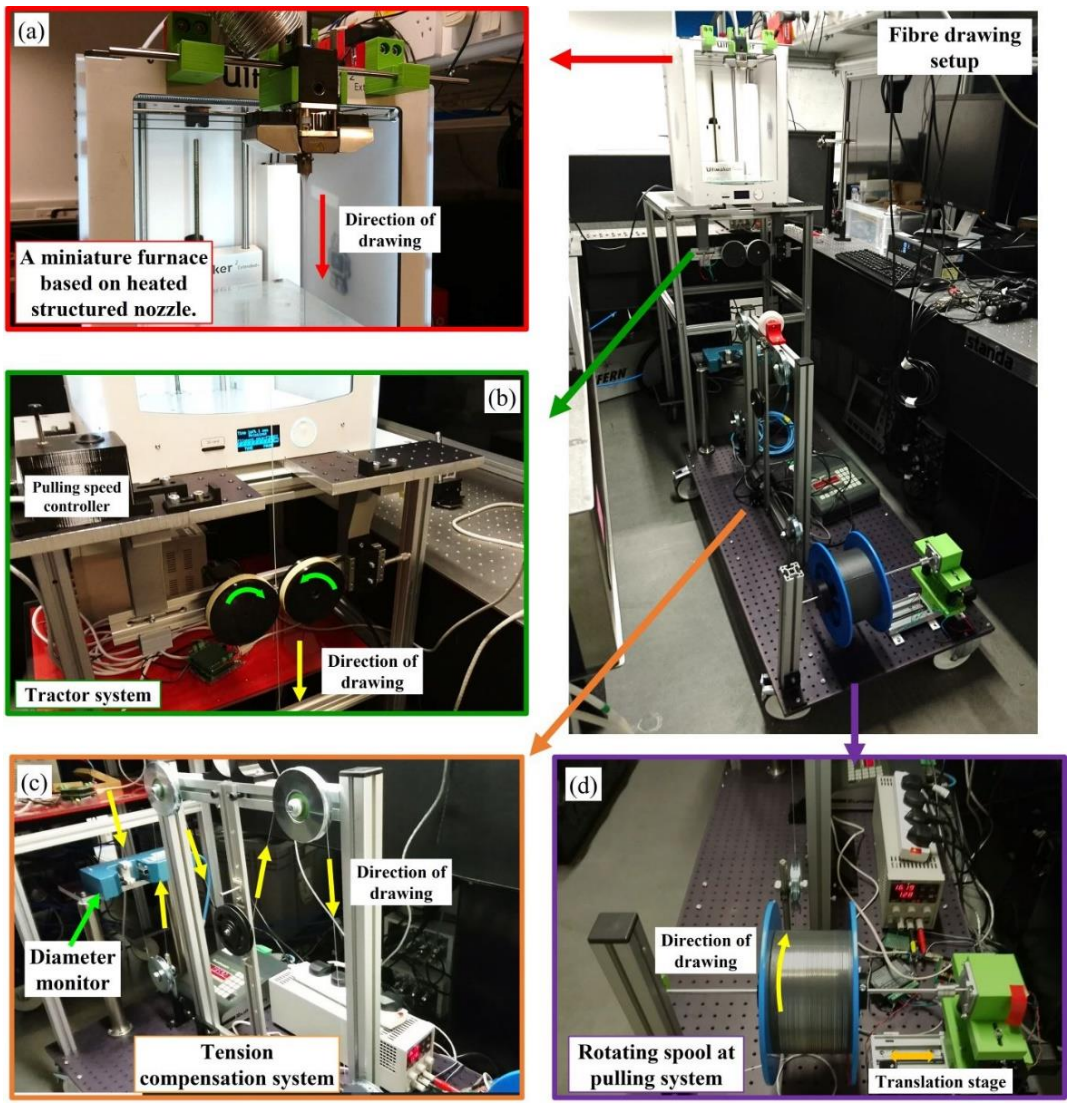

Figure 5.7 Fibre drawing setup. (a) A close-up view of the 3D printer heater head and a structured nozzle. (b) Primary fibre pulling system. (c) Diameter gauge and tension compensation system. (d) Main fibre pulling system including the rotating spool connected to the high torque stepper motor and speed controllable linear translation stage.

A photograph of the fully assembled miniature fibre drawing setup based on the 3D printer is presented in Figure 5.7. As shown in Figure 5.7(a), the structured nozzle is connected to the heater head, which is mounted outside the printer. Fume extraction is applied at the heater head to remove any fumes produced from the heated polymer during the fibre fabrication process. The tractor system is positioned underneath the heater head (Figure 5.7(b)) to draw the extruded polymer. The winding system then includes fixed wheels and one movable wheel with a diameter of 10 cm: the fixed wheel

is connected to the stepper motor (RS-535-0372) to control the drawing speed by changing the speed of rotation, while the movable wheel is connected to a linear translation stage. The gap between each fibre turn can be adjusted by moving the translation stage. The diameter gauge is placed underneath the tractor system to monitor the diameter of the drawn fibre. The tension compensation system is located after the diameter monitor system to maintain fibre tension during the fabrication process (Figure 5.7(c)). The main part of the fibre drawing setup is shown in Figure 5.7(d). The spool with a diameter of 16 cm is connected to a high torque stepper motor (RS-535-0502), which is used to control the fibre drawing speed. The stepper motor is placed on top of the linear translation stage to move the spool with the same moving distance as the fibre diameter. This system is used to align the drawn fibre along the spool. The translation stage is connected to another stepper motor (RS- 535-0372) which is used to provide fine feedback and control the fibre diameter.

5.1.2 Software design

5.1.2.1 3D Printer G-code Commands

In the manufacturing of the fibre drawing setup, the software used to control all the mechanics and electronics in the system is a very important part. The filament feeding speed is controlled by the built-in filament feeding system of the 3D printer. Typically, the position of the nozzle in the XYZ directions and the filament feeding speed can be computer-controlled using a G-code file containing commands in G-code, a language used to describe how a 3D printer should print a 3D model. The file stores instructions in plain text with each line representing a different command such as filament feeding speed, speed of printing, nozzle temperature, time (different between each layer), and nozzle position at each location in the 3D model. G-code files can be created using the slicing program by importing the designed CAD 3D model into the slicing software. Then, the CAD drawing is translated into G-code, which a 3D printer can read. For the printer *Ultimaker 2 extended* used in this work, the Cura© software was used to generate the G-code file.

The G-code is a list of fields separated by white spaces or line breaks. A field can be interpreted as a command, parameter, or for any other special purpose. The code consists of one letter directly followed by a number or can be only a stand-alone letter. The letter will provide information about the meaning of the field. Typically, G-code includes 2 main command types which are G-commands and M-commands. G-commands dictate the nozzle movement, while M-commands control the mechanics and electronics. A list of basic commands in the G-code that are commonly used in this work is presented in Table 5-1.

Table 5-1 Basic commands for printing a 3D CAD model using a Ultimaker 2 extended 3D printer.

Code	Meaning
Gnnn	Standard G-code command such as move to a point
Mnnn	RepRap-defined command, such as turn on a cooling fan
Fnnn	Filament feeding speed (mm/min)
Xnnn	A X coordinate to move heater head
Ynnn	A Y coordinate to move heater head
Znnn	A Z coordinate of build plate
Ennn	Length of filament to be used compared with the initial length
G0	Rapid move
G1	Linear move
G10	Retract filament
G11	Unretract filament
G92	Set initial position
M107	Fan off

Figure 5.8 presents the basic G-code file generated from the Cura software for printing many CAD 3D models using the *Ultimaker 2 extended* 3D printer. The commands list can be separated into 3 main sections. The first section includes parameters related to the specifications of the printer, such as the nozzle size, the required printing time and length of material. This part is only a comment and not a real command for the nozzle. The second section includes a set of primary commands to set up the initial conditions for the heater head and filament feeding system. Code in the primary command typically starts from the initial position setup (G92), and then rapidly moves the nozzle to the starting point of the first printing layer including the filament feeding speed (F4800) and position of the heater head in the X, Y and Z (distance between build plate and heater head) directions. At the end of this set of commands, the filament is fed into the nozzle (G11). The third group of commands includes the printing commands, which starts with the filament feeding speed (F1800) and is then followed by the position of the nozzle at each point in the first layer, and by the length of the extruded filament. Each layer of the printing model is separated by the command for changing layer in which the nozzle is moved rapidly (G0) and there is no filament fed while the heater head is moved to the initial position of the next layer.

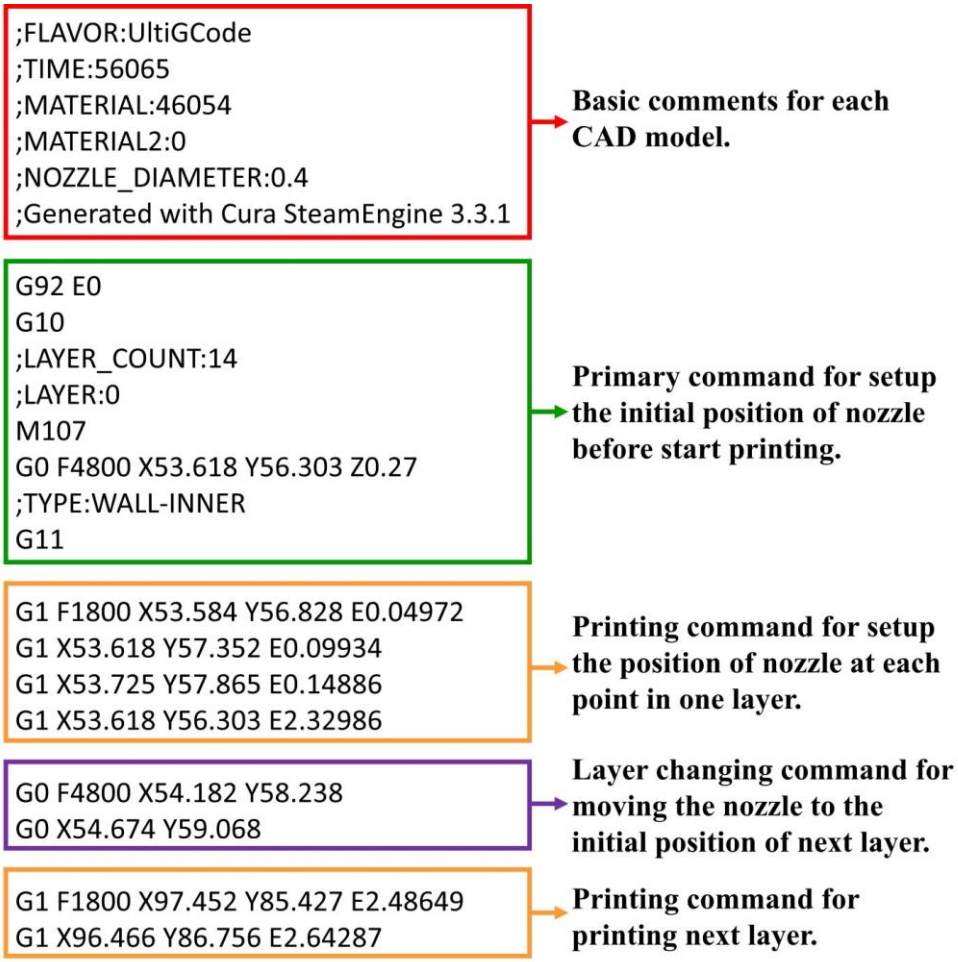

Figure 5.8 List of commands in G-code generated from the Cura® software for printing a 3D model using the *Ultimaker 2 extended* 3D printer.

To extrude the polymer through the heated nozzle, the nozzle position is fixed, as 3D movements are not required. Therefore, the list of commands in the G-code file needed to be modified so that the nozzle position remains fixed while the filament continues moving with the desired feeding speed.

For the modified G-code to extrude the filament, the basic comments have been removed as they are not necessary. The code starts with the primary command to set up the position of the nozzle before starting extrusion. The heater head position is set to the centre front of the printer (x = 111.5 mm, y = 20 mm). As the build plate will not be used for extrusion, the distance between build plate and heater head is fixed to z = 280 mm, so that the build plate is set to the lowest position within the printer. Then, the extrusion commands start with the feeding speed set up as presented in Figure 5.9. The filament feeding speed is set to 250 mm/min (F250) when the position of the heater head is fixed. In the first line of extrusion commands, the initial length of filament extruded is set to 0.0 mm. The desired filament length will be set in the second line of commands. As shown in Figure 5.9, the filament length is 6000 mm. This value is the printer limit in one command line. To extrude the filament with longer lengths, extra lengths of filament can be set in the next line (E12000). Extrusion

will finish when the filament has been fed into the nozzle with the length set at the final line in the command. The commands G10 and M107 signal the end of extrusion and retract the filament and turn off the cooling fan, respectively. In the final setup to fabricate the MPOF from the 3D printer, the heater head was moved out of the 3D printer. Thus, the position of heater head (x and y) can be set arbitrarily.

Figure 5.9 The commands in G-code to extrude the filament during the fibre fabrication process.

5.1.2.2. Microcontroller and controlling software (Arduino)

All the stepper motors' driving systems are controlled by an Arduino board. The Arduino board uses a variety of microprocessors and microcontrollers. The boards are equipped with sets of digital and analogue input/output pins that can communicate with various expansion boards (shields) or breadboards and other circuits. The boards feature serial communications interfaces, including USB on some models, which are also used for loading programs from computers. There are a number of commercial software packages that can be used to implement the process monitoring. In this work, MATLAB© was used as a user-interface for controlling and monitoring the translation speed of the spool, spool rotation speed, and drawn MPOF diameter. The controlling interface for adjusting and monitoring the motor speed which controls the rotation of the spool and its movement is presented in Figure 5.10(a). In this control interface, the direction of rotation, acceleration, and deceleration of the motor can be set before starting the motor rotation, while the speed of rotation can be adjusted at any time, even while the motor is operational. The control interface for monitoring the diameter, rotation speed, and translation speed is shown in Figure 5.10(b). These parameters can be monitored in real time during the fibre fabrication process.

The most commonly-used option to maintain constant MPOF diameter while drawing is to use a feedback controller that adjusts pulling speed on the basis of the deviation between the measured and set-point diameter values. So far, the feedback system was not implemented in this fibre drawing system, as it needs precise linear drawing speed of the spool at different spool diameters (when long lengths of fibre are wrapped around the spool, the spool effective diameter increases, as the newly

wound fibre is layered over the previously wound fibre). The control system for this prototype has been manually operated to change the speed and achieve the desired diameter during the fibre fabrication process. The proportional–integral–derivative (PID) feedback controller will be added as an upcoming improvement.

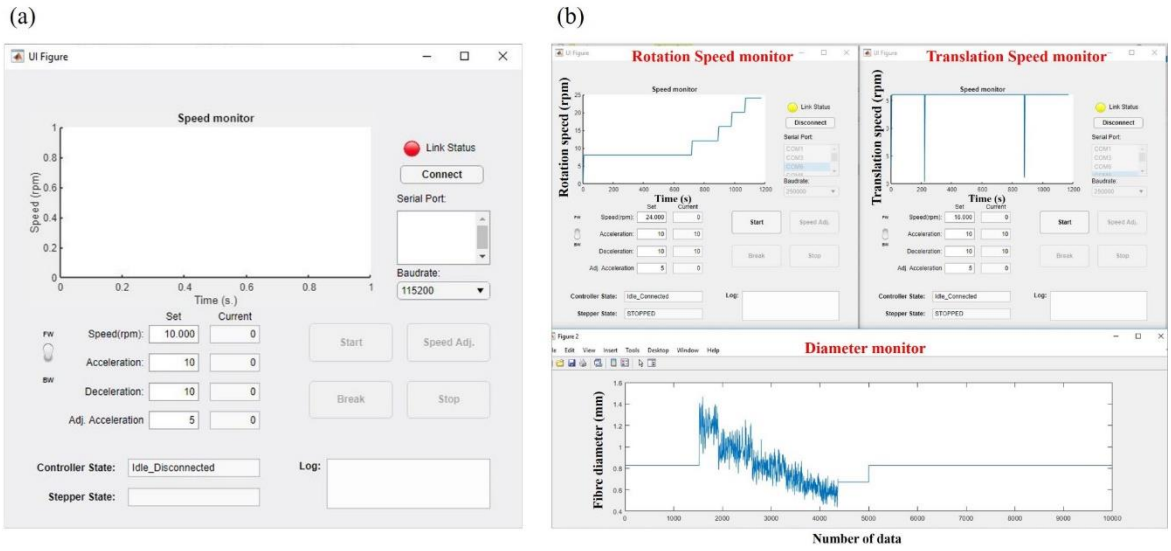

Figure 5.10 (a) Interface for adjusting and monitoring the speed of the stepper motor for rotating and moving the pulling spool. (b) Interface for real time monitoring of diameter and speed during the drawing process.

5.2 MPOF fabrication

The MPOF was fabricated by feeding the filament at a speed in the range of *s*~150 - 300 mm/min. The filament feeding speed is chosen depending on the type of polymer and required drawing temperature of the polymer.

To further reduce the MPOF diameter, the extruded structured cane was pulled manually and connected to the spool of the primary pulling system, the speed of which was adjusted until the fibre diameter was approximately d_{fibre} ~ 2 mm. The fibre drawn by using the primary pulling setup was cleaved with a razor blade, to check the fibre cross-section before inserting the fibre into the tension compensation system as presented in Figure 5.11(a). Then, the fibre was connected to the rotating spool, which acted as the main fibre drawing system. When the fibre was connected properly to the main fibre drawing system, the primary pulling system was then removed and the motor for controlling the linear translation stage was turned on to move the rotating spool. The speed of the motor was adjusted to avoid overlap between the incoming fibre and fibre already wrapped around the spool. After one full layer of fibre had been wrapped around the spool, the translation stage was moved in the opposite direction.

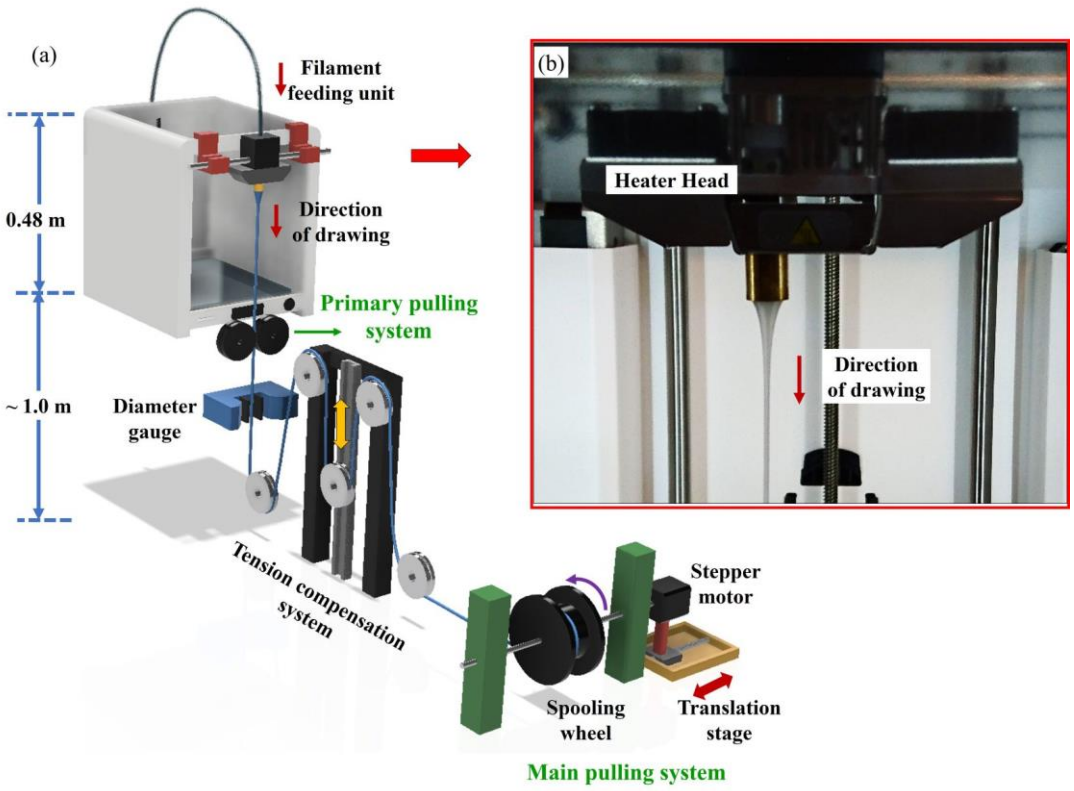

Figure 5.11 (a) Schematic of the drawing setup used to extrude the suspended-core microstructured polymer optical fibre. (b) Close-up view of the 3D printer heater head and the neck-down region of the drawn MPOF.

When an object moves along a circle of radius (r), a travelling distance (l) over a period of time (t) is presented in Figure 5.12(a): the linear speed of the object can be defined as eq.(5-2). After a full rotation (Figure 5.12(b)), the travelling distance corresponds to the circumference of the circle and the corresponding linear speed is given by eq. (5-3).

$$v = \frac{l}{t} \quad 5\text{-}2$$

$$v = \frac{2\pi r}{t} \quad 5\text{-}3$$

$$v_{draw} = \frac{2\pi r_{spool}}{t} \quad 5\text{-}4$$

$$v_{draw} = \frac{2\pi(r_{spool}+(m\times d_{fibre}))}{t} \quad 5\text{-}5$$

As the fibre is drawn by using the rotating spool with radius r_{spool}, the fibre drawing speed (v_{draw}) for the first layer of fibre can be expressed as eq. (5-4). When the first layer of fibre is wrapped around the spool, the effective radius experienced by the newly deposited fibre is increased by the diameter of the fibre, as shown in Figure 5.12(d). Therefore, the linear speed of fibre drawing will be increased with the number of fibre layers (m) wrapped around the rotating spool as shown in eq.(5-5). To maintain the fibre diameter, the fibre drawing speed should be constant, so the speed of

spool rotation must be reduced to maintain the drawing speed constant each time a new fibre layer begins to wrap around the spool.

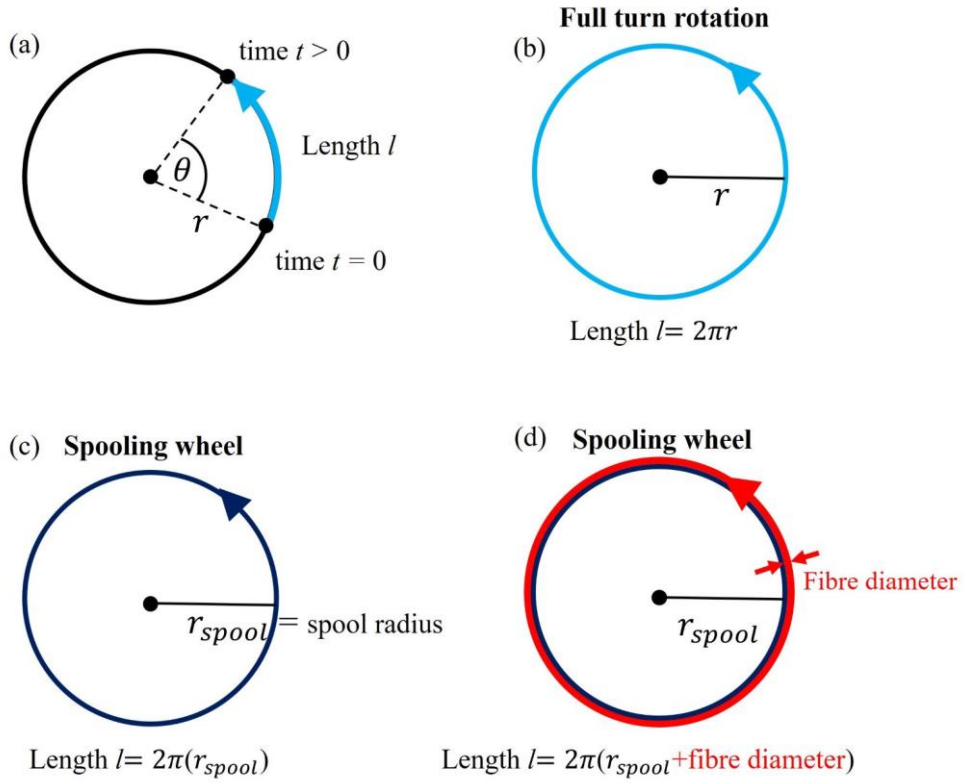

Figure 5.12 Length of fibre (l) deposited (a) after a rotation θ of the spool; and (b) after the full rotation. (c) Length of the first layer of fibre wrapped around the spool. (d) Length of the second layer of fibre wrapped around the spool.

Figure 5.13 shows the fibre diameter versus the drawing time of the hollow-core MPOF fabricated using the drawing setup including the tension compensation system. The hollow-core MPOF was fabricated from a PETG filament with feeding speed of 250 mm/min and nozzle temperature of 270 °C. Figure 5.13(a) shows the change in the fibre diameter when the fibre drawing speed is continuously increased from 1000 to 3500 cm/min. The result shows that the developed control software can be used to vary the fibre diameter during the fibre drawing process. The cross section of the fibre drawn at a speed of 3000 cm/min is shown in Figure 5.13(b), and presents a diameter of d_{fibre}~380 µm with a well preserved microstructure (Figure 5.13(c)). Significant improvement in diameter control by using the commercial spool together with the tension compensation system can be observed. Fluctuations in the fibre diameter are ~ ±50 µm, 4 times smaller than those observed (± 200 µm) in the first design of the drawing set-up. This result shows that the improvement in the fibre drawing setup by adding the tension compensation system, the primary pulling system, and also a good alignment between the heater head and the rotating spool, can significantly reduce the fluctuations in fibre diameter.

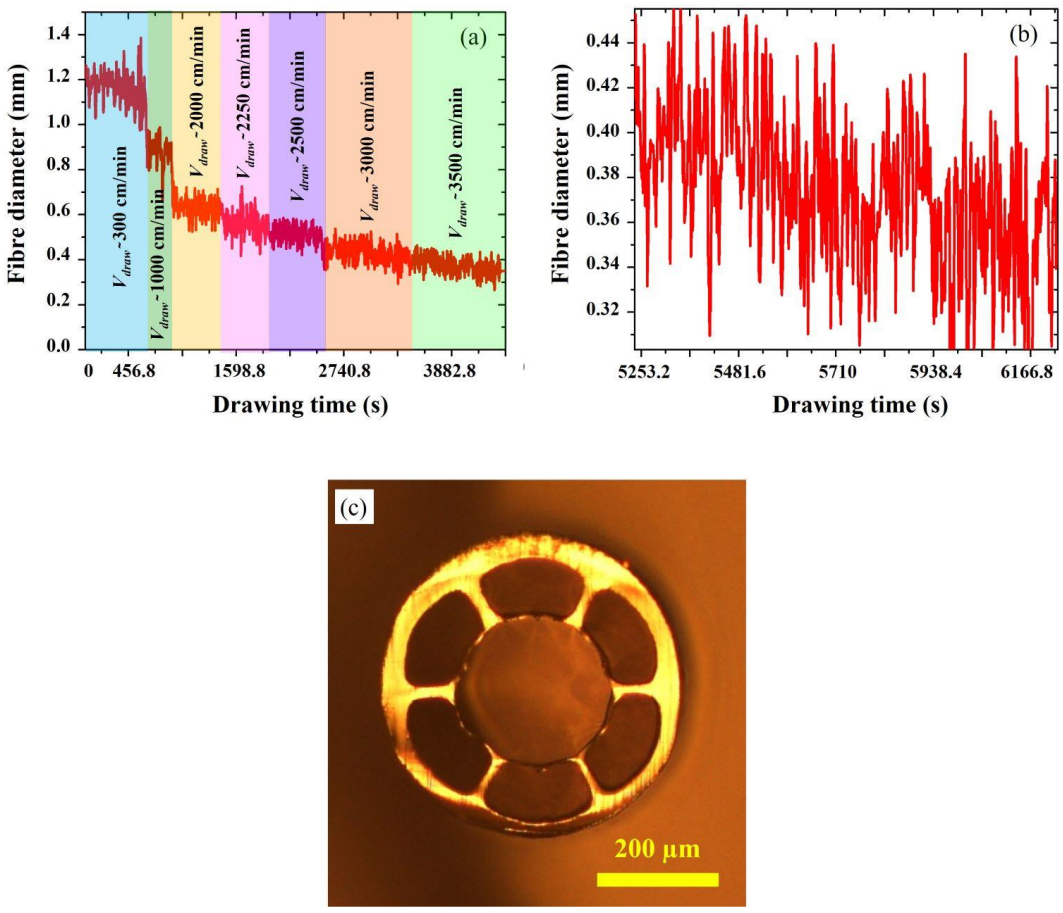

Figure 5.13 (a) Fibre diameter monitored when the drawing speed was varied from 300 to 3500 cm/min. (b) Fibre diameter at a drawing speed of 3000 cm/min. (c) Microscope image of the hollow-core MPOF cross section when the fibre was drawn at a speed of 3000 cm/min, a nozzle temperature of 270 °C and filament feeding speed of 250 mm/min.

More details on the optimisation of the filament feeding speed and drawing temperature for different types of polymer, fibre structure, and types of nozzles will be presented in chapters 6 and 7.

5.3 Summary

In conclusion, the direct drawing of microstructured polymer optical fibres using a cheap desktop 3D printer has been demonstrated. A drawing set-up has been built utilizing a 3D printer heater as the furnace, a diameter gauge and customised pullers driven by rotary motors. A software was developed to control the heater head and various motors using Arduino and G-code. Analysis of the fibre produced during this work proves the ability to maintain the microstructure inside the fibre after drawing from a customised 3D printer head.

By using the optimised and clear structured nozzles together with the completed fibre drawing system, the MPOF with the length over 20 km can be fabricated from spool (1 kg) of polymer filament while the structures are maintained.

Chapter 6.

SUSPENDED-CORE MICROSTRUCTURED POLYMER OPTICAL FIBRE

Suspended-core microstructured optical fibres (SC-MOFs), first introduced in 2001 [46], are MOFs where a solid core is suspended in air within and protected by a solid outer cladding, to which it is connected by thin membranes. For sub-micron core dimensions, the core acts as a suspended nanowire. Such structures offer the robust practical handling characteristics of optical fibre while retaining the optical characteristics of nanowires. Due to the enhanced overlap of the evanescent field of the core mode with gases or liquids which can flow into the surrounding cavities, the SC-MOF is particularly attractive for applications in sensing [166-168]. Using this approach, it is possible to fabricate long lengths of fibres with sub-micron core dimensions that can be used as the basis for robust sensing devices and nonlinear media. Therefore, this type of fibre has been widely developed and studied extensively both for sensing and nonlinear applications.

In this chapter, the design and fabrication of suspended-core microstructured polymer optical fibres (SC-MPOFs) for near-IR and THz guidance will be presented. The results of extruded segmented core MPOFs from a 3D printer and near-IR guiding characterisation will be shown in Section 6.1. Section 6.2 will present the characterisation of suspended-core fibre in the THz regime. Finally, the results of fabrication and characterisation of suspended-core fibre from the 3D printer will be summarised in Section 6.3.

6.1 Near-Infrared Suspended-core microstructured polymer optical fibre

6.1.1 Near-IR SC-MPOF fabrication

To fabricate the SC-MPOF operating in the near-IR, the machined nozzle was mounted on the printing head and a commercially available 3D printer filament (acrylonitrile butadiene styrene (ABS)) was fed through it. The quality of the extruded polymer was tested by extruding a fibre cane without any additional drawing. Different extrusion parameters (feeding speed and nozzle temperature) were used to explore their impact on the quality of the cane and determine the optimal effective temperature experienced by the polymer during drawing. Good conditions for the drawing process were: a nozzle temperature of 240 °C and a filament feeding speed of 250 mm/min. Indeed, the fibre was drawn using the experimental setup in Figure 6.1 with these parameters.

The SC-MPOF was directly drawn from the 3D printer structured nozzle at Ω ~20 rpm (6.28 m/min). The final diameter was d_{fibre}~800 µm. To observe the fibre cross-section, the SC-MPOF was cleaved by using a razor blade, and optical microscope images of different cross-sections showed

that the microstructure inside the fibre was maintained after drawing (Figure 6.2(a-b)). The surface roughness of the extruded cane was reduced by fibre drawing. Note the slightly elliptical shape of the fibre cross-sections in Figure 6.2(a) and (b) is caused by fibre cleaving.

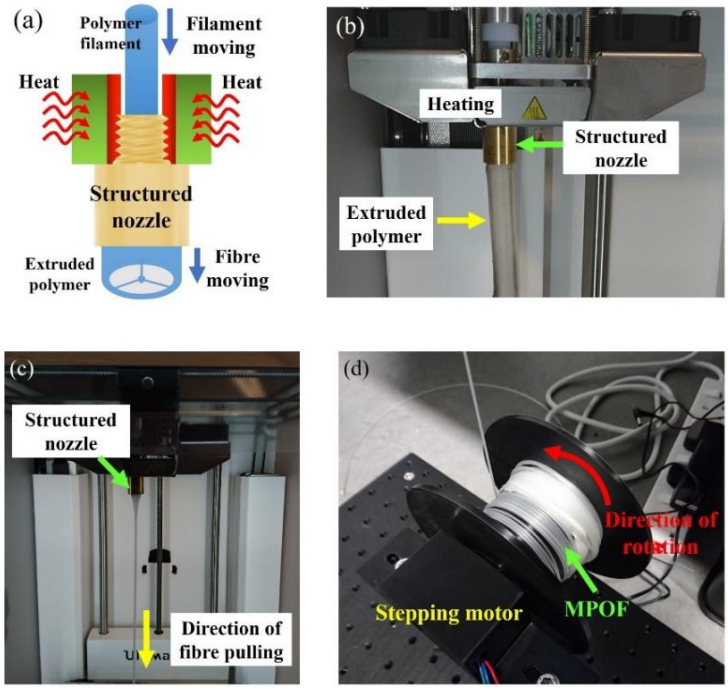

Figure 6.1 (a) Schematic and (b) photograph of the experimental setup used to extrude SC-MPOF. (c) Fibre drawn from the heated structured nozzle. (d) SC-MPOF wrapped onto the 3D printed spool connected to the stepper motor.

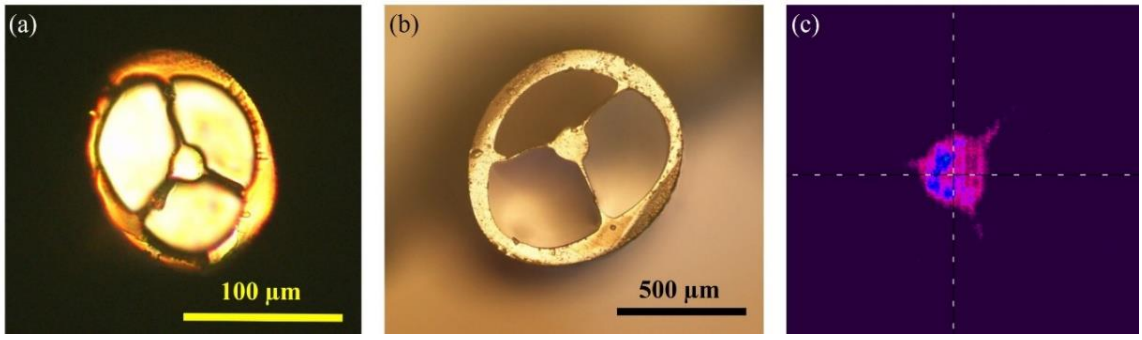

Figure 6.2 Microscope images of the fibre cross-section at different diameters. (c) Near field image (λ = 1550 nm) at the fibre output for a full turn winding (bend radius R~12.5 mm).

6.1.2 SC-MPOF characterisation in near-IR

In order to evaluate the SC-MPOF optical guidance properties in the near-IR, the near-field image of the transmitted light at λ=1550 nm from the fibre facet was recorded. A fiberized laser source (Thorlabs, SFL1550S) was launched into a 20 cm long section of the MPOF using a bare-fibre adapter. The output intensity profile was taken by collecting the output of the fibre shown in Figure 6.2(b) into a near-IR camera (Electrophysics, 7290A) using an objective lens with a 20 mm focal length.

The near field image of the fibre output was captured at different bending radii and confirmed guiding in the fibre core (Figure 6.2(c)). This not only corroborates that the fibre successfully guides light in the core, but also demonstrates that no scattered light is guided in the cladding. In this experiment, 5 m of SC-MPOF were fabricated, but the fibre structure collapsed after 50 cm. This collapse depends on the drawing parameters such as drawing speed, temperature, and air pressure inside the fibre cavities as presented in chapter 4. Due to the fibre structure deformation, 20 cm of MPOF were used to characterise the propagation loss.

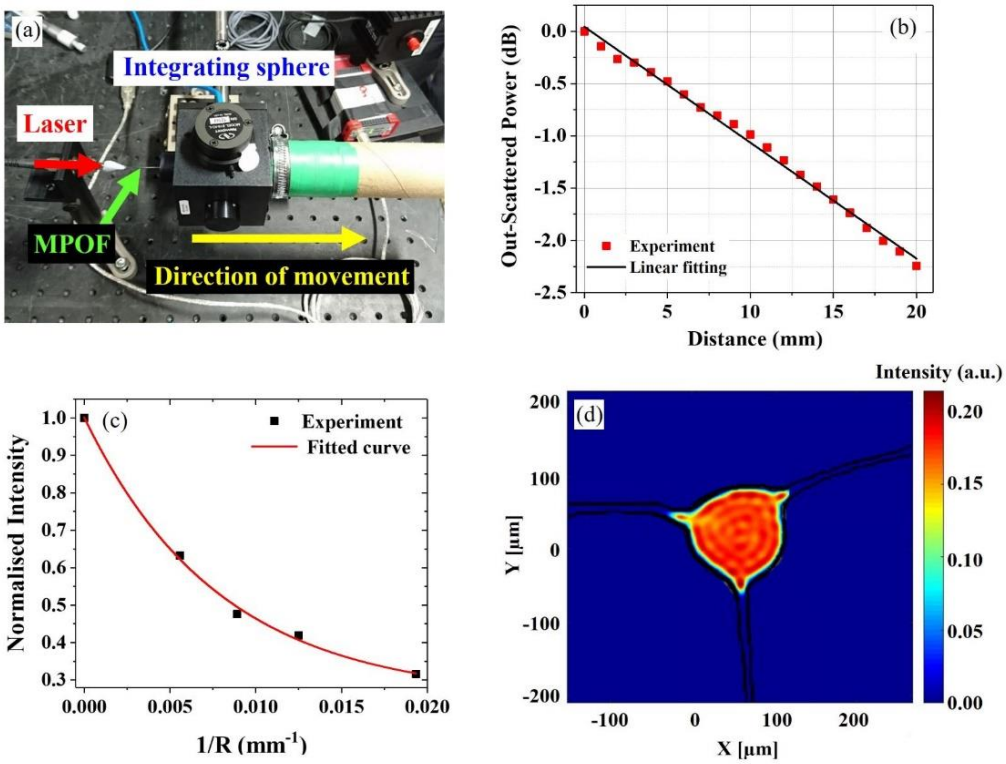

Figure 6.3 (a) Experimental setup used to measure propagation loss, (b) Relationship between OSSR scattered power at λ = 1557 nm and distance, (c) Normalized transmitted intensity at different bend radii (R) at λ= 1550 nm. (d) Simulated intensity profile of the mode supported by fibre core at λ = 1550 nm.

An optical side scattering radiometry (OSSR) technique [3, 169, 170] was used to measure the fibre attenuation by using an integrating sphere (Newport 819D-SL-2). In this setup, light from a fiberized laser source at λ = 1557 nm was launched into the MPOF. Then, the optical fibre was inserted into the integrating sphere and the scattered light coming out from the fibre side was collected by the sphere on a detector as shown in Figure 6.3(a). The scattered light at different sections of the fibre was measured by scanning the integrating sphere along the fibre in 1 mm steps over a length of 2.0 cm, and confirmed a propagation loss of 1.1 dB/cm at λ = 1557 nm (Figure 6.3(b)). Attenuation was measured higher close to the input of the fibre and included spurious values of radiation and higher order modes that were still guided over this transition region. Therefore, lower attenuation is expected at longer fibre lengths. Also, the surface roughness of a fibre core can

contribute to propagation loss. This can be improved by smoothing the inner surface of the nozzle die and by reducing the structural deformations associated with fibre drawing.

Bend loss measurements were performed with different bend radii of 51.7, 80.0, 112.1 and 179.4 mm. As before, light from the fiberized laser source was coupled into a section of the fibre and the intensity at the output was measured using a power meter at different bend radii. From the experimental results presented in Figure 6.3(c), the bend loss at λ = 1550 nm for R~ 51.7 mm was estimated to be 20 dB/m.

Simulations of the mode propagating through the extruded and drawn SC-MPOFs were performed by importing the microscope image cross-section (Figure 6.2(b)) of the fibre used for loss measurements into a commercial finite element method software (Lumerical©). Figure 6.3(d) shows the intensity distribution of a linear superposition of equally weighted supported modes at λ ~ 1550 nm. This result is consistent with the experimental result of Figure 6.2(c), where light is mostly confined in the fibre core and there is a small overlap with the three struts. The different intensity distribution between experiments and simulations is attributed to mode mismatch between the light source and fibre, which resulted in an unpredictable power distribution between the various modes guided in the core. Bending could also affect the weighting and number of propagating modes. Indeed, the fibre is heavily multimoded (more than 70 modes) at λ =1550 nm, due to the large fibre core, and the leaking into the three struts around the core, observed in both experimental and simulated result, can be attributed to higher order modes. Single mode operation can be achieved in a fibre with a smaller core size, which could be manufactured by pressurizing the air holes around the fibre core and optimizing the drawing speed to reach a regime driven by viscosity and not surface tension. The drawing parameters and optical properties of near-IR SC-MPOF directly drawn from a 3D printer are presented in Table 6-1.

Table **6-1** Summary of the SC-MPOF drawing parameters, fibre geometry and optical properties

Parameter		**Value**	**Units**
Material and drawing parameters	Material	ABS	-
	Feeding speed	250	mm/min
	Temperature	240	^{o}C
	Drawing speed	20	rpm
Geometry	Core diameter	133	µm
	Fibre diameter	800	µm
Optical properties	Bending loss (λ = 1550 nm; R= 51.7 mm)	20	dB/m
	Attenuation (λ = 1557 nm)	1.1	dB/cm

6.2 THz Suspended-core microstructured polymer optical fibre

Terahertz (THz) is electromagnetic radiation with frequency $\nu \sim 0.1\text{-}10$ THz (corresponding to the free-space wavelength range from $\lambda \sim 3$ mm down to 30 μm), which lies in the gap between the microwave and infrared regions. THz waves have attracted a significant interest in the last decade owing to their unique characteristic ability to penetrate most dielectric materials. THz waves provide better resolution in imaging because the wavelengths are shorter compared to microwave and millimeter waves [25, 171-174]. Thus, imaging, and non-destructive testing are amongst the most promising THz applications. THz waves can also interact with organic tissue without causing any damage, because of the non-ionizing nature. Therefore, THz waves can be also be applied for nondestructive medical or biomedical sensing and endoscopy [175-180]. Most importantly, THz waves can also be used in wireless communications to increase data transmission, due to the large bandwidth of the THz band [181]. Traditionally, in astronomy and meteorological satellites [182] there is an interest in THz waves for imaging and spectroscopy [183, 184].

Despite THz waves being shown to be beneficial for many applications, most THz systems are based on free-space optics which are complex, delicate, and require frequent alignment. Terahertz waveguides and optical fibres have been developed to allow THz waves to be delivered to remote locations in environments that may be hazardous, to reduce the complexity in optical alignment and for efficient coupling between emitters and detectors. Many applications of THz waveguides have been demonstrated for applications such as imaging [185], microscopy [28], and terahertz quantum-cascade lasers [186]. Moreover, THz waveguides could also be used for detection of chemical reactions [187], and for medical endoscopy of internal organs by utilizing flexible waveguides [188]. Over the past decade, a large amount of research in THz waveguide design and fabrication has focused on achieving low-loss and low-dispersion THz waveguides and THz optical fibres.

Several polymer optical fibres were exploited as THz waveguides because of their low cost and accessibility of materials [189, 190]. However, THz waves are strongly absorbed by most polymeric and vitreous materials leading to high loss. A challenge in the design of a polymer optical fibre for THz guiding lies in the high material absorption for these frequencies. The first low loss THz polymer waveguide was proposed in 2000 by using thick high-density polyethylene (HDPE) [191]. In 2002, HDPE was used to fabricate a THz-guiding microstructured polymer optical fibre, which exhibited a guiding in THz range of 1 – 3 THz over a 2 cm long sample [23]. Polytetrafluoroethylene (PTFE or Teflon) is one of the polymers that has low absorption loss in the THz range. In 2004, a PTFE THz fibre with the loss 0.3 dB/cm over a 10 cm length was demonstrated [24]. Although HDPE and PTFE have a low material absorption coefficient (0.3 cm^{-1}) in the THz range compared with conventional polymers used for optical fibres, low loss operation is located

only at ~1 THz. For this reason, extensive research has been carried out to identify polymers with lower loss over a wide range of frequencies in the THz regime.

Thermoplastic cyclic olefin copolymer (COC, also called TOPAS) has quickly become one of the choice polymers to fabricate THz optical fibre due to its low material attenuation in the THz. TOPAS optical fibres with hexagonal hole arrays and lengths of 9 cm were demonstrated in 2009 [192], and exhibited a loss smaller than 0.1 dB/cm at the frequency of 0.6 THz. In 2013, a hollow-core terahertz photonic crystal fibre made of TOPAS was designed and fabricated with a propagation loss of 0.75 dB/m at 0.6 THz [193]. More designs of TOPAS THz fibres were proposed in 2017 including the THz suspended porous microstructured fibre for 2.5 THz wave guiding and the hybrid core porous THz fibre [194, 195].

6.2.1 THz SC-MPOF fabrication

In this work, TOPAS was the material of choice because of its low absorption coefficient in THz, about 100 times lower than that of commercially available filaments, such as acrylonitrile butadiene styrene (ABS) [189]. The TOPAS (8007S-04) filament was produced by the Institute for Material Science and Plastics Processing, University of Applied Sciences Eastern Switzerland, Rapperswil, 8640, Switzerland, where a filament was extruded and drawn to the desired diameter of 2.85 mm. TOPAS 8007S-04 has a glass transition temperature (T_g) and a melting point (T_m) of 70-185°C and 190-250°C, respectively. During the process, the nozzle temperature (T_n) was varied from 230 to 260°C, and at T_n = 240°C the surface of the polymer became smooth and shiny, with significantly reduced bubble formation compared to other nozzle temperatures. Initially, the filament feeding speed of s ~ 50 mm/min was selected, resulting in air bubbles and rough surface due to excessively high fictive temperature. The extrusion velocity was then gradually increased and an extruded fibre blank with a smooth surface was successfully achieved at s = 180 mm / min and T_n = 240 °C.

The SC-MPOF was fabricated by feeding the filament using a built-in feeding motor operating at s=180 mm/min, corresponding to an extrusion speed of 0.84 mm/s. To further reduce the SC-MPOF diameter, the extruded cane was connected to a spool (10 cm diameter) which was rotated at a constant speed by a stepper motor as shown in Figure 6.1(d): the spool was rotated at 4 rpm, resulting in a fibre drawing speed of 21 mm/s. The size of the extruded cane was 8 mm, while the final fibre diameter was d_{fibre}~1600 µm.

To observe its cross-section, the SC-MPOF was cleaved using a heated razor blade. Figure 6.4 (a) and (b) show the bottom views of the structured nozzle and of the drawn SC-MPOF, respectively. By comparing the microscope images, it is possible to see that the microstructure inside the fibre was maintained after drawing. The core is optically isolated from the outer polymer region by three fine supporting struts. The tension between the core and outer polymer region through the three

supporting struts deforms the circular core into a triangular core. The SC-MPOF outer cladding, core diameter, strut length and thickness were measured from cross-sectional microscope images imported into ImageJ software. For the SC-MPOF triangular core profile, the measured core diameter is defined as the diameter of the largest circle that can be inscribed in the core region (Figure 6.4(c)). The fibre with total diameter d_{fibre} ~1600 µm had a core diameter of d_{core}~300 µm, and the struts were 500 µm long and 25 µm thick. A large strut length to core diameter ratio is needed to prevent light in the core from leaking into the cladding. The surface roughness observed in the extruded cane was further reduced by fibre drawing and most of the bubbles inside the fibre cane disappeared as the gas was released into the surroundings. The improvement in surface roughness of the drawn polymer optical fibre compared with the extruded cane is a result of realignment of the polymer chains during fibre drawing. The contact between the soft polymer and the nozzle inner surface is believed to be the source of the large surface roughness observed on the outer cladding of the extruded cane, and polymer reflow during fibre drawing mitigates this effect, reducing corrugations on the surface and minimizing bubbles trapped in the polymer. The crack observed in the outer cladding of the fibre cross-section (Figure 6.4(b)) was attributed to the fibre cleaving. These cracks are 1 mm in length and occur only at the fibre tip. The cracks do not affect the main SC-MPOF structure and the fibre microstructure is preserved along the fibre length.

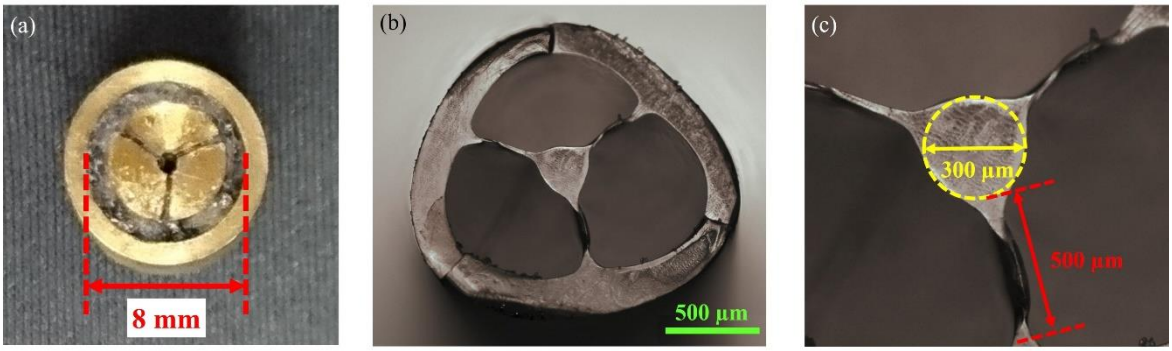

Figure 6.4 (a) Bottom view of the structured nozzle used to fabricate the SC-MPOF. (b) Cross-section of the TOPAS SC-MPOF with outer diameter d_{fibre}~1600 µm. (c) Close-up view of the fibre core showing a 300 µm core diameter and 500 µm long strut.

6.2.2 SC-MPOF characterisation in THz

At these dimensions, the fibre is expected to operate under single mode guidance in the frequency range ν~0.5 – 1.0 THz. To confirm this, finite element simulations (using the commercial FEM solver Lumerical© Mode Solution) were performed by importing the cross-section image of the fibre into the software. Lumerical has been chosen for this simulation as it can be used to scan over the interested frequency with 2 time faster in simulation time than other FEM solver software such as Comsol. The mode analysis (Figure 6.5(a-b)) reveals that the field is confined in the central solid core and guided by total internal reflection as illustrated by the output profiles at 0.6 THz and 1.0 THz. As expected, field confinement becomes stronger as the frequency increases such that for

ν =1.0 THz the vast majority of the power propagates within the solid core. Figure 6.5(c) and (d) reveal the simulated effective refractive index (n_{eff}) and confinement loss of the fundamental mode guided in the fibre core when ν was scanned from 0.55 to 1.5 THz. Due to the larger mode field diameter at larger wavelengths, n_{eff} decreases for decreasing frequencies. The gradual decrease of n_{eff} over ν=1.5 to 0.8 THz shows that the fundamental mode is mostly confined within the solid core. From ν~0.8 to 0.55 THz, the mode expands more into the air holes surrounding the core resulting in a more pronounced decrease of n_{eff}. The effect of mode field expansion from ν=0.8 to 0.55 THz is even more evident in Figure 6.5(d), where the confinement loss of the fundamental mode increases dramatically. Simulations also show that the core does not support any other guiding mode at ν < 0.5 THz due to the large ratio between the wavelength (600 μm) and core diameter (300 μm).

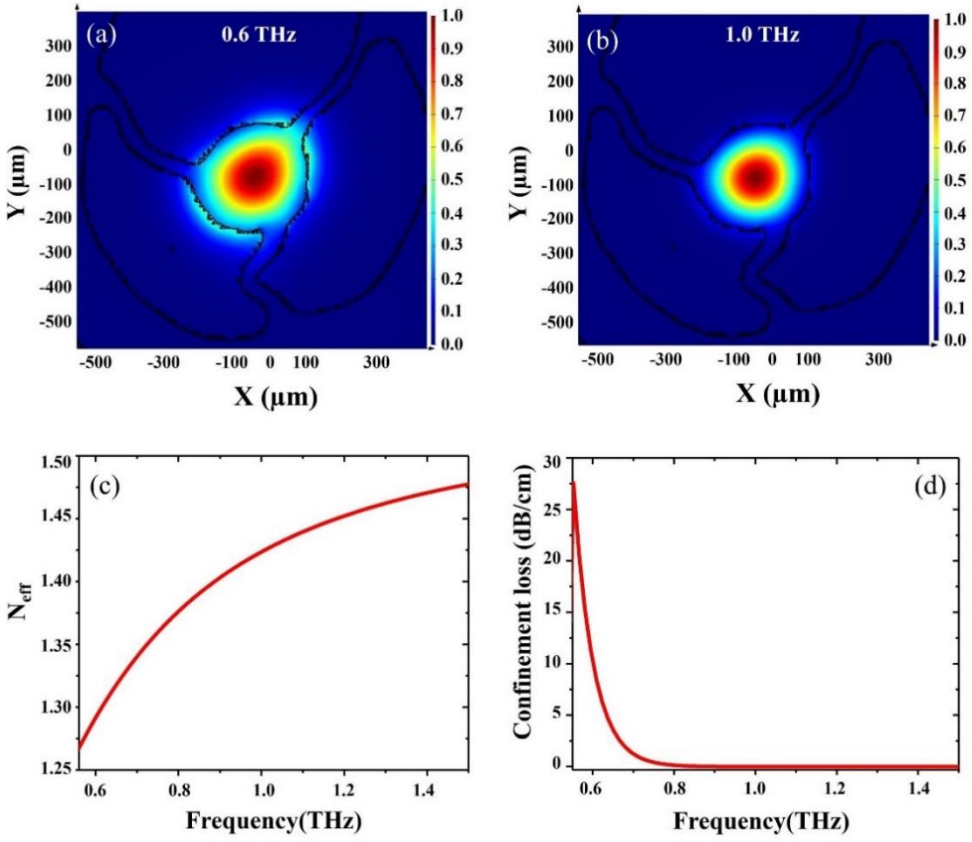

Figure 6.5 Simulated mode profiles in the fibre core at (a) ν=0.6 THz and (b) ν=1.0 THz. (c) Effective index and (d) confinement loss of the fundamental mode in the frequency range ν=0.55 – 1.5 THz.

The optical properties of the SC-MPOF were characterised using THz time-domain spectroscopy (THz-TDS) (Figure 6.6). To ensure a constant amount of light coupled to the fibre, the SC-MPOF was mounted in a custom-made holder with lenses attached at the ends. The holder allowed the input end of the fibre to be securely fixed at the focal point of the focusing lens. Another lens with a focal length of 37 mm was inserted at the other end of the holder and designed for collimation of the outgoing fibre radiation. The THz source used in the experiment (Laser Quantum

GMBH's Tera-SED with GaAs photoconductor) emitted broadband THz waves up to ν~2.5 THz. The detector function was performed by the Menlo GMBH TERA8-1 fibre optic antenna with a bandwidth of up to 4 THz. Although the source and detector are active up to ν~2.5 THz and ν~4 THz, respectively, the spectroscopic bandwidth is limited by ambient noise and component misalignment, which in particular limits the high end of the frequencies.

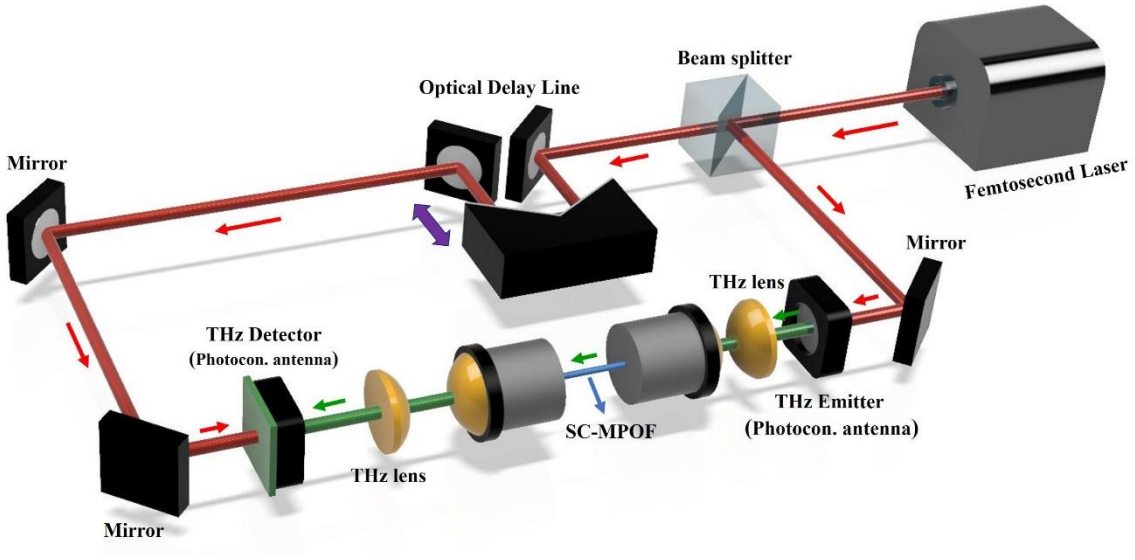

Figure 6.6 Experimental setup for characterising THz transmission properties of the extruded TOPAS SC-MPOF.

Transmission in the THz part of the spectrum was characterised using the setup of Figure 6.6. The time domain data and the time-frequency diagram (spectrogram) of the THz signal for these measurements are presented in Figure 6.7(a) and (b). This clearly shows that the effective bandwidth over which useful spectroscopic data was obtained lies in the range ν=0.1 - 1.0 THz. The broadband THz wave was launched into an 8 cm long section of the TOPAS SC-MPOF fibre using a THz focusing lens with focal length of 37 mm. The fs-laser pulse from the time delay line and the transmitted THz wave from the fibre were simultaneously incident onto the THz detector to generate the signal using the THz-TDS detector. The time domain signal of the transmitted wave from the fibre was recorded in real time and a subsequent Fourier transform generated the transmission spectrum in the frequency domain.

At the focal point, the THz beam waist diameter was estimated to be ~1 mm at 1 THz, comparable to the outer diameter of the SC-MPOF fibre. The microscope image in Figure 6.4(b) shows that the cladding has an outer shell thickness of 200 μm, which supports THz wave propagation at ν=0.5-1.0 THz. High frequency signals in the time domain at time delays of t =60-180 ps were observed (Figure 6.7(c)) prior to the removal of the cladding modes, and were ascribed to the multimode guidance in the outer cladding. These cladding modes were stripped by applying graphite paste to the fibre outer surface, which exhibits a higher refractive index than most polymers

[196], resulting in the disappearance of the high frequency signal as shown in Figure 6.7(c) (red line). The transmission spectrum of THz waves guided in the fibre core indicates that at ν~1.0 THz, the output intensity is higher than the noise level (Figure 6.7(d)), while it drops to the noise level at ν<0.5 THz, confirming core guidance in the spectral range of ν=0.5 – 1.0 THz, in accordance with simulations. The graph in Figure 6.7(c) shows that the signal from the fibre is significantly decreased due to the cladding mode removal. The signal to noise ratio in single-mode operation is ~ 7 dB, which is acceptable to perform measurements in the THz regime.

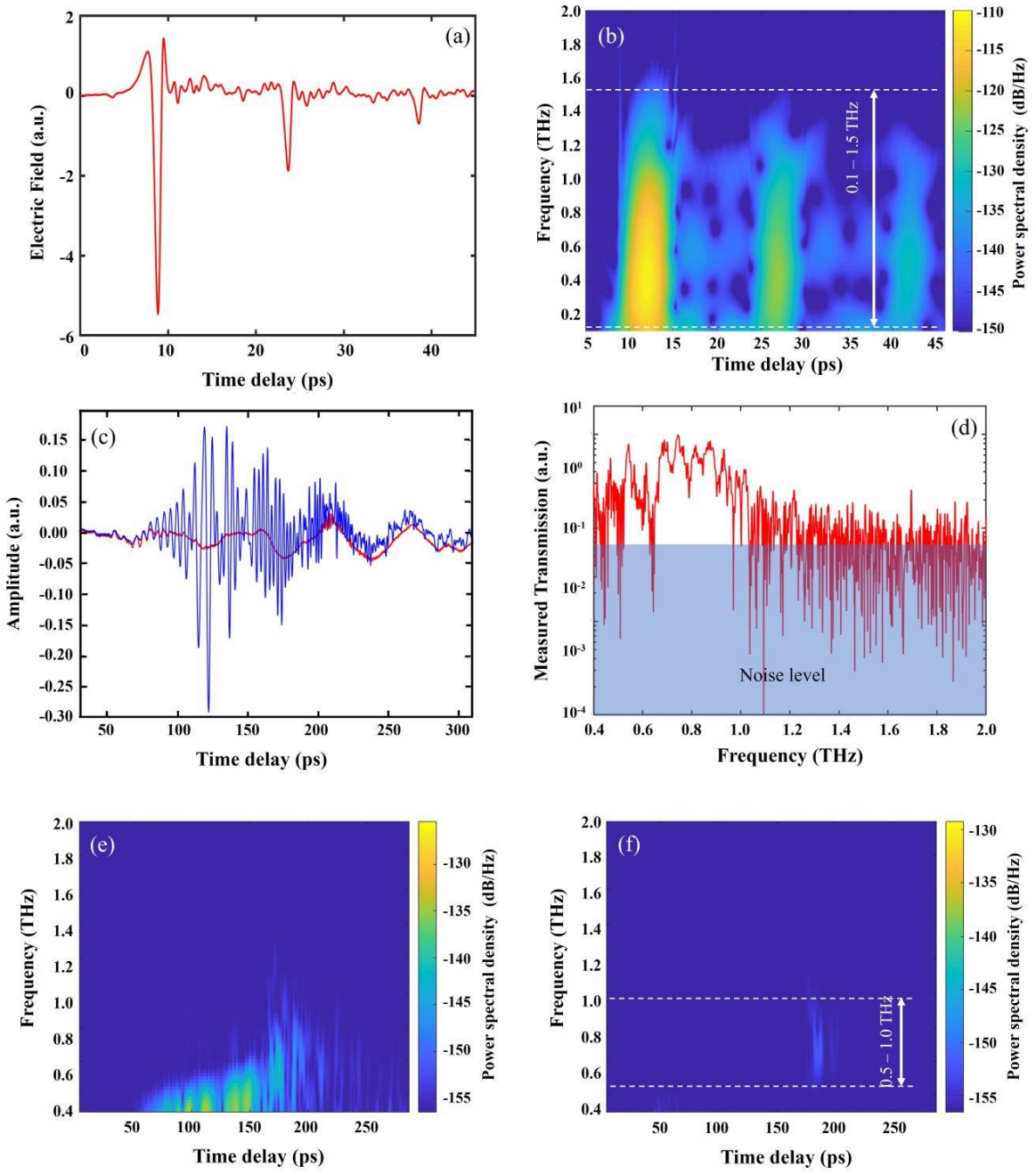

Figure 6.7 (a) Time domain measurement and (b) spectrogram of the THz emitter. (c) Time domain measurement of the E-field of the THz waves transmitted through the SC-MPOF; the blue and red lines represent the signal from the whole fibre (core and outer cladding) and from the fibre core only, respectively. (d) Spectral profile of the THz waves transmitted through the

SC-MPOF. Spectrogram of the THz wave guided (e) in the whole fibre cross section (outer cladding and core) and (f) fibre core only, for an 80 mm long SC-MPOF.

The time-frequency diagram clearly demonstrates guidance in the SC-MPOF (Figure 6.7(f)). The spectrogram is calculated from the measured time trace of the THz output pulses using a sliding Gaussian-shaped sample window of 128 samples. The windowed time domain scans are then Fourier transformed into the frequency domain, with spectral components plotted against the window position in time. The spectrograms show a few qualitative features of the fibres: Figure 6.7(e) demonstrates that before removing the cladding modes, there is evidence of dispersion at ν~0.4-1.2 THz, as seen by the earlier arrival of the low frequency components. This dispersion is associated with the modal dispersion of multimode guiding. After cladding modes were stripped, the spectral components of the pulse aggregate at around the arrival time t = 180 ps (Figure 6.7(f)). Higher-order modes have effective phase indices lower than that of the fundamental mode, which would result in several temporally displaced islands of spectral components. Absence of this effect indicates that the wave in the fibre core is guided in a single mode regime. The pulse has negligible dispersion as indicated by the simultaneous arrival of all frequency components. The zero-dispersion frequency range is estimated to be at ν~0.5-1.0 THz, centred at 0.8 THz. The low frequency components (ν~0.4-0.6 THz), arriving at t = 50 – 150 ps, disappeared when the graphite paste was applied, confirming that these are high order modes guided in the outer cladding. The temporal components arriving after 200 ps also disappear in the graphite coated fibre and are also ascribed to the index guided modes in the outer cladding.

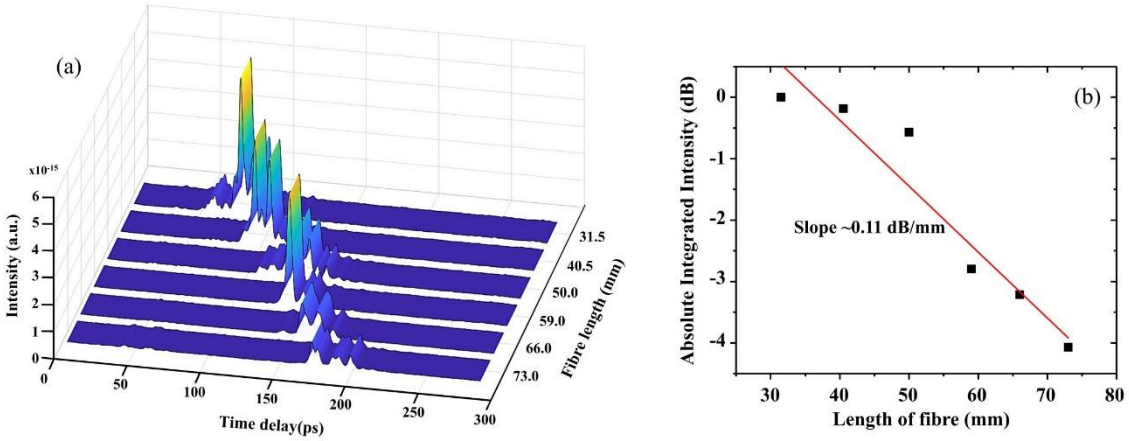

Figure 6.8 (a) Temporal profile of THz wave after propagation through different lengths of SC-MPOF. (b) Relationship between THz transmission and fibre length.

Fibre propagation losses were estimated using the cut-back method. The length of the fibre was gradually shortened from 73 mm to 30 mm by using a razor blade. The transmission of the THz wave propagated through the fibre of different lengths was measured using a Meno GMBH TERA8-1 photoelectric antenna. The resulting data was analysed using a spectrogram, which provides a clear view of the delay occurring due to different fibre lengths. Signal intensity was calculated by

integrating all spectral components in the ν~0.5–1.1 THz range (Figure 6.7(f)) for each fibre length. The results in Figure 6.8 show that the THz pulse arrives at the detector at t = 180 ps for the longest fibre (73.0 mm), and at t ~ 80 ps when propagating through the shortest fibre (31.5 mm). The graph clearly shows a drop in the signal amplitude as the fibre length increases. The effective index (n_{eff}) of the fundamental mode guided in the fibre core can be calculated from the result in Figure 6.8(a). The result shows that the calculated n_{eff} of this mode is 1.428, in agreement with the value obtained in the simulations of Figure 6.5(c) (n_{eff}~1.424). The average propagation loss was 0.11 dB/mm across the frequency range ν=0.4-1.1 THz (Figure 6.8(b)).

The drawing parameters and optical properties of the THz SC-MPOF are presented in Table 6-2.

Table 6-2 Summary of the THz SC-MPOF drawing parameters, fibre geometry and optical properties

Parameter		Value	Units
Material and drawing parameters	Material	TOPAS	-
	Feeding speed	180	mm/min
	Temperature	240	°C
	Drawing speed	21	mm/s
Geometry	Core diameter	300	µm
	Fibre diameter	1600	µm
Optical properties	Attenuation (at ν~0.5-1.0 THz)	1.1	dB/cm

6.3 Summary

In conclusion, extrusion of microstructured polymer optical fibres from a low-cost desktop 3D printer has been demonstrated. Images of the final fibre cross-sections indicate it is possible to maintain the microstructure inside the fibre after the drawing process. Although the size of the fibre for near-IR guidance is large compared with commercial optical fibres, this demonstrates the potential to directly draw microstructured polymer optical fibre using a customised 3D printer head. The near-field end facet image and the modal profile simulations show the ability to confine light at λ = 1550 nm in the fibre core. The measured maximum propagation loss reveals an attenuation of 1.1 dB/cm at λ = 1557 nm.

For the THz SC-MPOF, the near field and modal profile simulations demonstrate the ability to confine light in the fibre core over the spectral range ν=0.5-1.0 THz. Time and frequency domain spectrograms confirmed core guidance and an average propagation loss of 1.1 dB/cm for ν=0.4-1.1 THz. The delivery of THz beams to enclosed locations such as chemical reactors are difficult in free space, so the ability to confine the beam within a bendable fibre is extremely beneficial even if at the

expense of relatively large losses. By improving the launching conditions and the fibre structure symmetry, the loss can be further reduced, and this will be pursued in future work.

Loss comparison between the SC-MPOF fabricated from the direct extrusion technique using 3D printer and another polymer optical fibre fabricated from the 3D printed preform are revealed in Table 6-3.

Table 6-3 Summary of loss from the polymer optical fibre fabricated from 3D printing technique.

Fibre Type	**Core material**	**α (dB/cm)**	**λ (nm)**	**Year Report**	**Ref.**
Suspended-core multimode fibre for NIR guiding (Optical fibre implemented in this work.)	ABS	1.1	1553	2018	[197]
Solid-core air structure fibre (Microstructure fibre)	ABS	1.51	1550	2015	[34]
Step index multimode fibre (Conventional fibre)	ABS	0.42	1550	2016	[33]
Coreless multimode fibre (Conventional fibre)	ABS	0.38	1550	2016	[120]
Coreless multimode fibre (Conventional fibre)	PETG	0.26	1550	2016	[120]
Circular solid-core fibre (conventional fibre)	PC	0.7	633	2017	[118]
Triangular solid-core fibre (Conventional fibre)	PC	1.3	633	2017	[118]
Rectangular solid-core fibre (Conventional fibre)	PC	1.8	633	2017	[118]

Chapter 7.

HOLLOW-CORE MICROSTRUCTURED POLYMER OPTICAL FIBRE

Polymer optical fibres were proposed for waveguiding because of their low cost, widely accessible materials and low-temperature processing. However, most polymers have high material absorption, especially in the mid-infrared (mid-IR) and terahertz (THz) regions, leading to high losses in solid-core polymer waveguides. To overcome this issue, hollow-core waveguides or fibres have been proposed: since the mode is mostly confined in a hollow air-core, the effect of material loss is minimal. The hollow-core can be easily filled with dry air, eliminating water vapour and its absorption [190]. Many types of hollow-core fibres were developed with different guiding mechanisms for THz guidance [198, 199], including the photonic bandgap (PBG) and antiresonant (AR) effect.

In this chapter, the design and fabrication of hollow-core microstructured polymer optical fibre (HC-MPOF) based on antiresonant guidance will be presented. The results of extruded hollow-core MPOFs from a 3D printer and THz guiding characterisation will be shown in Section 7.1. Section 7.2 will present the fabrication and characterisation of hollow-core MPOF for mid-IR guidance. Finally, the results will be summarised in Section 7.3.

7.1 THz Hollow-core microstructured polymer optical fibre

Although TOPAS is one of the materials with low absorption in the THz region, the transmission loss of index guiding THz fibres is still over 2 dB/cm at 1 THz [190]. To overcome this issue, several designs based on hollow-core (HC) fibres have been proposed, because the mode is mostly confined in the hollow air-core with a relatively small fraction of the field in the solid material. Thus, the material loss can be minimized [27, 30, 198, 200]. Many types of guiding mechanisms have been developed for hollow-core fibres. In 2008, the first hollow-core polymer fibre for THz guiding was made by drilling PMMA to produce a Bragg fibre structure [201] with an overall loss of 0.5 cm^{-1}, 30–60 times smaller than the PMMA material loss at ν~1.0–1.3 THz. The waveguide design was not optimised, and the total diameter was approximately 6 mm. Other THz Bragg fibres, reported in 2011 [88, 202], were fabricated by depositing a layer of TiO_2-doped polymer on a polymer film and then rolling it to create periodic layers around the hollow fibre core. These fibres had a total diameter of 12 mm with estimated losses of ~0.1 cm^{-1} within the THz transmission window.

Another category of hollow-core THz fibres relies on the use of the antiresonant effect [29, 30] to confine the THz wave in an air-core. THz waves propagating in the antiresonant fibre can be confined to the central air-core because of the resonant reflection of the guided wave at the membranes surrounding the core, behaving effectively as a Fabry-Perot cavity in the transverse direction with respect to propagation. In AR fibres, the core mode has a small overlap with the solid fibre material and does not couple to the cladding in specific wavelength ranges. To achieve low loss, AR fibres do not require small core diameters, unlike other microstructured optical fibres, and exhibit several transmission bands and broadband guidance. In 2018, a simple stacking technique was proposed to fabricate negative curvature antiresonant polymer THz fibres [200, 203]. In the same year, another antiresonant polymer THz fibre was fabricated via 3D printing, significantly reducing the fabrication time [29, 30].

7.1.1 THz HC-MPOF fabrication

A fibre design with 6-fold rotational symmetry was chosen for extruding antiresonant HC-MPOFs because of its relatively simple geometry. 3D models of the nozzle with the fibre cross section inverse structure profile were designed and fabricated from stainless steel using a metal 3D printer, as presented in chapter 4. The HC-MPOF used in this experiment consists of a hexagonal air-core with a diameter of 2.2 mm. The thin layer surrounding the fibre core has a thickness of 0.65 mm and the outer diameter of the extruded fibre is 8 mm (Figure 7.1(a)). The gray shaded region in the schematic of Figure 7.1(b) is TOPAS, while the white region represents air. Light in the antiresonant HC-MPOFs can be confined to the central air-core owing to the resonant reflection of the guided wave in the air-core with a membrane surrounding the core which behaves effectively as a Fabry-Perot cavity (the 0.65 mm thick layer/struts).

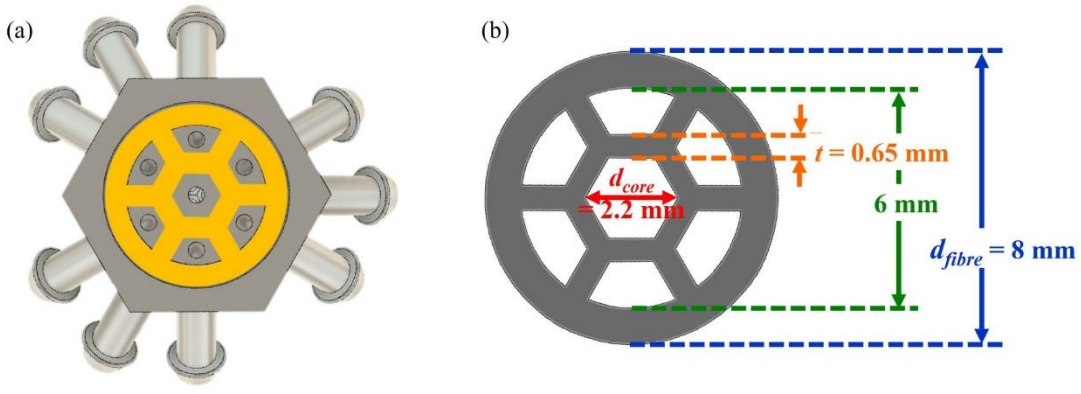

Figure 7.1 (a) Bottom-view of the nozzle. Yellow represents the area filled by the polymer. (b) Schematic of the cross section of the extruded TOPAS hollow-core fibre.

To fabricate the THz HC-MPOF, the metal 3D printed structured nozzle was connected with the heater block at the 3D printer head (Figure 7.2(b)). Heat from the heater cartridge (24 V, 35 W) was applied to the upper thread of the nozzle via the heater block. As before, extrusion parameters,

including feed rate and nozzle temperature, were varied to investigate their effect on the transparency and surface roughness of the extruded fibre and to find the fictive temperature for optimal fibre fabrication. During the process, the nozzle temperature (T_n) was varied from 230°C to 290°C, and at T_n ~ 240°C the surface of the polymer became smooth and shiny, with significantly reduced bubble formation compared to other nozzle temperatures.

The filament feeding velocity was then gradually varied and an extruded fibre blank with a smooth surface was successfully achieved at *s* = 180 mm/min with T_n = 240 °C. The HC-MPOF was fabricated by feeding the TOPAS filament using a built-in feeding motor operating at *s* = 180 mm/min, corresponding to an extrusion speed of 0.84 mm/s. Figure 7.2(a) shows the schematic of the microstuctured fibre drawing tower which includes the FDM 3D printer head. A photograph and schematic of the extrusion of HC-MPOF from the structured nozzle are presented in Figure 7.2(b-c).

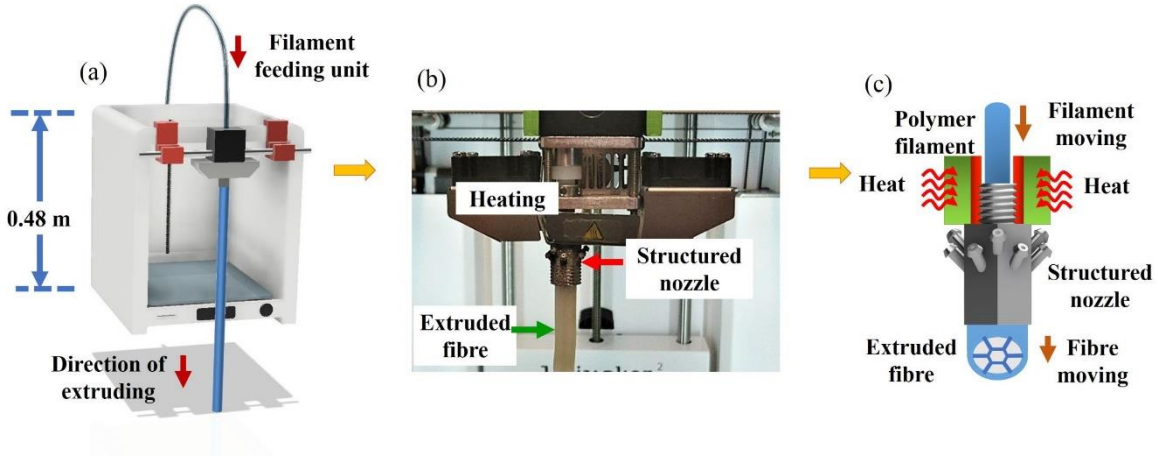

Figure 7.2 (a) Schematic of the experimental setup used to extrude the HC-MPOF from the 3D printer. (b) Photograph and (c) schematic of the HC-MPOF extruded from the heated metal 3D printed structured nozzle.

7.1.2 HC-MPOF characterisation in THz

The extruded THz HC-MPOF was cleaved by using an electronic saw and its tip surface was polished using sandpaper to reduce surface roughness at the fibre input and output due to the cleaving. The cross-section image of the extruded HC-MPOF showed that the microstructure inside fibre was maintained after the extrusion process (Figure 7.3 (a-b)).

The optical properties of the TOPAS SC-MPOF were characterised using THz time-domain spectroscopy (THz-TDS) (Figure 7.3) as described in section 6.2.2.

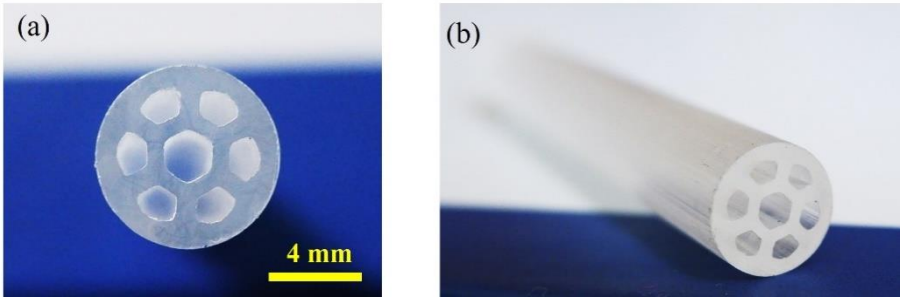

Figure 7.3 (a) Cross-section and (b) photograph of the TOPAS hollow-core antiresonant THz fibre extruded from the metal 3D printed structured nozzle.

Mode coupling between core and cladding modes in HC-MPOFs occurs at resonant frequencies and results in high loss. The frequencies in the transmission window between resonant frequencies exhibit low loss, in which the modes are confined to the air-core. The mode coupling occurs when the two modes are phase matched, therefore, the frequencies of these (high loss) resonance (ν_m) can be calculated by the following formula [204]:

$$\nu_m = \frac{mc}{2t\sqrt{n_{polymer}^2 - n_{air}^2}} \qquad 7\text{-}1$$

where c is the speed of light in vacuum, $n_{polymer}$ is refractive index of polymer, n_{air} is the refractive index of air, t is the thickness of struts surrounding the fibre core and m = 1, 2, 3,

The confinement loss (CL) of the proposed antiresonant fibre is given by the following formula [200]:

$$CL = \frac{20}{\ln 10} k_0 \mathrm{Im}(n_{eff}) \qquad 7\text{-}2$$

where k_0 is the wave vector, and $\mathrm{Im}(n_{eff})$ is the imaginary part of the effective refractive index.

Loss in the antiresonant HC-MPOFs is dominated by radiative mode leakage, since only a very small fraction of light, typically less than 0.1% at antiresonance, propagates in the solid material. As shown in eq.(7-1), the optical properties of the HC-MPOFs, including resonant frequencies and transmission windows, can be controlled by varying the thickness of the strut surrounding the fibre core. The loss profile of the designed HC-MPOFs was calculated for different strut thicknesses of 0.55, 0.65, and 0.75 mm, while the core diameter was fixed at 2.5 mm. In order to evaluate the theoretical transmission characteristics of the HC-MPOF, finite element simulations was used to numerically solve Maxwell's equations in the frequency domain and get the electric field distribution. For the simulation of antiresonant fibre, the FEM solver was changed from Lumerical© to Comsol© as the Lumerical software cannot keep the continue frequency scanning over the unguided frequency. As the loss profile of antiresonant fibre will present the loss of both guided

(antiresonant) and unguided (resonance) mode, thus, the simulation using Lumerical have to separate into many frequency ranges to cover all interested frequency which take more time to get the result when comparing with Comsol. Therefore, Comsol has been chosen for this simulation. The simulation was performed by creating a 2D model of the fibre cross section structure with the same dimensions as the extruded fibre. The modelling geometry is presented in Figure 7.4(a).

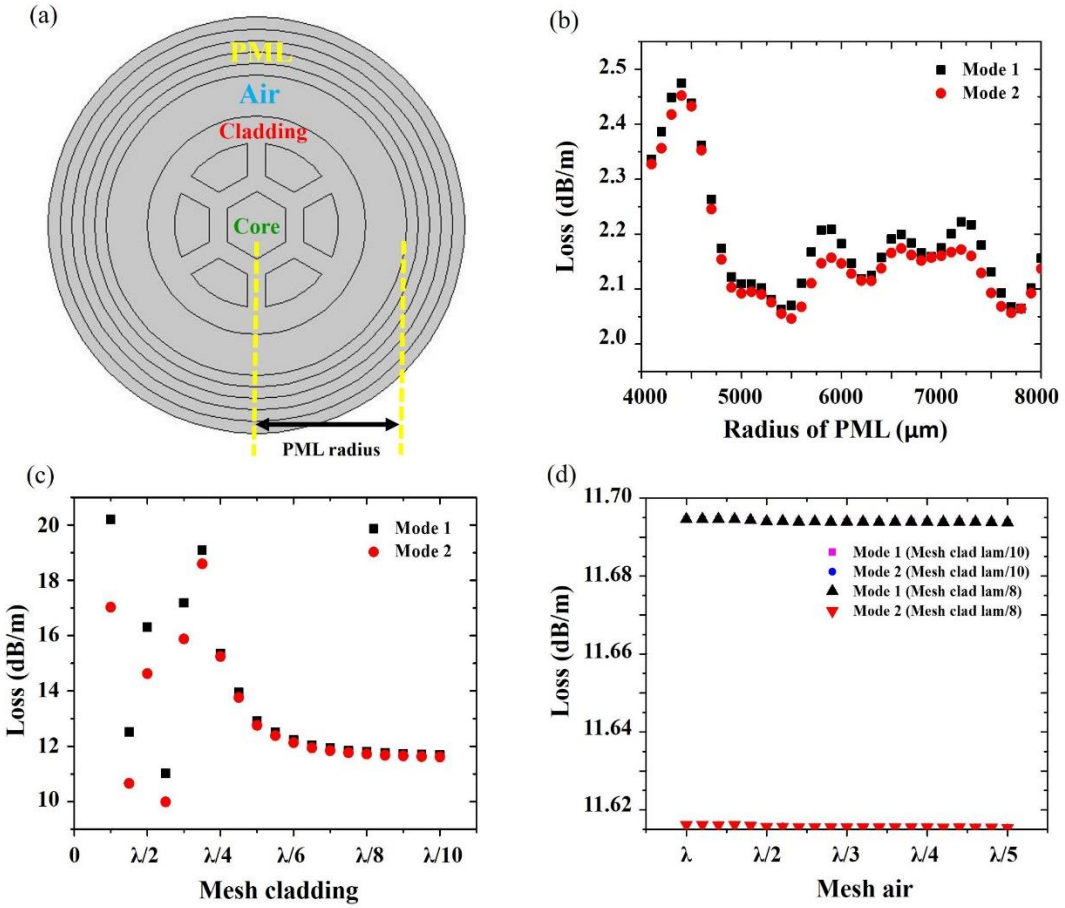

Figure 7.4 (a) Schematic of the THz HC-MPOF modelling geometry including the PML boundary region. Simulated loss plotted against (b) PML boundary radius, (c) cladding mesh size, (d) air-mesh size to optimise the simulation parameters.

To accurately model and account for confinement losses due to leakage, the type of boundary condition around the fibre plays an important role in the simulations: the perfectly matched layer (PML) is an absorbing boundary region which is designed to absorb incident light with minimal reflection. PML boundaries are basically implemented as an absorbing material that is also impedance matched to the surrounding material to minimize reflection. The guided modes considered in this work are leaky modes, thus a PML boundary condition was chosen for this simulation. In the FEM solver, the size of boundary compared with the simulation model can affect the loss of leaky modes. Too small a PML radius can cause high loss by inadvertently increasing leakage (from the fibre to the PML). To solve this problem, the PML should be positioned further away from the core region, so that it does not perturb the mode distributions and introduce spurious losses. However,

simulation time increases with the size of the PML. Therefore, to find the optimal PML size, the loss of the modes of interest was monitored while varying PML radius. As the fibre radius was 4 mm, the PML radius was varied in the range 4 – 8 mm. Figure 7.4(b) shows that the HC-MPOF confinement loss decreases significantly when the PML radius is larger than 4500 mm. The first lowest confinement loss is achieved when the PML radius is ~5500 mm, while at PML radii larger than 5500mm, the HC-MPOF confinement loss is relatively stable with small fluctuations due to resonances associated to small reflections in the PML. Indeed, the PML radius of 5500 mm was chosen for the simulations as it is the radius at which the effect of PML thickness can be ignored.

Apart from the size of the boundary condition, the mesh size at different locations in the simulation geometry is also an important parameter that can affect the accuracy of the simulated loss. Generally, the mesh sizes in the guiding region (core) are set at λ/10, while in other regions typically larger. Very fine mesh sizes in the cladding and in the outer region can unnecessarily increase simulation time, while rough mesh sizes result in inaccurate simulation results. To optimise the cladding mesh size, the guided mode losses were calculated while varying cladding mesh size (with the PML radius fixed at 5.5 mm). As shown in Figure 7.4(c), loss becomes stable when the cladding mesh size is smaller than λ/6, while at larger mesh sizes large fluctuations can be observed. Figure 7.4(d) shows the loss when the mesh size of the air region is varied from λ to λ/5: no fluctuation in loss can be observed. Based on this optimisation, a PML radius of 5.5mm with the thickness of 5λ, cladding mesh size of λ/8 and air mesh size of λ/3 were used for the modal simulation of THz HC-MPOF.

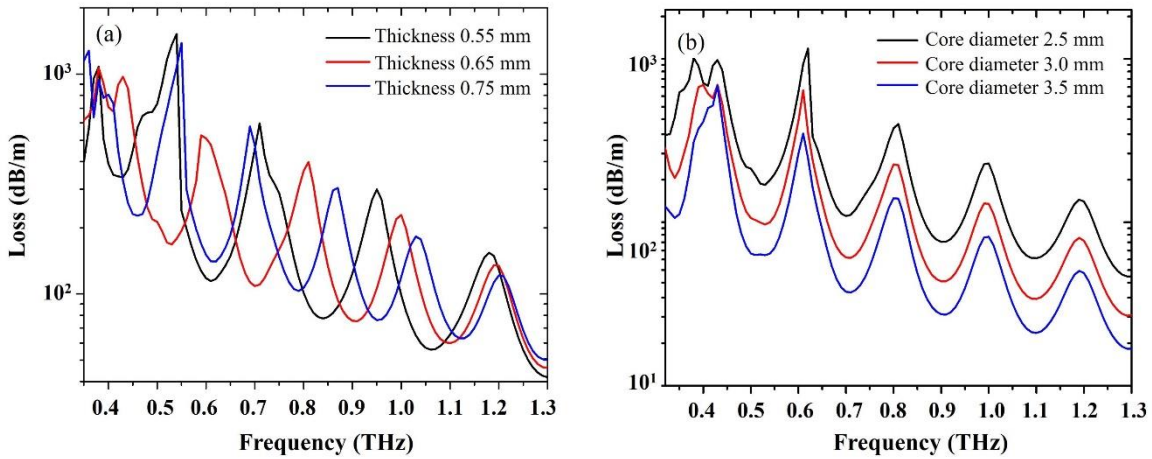

Figure 7.5 Simulated HC-MPOF transmission loss (Comsol©) for (a) different strut thicknesses, and (b) different core diameters, when the strut thickness is fixed at 0.65 mm.

The loss profiles in Figure 7.5(a) indicate that the peaks of the resonant frequencies shift with the variation of strut thickness. For the HC-MPOFs, the core diameter is also one of the parameters that affects the fibre confinement loss. With the well-known hollow-core fibre λ^2/r^3 loss dependence [205], the results in Figure 7.5(b) show that the smaller core diameter results in higher confinement

loss when the thickness of the strut is fixed at 0.65 mm. Therefore, to achieve low loss guidance at the desired range of frequencies, both the thickness of struts and core diameter should be varied. This can be achieved simply by using the direct extrusion technique owing to the possibility to apply pressure through the air-holes, control temperature and set material feeding speed while extruding the fibre.

Here, $n_{polymer}$ = 1.54, which is the average refractive index of TOPAS in the frequency range 0.1–1.5 THz (TOPAS Advanced Polymers GmbH), n_{air} = 1, and the thickness of struts surrounding the fibre core is t = 0.65 mm. By using the formula in eq.(7-1), the resonant frequencies in the range of interest (0.4 – 1.3 THz) are calculated to be ν_m = 0.44, 0.59, 0.74, 0.89, 1.04, and 1.19 THz. The modal analysis of THz in the HC-MPOF structure (Figure 7.6(a)) shows that at the resonant frequency (0.59 THz), the field of the THz wave is poorly confined in the central air core, and the mode in the fibre core is coupling with the surrounding material and leaks out into the cladding, resulting in high loss. Figure 7.6(b) shows that at the antiresonant frequency (0.7 THz) the field is confined in the central air core.

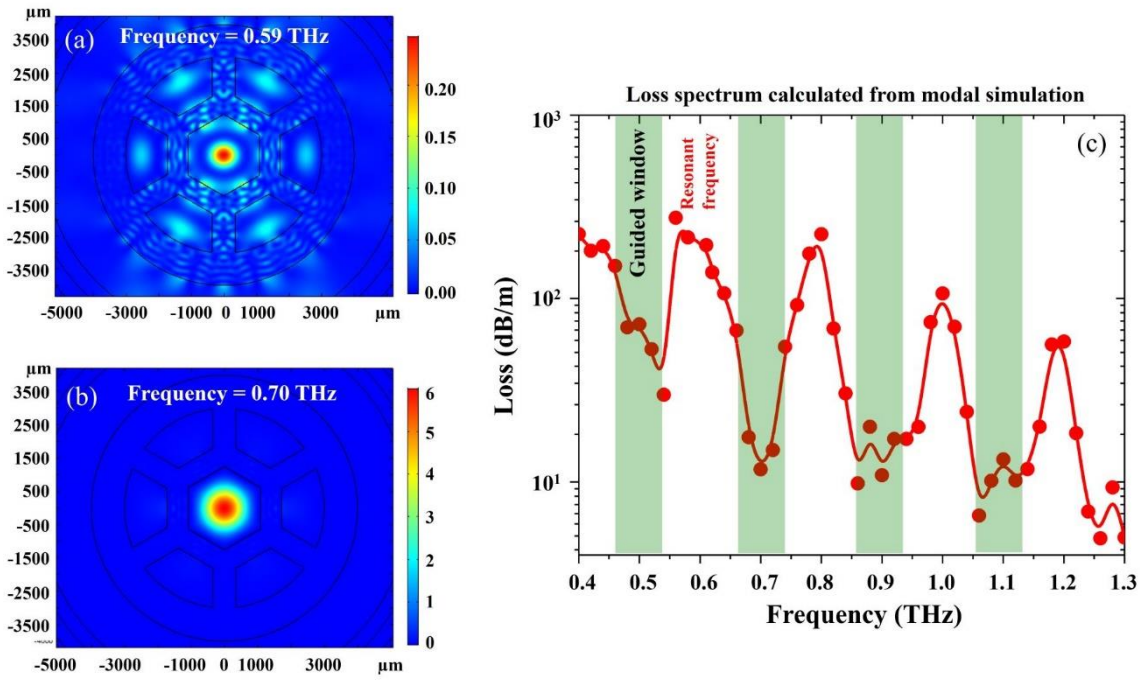

Figure 7.6 Simulated modal intensity profiles in the fibre core at (a) resonant frequency (ν=0.59 THz) and (b) antiresonant frequency (ν=0.70 THz). (c) Simulated confinement loss of HC-MPOF designed with core diameter d_{core} = 2.2 mm and strut thickness t = 0.65 mm.

The FEM calculated loss spectra from Comsol© of this designed THz fibre is shown in Figure 7.6(c). Simulations indicate that the peaks of high loss are located at the resonant frequencies, which correspond to the calculated values. The loss profile in Figure 7.6(c) shows that THz waves in the range ν~ 0.4 – 1.3 THz experience the antiresonant effect. The chosen HC-MPOF geometry should effectively guide THz radiation in the antiresonant regions, and the resonant peaks (where losses are

high) are clearly defined. As expected, field confinement becomes stronger as the frequency increases, whereas at lower frequencies the core size is smaller compared to the wavelength, thus pushing light into the surrounding material. This confirms that on antiresonance most of the power is confined within the central air core. The antiresonant effect makes the waveguide suitable for guiding certain frequency bands, and less suitable for frequencies where there is resonance. To achieve guidance at specific frequencies, a certain thickness of the cladding elements is needed to shift the resonant peaks. The loss at resonant frequencies can be higher than the bulk loss of the cladding material, as the loss is dependent on the geometry of the cladding.

To confirm THz guidance in the fabricated HC-MPOF, the fibre was characterised with the THz time domain spectroscopy (TDS) setup shown in section 6.2.2. Pulses from a femtosecond laser with a central wavelength of λ~800 nm passed through a beam splitter and one part of the fs-laser beam was directed through an optical delay line used to adjust the propagation time of the pulse, while the other irradiated the THz emitter generating a THz beam [206]. The time domain spectrograph of the THz pulses passing through the air and after being collimated by a pair of Polymethylpentene (TPX) lenses is presented in Figure 7.7(a). The reference signal was performed by launching the THz wave through an additional two TPX convex lenses to focus the THz beam, without any optical fibre leaving the distance between the detector and the emitter unchanged.

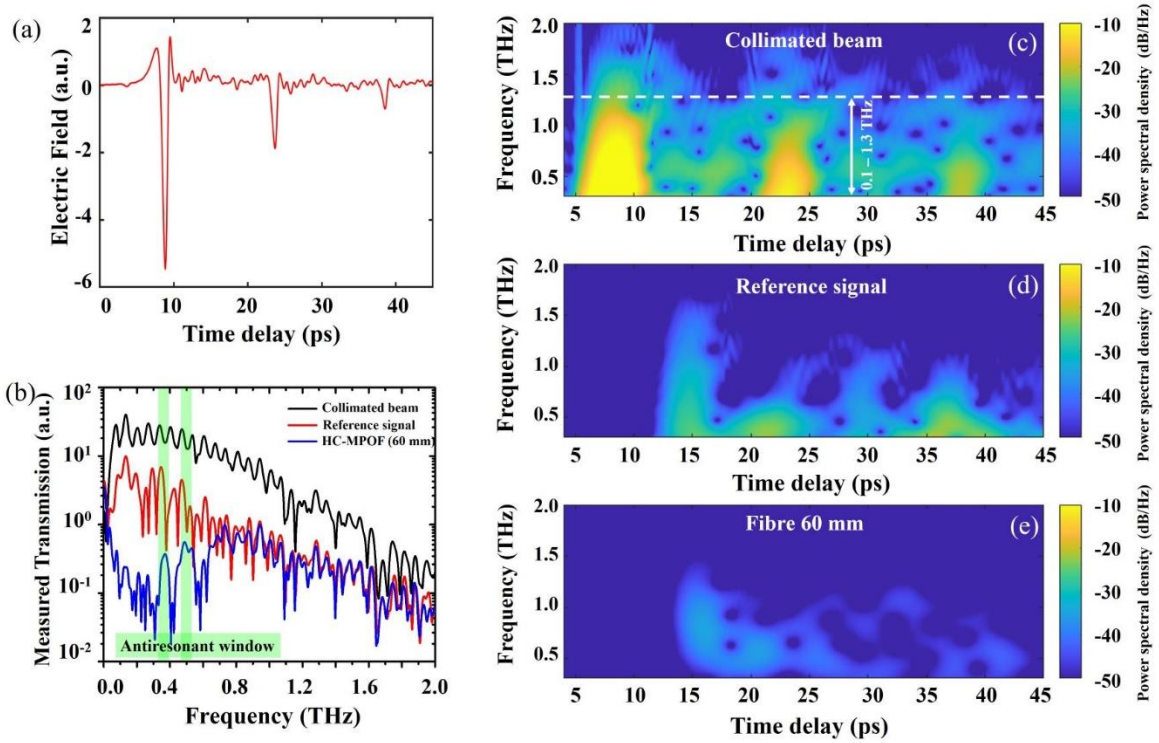

Figure 7.7 (a) Time domain measurement of the THz wave from the THz emitter (collimated beam). (b) Spectral profile of the THz waves from the emitter (black line), when it passes through two THz convex lenses (red line), and when it is transmitted through the HC-MPOF (blue line). (c) Spectrograms of the THz wave from the THz emitter, (d) after propagating through two THz convex lenses and (e) through the two convex lenses and a 60 mm long HC-MPOF.

To characterise the fibre, the broadband THz wave was launched into a 60 mm long section of the HC-MPOF fibre using the THz focusing lens with focal length of 50 mm. At the focal point, the THz beam waist diameter was estimated to be ~1 mm at 1 THz, comparable to the air-core diameter of the HC-MPOF fibre. The train of fs-laser pulses from the time delay line and the transmitted THz wave from the fibre were simultaneously shone onto the THz detector to detect the signal using the THz-TDS detector. The time domain signal of the transmitted electric field from the fibre was recorded and a subsequent Fourier transform produced the signal spectrum in the frequency domain. The Fourier transform spectra of the THz wave from the THz emitter (black line) and when it was launched through the lens (red line) are presented in Figure 7.7(b). When the THz wave was launched through the lens, the amplitude of the spectrum was dramatically decreased compared with the spectrum from the THz emitter due to material absorption of the lens and coupling losses. The spectrum of the THz wave guided in the 60 mm length HC-MPOF fibre is reported in Figure 7.7(b) (blue line). When compared with the spectrum from the THz emitter, troughs of high-loss at the resonant frequencies can be clearly observed. The peaks of low-loss (antiresonant frequencies) are also visible as indicated in Figure 7.7(b). These windows arise from the antiresonant propagation condition between two consecutive high-loss resonances.

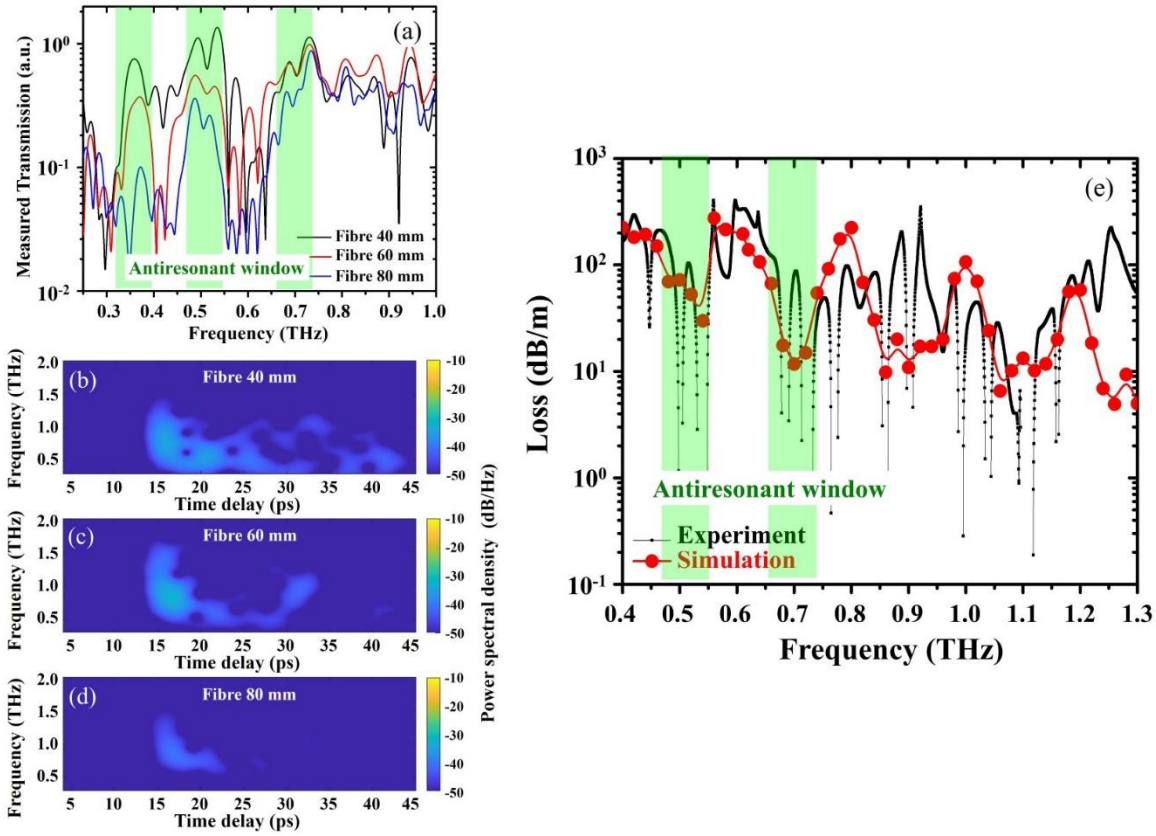

Figure 7.8 (a) Output THz spectral profiles from HC-MPOF with lengths of 40, 60, and 80 mm. (b) Spectrograms of the THz wave from HC-MPOF with lengths of 40 mm, (c) 60 mm, (d) 80 mm. (e) Experimental and numerical simulation of the loss for the TOPAS HC-MPOF.

The time-frequency diagrams (spectrograms) were calculated from the measured time traces of the THz output pulses using a sliding Gaussian-shaped sample window of 128 samples. The windowed time domain scans were then Fourier transformed into the frequency domain, with spectral components plotted against the window position in time. The spectrogram from the THz emitter indicates that the THz pulses aggregate at around an arrival time of $t \sim 5$ ps. The spectrogram shows that this THz emitter has an effective bandwidth over which useful spectroscopic data can be obtained ranging in the frequency range $\nu = 0.1$ - 1.3 THz (Figure 7.7(c)). For the reference signal presented in Figure 7.7(d), the THz wave propagated through two convex lenses and arrived at the detector at $t \sim 12$ ps. The slowdown in the pulse velocity is due to the higher refractive index of the lenses. The temporal components that propagated through the 60 mm long HC-MPOF arrived at $t \sim 14$ ps (Figure 7.7(e)). The arrival time of the THz wave from the fibre is 2 ps slower than the reference signal, which is ascribed to the overlap of the guided mode with the high index material surrounding the core.

Fibre propagation losses were measured using the cut-back method. Three HC-MPOF sections were fabricated with different lengths of 40 mm, 60 mm, and 80 mm. The transmitted THz signal through the fibres was measured using a MenloSystems TERA8-1 photoconductive antenna. To maintain consistency during these measurements, all three optical fibres were aligned using the modified cylindrical fibre holder. The signal transmitted through each length of fibre was measured three times and averaged to reduce the effect of the difference in coupling for each attempt. The results show that the signal at the frequencies within the guiding window (green highlight in Figure 7.8(a)) decreases significantly for increasing fibre length. The resulting data was also analysed using a spectrogram, which provides a clear view of the decreasing signal amplitude from the fibre output due to longer fibre lengths (Figure 7.8(b-d)). To study the performance of the waveguide further, confinement loss of the extruded HC-MPOF was experimentally analysed. The comparison between the simulated (red line) and measured (black line) loss can be seen in Figure 7.8(e): two antiresonant windows can be clearly seen at the expected spectral regions around $\nu \sim 0.5$ and 0.7 THz, while simulations of confinement loss reveal four antiresonant windows. This discrepancy can be explained by the characteristics of the THz source that has low intensity at $\nu > 1$ THz. Although only two antiresonant windows can be experimentally observed, their location is in good agreement with the simulations. The confinement loss at the antiresonant frequencies from experiments is also close to the simulated value of 0.12 dB/cm at $\nu = 0.7$ THz.

7.2 Mid-Infrared Hollow-core microstructured polymer optical fibre

Since the invention of laser sources in the mid-IR range spectral region (2.5 to 25 μm), there has been a growing interest in the development of optical fibres transparent at these wavelengths for applications in chemical, biological and atmospheric sensing [207-210], where the unique molecular

absorption associated to the excitation of specific fundamental vibrational and rotational modes allows for an accurate chemical fingerprinting [211].

Although over the last 3 decades silica optical fibres have become the backbone of optical communications and distributed optical sensing, they cannot guide light in the mid-IR as the silica network has strong overtone absorptions above 2 μm, resulting in an overall attenuation that increases for increasing wavelengths. Thus, the search for optical fibres operating in the mid-IR has focused on materials that have high transmittance in the wavelength range λ = 2-20 μm such as chalcogenide glasses, heavy metal fluorides, polycrystalline silver halides (AgX), single-crystal sapphire, and tellurium halides (TeX) [212-214], which still require extraordinary purification processes and are extremely hard to handle.

An alternative approach relies on the use of hollow-core fibres (HCF) such as photonic bandgap fibres and anti-resonant fibres, where light is confined within the hollow-core, greatly decreasing the influence of the material optical properties. Such fibres have been already exploited for numerous applications in infrared spectroscopy such as laser surgery, gas sensing, label-free biological sensing, thermal imaging and infrared countermeasures [215-219]. In initial attempts, mid-IR HCFs were fabricated by coating the inner surface of a capillary tube with a metallic film and dielectric material. However, the coating procedure is relatively cumbersome and used toxic materials. Lately, pure silica HCFs have been investigated [220]. As the mode propagates in the microstructured fibre hollow-core, the effect of the silica's high material absorption is minimized owing to the low overlap (<1%) of the guided mode with the glass.

The metal 3D printing technique unlocked the flexibility of structured nozzle design and fabrication. As presented in chapter 4, two designs of the structured nozzle for fabricating HC-MPOF with different thicknesses of struts and core diameters were manufactured. The difference in the design allows the fabrication of HC-MPOF for various guidance ranges from THz to mid-IR.

7.2.1 Mid-IR HC-MPOF fabrication

In this experiment, the metal 3D printed structure nozzle for fabricating HC-MPOF with thinner struts was selected to fabricate mid-IR guiding fibre. The HC-MPOF structured nozzle consists of a hexagonal air-core with a diameter of 3.2 mm. The thin layer surrounding the fibre core has a thickness of 0.35 mm and the outer diameter of the extruded fibre is 8 mm (Figure 7.9 (a)). The green shaded region in the schematic of Figure 7.9(b) is polymer while the white region represents air. The waves propagating in this fibre are confined by the antiresonance effect owing to the resonant reflection of the guided wave in the air-core with a membrane surrounding the core which behaves effectively as a Fabry-Perot cavity. Thus, the drawing system is required to future reduce the size of the extruded fibre and decrease the strut thickness, as needed for mid-IR guidance based on eq.(7-1).

In this work, guidance in the wavelength range 2 - 6 μm will be targeted because it contains the absorption peaks of C-H and C-O, common bonds for many biological and chemical materials. Therefore, this wavelength range will be useful for biological and chemical sensing applications. By using the relationship between the strut thickness of HC-MPOF and guiding wavelength in eq.(7-1), the thickness of struts should be in the range of 3 - 5 μm to guide mid-IR light in the wavelength range λ~2-6 μm.

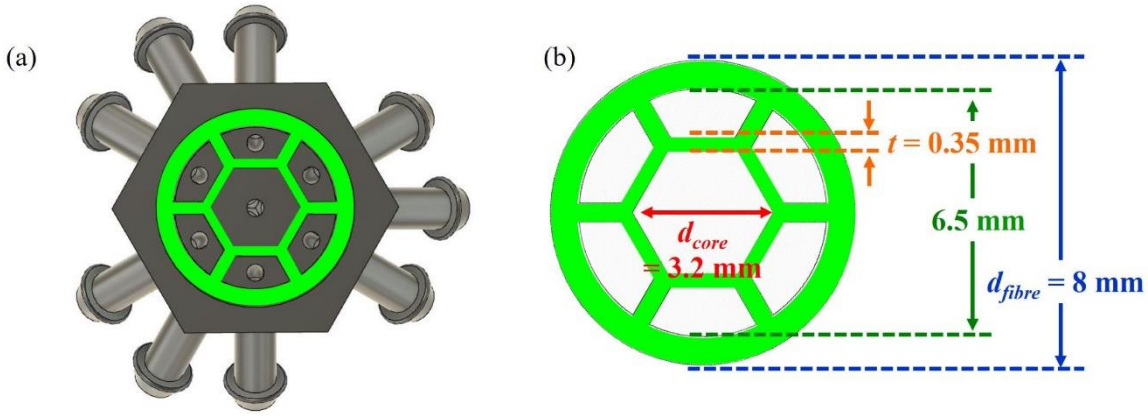

Figure 7.9 (a) Bottom-view cross section of the nozzle for fabricating mid-IR HC-MPOF. Green represents the area filled by the polymer. (b) Schematic of the cross section of the extruded HC-MPOF.

To fabricate the HC-MPOF, the complete fibre drawing setup presented in chapter 5 was used. The printer standard nozzle was replaced by the metal 3D printed HC-MPOF structured nozzle. In this work, Polyethylene terephthalate glycol (PETG) was chosen to fabricate the mid-IR HC-MPOF.

The optimal heater temperature and polymer feed rate were determined empirically from checking the fibre surface quality. During the process, the nozzle temperature (T_n) was varied from 230°C to 290°C, and at T_n ~ 270°C the surface of the polymer became smooth and shiny, with significantly reduced bubble formation compared to other nozzle temperatures. The filament feeding velocity was then gradually varied and an extruded fibre blank with a smooth surface was successfully achieved at s = 250 mm/min and T_n = 270 °C. To further reduce the mid-IR HC-MPOF diameter, the extruded structured polymer fibre cane was connected to the primary drawing system and the fibre was first drawn at a drawing speed of ~1000 cm/min. Then, the drawn fibre from the primary drawing system was connected with the rotating spool of the main drawing system. The drawing speed was started slowly at ~1000 cm/min, then gradually increased to reduce the HC-MPOF diameter. A fibre diameter of d_{fibre}~500 μm (Figure 7.10(a)) was achieved when the drawing speed was ~3000 cm/min. Microscope images of the HC-MPOF cross-section (Figure 7.10) show that the strut thickness is ~4.5 μm when the fibre diameter is 500 μm.

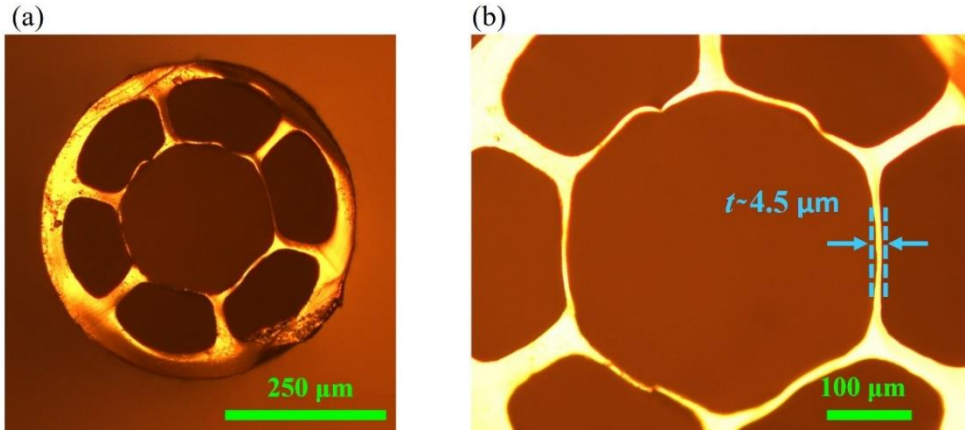

Figure 7.10 (a) Cross-section of the extruded and drawn mid-IR HC-MPOF with fibre diameter of d_{fibre}~500 µm. (b) Close-up view of fibre core showing a 4.5 µm thickness layer surrounding the fibre core.

7.2.2 HC-MPOF characterisation in mid-IR

The HC-MPOF theoretical transmission characteristics were evaluated by using the FEM solver Comsol© mode solution to numerically solve Maxwell's equations in the frequency domain for the electric field. The simulation was performed by creating a 2D model of the fibre cross section structure with the same dimensions as the fibre with a strut thickness of 4.5 µm. By using the formula in eq. (7-1), the resonant wavelengths in the range of interest (2 - 6 µm) are calculated to be λ_m = 2.1, 2.7, 3.6, and 5.4 µm. The modal analysis of the HC-MPOF structure (Figure 7.11(a)) shows that at the resonant wavelength (5.05 µm), the field is poorly confined in the central air core, and the mode in the fibre core is coupling with the surrounding material and leaks out to the cladding, resulting in high loss. Figure 7.11(b) shows that at the antiresonant wavelength (4.0 µm) the field is well confined in the central air core.

The FEM calculated loss spectra are shown in Figure 7.11(c): the peaks of high loss are located at the resonant wavelengths, which correspond to the calculated resonant frequencies. The loss profile in Figure 7.11(c) shows that specific mid-IR wavelength regions in the range λ = 2 – 6 µm experience the antiresonance effect. The chosen HC-MPOF geometry should effectively guide mid-IR in the antiresonant regions and the resonant peaks (where losses are high) are clearly defined. As expected, field confinement becomes stronger as the wavelength decreases because the core size is relatively larger compared to the wavelength. This confirms that most of the power is confined within the central air core.

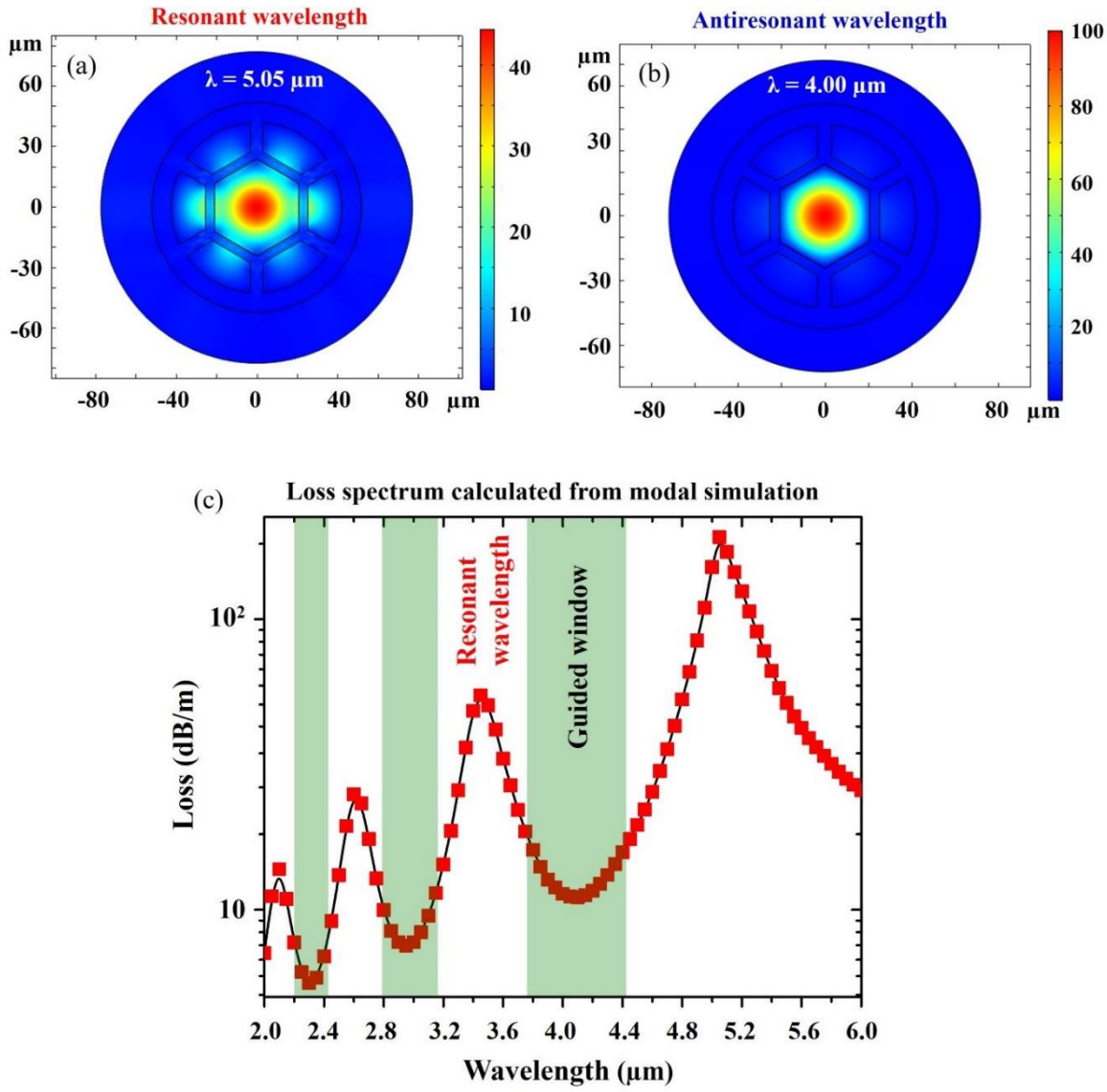

Figure 7.11 Simulated modal intensity profile in the fibre core at (a) resonant (λ_m = 5.05 µm) and (b) antiresonant (λ = 0.40 µm) wavelengths. (c) Calculated loss spectrum for strut thickness t = 4.5 µm.

In order to evaluate the optical guidance properties of the HC-MPOF in the mid-IR, the output from a broadband lamp with emission over λ = 0.45 - 5.5 µm (Thorlabs SLS202) was coupled into a 15 cm long section of a fibre using a bare-fibre adaptor. The modal image was taken by collecting the fibre output at λ = 3.5 – 5 µm with a thermal infrared camera (Onca-MWIR-Insb) using its 100 mm lens. Figure 7.12 presents the thermal image at the HC-MPOF output showing that mid-IR light is guided in the air-core. To confirm the mid-IR HC-MPOF guiding capability, the near-field image of the transmitted light at λ = 3.5 – 5 µm was recorded under different degrees of fibre bending. The bending angle was varied from 0 to 90°. Figure 7.12(a)-(c) shows the HC-MPOF output and its intensity profile for both straight and bent fibres. While for the straight fibre most of the light is guided in the central air-core (Figure 7.12(a)), as the fibre is bent, the peak of the intensity profile increasingly shifts to the side of the air core (Figure 7.12(b)). This behaviour of the HC-MPOF under

different bending conditions is attributed to the multimode guidance (high order modes), which is what is expected for the HC-MPOF with large air core.

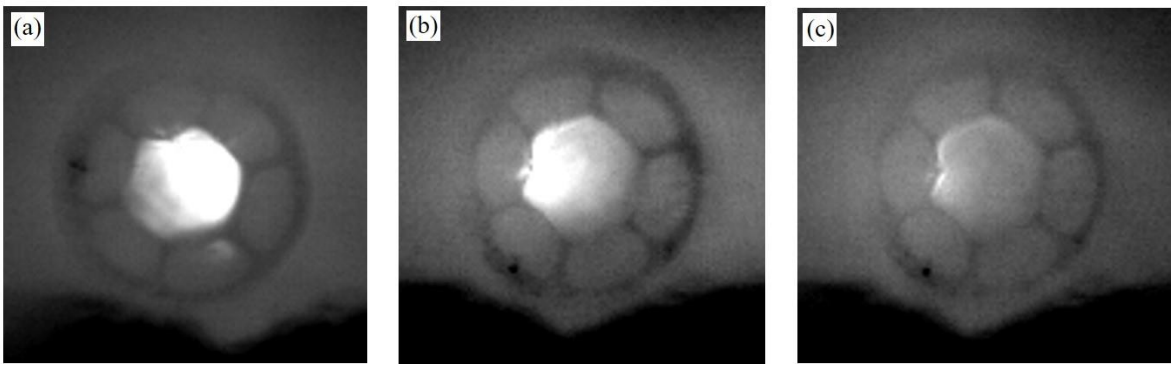

Figure 7.12 (a) Modal intensity profile of mid-IR light transmitted through the hollow-core fibre when straight, (b) at 45° bending (bend radius ~10.4 cm), and (c) 90° bending (bend radius ~6.1 cm).

7.3 Summary

For THz guidance, a TOPAS hollow-core antiresonant fibre fabricated by direct extrusion using a 3D printer has been demonstrated. By using this technique, 1 meter of fibre was fabricated within 30 mins. The modal profile simulations showed the ability of the fibre to confine THz waves at the antiresonant frequencies in the air-core. Time and frequency domain spectrograms also confirmed air-core guidance of the hollow-core fibre. By fabricating the THz HC-MPOF from TOPAS polymer, the propagation loss was measured to be 0.12 dB/cm at 0.7 THz. Both simulations and experimental loss profiles revealed the potential to use the extruded fibre as a THz waveguide in the spectral range 0.4 – 1.0 THz.

For the mid-IR HC-MPOF, modal and loss profile simulations demonstrated the ability to confine light in the air-core in the spectral range λ = 2 - 6 μm. Near field thermal images confirmed the mid-IR guidance in the fibre air-core. By improving the launching conditions and the fibre structure symmetry, the loss can be further reduced, and this will be pursued in future work.

A natural next step of this work would be designing the nozzle die for different optical fibre geometries. The development of new 3D printer filaments, made of different polymers or even soft glasses, can be envisaged. 3D printing can provide a cost-effective production process, for both polymer preforms and optical fibres, compared to conventional high-cost and lengthy two-step fabrication methods.

Loss comparison between the HC-MPOF fabricated from the direct extrusion technique for THz guiding and another hollow-core THz optical fibre fabricated from the 3D printed preform are revealed in Table 7-1.

Table 7-1 Summary of loss from the hollow-core polymer optical fibre for THz guidance fabricated from 3D printing technique.

Fibre Type	**Material**	α **(dB/cm)**	υ **(THz)**	**Year Report**	**Ref.**
Hollow-core antiresonant fibre (Optical fibre implemented in this work.)	TOPAS	0.12	0.7		
Hollow-core photonic bandgap fibre	UV-resin	0.3	0.1	2011	[108]
Hollow-core photonic bandgap fibre	UV-resin	0.08	1	2016	[111]
Hollow-core antiresonant fibre	ABS	0.3	0.47	2015	[105]
Hollow-core antiresonant fibre	PC	10	0.3	2018	[30]
Hollow-core Bragg fibre	ABS	0.1	0.4	2015	[112]
Hollow-core Bragg fibre	UV-resin	0.65	0.35	2017	[106]
Hollow-core Bragg fibre	UV-resin	0.03	0.27	2018	[113]

Chapter 8.

CONCLUSION AND FUTURE WORKS

8.1 Conclusion

The initial aim of this thesis was to explore a novel fabrication method for fabricating microstructured polymer optical fibres (MPOF) capable to overcome the drawbacks of the tower-based fabrication technique, including time-consuming, impossibility of producing more complex non-geometrical structures, and high-cost. When this project started, additive manufacturing (3D printing) was quickly becoming widespread to manufacture optical devices, from lens to optical fibre preforms, due to its simplicity in operating and extreme flexibility. In this thesis, I have shown how 3D printing can be used to fabricate MPOFs for near-IR, mid-IR and THz guidance.

The use of 3D printer for fabricating the MPOFs started from the fabrication of polymer optical fibre preforms. The hollow-core microstructured fibre preform was manufactured with the aim to fabricate mid-IR hollow-core MPOFs for biological sensing applications. A Polyethylene terephthalate glycol (PETG) preform was 3D printed by optimising the printing parameters, including temperature, material flow rate, and material infill pattern. A hollow-core MPOF was achieved by drawing the preform in a furnace for polymer fibre drawing. Mid-IR guidance in the wavelength range 3.5 – 5 µm, was observed in the hollow-core MPOFs by monitoring the near-field image when the fibre was bent up to a bend radius of ~76 mm. A propagation loss of 0.3 dB/mm was observed at the wavelength of 4.5 µm, which is 39 times smaller than the material loss. Yet, deformations in the final structure of the MPOF occurred during the drawing, compromising its guiding properties.

To overcome this issue, a technique was proposed to fabricate MPOFs in a single step using a commercial 3D printer. By using this technique, MPOFs were extruded from the 3D printer through a structured nozzle. The 3D printer nozzle was designed with a cross section complementary to that of the fibre. Five generations of structured nozzles were developed to explore the optimal design parameters for extruding the polymer with a uniform velocity. Simulations of the heat transfer and of the polymer flow through the nozzles were performed. Structured nozzles were also fabricated using metal 3D printing from stainless steel powder with the continuous scan pattern. The metal 3D printed nozzle withstood temperatures of 300 °C and high pressures, demonstrating that 3D printed nozzles have sufficient mechanical strength to enable extrusion of optical fibres.

A fibre drawing set-up was built utilising a 3D printer heater as furnace, a diameter gauge and customised pullers driven by rotary motors. A software was developed to control the heated head and the various motors using Arduino and G-code. The structured nozzle acted as both extrusion die

and also as furnace. The polymer filament was extruded through the heated structured nozzle and the extruded structured fibre cane was drawn directly into a MPOF. For the direct drawing of MPOF using a 3D printer, the drawing parameters including filament feeding speed, nozzle temperature, and drawing speed were optimised to achieve optical fibres with uniform features. Analysis of the fibre produced in this work proved the ability to maintain the microstructure inside the fibre after extrusion and drawing from a customised 3D printer structured nozzle. This demonstration indicates potential to design and fabricate structured nozzles for manufacturing low-cost MPOFs with various geometries. This technique has huge potential, as the microstructure inside the MPOF can be maintained after drawing.

Guiding properties of the drawn suspended-core MPOFs and hollow-core antiresonant MPOFs were characterised. Suspended-core MPOFs were fabricated from two different polymers: ABS for guiding in near-IR, and TOPAS for the THz. For the near-IR characterisation, a measured maximum propagation loss of 1.1 dB/cm at $\lambda \sim 1557$ nm was obtained while the near-field end facet image and the modal profile simulations showed the ability to confine light at $\lambda \sim 1550$ nm in the fibre solid-core. The near field and modal profile simulations demonstrated the ability to guide light in the spectral range ν=0.5-1.0 THz. Time and frequency domain spectrograms confirmed core guidance and allowed to measure an average propagation loss of 0.11 dB/mm at ν=0.4-1.1 THz.

Hollow-core antiresonant MPOFs were also fabricated from two materials for guidance in mid-IR (PETG) and THz (TOPAS). Time and frequency domain spectrograms confirmed air-core guidance, with a confinement loss of 0.12 dB/cm at 0.7 THz. Both simulations and experimental loss profiles revealed the potential to use the extruded fibre as THz waveguide in the spectral range 0.4 – 1.0 THz. For the mid-IR hollow-core antiresonant MPOF, modal profile and loss profile simulations demonstrated the ability to confine light in the fibre air-core in the spectral range $\lambda = 2 - 6$ µm. The near field thermal images confirmed mid-IR guidance in the fibre air-core.

The aim of this research was to use the MPOFs as optical fibre sensors, thus the fabrication and analysis of optical fibre sensors were demonstrated in the first year of this research project.

Temperature and refractive index sensors based on nanofibre couplers (NFC) with sub-micron diameters were fabricated. Temperature and refractive index sensitivity were analysed by monitoring the change of the output spectrum at different applied temperatures. Heat applied to the NFC caused the change of coupler diameter and length due to the thermal expansion of silica and of the refractive index of silica owing to the thermo-optic effect. The NFC temperature sensitivity was analysed by measuring the shift of the wavelength dips close to the cut-off region at different applied temperatures. The temperature sensor based on NFC exhibited a temperature sensitivity of 60 pm/^{o}C at the highest temperature (620 ^{o}C) and a fast response time of $\sim$ 7.2 ms. Ambient refractive index sensitivity of the NFC was also analysed by monitoring shifts in the wavelength dips of the output

spectrum when the refractive index of liquid surrounding the coupling region was varied. A high refractive index sensitivity of 4.80×10^5 nm/RIU was achieved. The use of the microfibre coupler was also expanded to biological sensing, making a DNA sensor. The coupler surface was functionalised to attach the DNA strands on the coupler surface. The aim of this work was to detect the variation of DNA concentration by using DNA functionalised fibre couplers. The successful DNA functionalisation of the coupler surface has been confirmed by taking a fluorescent image of coupler after a fluorescent DNA strand has been attached on the coupler surface. The detailed experimental and sensing analysis of theses sensors was reported in appendix A and B. These results showed the ability to use the optical fibres as various types of sensors which can be applied to the MPOFs fabricated from the novel fibre fabrication technique developed in this research.

8.2 Future works

A number of promising projects could explore and extend the currently presented work further.

1) To apply pressure through the air channels inside the structured nozzle. With applied pressurisation, the fibre geometry could be adjusted to increase the hole size, reduce the struts thickness or the size of solid core. The modification in the fibre geometry during the drawing process allows to decrease the loss of the hollow-core MPOFs by increasing the core diameter, the variation of guiding wavelengths in the hollow-core MPOFs by varying the thickness core surrounding struts, or reducing the core size of solid-core fibre for nonlinear application.
2) To design the nozzle die for different optical fibre geometries. A variety of applications based on MPOFs can be explored for different geometries. The developments in new 3D printer filaments made of different polymers or even soft glasses can also be envisaged.
3) The development in the polymer filament for the 3D printer can be widely expanded. Research on polymer filament fabrication for the low absorption loss in different range of wavelength can be envisages. Dopant polymer with some specific chemical molecules could induce the interaction property of polymer to be use as the optical fibre sensors.
4) The micro/nano fibre coupler can be further developed and optimised for sensing applications because it shows high sensitivity and high compactness. Furthermore, it is possible to configure the micro/nano fibre coupler to be wrapped around a fluidic channel, in which the analyte and microfiber would be in direct contact. Initial calculations were performed to model the dimensions of the fluidic channel required for the purpose of DNA detection. Moreover, a cut-off region in the nanofibre coupler showing attractive sensitivity and tailored detection limit.
5) Surface plasmons could be investigated on micro-coupler tips which gives plenty of advantageous, such as the input and the output will be integrated on the same device, the

possibility to customise the device performance by manipulating the coupler dimensions, and the selective excitation of modes by monitoring modes filtering in the coupler.

6) The applications of the MPOFs can be explored. Optical fibre sensors based on MPOFs can be possible applications due to the intrinsic air holes inside the MPOFs, which allow for ambient materials to get into the optical fibre. After confirming the possibility of attaching DNA to the surface of the microfibre, it is possible to investigate more sensing devices that can show enhanced sensitivity and stability for single molecule detection. Functionalisation on the surface of the inner holes of MPOFs by using specific biological and chemical materials will allow the MPOFs to be used as a biological or chemical sensor such as gas detection, and biomolecules sensing. The built-in air-pressurise channels in the structured nozzles will allow for the gas flow functionalisation during the drawing process. This will be a single step fabrication of the MPOFs for biological or chemical sensor.

The MPOF fabrication in a single step using 3D printers can provide a cost-effective production process, both in terms of polymer preform and optical fibres, compared to conventional high-cost and lengthy two-step fabrication methods which rely on drawing towers. Various types of polymers are commercially available include ABS, PLA, PMMA, Vinyl, PVC, PETG, TOPAS and many more to fabricate the MPOFs by using this developed technique. To date, this technique is limited to fabricate only the polymer optical fibre due to the limitation in the maximum working temperature of 3D printer heater head and the structured nozzle. However, the MOFs fabricated from material with the higher melting temperature such as soft-glass could be achieved when the heater head of 3D printer and structured nozzles have been changed to support the higher temperature than 300 °C. The improvement in the variety of material will allow this technique to be able to fabricate the optical fibre for many guiding regions covering from visible to THz. Ultimately, with a growing interest in the 3D printing for optical applications from institutes around the world, it is envisaged that the research community will continue to offer novel insights into their optical device fabrication based 3D printer and develop innovative applications over the coming years.

Appendix A

TEMPERATURE AND REFRACTIVE INDEX SENSING BASED ON NANOFIBRE COUPLERS

Temperature and ambient refractive index are important parameters that are well known to affect the sensitivity of an optical fibre sensor. In order to be familiar with the fabrication and sensitivity analysis of optical fibre sensors, this project started with the fabrication the temperature and refractive sensors. A submicron size optical fibre coupler guides light mainly in a mode with a large evanescent field surrounding its waist. A peculiar pattern in the coupler transmission spectrum was noticed when the coupler diameter (a) was less than 1 μm. In this work the nanofibre coupler with diameter less than 1 μm has been optimised to fabricate the temperature and refractive index sensor. The fabrication and characteristics of the nanofibre coupler are discussed in section A.1. In section A.2 the experimental setup used to measure the temperature sensitivity and the experimental results are presented. The experimental setup used to measure the refractive index using the nanofibre coupler and the measurement of refractive index are illustrated in section A.3.

A.1 Properties and fabrication of nanofibre couplers

A standard optical fibre coupler is a four-port device (Figure A.1) composed of two independent optical fibres that have been combined together by fusing, polishing, and etching over a small region. When two fibres are stretched or polished and positioned in the close proximity, the core modes interact by exchanging power due to the overlap of the modes inside the common cladding. Modes propagating in the waist region of the fibre coupler are frequently described as supermodes, a superposition of the fundamental and high order modes of the two fibres. When the light is launched at the input port, a number of supermodes is excited in the coupling region of the coupler. Although the coupler supports multiple supermodes, only the first two (even and odd supermodes generated from the interaction of LP_{01}) are excited for an adiabatic coupler.

In the coupling region, both the even and odd modes are interfering in and out of phase due to the accumulated phase along the coupling length. These supermodes experience both constructive and destructive interference in different positions along the coupler longitudinal direction. The power transfer at the output pigtails occurs due to the beating between a symmetric (even) and an asymmetric (odd) supermodes of the composite structure. The beating of supermodes with different propagation constants provide a continuous change in the power distribution along the coupler, which results in a different power splitting at the output ports for different optical paths. In

2009, a microfibre coupler (MFC) with a waist diameter in the region of few microns was fabricated and used as a broadband modal filter [221].

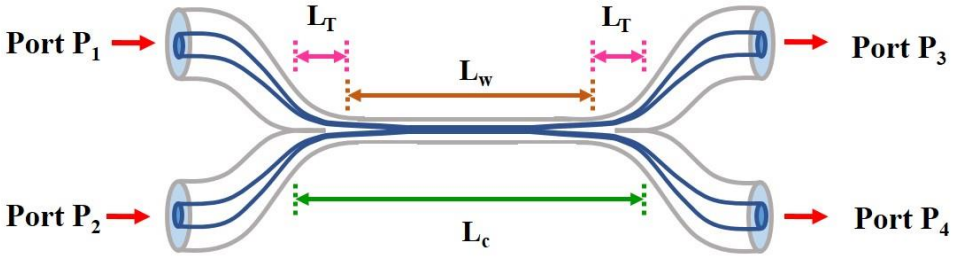

Figure A.1 Schematic of a bi-conical fibre coupler when LC is length of coupling region, which is composed of length of two tapered region (L_T) and length of waist region (L_W).

Consider a 2x2 coupler, where light is launched into Port 1, the normalized field amplitudes of even (A_e(z)) and odd (A_o(z)) supermodes at the coupler input (z = 0) can be expressed by:

$$A_e(0) = \frac{A_1(0) + A_2(0)}{\sqrt{2}} \qquad \text{A-1}$$

$$A_o(0) = \frac{A_1(0) - A_2(0)}{\sqrt{2}} \qquad \text{A-2}$$

where (even $A_e(0)$) and odd ($A_o(0)$) are the normalized amplitudes of the field launched into the two input port 1 (P1) and port 2 (P2), respectively. For single port excitation, $A_1(0) = 1$ and $A_2(0) = 0$, eq. (A-)1 and eq. (A-2) will become $A_e(0) = A_o(0) = 1/\sqrt{2}$, and light launched into one input port of the coupler is excited equally to the two lowest-order (even and odd) supermodes along the coupling region. In an adiabatic coupler, the two supermodes propagate adiabatically along the coupling region with propagation constant $\beta_e(z)$ and $\beta_o(z)$ for even and odd supermodes, respectively. Therefore, the propagation of the electric field at any point along the coupler is described by:

$$E_T(z) = E_e(z) + E_o(z) = A_e(z)e^{-i\int_0^z \beta_e(\zeta)d\zeta} + A_o(z)e^{-i\int_0^z \beta_o(\zeta)d\zeta} \qquad \text{A-3}$$

The even and odd supermodes sustain their amplitude (A_e(z) = A_e(0) and A_o(z) = A_o(0)) during adiabatic propagation and change only their relative phase. This gives rise to the beating between two supermodes along the coupler waist and power distribution between the individual fibres of coupler. The relative accumulated phase difference between the even and odd supermodes is $\phi_{eo}(z) = \int_0^z \triangle\, \beta_{eo}(\zeta)d\zeta = \int_0^z [\beta_e(\zeta) - \beta_o(\zeta)]d\zeta$. So, the electric field of each individual fibre, Fibre1 ($E_1(z)$ and Fibre 2 ($E_2(z)$), along coupling region can be approximated by:

$$E_1(z) = \frac{E_e(z) + E_o(z)}{\sqrt{2}} = \cos\left(\frac{1}{2}\phi_{eo}(z)\right) e^{-i\frac{1}{2}\int_0^z [\beta_e(\zeta) - \beta_o(\zeta)]d\zeta} \quad \text{A-4}$$

$$E_2(z) = \frac{E_e(z) - E_o(z)}{\sqrt{2}} = -i\sin\left(\frac{1}{2}\phi_{eo}(z)\right) e^{-i\frac{1}{2}\int_0^z [\beta_e(\zeta) + \beta_o(\zeta)]d\zeta} \quad \text{A-5}$$

The coupling coefficient (C) describing the strength of interaction between the supermodes is given by C(z) = $(\beta_e(z) - \beta_o(z))/2$. The coupler beat length ($L_B = \pi/C$) is defined as the minimum interaction length that two supermodes are in phase resulting in the constructive interference and all power of light are in the same fibre as launching fibre. The corresponding power of light carried by the individual fibre is given by:

$$P_{1(2)} = \left|E_{1(2)}\right|^2 \quad \text{A-6}$$

$$P_{1(z)} = \cos^2\left(\frac{1}{2}\phi(z)\right) \quad \text{A-7}$$

$$P_{2(z)} = \sin^2\left(\frac{1}{2}\phi(z)\right) \quad \text{A-8}$$

At the point of the coupling region, where ϕ is 0 or a multiple of 2π, the total power is dominantly present in the original fibre (P_1 = 1 and P_2 = 0) resulting in total power at output port 3. On the contrary, at the position along the coupler, where ϕ is the multiple of π, the total power is present dominantly around the coupled fibre (P_1 = 0 and P_2 = 1) resulting in total power at output port 4. Finally, at the position, where ϕ is a multiple of $\pi/2$, the power is equally split between the two parallel fibres ($P_1 = P_2$) result in the same power at output port 3 and port 4 as shown in Figure A.2.

The NFC was fabricated from two telecom fibres (Corning SMF-28e) using the modified flame brushing technique [222]. The two single-mode fibres were stripped of their acrylic coating over a length of ~50 mm and twisted 1.5 turns around each other. The twisted region was fused together using a resistive ceramic microheater (NTT-AT, Japan) at an estimated temperature of T~1450 ^{o}C. An optical microscope image and a scanning electron microscope (SEM) image of the NFC are shown in Figure A.3(a) and (b): the length of the uniform waist region of the fabricated NFC was 4 mm with a coupler waist diameter of ~ 1120 nm, providing a single nanofibre diameter of ~ 560 nm.

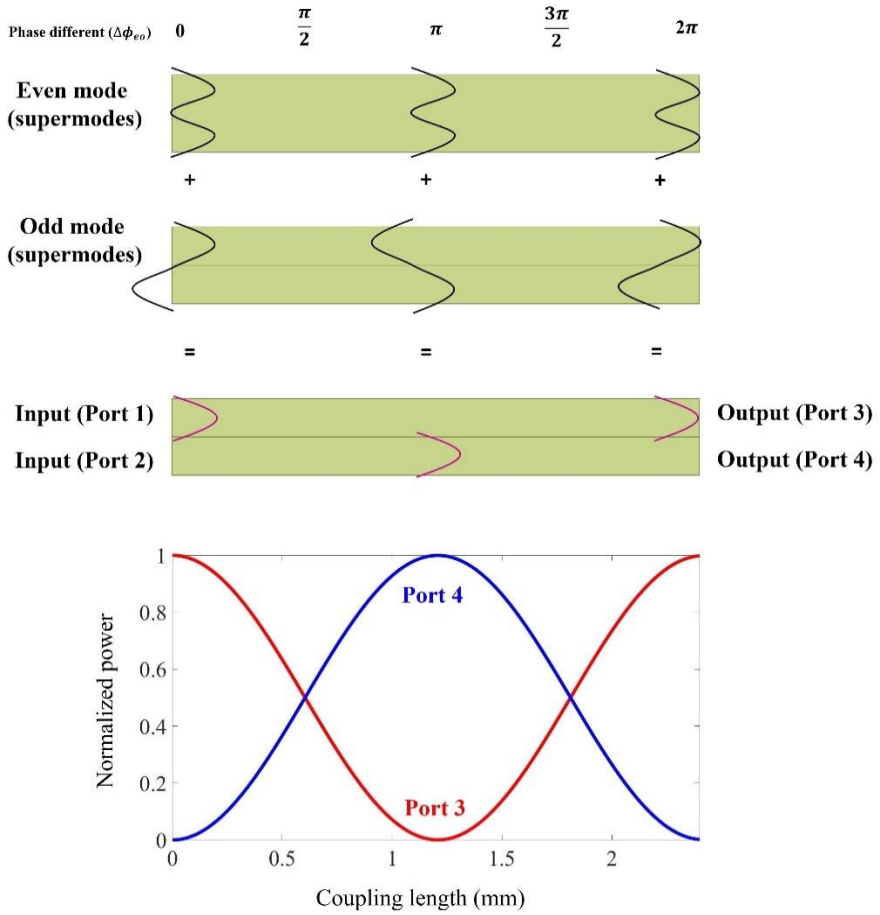

Figure A.2 Schematic of beating of even and odd supermodes and total power evolution along a 2x2 full-cycle coupler ($\Delta\phi_{eo} = 2\pi$) coupler.

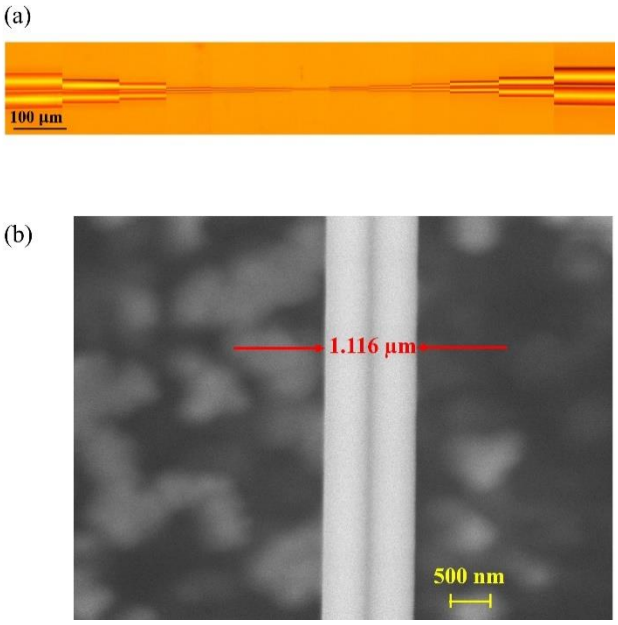

Figure A.3 (a) Microscope image of the NFC with a uniform waist diameter of 560 nm; (b) SEM image at the waist region.

The power of the nanofibre coupler was continuously monitored during the fabrication process. A laser diode (Thorlabs, CLD1015), operating at the telecom wavelength 1550 nm, was launched into the input port 1 of the coupler. The power at the two output ports was recorded in real time with a power meter. Figure A.4 illustrates the output power from the through and coupled port during the manufacturing. The result indicates that the power exchange starts when the coupler diameter is approximately 5 µm. The transmission power at this point reveals that the power of the output port 3 (port 1-3) is minimum, while the power of output port 4 (port 1-4) is maximum.

The beating frequency between two supermodes increases as the pulling continues resulting in the increase of the power transfer between two output ports (Figure A.4). This indicates an increase in the coupling coefficient caused by the increased degree of fusion.

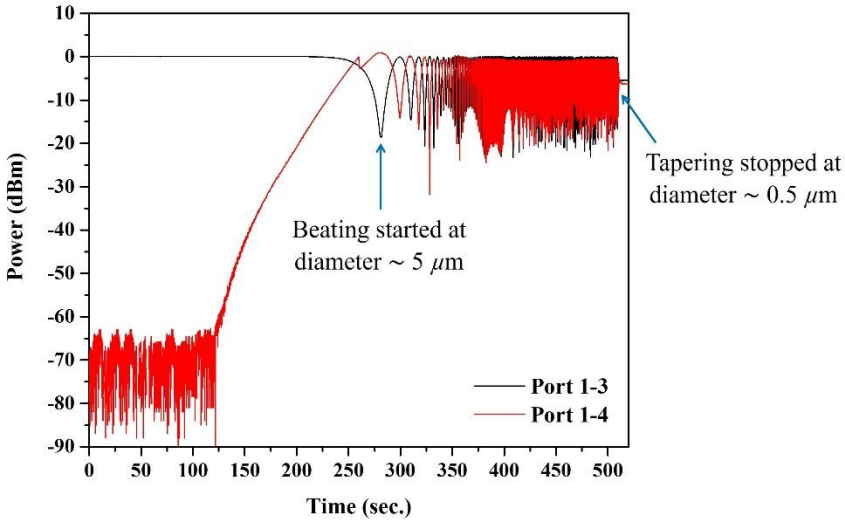

Figure A.4 Output spectrum of the optical nanofibre coupler with a waist diameter of ~ 560 nm.

Figure A.5(a) shows the spectrum of the coupler before fusing the two fibres together. No oscillation is observed. The oscillations featuring a high extinction ratio and low frequency (Figure A.5 (b)) appear at diameters smaller than 10 μm and indicate a relatively low coupling between the two fused fibres. At a smaller diameter (~ 2 μm, Figure A.5 (c)) the beating frequency between supermodes increases due to the increased coupling. The beating is much faster when the diameter is smaller (~ 1 μm) as presented in Figure A.5 (d) and Figure A.5 (e). When the diameter of the optical fibre coupler is about 0.5 μm (Figure A.5 (f)), deep oscillation (~ 10 dBm) can be noticed in the wavelength range λ~1350 -1550 nm. These deep oscillations result from the fact that only the first and second supermodes exist in the coupler. At a ~ 560 nm only one supermode is supported at λ>1560nm. In the multimode region at λ < 1520nm, the beating between two supermodes gives oscillations with high extinction ratios. In the cut-off region (1520nm < λ < 1560nm), the two supermodes stop beating as one of them is weakly guided because of the small diameter and the asymmetry of the coupler. This results in a bump with flat transmission over nearly 40 nm. At longer

wavelengths, only one supermode is supported by the NFC, resulting in a constant output at both ports as shown in the single-mode region in Figure A.6.

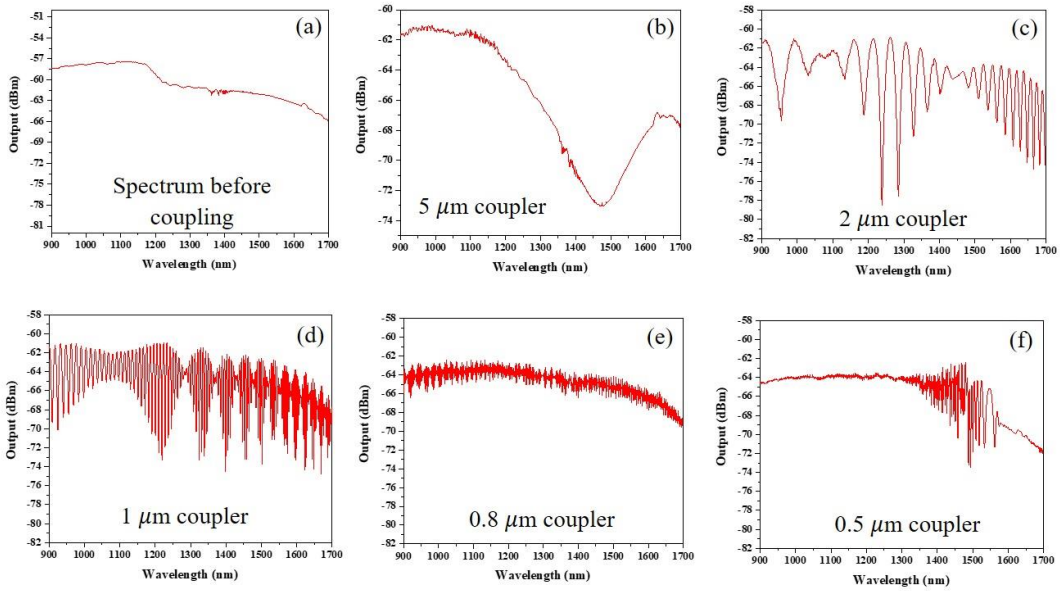

Figure A.5 Output spectra of the nanofibre coupler (output port 3) at different diameters: the coupler behaves differently at different waist diameters: (a) spectrum before coupling, (b) $a \sim 5$ μm, (c) $a \sim 2$ μm, (d) $a \sim 1$ μm, (e) $a \sim 0.8$ μm, (f) $a \sim 0.5$ μm.

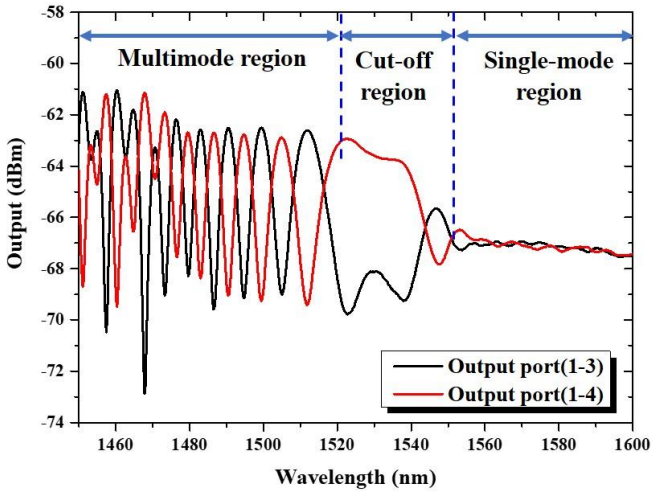

Figure A.6 Output spectrum of the optical nanofibre coupler with a waist diameter of 560 nm.

Optical paths of supermodes depend both on the coupling region length and its refractive index; since both depend on the refractive index of the surrounding environment thus on its temperature, the NFC can be used as a highly sensitive temperature or refractive index sensor.

A.2 A Temperature sensor based on NFC

In the temperature measurement, the same microheater used to fabricate the NFC was used to apply heat to the sensor. The coupling region of the NFC was inserted into the centre of the

microheater. Light from an incoherent white light source (Bentham, WLS100) was launched into Port 1 of the NFC and the output of Port 3 was connected to an optical spectrum analyser (Yokogawa, AQ6370) to monitor in real time the transmission spectrum. The microheater temperature was altered by increasing the current from 0.2 A to 1.2 A in steps of 0.1 A. The increase of the applied current caused an increase of the microheater temperature from T=84ºC to T=661ºC. In this experiment, the current was maintained for 15 minutes at each step to ensure that the microheater temperature is stabilized.

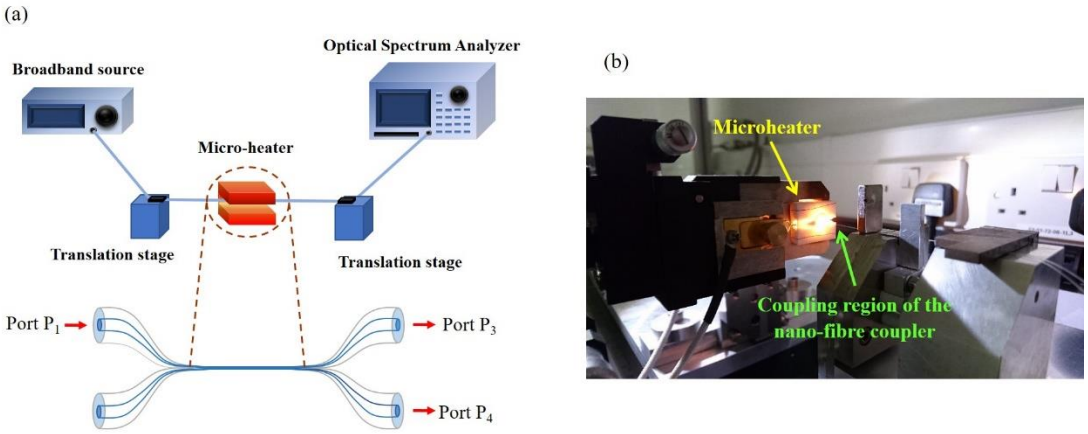

Figure A.7 (a) Schematic, (b) Experimental setup used to measure the NFC output spectrum at different temperatures.

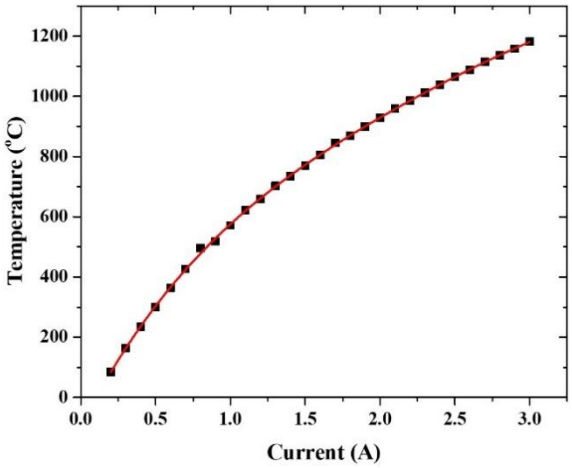

Figure A.8 Microheater calibration curve.

To evaluate the sensitivity of the nanofibre coupler thermometer, the three transmission wavelength dips closest to the cut-off region at the lowest temperature (84ºC) were monitored (Figure A.9). The wavelengths of dip1, dip2, and dip3 are λ=1505 nm, 1495 nm, and 1487 nm, respectively. When the coupler is heated, the refractive index of silica increases due to the thermo-optic effect while the coupler diameter and coupler length increase because of thermal expansion. These changes cause the shift of the destructive interference responsible for the dips to longer wavelengths. A red

shift of transmission spectrum can be clearly observed for increasing temperatures. At T= 478ºC, dip1 moved into the cut-off region and the weak guidance of the odd supermode resulted in the disappearance of dip1. Similarly, dip2 disappeared at T= 661ºC.

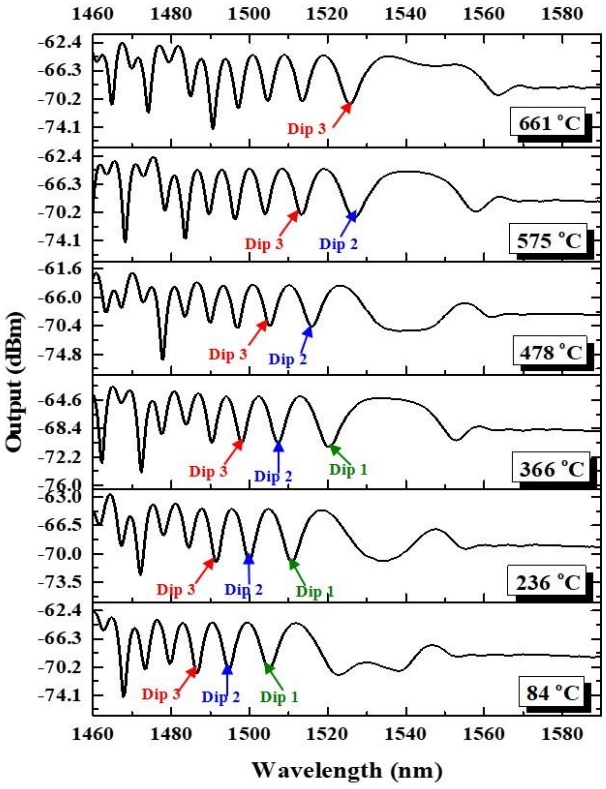

Figure A.9 Optical nanofibre coupler transmission spectrum at different temperatures.

Results indicate that the wavelength of dip1 can be used to measure temperatures from 0 to 424ºC, while those of dip2 and dip3 up to the temperatures of 620ºC and 661ºC, respectively (Figure A.10). By fitting a polynomial function of second degree, the slope of dip1 at the highest temperature of 424ºC was calculated to be equal 50.80 pm/ºC while the slope of dip2 and dip3 at the highest temperatures of each dip were calculated to be equal 60.17 pm/ºC, and 55.23 pm/ºC, respectively.

To compare the temperature sensitivity of the three wavelength dips, the slope of each graph was measured at the same temperature of 424 ºC (Figure A.10(d)). In the temperature range of 0 - 424 ºC, the sensitivity of dip1, dip2, and dip3, are S_1=50.80 pm/ºC, S_2=37.21 pm/ºC, and S_3=33.14 pm/ºC, respectively. The result shows that spectral features at longer wavelengths, especially those in close proximity to the cut-off region, exhibit higher temperature sensitivity than those at shorter wavelengths. Yet, wavelength dips closer to the cut-off region present a smaller dynamic range.

The NFC thermometer repeatability was measured by recording the output spectra for increasing and decreasing temperatures with an interval of one hour. The wavelength shift of the resonance wavelength at dip 3 at different values of T is shown in Figure A.11. Results show that the NFC thermometer has good repeatability.

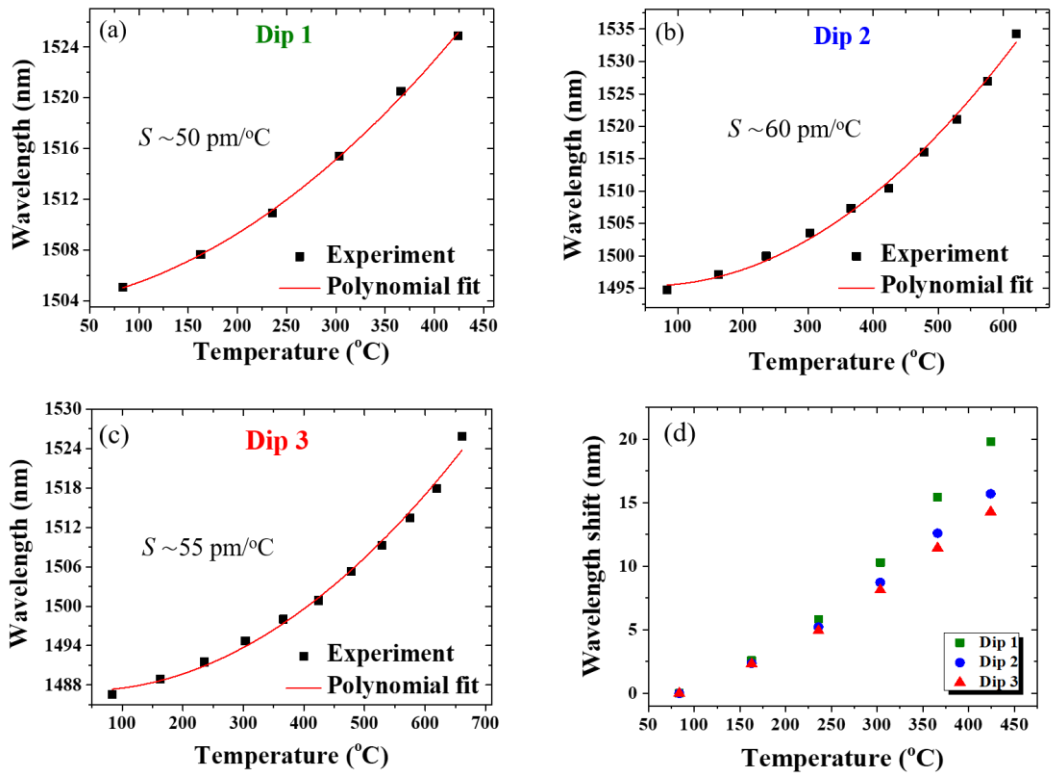

Figure A.10 Relationship between wavelength and applied temperature for different wavelength dips (a) Dip1, (b) Dip 2, (c) Dip 3, (d) Dip 1 – 3 with the same applied temperature (424 °C).

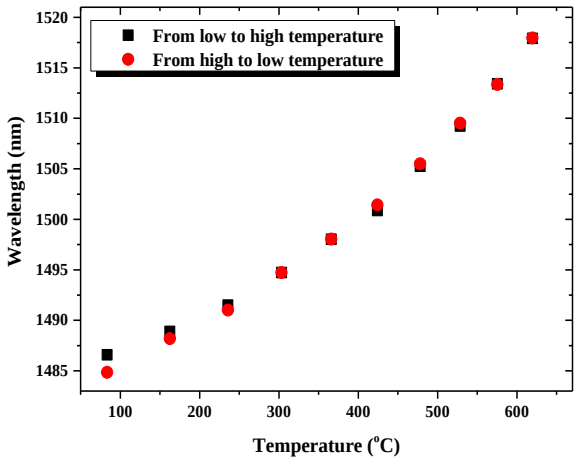

Figure A.11 The wavelength shifts of wavelength dip 3 at different T. The red dots and the black dots report measurements for decreasing and increasing temperatures, respectively.

The response time of the NFC thermometer was evaluated monitoring the transmission change at $\lambda \sim 1496.5$ nm for $a \sim 560$ nm diameter NFC. Figure A.12(a) shows the transmission wavelength at $\lambda \sim 1496.5$ nm at room temperature (blue dash curve) and at T~661 °C (red solid curve). When the temperature decreases, the transmission wavelength dip moves to short wavelengths, but temperature monitoring can also be carried out evaluating the power change over a bandwidth of 1

nm at a fixed wavelength as shown in Figure A.12(a). Here the OSA was used as a replacement for a passband filter and a power meter at λ = 1499 nm. Figure A.12(b) shows that when the temperature was decreased, the recorded intensity at λ = 1499 nm increased, with a response time of τ~7.2ms.

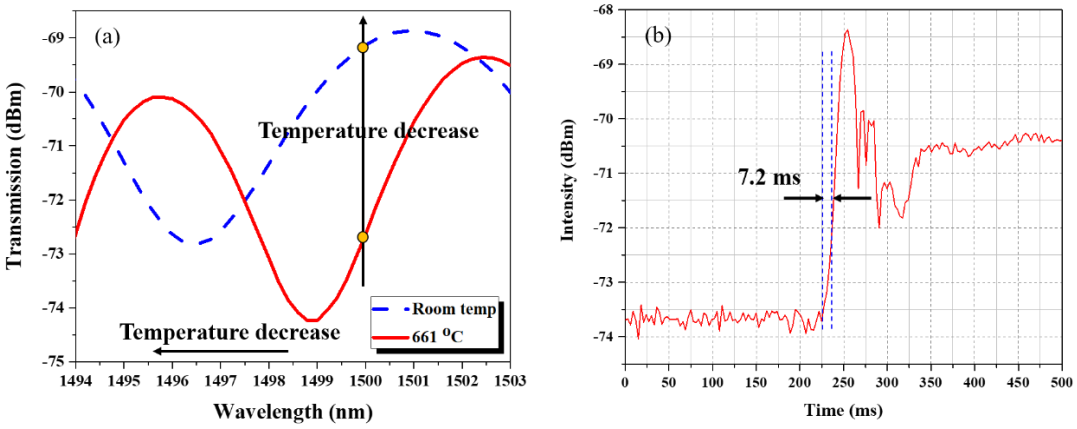

Figure A.12 (a) NFC transmission spectrum at two different temperatures, (b) Temporal dependence of the NFC transmitted intensity recorded at λ = 1499 nm for a rapid temperature change.

A.3 Refractive index sensor based on NFC

In refractive index measurements, the waist region of NFC was immersed in 100 ml of distilled water. As before, light was launched from an incoherent white light source into Port 1 of the NFC, while the output of Port 3 was connected to an optical spectrum analyser to monitor the transmission spectrum in real time. The refractive index (RI) of the solution was increased by adding ethanol into the distilled water by 20 µl at each step. In the experiment, the broad peak in the transmission spectrum was monitored at different ambient RI to achieve a large dynamic range.

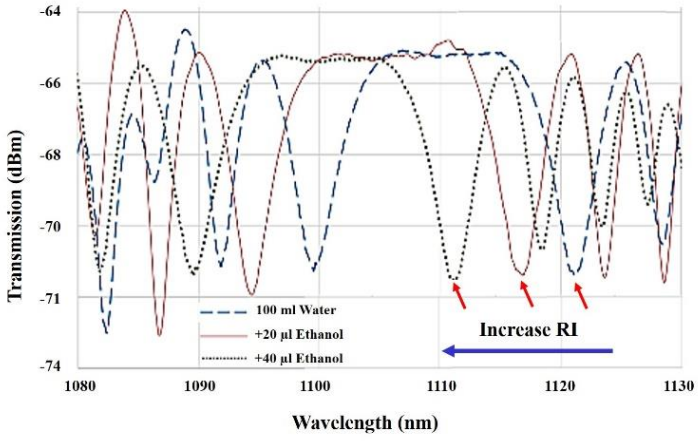

Figure A.13 Change in transmission in the NFC cut-off region at different ambient refractive indexes. Arrows point at the peak used for the sensitivity measurement of figure A.14.

Results show that the NFC transmission spectrum shifted to shorter wavelengths with increasing ambient RI (Figure A.13). To measure RI sensitivity of the sensing device, the RI of an

ethanol solution was calculated from the calibration curve of ethanol and water mixture [223],reported in Figure A.14(a). Figure A.14(b) shows the measured spectral response with the ambient RI values which were calculated from the equation presented in Figure A.14(a). By fitting the wavelength dip and the ambient RI with a linear fit, a slope equal to -4.80x10^5 nm/RIU was calculated, providing an overall refractive index sensitivity of S=4.80x10^5 nm/RIU.

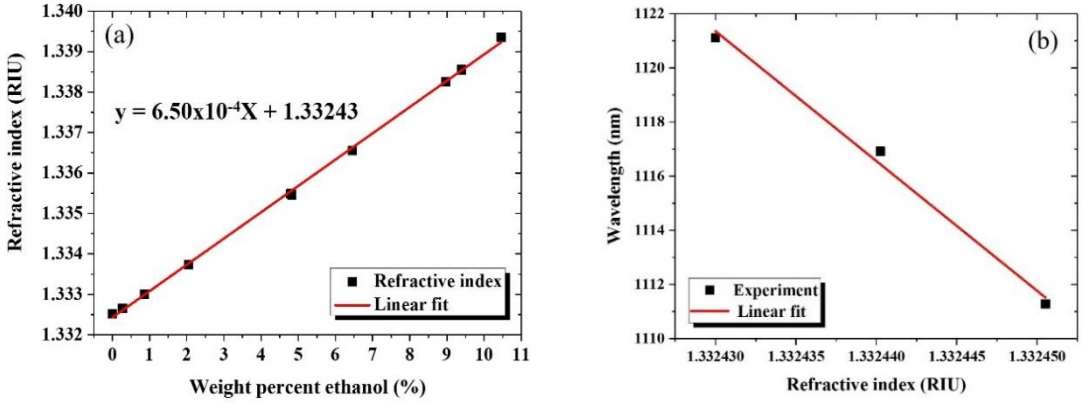

Figure A.14 (a) Dependence of the refractive index of water/ethanol mixtures on the weight percent of ethanol [223], (b) Relationship between wavelength dip and the RI value of the surrounding medium.

A.4 Summary

In conclusion, a thermometer and refractometer based on the cut-off wavelength region of a nanofibre coupler have been investigated. These temperature and refractive index sensors have numerous advantages such as compact size, high sensitivity, and fast response. By monitoring the wavelength of the transmission dips as the temperature increase, a thermometer based on the NFC with the large dynamic range and a high temperature sensitivity of 55.2 pm/^{o}C has been achieved. It efficiently detected high temperatures changes, up to 661^{o}C with a response time of 7.2 ms. The temperature sensitivity achieved by using the NFC is approximately 5 times larger than that of sensors based on microfibre couplers. This is a significant improvement compared with earlier demonstrations using larger micron-size fibre coupler thermometers [224]. The NFC also revealed a high sensitivity with the ambient refractive index owing to the large evanescent field. A record refractive index sensitivity of S=4.80x10^5 nm/RIU was obtained. These results show that fibre nanocoupler have strong potential as a high sensitivity refractive index-based sensor for biological and chemical sensor.

Appendix B

MICROFIBRE COUPLER FOR DNA DETECTION

Biological and chemical sensors are attracting increasing attention because of their application in medical diagnostics, development of novel drugs, testing food for hazardous substances, and forensic. Currently, biological and chemical sensors based on an optical fibre are of the great interest due to the miniaturisation of a sensing device, flexibility of the geometry, the ability to measure small volume of a sample, remote sensing in harsh environment, and multi-sensing possibility. Optical fibre sensors based on biological sensing have been developed for detecting many of biological analytes; such as protein, glucose, molecule, biological cell, and DNA. In this decade, detection of DNA interactions using optical fibre sensors have been investigated for many applications, such as biotechnology, genetics, medical diagnostics, and pathogen detection.

Biological sensors based on optical fibres can be differentiated into two types. The first one is intrinsic fibre-based sensors, where the fibre itself can provide the sensing area, either through its external surface or, in the case of microstructure fibre, through the capillary holes running along its length. The other type is extrinsic fibre-based sensors, where a functionalization of the external or of the internal fibre surface with biological analyte sensing probes, and a mechanism for the transduction of the binding event into an optical signal are needed.

In general, in order to generate a physical signal, the surface of a biosensor requires a modification with materials (probes) able to change their status upon interaction with the molecule (analyte) to be detected. In the case of DNA detection, a functionalization process such as a chemical treatment, or derivatization, is needed. So, the optically sensitive surface is able to bind to a specific DNA sequence, a phenomenon referred to as DNA hybridization.

In appendix A, the possibility to use a micro/nanofibre coupler as a refractive sensor has been revealed. High refractive index sensitivity can be achieved due to its small diameter and large evanescent field. Microfibre coupler (MFC) sensors based on evanescent fields rely upon a refractive index (RI) change induced by molecular interactions, with receptors associated on the surface; this RI change gives an indication of the substance concentration or surface density. MFCs with their attractive features of large evanescent field and low coupling losses, represent the ideal transducer element for biosensors. Devices that are fabricated with these MFCs are compact, low loss and highly sensitive. In addition, they are suitable for the analysis of small sample volumes. Moreover, the sensitivity, response range and detection limit can be maximized by optimising the device dimensions. To detect the variation of ambient refractive index causes by the changing of DNA concentration, microfibre coupler (MFC) was chosen to fabricate DNA sensor in this work.

In this work, the possibility of using a microfibre coupler as DNA sensor is presented. This chapter begins with the description of the microfibre coupler fabrication and preparation of sample before functionalisation (section B.1). In section B.2, the process of DNA functionalisation to modify surface of coupling region in microfibre coupler will be presented. Finally, the experimental result of DNA functionalisation will be described in section B.3.

B.1 Simulation and fabrication of microfibre coupler DNA sensors

Before fabricating the MFC for DNA detection, the fabrication parameters needed to be simulated to obtain optimal sensor sensitivity and detection limit. As described previously, the MFC is very sensitive to any change in the coupler waist diameter and coupling length. Thus, it is important to calculate the expected wavelength shift induced by changing refractive index of environment with the coupler diameter and coupling length. The change in the surrounding medium of the coupler affects the light guided inside the coupler, and this can be related to the quantity of DNA on the surface. The change in the index is evaluated from the wavelength shift of the coupler transmission spectrum in comparison to the input. The ambient refractive index changes of MFC produced by depositing the DNA is expected to be relatively large, therefore it is possible that the coupler dynamic range can be exceeded.

DNA hybridization to functionalise silica yields a refractive index change (Δn) in the range of $\sim 10^{-5}$- 10^{-2} for DNA concentrations between 0.5 – 2 µg/mL [225]. The sensitivity of the sensor depends on the coupler waist diameter. The MFC can be seen as a weakly fused coupler, approximated as two touching cylindrical waveguides. In this case, the coupling coefficient for the X polarization (C_x) and Y polarization (C_y) are given by [226]:

$$C_x + C_y = \frac{2^{7/2}(n_1^2 - n_0^2)^{1/2}U_\infty^2}{n_1 a(\sqrt{\pi})V^{5/2}} \quad \text{B-1}$$

$$C_x - C_y = \frac{2^{5/2}(n_1^2 - n_0^2)^{1/2}U_\infty^2}{n_1^3 a(\sqrt{\pi})V^{7/2}} \quad \text{B-2}$$

where a is the nanofibre diameter, U_∞= 2.405 and $V = [(2\pi a)/\lambda](n_1^2 - n_0^2)^{1/2}$ and n_1 and n_0 are the refractive indices of the silica and ambient air, respectively.

If the light injected at the input Port 1 in the NFC is unpolarised, the normalized power at the output port is described by [226]:

$$P = \frac{1}{2}\left[1 + \cos\left((C_x + C_y)\cdot L\right)\cos(C_x - C_y)\cdot L\right] \quad \text{B-3}$$

where L is the coupling region length of the NFC.

By using the coupling equations described above, the MFC wavelength shift dependence on the change of ambient refractive index (in the order of 10^{-2}) have been simulated with different coupler waist diameters. The modelling result in Figure B.1 shows that a 2 μm diameter MFC has a wavelength shift 4 times larger than that experienced by a 5 μm diameter. So, a higher DNA sensitivity is obtained for smaller diameter couplers. However, there is a trade off as the smaller couplers have a limited dynamic range but are likely to be more sensitive and have a better limit of detection.

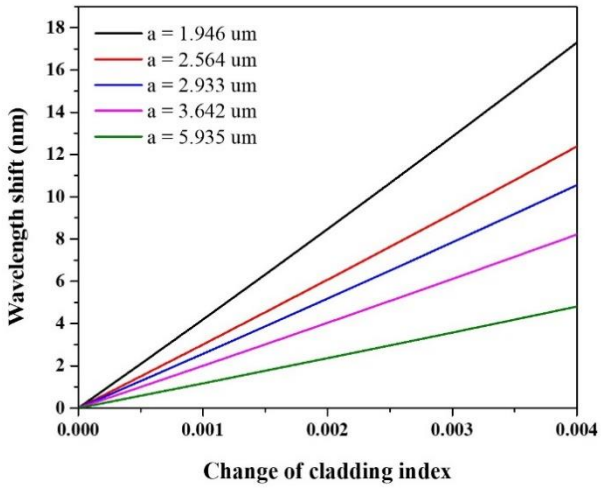

Figure B.1 Dependence of the output wavelength shift on the increase of the cladding refractive index for different coupler waist diameters.

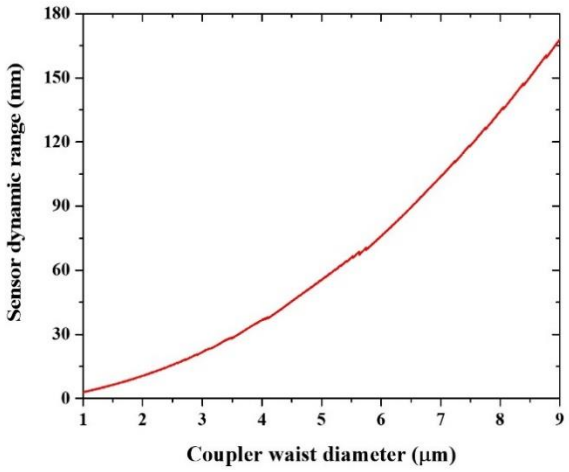

Figure B.2 Relationship between dynamic range of sensor based MFC and the coupler waist diameter

As presented in Figure B.2, the dynamic range of the sensor based MFC decreases at smaller coupler diameters, thus the fabrication parameters need to be considered as a function of the sensitivity and detection limit required. On the other hand, the wavelength shift is consistent at different values of coupler length. A change in the coupling length does not induce a variation in the coupler transmission wavelength shift. So, the RI sensitivity does not change with the variation of

coupling length. To use small volumes of solution for DNA detection, the short coupling length will be selected as it reveals the same RI sensitivity as long coupling lengths. Furthermore, the sensor based MFC with short coupling lengths will provide more stability than long coupling lengths.

Results reveal the expected dependency of the shift of the coupler transmission profile on the DNA concentration at the coupler surface, where the required sensitivity and dynamic range could be obtained by carefully matching the coupler geometry with the required DNA molecule concentration levels to be tested. By modelling the wavelength shift, the optimised MFC dimensions for DNA sensor were found to be 2 µm for the coupler diameter and 4 mm for the coupling length. The simulated output spectrum for such MFC is presented in Figure B.3(a). Figure B.3(b) shows the predicted wavelength shift of the coupler transmission produced by the DNA binding. Results show that the wavelengths are shifted to shorter wavelength with an increasing of the ambient refractive index.

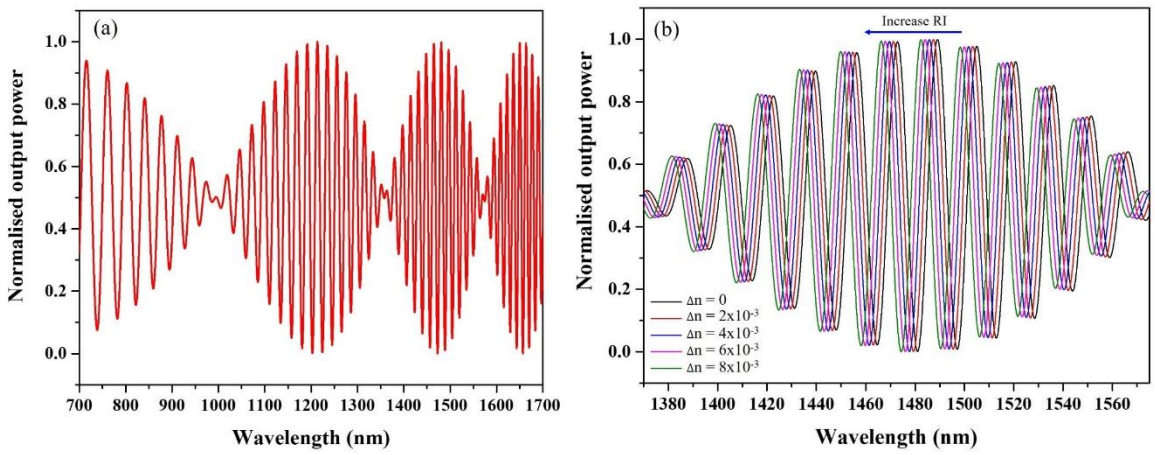

Figure B.3 (a) Simulated transmission spectrum from a 2 µm diameter coupler with coupling length of 4 mm; (b) Shift of the output spectrum associated to increases in the surrounding environment refractive index.

The MFC was fabricated by pulling and stretching two telecom fibres (Corning SMF-28e, United States) using the microheater brushing technique presented in Chapter 3. The final dimension of the MFC for a DNA sensor were 2 µm diameter and 4 mm coupling length.

The simple optical fibre biosensor (shown in Figure B.4) is based on the immobilization of the biorecognition molecules, which in this case will be a target DNA strand. Typically, sensors are kept in a buffer to maintain the integrity of the surface attached biorecognition molecules. The analyte of an unknown concentration is then added to the surface and then associates with the recognition molecule. The detection is a result of the difference in the RI, due to an increase in refractive index upon surface attachment of the analyte. This RI change can optically detect by the light guided by sensor.

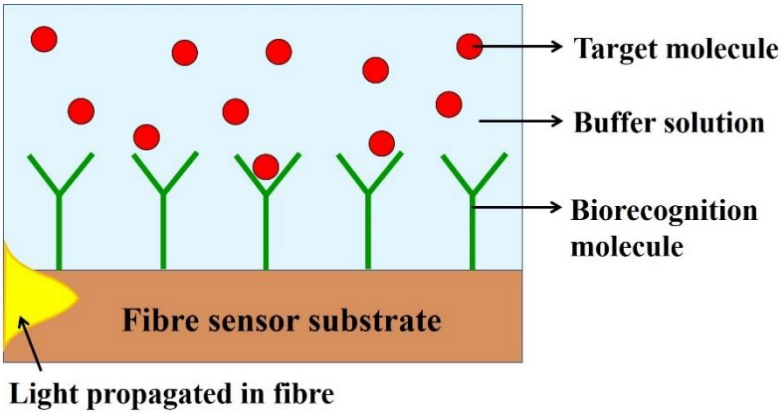

Figure B.4 Schematic of an optical-based biosensor

The method used for external covalent attachment of single stranded DNA to the coupler surface involved first inserting a fibre coupler into a fluidic channel as shown in Figure B.5(a). The materials used for fabricating fluidic channels are bio- and chemical-compatible material. Firstly, a polytetrafluoroethylene (PTFE) tube with an inner diameter of 1.5 mm was used as a fluidic cavity Figure B.5(a)). A MFC with a single fibre diameter of 2 µm was threaded through the tube. The coupling region was placed at the centre of the tube and two coupler ends were fixed at the tube inlet and outlet by using a plastic tape. During the functionalisation process, chemical liquids were flushed through the coupler surface and nitrogen gas was flushed through the channel in the next step to clean the tube and surface of the sample. The electrostatic force between the thin coupler waist and the inner surface of the tube is the main reason for breaking the fibre at this stage of the experiment. The stability of MFC during the functionalisation process was improved by making a teflon (PTFE) chamber with inlet and outlet valves as shown in Figure B.5(b). By using this fluidic cavity, the fibre can be placed in a vertical direction inside the cavity and the stability of fibre can be improved when the cover is placed on top of the cavity. The coupler can detach from the surface of the cavity when the liquid is flushed through the coupler in the vertical direction. Yet, the chemical liquid cannot be cleaned properly during the functionalisation process due to the small gap between the tank and lid. This lead to an incomplete of covalent attachment of DNA on the fibre surface. Therefore, the fluidic cavity for the MFCs functionalization is redesigned to improve the stability of the coupler during and after functionalisation process and to achieve complete covalent attachment of DNA to the coupler. The holder with a 30 mm length and 5 mm width cavity was 3D printed using PETG. The fibre coupler was placed into the cavity and two coupler ends were fixed to the channel by using a bio-compatible epoxy glue (Araldite Rapid) (Figure B.5(c)). The transmission spectrum of a 2 µm diameter MFC was monitored before and after fixing the fibre to PETG holder as presented in Figure B.6.

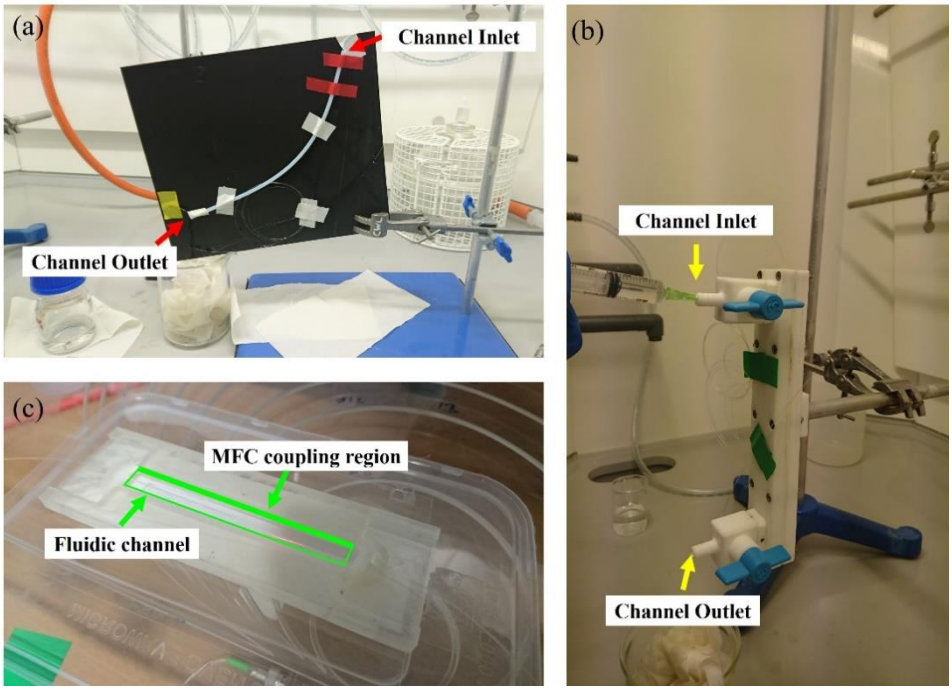

Figure B.5 Experimental arrangement of DNA functionalisation when MFC was inserted in (a) PTFE tube with inner diameter of 1.5 mm, (b) a Teflon™ fluidic channel, (c) 3D printed PETG™ holder with fluidic cavity.

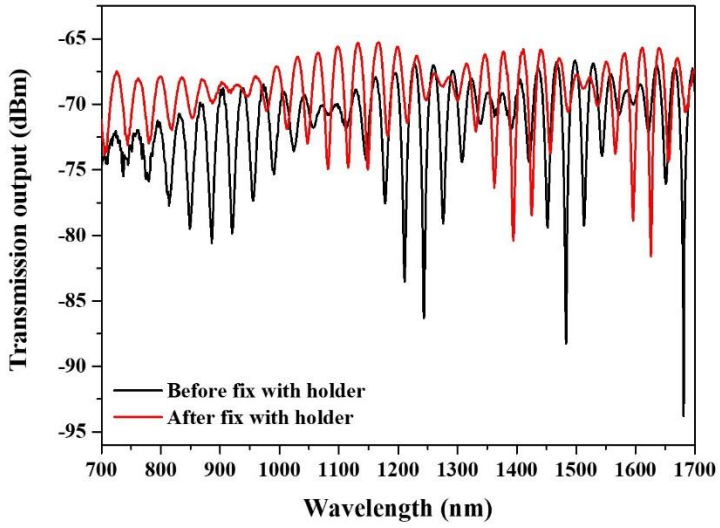

Figure B.6 Shift in the output spectrum of the fabricated optical microfibre coupler during fixing to the holder. Waist diameter: 2 µm, coupling length: 4 mm.

B.2 DNA functionalisation

The method to covalently attach a single DNA strand and its fluorescent label to the surface of a MFC coupling region is divided into 4 steps including fibre cleansing, silanization, cross link, and hybridisation, by following the step of covalent attachment of synthetic DNA to self-assembled monolayer films on fused silica surface [227].

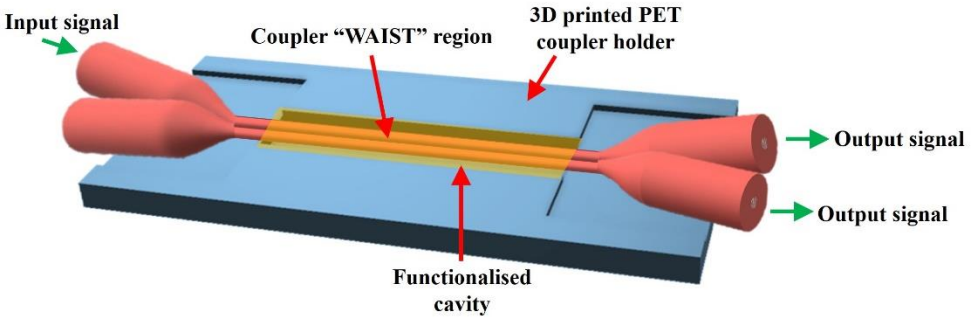

Figure B.7 Schematic of the experiment configuration used to functionalise DNA on the coupler surface.

B.2.1 Cleaning

The surface of the coupler was cleaned with a solution of 1:1 concentrated hydrochloric acid (HCl): methanol (MeOH) for 30 min at room temperature, and then rinsed with deionised (DI) water. This process activates the surfaces prior to silanization, generating accessible hydroxy groups (SiOH) which displace the alkoxy groups on the silane, forming a covalent -Si-O-Si- bond on the glass surface.

B.2.2 Silanization

The coupler waist was functionalised using a 1% solution of distilled N-(2-aminoethyl)-3-aminoethylamino propyl trimethoxysilane in 1 *mM* acetic acid in DI water for 20 min at room temperature. Then, it was rinsed three times with DI water and dried under nitrogen (N_2).

B.2.3 Cross-linking

In order to provide a chemical moiety suitable for the surface modification [228], and to link the biomolecule to the silanized surface, the surface of the MFC was then modified with the heterobifunctional crosslinker , N--maleimidobutryl oxysuccinimide ester (GMBS), prepared as a 1*mM* solution. The crosslinker was dissolved in 100 µL Dimethyl sulfoxide (DMSO) and diluted to 3.7 ml in 80:20 MeOH:DMSO. The GMBS crosslinker solution was introduced into the PETG cavity around the silyl-functionalized MFC and left for 2 hours at a room temperature. The MFC was then rinsed three times with MeOH and dried with N_2. The transmission of the coupler at this point will be a reference for the starting point for probe DNA surface attachment. For the attachment of the DNA, 3' end labelled thiol hexyl-DNA oligonucleotide (5'CACAAAGACTGCTGTCATA-C7 THIOL) in deaerated 10 *mM* HEPES, 5 *mM* EDTA buffer (PH 6.6) was used. The concentration of the DNA solution was of the order of 0.5 µg/mL. Immobilization was completed by immersing the GMBS functionalised coupler in a thiolated-DNA solution for 2 hours at room temperature, then rinsed with HEPES/EDTA buffer several times and dried under N_2.

B.2.4 Hybridisation process

For the hybridization of the complimentary DNA: 3'-florescent end DNA oligonucleotide in deaerated 10 *mM* HEPES, 5 *mM* EDTA buffer was added and kept at 4 ºC in the fridge overnight. The DNA sequence for the single strand DNA and the fluorescent labelled complementary strand is shown in Figure B.8. The MFC functionalised with the probe oligonucleotide was hybridised with a fluorescein-labelled probe oligonucleotide.

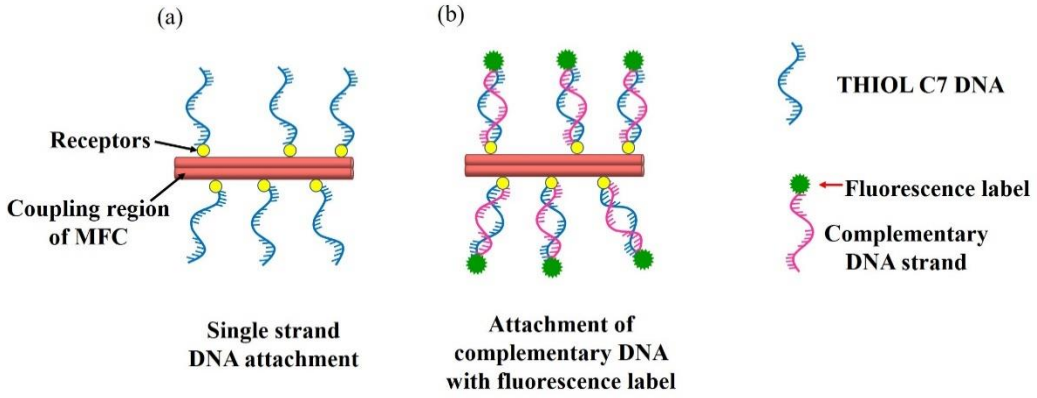

Figure B.8 Schematic of covalent DNA attachment on MFC coupling region (a) Single strand DNA attachment, (b) Complementary DNA strand attachment.

B.3 Experimental results

At this stage, the output spectrum of functionalised MFC cannot be measured due to the deformation of the structure of the coupling region after functionalisation. By using a 3D printed PETG holder as the fluidic cavity, the structure of the coupler can be maintained after the functionalisation process but the bending has occurred resulting in the low coupling efficiency between two fibres.

The covalent attachment of DNA to the MFC surface was confirmed by the fluorescent image of the functionalised MFC. After washing the functionalised MFC with a phosphate buffer, the coupling region of the MFC was visualized using a Zeiss Axiovert 200 inverted microscope with epifluorescence illumination fitted with a Zeiss Filter set 02 DAPI. The coupling region of the functionalised MFC was placed face down on a glass slide towards Epiplan Neofluar x20 objective lenses. The fluorescence in a coupling region of the MFC is clearly observed (Figure B.9). Non-uniformity of fluorescence on the coupler surface is a result of surface roughness of a coupler after tapering. This surface roughness can be improved by optimising the tapering parameters such as temperature. The result indicates successful covalent attachment of the DNA to the surface of the MFC. A fluorescently labelled target oligonucleotide was used (instead of an unlabelled target sequence) to provide the definitive evidence for the chemical attachment of hybridisable probe sequences on the MFC by fluorescence microscopy. By using the fluorescently labelled target,

fluorescent image of functionalised MFC is the first stage to confirm the successful of DNA covalent attachment. In the next step, the transmission wavelength shift of functionalised MFC with the variation of DNA concentration need to be observed to indicate the successful of DNA functionalisation process.

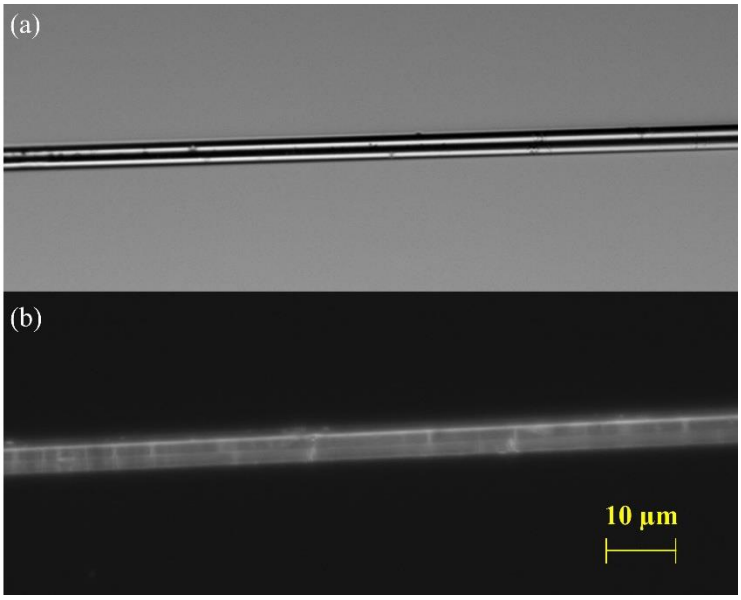

Figure B.9 (a) Microscope image of functionalised MFC without fluorescent emission filter, (b) Microscope image of functionalised MFC with 02 DAPI fluorescent filter.

B.4 Summary

The process of DNA functionalisation on the fibre surface for a DNA sensor has been successfully accomplished. The fluorescence image of functionalised MFC shows the possibility to attach the single strand of DNA to the fibre surface. To calibrate the sensor properly, it will be necessary to sequentially add small volumes of a target DNA to the functionalised sensor and monitor the shift of the optical signal. Once the microfibre is calibrated, then the sensor can be regenerated by flashing the DNA through thermal denaturation (de-hybridisation), washed and then the unknown DNA solution added. Once this has hybridised the optical signal (shift) can be measured and the unknown DNA solution concentration determined providing two readouts (1) the concentration of DNA present, and (2) the positive diagnosis of a disease - such as cancer.

Appendix C

LIST OF PUBLICATIONS

Journal Articles

1. W. Talataisong, J. Gorecki, R. Ismaeel, M. Beresna, D. Schwendemann, V. Apostolopoulos and G. Brambilla, "***Singlemoded THz guidance in bendable TOPAS suspended-core fiber directly drawn from a 3D printer***". Scientific Reports, 10, 11045, (2020).
2. W. Talataisong, R. Ismaeel, M. Beresna, and G. Brambilla, "***Suspended-core microstructured polymer optical fibers and potential applications in sensing***". Sensors, 19 (16), (2019).
3. W. Talataisong, R. Ismaeel, T. Marques, S. Abokhamis Mousavi, M. Beresna, M. Gouveia, S. Sandoghchi, T. Lee, C. Cordeiro, and G. Brambilla "***Mid-IR Hollow-core microstructured fiber drawn from a 3D printed PETG preform***". Scientific Reports, 8, 1-8, (2018).
4. W. Talataisong, R. Ismaeel, S. Sandoghchi, T. Rutirawut, M. Beresna, and G. Brambilla, "***Novel method for manufacturing optical fiber: extrusion and drawing of microstructured polymer optical fibers from a 3D printer***". Optics Express, 26 (24), (2018).
5. W. Talataisong, R. Ismaeel, and G. Brambilla "***A review of microfiber-based temperature sensors***". Sensors, 18 (2), 1-26, (2018).
6. W. Talataisong, R. Ismaeel, L. Timothy, M. Beresna, and G. Brambilla "***Optical nanofiber coupler sensors operating in the cut-off wavelength region***". IEEE Sensors Journal, 18 (7), (2018)
7. W. Talataisong, J. Gorecki, R. Ismaeel, M. Beresna, J. Williamson, K. Addinall, D. Schwendemann, V. Apostolopoulos and G. Brambilla, "***TOPAS hollow-core antiresonant THz fiber extruded from a 3D printer using a metal 3D printed nozzle.***". to be submitted

Conference Papers

1. W. Talataisong, R. Ismaeel, M. Beresna, and G. Brambilla "***Direct extrusion of hollow-core microstructured polymer optical fiber from 3D printer***". The 28th International Conference on Plastic Optical Fibers, Yokohama, Japan (2019).
2. W. Talataisong, L.D. Van Puttena, R. Ismaeel, M. Beresna, and G. Brambilla "***Direct extrusion of hollow-core THz fiber using a 3D printer***". The 6th Workshop on Specialty Optical Fiber and Their Applications, Charleston, USA, (2019).
3. W. Talataisong, R. Ismaeel, T. Lee, M. Beresna, and G. Brambilla "***Optical fibers for bio-sensing applications***". Journal of Physics: Conference Series, Singapore, (2019).
4. R. Ismaeel, A. Beaton, A. Donko, W. Talataisong,T. Lee, T. Brotin, M. Beresna, M. Mowlem, and G. Brambilla, *"**High sensitivity all-fibre methane sensor with gas permeable***

Teflon/cryptophane-A membrane" Conference on Lasers and Electro-Optics Europe & European Quantum Electronics Conference (CLEO/Europe-EQEC), Munich, Germany. 23 - 27 Jun 2019.

5. W. Talataisong, R. Ismaeel, M. Beresna, and G. Brambilla "***Direct extrusion of suspended-core polymer optical fibers from 3D printers***". In Frontiers in Optics, FIO, Washington D.C. (2018).
6. R. Ismaeel, A. Masoudi, Y. Wang, W. Talataisong, N. Chiodini, T. Lee, M. Beresna, and G. Brambilla ***"Giant Faraday rotation in gadolinium doped silica optical fibers for high performance optical isolators"*** Optical Fiber Communication Conference 2018.
7. A. Masoudi, A. Donko, W. Talataisong, R. Ismaeel, M. Beresna, and G. Brambilla **"New approaches to optical fiber sensing"** In Conference on Lasers and Electro-Optics Pacific Rim (CLEO-PR 2018).
8. W. Talataisong, R. Ismaeel, M. Beresna, and G. Brambilla, "***A nano-fibre coupler thermometer***", CLEO Pacific rim conference, Singapore, (2017).
9. R. Ismaeel, W. Talataisong, M. A Gouveia, M. Beresna, and G. Brambilla ***"Anomalous spectral behaviour of weakly-fused optical fibre couplers with sub-micron diameters"*** CLEO/Europe - EQEC 2017, Munich, Germany. 25 - 29 Jun 2017.
10. W. Talataisong, R. Ismaeel, M. Beresna, and G. Brambilla "***Fast-response and High sensitivity nanofiber coupler thermometer***", Optical Nanofiber Applications: From Quantum to Bio Technologies, Japan, (2017).
11. W. Talataisong, R. Ismaeel, M. Beresna, and G. Brambilla "***A nano-fibre coupler refractrometer***", accepted by CLEO Europe conference, Germany, (2017).
12. W. Talataisong, R. Ismaeel, A. Masoudi, M. Beresna, and G. Brambilla, "***Magnetic field sensor based on multi-port microcoil resonator***", OFS 25 conference, Korea, (2017).

References

1. J. Hecht, *City of light: the story of fiber optics*. 1999: Oxford University Press.
2. K. C. Kao and G. A. Hockham, *Dielectric-fibre surface waveguides for optical frequencies.* Proceedings of the Institution of Electrical Engineers, 1966. **113**(7): p. 1151-1158.
3. F. P. Kapron, D. B. Keck and R. D. Maurer, *Radiation losses in glass optical waveguides.* Applied Physics Letters, 1970. **17**(10): p. 423-425.
4. T. Miya, *et al.*, *Ultimate low-loss single-mode fibre at 1.55 μm.* Electronics Letters, 1979. **15**(4): p. 106-108.
5. P. Kaiser and H. W. Astle, *Low-loss single-material fibers made from pure fused silica.* The Bell System Technical Journal, 1974. **53**(6): p. 1021-1039.
6. E. Yablonovitch, *Inhibited spontaneous emission in solid-state physics and electronics.* Physical Review Letters, 1987. **58**(20): p. 2059-2062.
7. J. Sajeev, *Strong localization of photons in certain disordered dielectric superlattices.* Physical Review Letters, 1987. **58**(23): p. 2486-2489.
8. T. A. Birks, *et al.*, *Full 2-D photonic bandgaps in silica/air structures.* Electronics Letters, 1995. **31**(22): p. 1941-1943.
9. J. C. Knight, *et al.*, *All-silica single-mode optical fiber with photonic crystal cladding.* Optics Letters, 1996. **21**(19): p. 1547-1549.
10. J. C. Knight, *et al.*, *Photonic band gap guidance in optical fibers.* Science, 1998. **282**(5393): p. 1476-1478.
11. S. E. Barkou, J. Broeng and A. Bjarklev, *Silica–air photonic crystal fiber design that permits waveguiding by a true photonic bandgap effect.* Optics Letters, 1999. **24**(1): p. 46-48.
12. R. F. Cregan, *et al.*, *Single-mode photonic band gap guidance of light in air.* Science, 1999. **285**(5433): p. 1537-1539.
13. G. Vienne, *et al.*, *Ultra-large bandwidth hollow-core guiding in all-silica Bragg fibers with nano-supports.* Optics Express, 2004. **12**: p. 3500-3508.
14. Y. Fink, *et al.*, *A dielectric omnidirectional reflector.* Science, 1998. **282**(5394): p. 1679-1682.
15. F. Benabid, *et al.*, *Stimulated raman scattering in hydrogen-filled hollow-core photonic crystal fiber.* Science, 2002. **298**(5592): p. 399-402.
16. A. Argyros, *et al.*, *Antiresonant reflection and inhibited coupling in hollow-core square lattice optical fibres.* Optics Express, 2008. **16**(8): p. 5642-5648.
17. A. D. Pryamikov, *et al.*, *Demonstration of a waveguide regime for a silica hollow - core microstructured optical fiber with a negative curvature of the core boundary in the spectral region > 3.5 μm.* Optics Express, 2011. **19**.
18. J. R. Hayes, *et al.*, *Anti-resonant hexagram hollow core fibers.* Optics Express, 2015. **23**: p. 1289-1299.
19. W. Belardi, *Design and properties of hollow antiresonant fibers for the visible and near Infrared spectral range.* Journal of Lightwave Technology, 2015. **33**(21): p. 4497-4503.
20. W. Belardi and J. C. Knight, *Effect of core boundary curvature on the confinement losses of hollow antiresonant fibers.* Optics Express, 2013. **21**: p. 21912-21917.
21. A. N. Kolyadin, *et al.*, *Light transmission in negative curvature hollow core fiber in extremely high material loss region.* Optics Express, 2013. **21**: p. 9514-9519.

22. Z. Liu, *et al.*, *Microstructured optical fiber sensors.* Journal of Lightwave Technology, 2017. **35**(16): p. 3425-3439.
23. H. Han, *et al.*, *Terahertz pulse propagation in a plastic photonic crystal fiber.* Applied Physics Letters, 2002. **80**(15): p. 2634-2636.
24. M. Goto, *et al.*, *Teflon photonic crystal fiber as terahertz waveguide.* Japanese Journal of Applied Physics, 2004. **43**(No. 2B): p. L317-L319.
25. J. F. Federici, *et al.*, *THz imaging and sensing for security applications—explosives, weapons and drugs.* Semiconductor Science and Technology, 2005. **20**(7): p. S266-S280.
26. S. Atakaramians, *et al.*, *THz porous fibers: design, fabrication and experimental characterization.* Optics Express, 2009. **17**(16): p. 14053-14062.
27. M. Navarro-Cía, *et al.*, *Terahertz wave transmission in flexible polystyrene-lined hollow metallic waveguides for the 2.5-5 THz band.* Optics Express, 2013. **21**(20): p. 23748-23755.
28. S. R. Andrews, *Microstructured terahertz waveguides.* Journal of Physics D: Applied Physics, 2014. **47**(37): p. 374004.
29. A. L. S. Cruz, C. M. B. Cordeiro and M. A. R. Franco, *3D printed hollow-core terahertz fibers.* Fibers, 2018. **6**(3): p. 43.
30. L. D. van Putten, *et al.*, *3D-printed polymer antiresonant waveguides for short-reach terahertz applications.* Applied Optics, 2018. **57**(14): p. 3953-3958.
31. M. A. van Eijkelenborg, *et al.*, *Microstructured polymer optical fibre.* Optics Express, 2001. **9**(7): p. 319-327.
32. Y. Zhang, *et al.*, *Casting preforms for microstructured polymer optical fibre fabrication.* Optics Express, 2006. **14**(12): p. 5541-5547.
33. K. Cook, *et al.*, *Step-index optical fiber drawn from 3D printed preforms.* Optics Letters, 2016. **41**(19): p. 4554-4557.
34. K. Cook, *et al.*, *Air-structured optical fiber drawn from a 3D-printed preform.* Optics Letters, 2015. **40**(17): p. 3966-3969.
35. T. A. Birks, J. C. Knight and P. St. J. Russell, *Endlessly single-mode photonic crystal fiber.* Optics Letters, 1997. **22**(13): p. 961-963.
36. A. Ortigosa-Blanch, *et al.*, *Highly birefringent photonic crystal fibers.* Optics Letters, 2000. **25**(18): p. 1325-1327.
37. J. C. Knight, *et al.*, *Anomalous dispersion in photonic crystal fiber.* IEEE Photonics Technology Letters, 2000. **12**(7): p. 807-809.
38. N. G. R. Broderick, *et al.*, *Nonlinearity in holey optical fibers: measurement and future opportunities.* Optics Letters, 1999. **24**(20): p. 1395-1397.
39. J. K. Ranka, R. S. Windeler and A. J. Stentz, *Visible continuum generation in air–silica microstructure optical fibers with anomalous dispersion at 800 nm.* Optics Letters, 2000. **25**(1): p. 25-27.
40. L. Rindorf, *et al.*, *Towards biochips using microstructured optical fiber sensors.* Analytical and Bioanalytical Chemistry, 2006. **385**(8): p. 1370-1375.
41. T. P. Hansen, *et al.*, *Highly birefringent index-guiding photonic crystal fibers.* IEEE Photonics Technology Letters, 2001. **13**(6): p. 588-590.
42. N. A. Mortensen, *et al.*, *Improved large-mode-area endlessly single-mode photonic crystal fibers.* Optics Letters, 2003. **28**: p. 393-395.
43. B. Eggleton, *et al.*, *Cladding-mode-resonances in air-silica microstructure optical fibers.* Journal of Lightwave Technology, 2000. **18**: p. 1084-1100.

44. H. T. Munasinghe, *et al.*, *Lead-germanate glasses and fibers: a practical alternative to tellurite for nonlinear fiber applications.* Optics Material Express, 2013. **3**: p. 1488-1503.
45. H. Ji, *et al.*, *Microstructured suspended core fiber for cylindrical vector beams propagation*. in *in CLEO: 2015, OSA Technical Digest (online) (Optical Society of America, 2015),*. 2015.
46. T. M. Monro, *et al.*, *Sensing with microstructured optical fibres.* Measurement Science and Technology, 2001. **12**(7): p. 854-858.
47. K. M. Kiang, *et al.*, *Extruded singlemode non-silica glass holey optical fibres.* Electronics Letters, 2002. **38**(12): p. 546-547.
48. P. Petropoulos, *et al.*, *Highly nonlinear and anomalously dispersive lead silicate glass holey fibers.* Optics Express, 2003. **11**(26): p. 3568-3573.
49. V. V. Ravi Kanth Kumar, *et al.*, *Tellurite photonic crystal fiber.* Optics Express, 2003. **11**: p. 2641-2645.
50. B. Temelkuran, *et al.*, *Wavelength-scalable hollow optical fibres with large photonic bandgaps for CO_2 laser transmission.* Nature, 2002. **420**(6916): p. 650-653.
51. F. Benabid, J. C. Knight and P. St. J. Russell, *Particle levitation and guidance in hollow-core photonic crystal fiber.* Optics Express, 2002. **10**: p. 1195-1203.
52. N. M. Litchinitser, *et al.*, *Antiresonant reflecting photonic crystal optical waveguides.* Optics Letters, 2002. **27**: p. 1592-1594.
53. R. F. Cregan, *et al.*, *Single-Mode Photonic Band Gap Guidance of Light in Air.* Science, 1999. **285**(5433): p. 1537.
54. D. Passaro, *et al.*, *All-silica hollow-core microstructured Bragg fibers for biosensor application.* IEEE Sensors Journal, 2008. **8**(7): p. 1280-1286.
55. F. Poletti, *Nested antiresonant nodeless hollow core fiber.* Optics Express, 2014. **22**: p. 23807-23828.
56. X. Yu, *et al.*, *Optical fibers for high-power lasers*. 2018: Springer, Singapore.
57. E. A. J. Marcatili and R. A. Schmeltzer, *Hollow metallic and dielectric waveguides for long distance optical transmission and lasers.* The Bell System Technical Journal, 1964. **43**(4): p. 1783-1809.
58. M. Miyagi and S. Nishida, *A proposal of low-loss leaky waveguide for submillimeter waves transmission.* IEEE Transactions on Microwave Theory and Techniques, 1980. **28**(4): p. 398-401.
59. M. Miyagi, *Bending losses in hollow and dielectric tube leaky waveguides.* Applied Optics, 1981. **20**: p. 1221-1229.
60. W. Belardi and J. C. Knight, *Hollow antiresonant fibers with low bending loss.* Optics Express, 2014. **22**(8): p. 10091-10096.
61. T. Kaino, K. Jinguji and S. Nara, *Low loss poly(methylmethacrylate-d8) core optical fibers.* Applied Physics Letters, 1983. **42**(7): p. 567-569.
62. Y. Koike and T. Ishigure, *High-bandwidth plastic optical fiber for fiber to the display.* Journal of Lightwave Technology, 2006. **24**(12): p. 4541-4553.
63. K. Toshikuni, *Polymers for lightwave and integrated optics*, ed. L A Chapter 1. In Hornak, editor. 1992, New York: Marcel Dekker.
64. M. Murofushi, *Low loss perfluorinated POF*. in *International Plastic Optical Fibres conference*. 1996.
65. J. Zubia and J. Arrue, *Plastic optical fibers: an introduction to their technological processes and applications.* Optical Fiber Technology, 2001. **7**(2): p. 101-140.

66. R. Lwin, *et al.*, *Beyond the bandwidth-length product: graded index microstructured polymer optical fiber.* Applied Physics Letters, 2007. **91**(19): p. 191119.

67. A. Argyros, *et al.*, *Hollow-core microstructured polymer optical fiber.* Optics Letters, 2006. **31**: p. 172-174.

68. M. Szczurowski, *et al.*, *Sensing characteristics of birefringent microstructured polymer optical fiber*. 21st International Conference on Optical Fibre Sensors (OFS21). Vol. 7753. 2011: SPIE.

69. M. A.van Eijkelenborg, *et al.*, *Recent progress in microstructured polymer optical fibre fabrication and characterisation.* Optical Fiber Technology, 2003. **9**(4): p. 199-209.

70. G. Emiliyanov, *et al.*, *Localized biosensing with Topas microstructured polymer optical fiber.* Optics Letters, 2007. **32**(5): p. 460-462.

71. M. A. van Eijkelenborg, A. Argyros and S. G. Leon-Saval, *Polycarbonate hollow-core microstructured optical fiber.* Optics Letters, 2008. **33**: p. 2446-2448.

72. A. Dupuis, *et al.*, *Prospective for biodegradable microstructured optical fibers.* Optics Letters, 2007. **32**: p. 109-111.

73. G. Woyessa, *et al.*, *Zeonex microstructured polymer optical fiber: fabrication friendly fibers for high temperature and humidity insensitive Bragg grating sensing.* Optical Materials Express, 2017. **7**(1): p. 286-295.

74. G. Barton, *et al.*, *Fabrication of microstructured polymer optical fibres.* Optical Fiber Technology, 2004. **10**(4): p. 325-335.

75. A. Tuniz, *et al.*, *Fabricating metamaterials using the fiber drawing method.* Journal of visualized experiments : JoVE, 2012(68): p. 4299.

76. C. Markos, *et al.*, *High-Tg TOPAS microstructured polymer optical fiber for fiber Bragg grating strain sensing at 110 degrees.* Optics Express, 2013. **21**(4): p. 4758-4765.

77. M. C. J. Large, *et al.*, *Microstructured polymer optical fibres: new opportunities and challenges.* Molecular Crystals and Liquid Crystals, 2006. **446**(1): p. 219-231.

78. H. P. Nadel, J. E. Spruiell and J. L. White, *Drawing and annealing of polypropylene fibers: structural changes and mechanical properties.* Journal of Applied Polymer Science, 1978. **22**(11): p. 3121-3133.

79. A. Argyros, *et al.*, *Ring structures in microstructured polymer optical fibres.* Optics Express, 2001. **9**(13): p. 813-820.

80. A. Argyros and J. Pla, *Hollow-core polymer fibres with a kagome lattice: potential for transmission in the infrared.* Optics Express, 2007. **15**(12): p. 7713-7719.

81. A. Argyros, S. G. Leon-Saval and M. A. van Eijkelenborg, *Twin-hollow-core optical fibres.* Optics Communications, 2009. **282**(9): p. 1785-1788.

82. A. Filipkowski, *et al.*, *Development of large core microstructured polymer optical fiber*. in *Microstructured and Specialty Optical Fibres*. 2012. Brussels, Belgium: SPIE PHOTONICS EUROPE.

83. M. L. V. Tse, *et al.*, *Superlattice microstructured optical fiber.* Materials, 2014. **7**(6): p. 4567-4573.

84. J. Olszewski, *et al.*, *Highly birefringent microstructured polymer fibers optimized for a preform drilling fabrication method.* Journal of Optics, 2013. **15**(7): p. 075713.

85. G. Wójcik, *et al.*, *High birefringent microstructured polymer optical fiber with frozen stresses*. Twelfth Integrated Optics – Sensors, Sensing Structures and Methods Conference. Vol. 10455. 2017: SPIE.

86. P. Mergo, T. Martynkien and W. Urbanczyk, *Polymer optical microstructured fiber with birefringence induced by stress-applying elements.* Optics Letters, 2014. **39**(10): p. 3018-3021.

87. M. Becker, *et al.*, *Laser-drilled free-form silica fiber preforms for microstructured optical fibers.* Optical Fiber Technology, 2013. **19**(5): p. 482-485.

88. A. Dupuis, *et al.*, *Transmission measurements of hollow-core THz Bragg fibers.* Journal of the Optical Society of America B, 2011. **28**(4): p. 896-907.

89. B. Gauvreau, *et al.*, *Color-changing and color-tunable photonic bandgap fiber textiles.* Optics Express, 2008. **16**(20): p. 15677-15693.

90. Y. Gao, *et al.*, *Consecutive solvent evaporation and co-rolling techniques for polymer multilayer hollow fiber preform fabrication.* Journal of Materials Research, 2011. **21**(9): p. 2246-2254.

91. E. Pone, *et al.*, *Drawing of the hollow all-polymer Bragg fibers.* Optics Express, 2006. **14**(13): p. 5838-5852.

92. X. Lu, H. Qu and M. Skorobogatiy, *Piezoelectric microstructured fibers via drawing of multimaterial preforms.* Scientific Reports, 2017. **7**(1): p. 2907.

93. L. Wang, *et al.*, *A new approach to mass fabrication technology of microstructured polymer optical fiber preform.* Chinese Optics Letters, 2005. **3**(S1): p. S94-S95.

94. H. Ebendorff-Heidepriem, *et al.*, *Extruded high-NA microstructured polymer optical fibre.* Optics Communications, 2007. **273**(1): p. 133-137.

95. H. Ebendorff-Heidepriem and T. M. Monro, *Extrusion of complex preforms for microstructured optical fibers.* Optics Express, 2007. **15**(23): p. 15086-15092.

96. A. Belwalkar, *et al.*, *Extruded tellurite glass optical fiber preforms.* Journal of Materials Processing Technology, 2010. **210**(14): p. 2016-2022.

97. H. Ebendorff-Heidepriem and T. M. Monro, *Analysis of glass flow during extrusion of optical fiber preforms.* Optical Materials Express, 2012. **2**(3): p. 304-320.

98. G. Tao and A. F. Abouraddy, *Drawing robust infrared optical fibers from preforms produced by efficient multimaterial stacked coextrusion*. in *Optical Components and Materials XI*. 2014. San Francisco, California, United States: SPIE OPTO.

99. R. R. Gattass, *et al.*, *Infrared glass-based negative-curvature anti-resonant fibers fabricated through extrusion.* Optics Express, 2016. **24**(22): p. 25697-25703.

100. H. Ji, *et al.*, *A six-strut suspended core fiber for cylindrical vector mode generation and propagation.* Optics Express, 2018. **26**(24): p. 32037-32047.

101. Z. Xue, *et al.*, *Infrared suspended-core fiber fabrication based on stacked chalcogenide glass extrusion.* Journal of Lightwave Technology, 2018. **36**(12): p. 2416-2421.

102. K. Cook and J. Canning, *3D printed photonics*, in *Asia Pacific Optical Sensors (APOS2018)*. 2018: Matsue, Shimane, Japan.

103. N. Vaidya and O. Solgaard, *3D printed optics with nanometer scale surface roughness.* Microsystems & Nanoengineering, 2018. **4**(1): p. 18.

104. A. Kaur, *et al.*, *Affordable terahertz components using 3D printing*. in *2015 IEEE 65th Electronic Components and Technology Conference (ECTC)*. 2015.

105. A. L. S. Cruz, *et al.*, *3D printed hollow core fiber with negative curvature for terahertz applications.* Journal of Microwaves, Optoelectronics and Electromagnetic Applications, 2015. **14**(1): p. 45-53.

106. J. Li, *et al., 3D printed hollow core terahertz Bragg waveguides with defect layers for surface sensing applications.* Optics Express, 2017. **25**(4): p. 4126-4144.

107. T. Ma, *et al., Metallized 3D printed hollow core waveguide Bragg grating for dispersion compensation in terahertz range*. in *2017 42nd International Conference on Infrared, Millimeter, and Terahertz Waves (IRMMW-THz)*. 2017.

108. Z. Wu, *et al., Terahertz electromagnetic crystal waveguide fabricated by polymer jetting rapid prototyping.* Optics Express, 2011. **19**: p. 3962-3972.

109. N. Yudasari, J. Anthony and R. Leonhardt, *Terahertz pulse propagation in 3D-printed waveguide with metal wires component.* Optics Express, 2014. **22**: p. 26042-26054.

110. D. W. Vogt, J. Anthony and R. Leonhardt, *Metallic and 3D-printed dielectric helical terahertz waveguides.* Optics Express, 2015. **23**: p. 33359-33369.

111. J. Yang, *et al., 3D printed low-loss THz waveguide based on Kagome photonic crystal structure.* Optics Express, 2016. **24**: p. 22454-22460.

112. A. L. S. Cruz, *et al., 3D-printed terahertz Bragg fiber*. in *2015 40th International Conference on Infrared, Millimeter, and Terahertz waves (IRMMW-THz)*. 2015.

113. B. Hong, *et al., Low-loss asymptotically single-mode THz Bragg fiber fabricated by digital light processing rapid prototyping.* IEEE Transactions on Terahertz Science and Technology, 2018. **8**(1): p. 90-99.

114. M. G. Zubel, *et al., 3D-printed PMMA preform for hollow-core POF drawing*. in *The 25th International Conference on Plastic Optical Fibers 2016*. 2016. Aston University.

115. T. H. R. Marques, *et al., 3D printed microstructured optical fibers*. in *International Microwave and Optoelectronics Conference*. 2017. Águas de Lindoia, Brazil.

116. W. Talataisong, *et al., Mid-IR hollow-core microstructured fiber drawn from a 3D printed PETG preform.* Scientific Reports, 2018. **8**(1): p. 8113.

117. A. L. S. Cruz, *et al., Exploring THz hollow-core fiber designs manufactured by 3D printing*. in *2017 SBMO/IEEE MTT-S International Microwave and Optoelectronics Conference (IMOC)*. 2017.

118. Q. Zhao, *et al., Optical fibers with special shaped cores drawn from 3D printed preforms.* Optik - International Journal for Light and Electron Optics, 2017. **133**(Supplement C): p. 60-65.

119. E. Arrospide, *et al., Polymers beyond standard optical fibres – fabrication of microstructured polymer optical fibres.* Polymer International, 2018. **67**(9): p. 1155-1163.

120. J. Canning, *et al., Drawing optical fibers from three-dimensional printers.* Optics Letters, 2016. **41**(23): p. 5551-5554.

121. D. Monzón-Hernández, *et al., Temperature sensor based on the power reflected by a Bragg grating in a tapered fiber.* Applied Optics, 2004. **43**(12): p. 2393-2396.

122. X. Zeng, *et al., A temperature sensor based on optical microfiber knot resonator.* Optics Communications, 2009. **282**(18): p. 3817-3819.

123. S. Zhu, *et al., Temperature sensor based on a tapered optical fiber with ALD nanofilm*. in *International Conference on Optical Fibre Sensors (OFS24)*. 2015. SPIE.

124. J. Li, *et al., Highly sensitive temperature sensing probe based on deviation s-shaped microfiber.* Journal of Lightwave Technology, 2017. **35**(17): p. 3699-3704.

125. N. Zhao, *et al., High temperature high sensitivity Mach-Zehnder interferometer based on waist-enlarged fiber bitapers.* Sensors and Actuators A: Physical, 2017. **267**: p. 491-495.

126. Y. Jiang, *et al.*, *Highly sensitive temperature sensor using packaged optical microfiber coupler filled with liquids.* Optics Express, 2018. **26**(1): p. 356-366.

127. G. Brambilla and F. Xu, *Demonstration of a refractometric sensor based on optical microfiber coil resonator*. in *Conference on Lasers and Electro-Optics/Quantum Electronics and Laser Science Conference and Photonic Applications Systems Technologies*. 2008. San Jose, California: Optical Society of America.

128. K. S. Lim, *et al.*, *Integrated microfibre device for refractive index and temperature sensing.* Sensors, 2012. **12**(9): p. 11782-11789.

129. K. J. Lee, *et al.*, *Refractive index sensor based on a polymer fiber directional coupler for low index sensing.* Optics Express, 2014. **22**(14): p. 17497-17507.

130. C. Wu, *et al.*, *Characterization of pressure response of Bragg gratings in grapefruit microstructured fibers.* Journal of Lightwave Technology, 2010. **28**(9): p. 1392-1397.

131. X. Zou, *et al.*, *Ultrafast Fabry-Perot fiber-optic pressure sensors for multimedia blast event measurements.* Applied Optics, 2013. **52**(6): p. 1248-1254.

132. F. Xu, *et al.*, *Fiber-optic acoustic pressure sensor based on large-area nanolayer silver diaghragm.* Optics Letters, 2014. **39**(10): p. 2838-2840.

133. W. Talataisong, *et al.*, *Fiber in-line Mach-Zehnder interferometer based on an inner air-cavity for high-pressure sensing.* Optics Letters, 2015. **40**(7): p. 1220-1222.

134. Y. Chen, *et al.*, *Optical fiber magnetic field sensor based on single-mode-multimode-single-mode structure and magnetic fluid.* Optics Letters, 2013. **38**(20): p. 3999-4001.

135. C. Feifei and J. Yi, *Fiber optic magnetic field sensor based on the TbDyFe rod.* Measurement Science and Technology, 2014. **25**(8): p. 085106.

136. M. Belal, *et al.*, *Optical fiber microwire current sensor.* Optics Letters, 2010. **35**(18): p. 3045-3047.

137. G. Y. Chen, *et al.*, *High frequency current sensing using optical fiber micro-wire*. in *2011 Conference on Lasers and Electro-Optics Europe and 12th European Quantum Electronics Conference (CLEO EUROPE/EQEC)*. 2011.

138. M. El-Sherif, L. Bansal and J. Yuan, *Fiber optic sensors for detection of toxic and biological threats.* Sensors (Basel, Switzerland), 2007. **7**(12): p. 3100-3118.

139. M. A. Pérez, O. González and J. R. Arias, *Optical fiber sensors for chemical and biological measurements*, in *Current Developments in Optical Fiber Technology*, Sulaiman Wadi Harun and Hamzah Arof, Editors. 2013, InTech: Rijeka. p. Ch. 10.

140. X. Wu, *et al.*, *Fiber-optic biological/chemical sensing system based on degradable hydrogel.* IEEE Sensors Journal, 2018. **18**(1): p. 45-52.

141. G. Y. Chen, *et al.*, *A review of microfiber and nanofiber based optical sensors.* The open optics journal, 2013. **7**: p. 32-57.

142. O. Ziemann, *et al.*, *POF - polymer optical fibers for data communication*, ed. 1. 2002.

143. A. Leung, P. M. Shankar and R. Mutharasan, *A review of fiber-optic biosensors.* Sensors and Actuators B: Chemical, 2007. **125**(2): p. 688-703.

144. K. Mileńko, *et al.*, *Hollow-core Bragg fiber for bio-sensing applications.* Acta Physica Polonica A, 2010. **118**: p. 1025-1028.

145. S. C. Xue, *et al.*, *Fabrication of microstructured optical fibers-part II: numerical modeling of steady-state draw process.* Journal of Lightwave Technology, 2005. **23**(7): p. 2255-2266.

146. S. C. Xue, *et al.*, *Fabrication of microstructured optical fibers-part I: problem formulation and numerical modeling of transient draw process.* Journal of Lightwave Technology, 2005. **23**(7): p. 2245-2254.

147. P. Latko-Durałek, K. Dydek and A. Boczkowska, *Thermal, rheological and mechanical properties of PETG/rPETG blends.* Journal of Polymers and the Environment, 2019. **27**(11): p. 2600-2606.

148. H. Ebendorff-Heidepriem, *et al.*, *Bismuth glass holey fibers with high nonlinearity.* Optics Express, 2004. **12**(21): p. 5082-5087.

149. X. Feng, *et al.*, *Extruded singlemode, high-nonlinearity, tellurite glass holey fibre.* Electronics Letters, 2005. **41**(15): p. 835-837.

150. J. Y. Y. Leong, *et al.*, *High-nonlinearity dispersion-shifted lead-silicate holey fibers for efficient 1-μm pumped supercontinuum generation.* Journal of Lightwave Technology, 2006. **24**(1): p. 183-190.

151. A. V. Shenoy and D. R. Saini, *Rheological models for unified curves for simplified design calculations in polymer processing.* Rheologica Acta, 1984. **23**(4): p. 368-377.

152. Engineering ToolBox (2009). *Thermal conductivities of heat exchanger materials*. Available from: https://www.engineeringtoolbox.com/heat-exchanger-material-thermal-conductivities-d_1488.html

153. *Indoor air velocity*. 2019 19 Aug 2019; Available from: https://www.designingbuildings.co.uk/wiki/Indoor_air_velocity.

154. P. Kosky, *et al.*, *Exploring Engineering*. 3rd ed. 2013: Elsevier Inc.

155. S. Hodgman and D. Charles, *Handbook of chemistry and physics*. 1954, Cleveland, Ohio: Chemical Rubber Publishing Company.

156. R. K. Gupta, *Polymer and composite rheology*, ed. 2. 2000, USA.: Marcel Dekker, Inc.

157. G. L. Wilkes, *An overview of the basic rheological behavior of polymer fluids with an emphasis on polymer melts.* Journal of Chemical Education, 1981. **58**(11): p. 880-892.

158. T. Sedlacek, *et al.*, *On the effect of pressure on the shear and elongational viscosities of polymer melts.* Polymer Engineering & Science, 2004. **44**(7): p. 1328-1337.

159. Engineering ToolBox. *Metals and alloys - melting temperatures*. 2005 [cited 2020 25 April]; Available from: https://www.engineeringtoolbox.com/melting-temperature-metals-d_860.html

160. H. Ebendorff-Heidepriem, *et al.*, *3D-printed extrusion dies: a versatile approach to optical material processing.* Optical Materials Express, 2014. **4**(8): p. 1494-1504.

161. R. Hölker, *et al.*, *Controlling heat balance in hot aluminum extrusion by additive manufactured extrusion dies with conformal cooling channels.* International Journal of Precision Engineering and Manufacturing, 2013. **14**(8): p. 1487-1493.

162. E. Utley. *An introduction to designing for metal 3D printing*. 2017 12 June 2017 [cited 2020 28 April]; Available from: https://blogs.solidworks.com/solidworksblog/2017/06/introduction-designing-metal-3d-printing.html.

163. B. Redwood. *Dimensional accuracy of 3D printed parts*. [cited 2020 8 May]; Available from: https://www.3dhubs.com/knowledge-base/dimensional-accuracy-3d-printed-parts/.

164. N. T. Aboulkhair, *et al.*, *3D printing of aluminium alloys: additive manufacturing of aluminium alloys using selective laser melting.* Progress in Materials Science, 2019. **106**: p. 100578.

165. O. Çetinkaya, G. Wojcik and P. Mergo, *Decreasing diameter fluctuation of polymer optical fiber with optimized drawing conditions.* Materials Research Express, 2018. **5**(5): p. 056201.

166. A. S. Webb, *et al.*, *Suspended-core holey fiber for evanescent-field sensing.* Optical Engineering, 2007. **46**(1): p. 010503-1-010503-3.

167. S. C. Warren-Smith, S. Afshar V and T. M. Monro, *Theoretical study of liquid-immersed exposed-core microstructured optical fibers for sensing.* Optics Express, 2008. **16**(12): p. 9034-9045.

168. T. Nemecek, *et al.*, *Suspended-core microstructured fiber for refractometric detection of liquids.* Applied Optics, 2015. **54**(30): p. 8899-8903.

169. A. R. Tynes, A. D. Pearson and D. L. Bisbee, *Loss mechanisms and measurements in clad glass fibers and bulk glass.* Journal of the Optical Society of America B, 1971. **61**(2): p. 143-153.

170. S. R. Sandoghchi, *et al.*, *Optical side scattering radiometry for high resolution, wide dynamic range longitudinal assessment of optical fibers.* Optics Express, 2015. **23**(21): p. 27960-27974.

171. G. C. Trichopoulos, *et al.*, *A broadband focal plane array camera for real-time THz imaging applications.* IEEE Transactions on Antennas and Propagation, 2013. **61**(4): p. 1733-1740.

172. U. R. Pfeiffer, *et al.*, *14.5 A 0.53THz reconfigurable source array with up to 1mW radiated power for terahertz imaging applications in 0.13µm SiGe BiCMOS*. in *2014 IEEE International Solid-State Circuits Conference Digest of Technical Papers (ISSCC)*. 2014.

173. E. V. Yakovlev, *et al.*, *Non-destructive evaluation of polymer composite materials at the manufacturing stage using terahertz pulsed spectroscopy.* IEEE Transactions on Terahertz Science and Technology, 2015. **5**(5): p. 810-816.

174. D. M. Mittleman, *Twenty years of terahertz imaging [Invited].* Optics Express, 2018. **26**: p. 9417-9431.

175. K. Wang and D. M. Mittleman, *Metal wires for terahertz wave guiding.* Nature, 2004. **432**(7015): p. 376-379.

176. M. Zhang and J. T. W. Yeow, *Nanotechnology-based terahertz biological sensing: a review of its current state and things to come.* IEEE Nanotechnology Magazine, 2016. **10**(3): p. 30-38.

177. P. Doradla, C. Joseph and R. H. Giles, *Terahertz endoscopic imaging for colorectal cancer detection: current status and future perspectives.* World journal of gastrointestinal endoscopy, 2017. **9**(8): p. 346-358.

178. M. Borovkova, *et al.*, *Terahertz time-domain spectroscopy for non-invasive assessment of water content in biological samples.* Biomedical Optics Express, 2018. **9**: p. 2266-2276.

179. M. S. Islam, *et al.*, *A novel approach for spectroscopic chemical identification using photonic crystal fiber in the terahertz regime.* IEEE Sensors Journal, 2018. **18**(2): p. 575-582.

180. D. F. Swearer, *et al.*, *Monitoring chemical reactions with terahertz rotational spectroscopy.* ACS Photonics, 2018. **5**(8): p. 3097-3106.

181. I. F. Akyildiz, J. M. Jornet and C. Han, *Terahertz band: next frontier for wireless communications.* Physical Communication, 2014. **12**: p. 16-32.

182. B. Moyna. *Terahertz and millimetre-wave receivers and radiometers*. 18 June 2020]; Available from: https://www.ralspace.stfc.ac.uk/Pages/Terahertz-and-Millimetre-Wave-Receivers-and-Radiometers.aspx.

183. S. U. Hwu, K. B. deSilva and C. T. Jih, *Terahertz (THz) wireless systems for space applications.* in *IEEE Sensors Applications Symposium*. 2013.

184. S. S. Dhillon, *et al.*, *The 2017 terahertz science and technology roadmap*. Journal of Physics D: Applied Physics, 2017. **50**(4): p. 043001.

185. D. W. Vogt and R. Leonhardt, *3D printed broadband dielectric tube terahertz waveguide with anti-reflection structure.* Journal of Infrared, Millimeter, and Terahertz Waves, 2016. **37**(11): p. 1086-1095.

186. R. Khabibullin, *et al.*, *Silver-based double metal waveguide for terahertz quantum cascade laser*. The International Conference on Micro- and Nano-Electronics 2018. Vol. 11022. 2019: SPIE.

187. B. You and J. Y. Lu, *Remote and in situ sensing products in chemical reaction using a flexible terahertz pipe waveguide.* Optics Express, 2016. **24**: p. 18013-18023.

188. G. C. Trichopoulos and K. Sertel, *Polarimetric terahertz probe for endoscopic assessment of malignancies*. in *2015 IEEE International Symposium on Antennas and Propagation & USNC/URSI National Radio Science Meeting*. 2015.

189. B. Ung, *et al.*, *Polymer microstructured optical fibers for terahertz wave guiding.* Optics Express, 2011. **19**: p. B848-B861.

190. A. Argyros, M. Hu and D. Kouznetsov, *Microstructures in polymer fibres for optical fibres, THz waveguides, and fibre-based metamaterials.* ISRN Optics, 2013. **2013**: p. 785162.

191. R. Mendis and D. Grischkowsky, *Plastic ribbon THz waveguides.* Journal of Applied Physics, 2000. **88**(7): p. 4449-4451.

192. K. Nielsen, *et al.*, *Bendable, low-loss Topas fibers for the terahertz frequency range.* Optics Express, 2009. **17**.

193. Q. Chen, *et al.*, *Design and fabrication of cyclic-olefin copolymer based terahertz hollow-core photonic crystal fiber*. in *2013 38th International Conference on Infrared, Millimeter, and Terahertz Waves (IRMMW-THz)*. 2013.

194. Q. Chen, *et al.*, *Development of 2.5THz suspended porous microstructured fiber based on cyclic-olefin copolymer.* Optik, 2017. **145**: p. 56-60.

195. M. S. Islam, *et al.*, *Ultra low-loss hybrid core porous fiber for broadband applications.* Applied Optics, 2017. **56**: p. 1232-1237.

196. H. Zhang, J. Horvat and R. A. Lewis, *Terahertz spectroscopic characterization for carbon-based materials*. in *2016 41st International Conference on Infrared, Millimeter, and Terahertz waves (IRMMW-THz)*. 2016.

197. W. Talataisong, *et al.*, *Novel method for manufacturing optical fiber: extrusion and drawing of microstructured polymer optical fibers from a 3D printer.* Optics Express, 2018. **26**(24): p. 32007-32013.

198. C. M. Smith, *et al.*, *Low-loss hollow-core silica/air photonic bandgap fibre.* Nature, 2003. **424**(6949): p. 657-659.

199. S. Atakaramians, *et al.*, *Terahertz dielectric waveguides.* Advances in Optics and Photonics, 2013. **5**: p. 169-215.

200. S. Yan, *et al.*, *High-birefringence hollow-core anti-resonant THz fiber.* Optical and Quantum Electronics, 2018. **50**(3): p. 162.

201. C. S. Ponseca, *et al.*, *Transmission of terahertz radiation using a microstructured polymer optical fiber*. Optics Letters, 2008. **33**: p. 902-904.

202. B. Ung, *et al.*, *High-refractive-index composite materials for terahertz waveguides: trade-off between index contrast and absorption loss.* Journal of the Optical Society of America B, 2011. **28**: p. 917-921.

203. A. Stefani, S. C. Fleming and B. T. Kuhlmey, *Terahertz orbital angular momentum modes with flexible twisted hollow core antiresonant fiber.* APL Photonics, 2018. **3**(5): p. 051708.

204. W. Lu and A. Argyros, *Terahertz spectroscopy and imaging with flexible tube-lattice fiber probe.* Journal of Lightwave Technology, 2014. **32**(23): p. 4621-4627.

205. F. Poletti, J. R. Hayes and D. J. Richardson, *Optimising the performances of hollow antiresonant fibres*. in *2011 37th European Conference and Exhibition on Optical Communication*. 2011.

206. V. Apostolopoulos and M. E. Barnes, *THz emitters based on the photo-Dember effect.* Journal of Physics D: Applied Physics, 2014. **47**(37): p. 374002.

207. C. W. Brown and Y. Li C. S. Chen, *Near- and mid-infrared chemical and biological sensors*. in *SPIE's 1995 International Symposium on Optical Science, Engineering, and Instrumentation*. 1995. SPIE.

208. A. Jha, *et al.*, *Recent advances in mid-IR optical fibres for chemical and biological sensing in the 2-15 μm spectral range*. in *Photonics North 2009*. 2009. SPIE.

209. F. Starecki, *et al.*, *Mid-IR optical sensor for CO_2 detection based on fluorescence absorbance of Dy^{3+}:$Ga_5Ge_{20}Sb_{10}S_{65}$ fibers.* Sensors and Actuators B: Chemical, 2015. **207**(Part A): p. 518-525.

210. J. Martínez, *et al.*, *Mid-infrared surface plasmon polariton chemical sensing on fiber-coupled ITO coated glass.* Optics Letters, 2016. **41**(11): p. 2493-2496.

211. B. Mizaikoff, *Waveguide-enhanced mid-infrared chem/bio sensors.* Chemical Society Reviews, 2013. **42**(22): p. 8683-8699.

212. J. S. Sanghera, L. B. Shaw and I. D. Aggarwal, *Applications of chalcogenide glass optical fibers.* Comptes Rendus Chimie, 2002. **5**(12): p. 873-883.

213. B. Bureau, *et al.*, *Chalcogenide optical fibers for mid-infrared sensing.* Optical Engineering, 2014. **53**: p. 8.

214. G. Tao, *et al.*, *Infrared fibers.* Advances in Optics and Photonics, 2015. **7**(2): p. 379-458.

215. J. A. Harrington, *A review of IR transmitting, hollow waveguides.* Fiber and Integrated Optics, 2000. **19**(3): p. 211-227.

216. J. M. Kriesel, *et al.*, *Hollow core fiber optics for mid-wave and long-wave infrared spectroscopy*. in *SPIE Defense, Security, and Sensing*. 2011. SPIE.

217. P. Patimisco, *et al.*, *Low-loss hollow waveguide fibers for mid-infrared quantum cascade laser sensing applications.* Sensors (Basel, Switzerland), 2013. **13**(1): p. 1329-1340.

218. V. Spagnolo, *et al.*, *Mid-infrared fiber-coupled QCL-QEPAS sensor.* Applied Physics B, 2013. **112**(1): p. 25-33.

219. A. Sampaolo, *et al.*, *Single mode operation with mid-IR hollow fibers in the range 5.1-10.5 μm.* Optics Express, 2015. **23**(1): p. 195-204.

220. J. D. Shephard, *et al.*, *Single-mode mid-IR guidance in a hollow-core photonic crystal fiber*. Optics Express, 2005. **13**(18): p. 7139-7144.

221. Y. Jung, G. Brambilla and D. J. Richardson, *Optical microfiber coupler for broadband single-mode operation.* Optics Express, 2009. **17**(7): p. 5273-5278.

222. G. Brambilla, *Optical fibre nanowires and microwires: a review.* Journal of Optics, 2010. **12**(4): p. 043001.

223. A. Troy and Jr. Scott, *Refractive index of ethanol-water mixtures and density and refractive index of ethanol-water-ethyl ether mixtures.* Journal of Physical Chemistry, 1946. **50**(5): p. 406–412.

224. M. Ding, P. Wang and G. Brambilla, *A microfiber coupler tip thermometer*. Optics Express, 2012. **20**(5): p. 5402-5408.

225. X. Fan, *et al.*, *Sensitive optical biosensors for unlabeled targets: A review*. Analytica Chimica Acta, 2008. **620**(1): p. 8-26.

226. F. P. Payne, C. D. Hussey and M. S. Yataki, *Polarisation analysis of strongly fused and weakly fused tapered couplers.* Electronics Letters 1985. **21**(13): p. 561-563.

227. L. A. Chrisey, G. U. Lee and C. E. O'Ferrall, *Covalent attachment of synthetic DNA to self-assembled monolayer films.* Nucleic Acids Research, 1996. **24**(15): p. 3031-3039.

228. C. R. Taitt, G. P. Anderson and F. S. Ligler, *Evanescent wave fluorescence biosensors.* Biosensors and Bioelectronics, 2005. **20**(12): p. 2470-2487.